


Development of Calibration Methods For A Ku-Band Polarimetric Terrestrial Radar Interferometer

Doctoral Thesis

Author(s):

[Baffelli, Simone](#) 

Publication date:

2019

Permanent link:

<https://doi.org/10.3929/ethz-b-000334412>

Rights / license:

[In Copyright - Non-Commercial Use Permitted](#)



Doctoral Thesis

Development of Calibration Methods For A Ku-Band Polarimetric Terrestrial Radar Interferometer

Author(s):

Baffelli, Simone

Publication Date:

2019

Permanent Link:

<https://doi.org/10.3929/ethz-b-000334412> →

Rights / License:

[In Copyright - Non-Commercial Use Permitted](#) →

This page was generated automatically upon download from the [ETH Zurich Research Collection](#). For more information please consult the [Terms of use](#).

DISS. ETH NO. 25673

DEVELOPMENT OF CALIBRATION METHODS FOR A KU-BAND POLARIMETRIC TERRESTRIAL RADAR INTERFEROMETER

A thesis submitted to attain the degree of

DOCTOR OF SCIENCES of ETH ZURICH
(Dr. sc. ETH Zurich)

presented by

SIMONE GIACOMO BAFFELLI

MSc. ETH in Electrical Engineering and Information Technology
Eidgenössische Technische Hochschule Zürich (ETHZ), Switzerland
born on 26.04.1988
citizen of Giornico TI

accepted on the recommendation of

Prof. Dr. Irena Hajnsek, examiner
Dr. Othmar Frey, co-examiner
Prof. Dr. Torbjørn Eltoft, co-examiner
Prof. Dr. Carlos López-Martínez, co-examiner
Prof. Dr.-Ing Marwan Younis, co-examiner

2019

Keywords: Terrestrial radar interferometry (TRI), atmospheric phase corrections, radar interferometry, polarimetry, interferometry, Ku-Band



ETH zürich

Copyright © 2018 - Simone Giacomo Baffelli

Chair of Earth Observation and Remote Sensing, Swiss Federal Institute of Technology, ETH Zürich, Switzerland. All rights reserved.

No part of the material protected by this copyright notice may be reproduced or utilized in any form or by any means, electronic or mechanical, including photocopying, recording or by any information storage and retrieval system, without prior permission of the author.

He has been eight years upon a project for extracting sunbeams out of cucumbers, which were to be put in phials hermetically sealed, and let out to warm the air in raw inclement summers. He told me, he did not doubt, that, in eight years more, he should be able to supply the governor's gardens with sunshine, at a reasonable rate: but he complained that his stock was low, and entreated me "to give him something as an encouragement to ingenuity, especially since this had been a very dear season for cucumbers".

Johnatan Swift's, Gulliver's travels

PREFACE

The main topic of this cumulative dissertation is KAPRI, a Ku-Band polarimetric terrestrial radar interferometer. The device is based on the Gamma Portable Radar Interferometer (GPRI) II a system developed for deformation monitoring using differential radar interferometry. This thesis explores several topics related to the device's calibration and applications for the monitoring of changes in natural terrain using radar interferometry and polarimetry by the means of three studies in the form of self-contained chapters (Chapters 2,3 and 4 in this thesis) that were published or submitted for publication in peer-reviewed scientific journals.

Chapter 1 provides an introduction for readers who have a technical education but no familiarity with terrestrial radar systems, radar interferometry and radar polarimetry. Section 1.2 provides an overview and a literature review of these techniques, while the rationale for this dissertation is discussed in Section 1.3.

After the introduction follow three self-contained investigations, Chapters 2,3 and 4, which document the core of this dissertation. Finally, the main findings of this work are discussed in Chapter 5 and suggestions for future research are provided as concluding remarks.

Simone Giacomo Baffelli
Zurich, 2018

ACKNOWLEDGEMENTS

As much as I like to think myself of a self-reliant individual, this is obviously not true: this thesis has only been possible thanks to many people that supported me, knowingly or not. This chapter was the most difficult to write: you are so many and did so much for me!

I am deeply grateful to my parents Gianni and Myriam, who provided me the best material and spiritual support a man could ever want. Their love, support, encouragement and example will be unsurpassed. I am thankful to my sister and sometimes flatmate Chiara, whose relaxed determination I always admire. Thanks to all my relatives for the positive example they provided, their support and the beautiful moments—usually sitting at a table and enjoying food and discussions—I shared with them. I cannot name you all, but you are never forgotten!

Of course, my friends everywhere deserve a mention: with some—like Lorenzo and Flavio—I grew up with and am still growing: they are my confidants and my models. The same gratitude I extend to Eros, whose confidence and determination I always looked up to. Others, like Gabriele—whose love for nature I deeply admire—I don't see as much as I like, but every time we meet it feels like we parted yesterday. I am thankful to all the friends I made while studying—Nicolò, Jonas, Ari, Sergio, Ema, Marcello, Davide, Michela, Stefano, Thomas, Romina, Samantha, and many more—with whom I spent fun and challenging times: meeting you is always a pleasure. Thanks to all my cycling mates (Samir, Stefano, Eugenio, Luca and the many other cyclists with whom I shared the road) for providing me challenges and recreation: see you soon on the road.

Thanks to the many flatmates I had the pleasure of living with in the course of the last decade: the first two, Simone and Alex, with whom I had great fun in the chaotic undergraduate times. I also had great times watching trash TV and discussing my worries with Manuela! Thanks, Inigo for the Basque cider: you only stayed for a short while, but I enjoyed discussing with you. Thanks to Matthew, I enjoyed our conversations about food and cooking. Thanks to Lilly for your wise words. Thanks to Rebecca for your Brazilian cooking and your cheerful mood.

I am very thankful to my thesis supervisor, Prof. Irena Hajnsek for her trust and support. Her guidance helped me to mature, both as a researcher and as a person. The same gratitude I owe to my co-supervisor and officemate Dr. Othmar Frey, who had confidence in my technical abilities. He supported me with his knowledge of radar techniques and precious scientific writing advice.

Thanks to my colleagues, who provided me with much-needed motivation, support and recreation. Thank you Adnan for the countless hours spent discussing academic and real world politics, religion and philosophy. The same to Philipp, with whom I had the pleasure to discuss science, but also nutrition, philosophy and public health policies. Thanks to Simon, whose erudition and endurance I envy: cycle tours with you were always a pleasure, especially so cake stops! Thank you, Silvan for the many conversation on physics and computer science, I wish was as adventurous as you! Grazie a Manuele, who always listened to my worries and who like me loved nonsensical jokes and puns. Thanks to Roberto: I wish I could be as positive as you are. Thanks to Armando, with whom I could discuss anything and who's always been supportive of my crazy ideas. Thanks to Celia, the most Swiss non-Swiss person I ever met, who helped me with fieldwork and with whom I shared our worries about KAPRI. Thanks to Onur for introducing me to *Ayran* and *Salgam*. Grazie a Virginia, who was always willing to discuss science, current affairs and cooking. *Merci vilmol* to Rita, whose bureaucratic and personal support has been

invaluable. Thanks to our other secretary Ani, which also did a flawless job to support us. Last —but only in temporal order— I would like to thank the colleagues that joined recently. Thanks to Jie Chen for providing us with delicious green tea and fascinating insight in Chinese culture. The same to Lanquin Huang, who taught me my first Chinese characters: and to whom I had the pleasure to show the first steps in radar polarimetry. Thanks, Marcel, we only briefly worked together, but I enjoyed showing you how KAPRI works and talking about cuisine, science, politics and flow-based programming.

Thanks to Paolo Di Tommaso and Samuel Lampa, whom I never met in person. Discussing with you on flow-based-programming helped me hone my programming skills and kept me motivated in difficult times.

Finally, thanks to all those of you I could not name individually!

SUMMARY

Imaging radar systems are a fundamental tool for remote sensing: by using the sensitivity of electromagnetic waves to the geometrical and dielectric properties of objects they interact with, these devices permit to observe many natural phenomena. These devices have been exploited for a range of applications in the geosciences; for example to monitor glacier flows, the inflation of volcanoes, to detect land subsidence or to estimate environmental parameters. Spaceborne imaging radars are used in the reconstruction of post-seismic displacements, for the observation of land subsidence, in maritime surveillance, for the estimation of vegetation height and growth stage, the production of digital elevation models and many other applications.

In most of the above cases, spaceborne —or to a lesser extent airborne— synthetic aperture radar (SAR) sensors are employed to acquire the data. These systems acquire images with excellent spatial resolution and coverage; their main drawback —particularly in the case of spaceborne SAR— is the inflexible acquisition schedule, which does not allow to image the same region more often than every few days at best. However, the study of many natural processes requires a denser temporal sampling to capture their dynamics.

Terrestrial radars —also known as ground based radars or ground based SAR— are complementary to space- and airborne SAR systems for the observation of fast changes of limited spatial extent since they permit greater flexibility in the acquisition mode and scheduling. This dissertation concentrates on KAPRI a Ku-Band polarimetric terrestrial radar interferometer based on the Gamma Portable Radar Interferometer II (GPRI-II), which was modified by the manufacturer to add polarimetric imaging capabilities. The thesis focuses on two aspects: on the one hand the data processing and calibration techniques needed to obtain radar data free from distortion caused either by the device's design and environmental effects; on the other hand the applications and the suitability of such data for the observation of changes in the natural environment. These two aspects are elaborated and assessed with three publications that are the main contributions of this research work; these papers focus respectively on data preprocessing and polarimetric calibration, phase calibration for differential interferometry and the analysis of polarimetric signatures of natural terrain.

The first investigation deals with the data processing and calibration needed to convert the raw data acquired by the radar into properly focused polarimetric radar images. Preprocessing methods to mitigate the geometric distortion caused by the antenna frequency response inducing beam squint and cross-range phase ramp induced by the polar acquisition geometry were developed, followed by a polarimetric calibration model adapted to the system's antenna design. These methods were validated by studying the response of corner reflectors, whose radar reflectivity and polarimetric signature is well-known. The results show that applying the proposed methods permits to obtain radar images with an imaging resolution close to the nominal resolution, free of cross-range phase ramps and with minimal residual polarimetric distortion.

The second investigation is dedicated to the statistical modeling and correction of the atmospheric phase screen (APS), a significant obstacle to precise deformation monitoring using radar interferometry: by exploiting the sensitivity of the radar signal's phase to variations in the distance between sensor and targets, this technique allows to measure displacements with a precision potentially limited only by the wavelength and by various sources of phase noise. However, other effects also modify the radar phase; among them variations in the distribution of atmospheric water vapor in the scene, which can

be of a magnitude comparable to the displacement signal and may severely reduce the precision of the displacement estimates. The spatio-temporal statistical behavior of the APS and its mitigation has been extensively studied: the main assumption being that the APS is correlated in space and uncorrelated in time for the typical acquisition scenarios. However, there is lack of research on whether these results can translate to terrestrial radar interferometry (TRI), where the spatial extension of the scene is typically smaller and the acquisition repeat time can be as short as a minute. In this study, these questions are assessed with the help of an interferometric stack acquired using KAPRI near the Bisgletscher glacier, in the Swiss Alps. The analysis shows that the APS is correlated both in space and time but that its spatio-temporal statistics are approximately separable, so that given a stack of interferograms a fraction of the phase variation can be corrected on individual interferograms by spatial interpolation from a set of locations known not to be affected by deformation, while the remaining residual phase variation is only correlated in time and can be corrected by a temporal filter operating on individual pixels along the stack reducing the computational complexity of the correction.

The third and last investigation returns to the polarimetric aspects of KAPRI and aims to assess the suitability of Ku-Band polarimetric data for the observation of natural terrain: while the polarimetric response of natural surfaces at L- and X- band are widely investigated thanks to the availability of space- and airborne sensors operating at these wavelengths, much less information is available at Ku-Band. Two datasets covering alpine terrain and an agricultural areas are used to this end by studying the polarimetric signatures of different terrain types, showing a consistently high cross-polarized power and Cloude-Pottier entropy for all land cover types but for individual highly reflective scatterers such as radar reflectors or single buildings. These observations suggest a high level of scattering randomness, likely due to the presence of depolarizing scattering from random media and to the combination of a short wavelength and a relatively large resolution cell size.

RIASSUNTO

I sistemi di imaging radar sono un strumento fondamentale per il telerilevamento. Poichè le onde elettromagnetiche sono sensibili alle proprietà geometriche e dielettriche degli oggetti con cui interagiscono, i sistemi radar permettono di osservare diversi fenomeni naturali. Tra gli esempi di applicazioni si possono citare il monitoraggio del flusso di ghiacciai e dell'espansione del terreno legata all'attività di vulcani, la misura di deformazioni post-sismiche e della subsidenza causata dal pompaggio di falde acquifere, la sorveglianza del traffico marittimo, la produzione di modelli digitali del terreno e la misura della struttura e dell'altezza di foreste e colture agricole.

Nella maggior parte dei casi, questi compiti di monitoraggio sono svolti utilizzando immagini acquisite con sistemi radar ad apertura sintetica (SAR) montati su satelliti in orbita polare o più raramente con sensori SAR aviotrasportati. Le immagini acquisite da tali sistemi hanno un'eccellente risoluzione e copertura spaziale, tuttavia i sistemi satellitari e aviotrasportati hanno lo svantaggio di elevati costi di acquisto e di operazione. Inoltre cicli di acquisizione molto brevi,—nell'ordine dei minuti— che sono necessari per osservare le dinamiche di molti processi sono difficili da ottenere con tali sistemi. In questo senso i radar terrestri —spesso conosciuti anche come radar ground-based- o GB-SAR— sono complementari ai sistemi su satellite e aviotrasportati; essi sono relativamente economici e consentono grande flessibilità nelle modalità e nei tempi di acquisizione, facendone degli ottimi strumenti per l'osservazione di rapidi cambiamenti la cui estensione è limitata.

Il fulcro di questa dissertazione è KAPRI, un radar polarimetrico terrestre operante in banda Ku. KAPRI è la versione polarimetrica di Gamma Portable Radar Interferometer II (GPRI-II), un radar concepito per il monitoraggio di spostamenti del terreno con la tecnica dell'interferometria differenziale. La dissertazione tratta due temi. Il primo aspetto riguarda la preparazione e la calibrazione dei dati acquisiti da KAPRI, affinché essi siano liberi da distorsioni causate dall'architettura hardware o da influssi esterni quali variazioni atmosferiche. Questa preparazione è necessaria per proseguire con il secondo aspetto di questo studio, dove si investiga il potenziale dei dati così preparati nelle applicazioni di monitoraggio di fenomeni naturali, con particolare riguardo allo studio dell'utilizzo di dati polarimetrici. I suddetti temi sono discussi tramite tre studi separati dedicati a differenti aspetti, ovvero preparazione dei dati e calibrazione polarimetrica, calibrazione di fase per l'interferometria differenziale e l'analisi della risposta polarimetrica di superfici naturali.

La prima investigazione si concentra sulla preparazione dei dati e la calibrazione necessarie per trasformare i dati grezzi acquisiti dal radar in immagini polarimetriche correttamente calibrate. A tal fine si sono sviluppati degli algoritmi capaci di ridurre le distorsioni geometriche causate dalla variazione in frequenza del diagramma d'antenna così pure di ridurre la variazione di fase azimutale dovuta alla geometria di acquisizione polare. A seguito viene presentato un modello di calibrazione polarimetrico adattato all'architettura di antenna di KAPRI. Tali metodi sono stati validati analizzando la risposta di retroreflettori triedrici; i risultati dimostrano i metodi proposti consentono di ottenere immagini polarimetriche correttamente calibrate, prive di rampe di fase azimutali e la cui risoluzione geometrica è prossima alla risoluzione nominale dell'apparecchio.

Il secondo studio è dedicato alla modellazione statistica e alla correzione di schermi di fase atmosferici per l'interferometria differenziale. Sfruttando la sensibilità della fase del segnale radar alla distanza tra il sensore e un obiettivo, questa permette di stimare spostamenti con una precisione limitata dalla lunghezza d'onda impiegata. Tuttavia, variazioni nella distribuzione del vapore acqueo nella scena

possono causare un ritardo di fase di magnitudine comparabile alla fase associata allo spostamento compromettendo gravemente la precisione delle stime di quest'ultimo. Le statistiche spazio-temporali del ritardo di fase come pure metodi per mitigarne l'effetto sono state ampiamente studiate; nella maggior parte dei casi essi si basano sulla supposizione che gli schermi di fase abbiano un certo grado di correlazione spaziale ma che siano decorrelati nel tempo; tuttavia la validità di tali assunzioni è incerta nel caso di dati acquisiti con radar terrestri, dove l'estensione della scena è ridotta e i cicli di acquisizione sono molto più brevi rispetto ai dati ottenuti tramite sensori satellitari o aviotrasportati. L'applicabilità di tali modelli ai dati di radar terrestri è studiata con l'aiuto di uno stack interferometrico acquisito con KAPRI nella regione del ghiacciaio Bisgletscher, nella valle del fiume Matter nel canton Vallese. L'analisi mostra che lo schermo di fase atmosferico è correlato sia nel tempo che nello spazio ma che la sua covarianza può essere approssimata con una covarianza separabile. Grazie a questa approssimazione, parte del ritardo di fase atmosferico può essere corretto con un interpolatore spaziale usando osservazioni prese da un insieme di punti che non subiscono spostamenti in modo tale che il ritardo residuo sia solamente correlato nel tempo e possa venire mitigato da un filtro spaziale operante su singoli pixel riducendo così la complessità della correzione.

Il terzo studio concerne nuovamente la polarimetria radar, in particolare la risposta polarimetrica delle superfici naturali in banda Ku. Questo studio preliminare è necessario per conoscere la validità dei modelli di scattering polarimetrico e dei metodi di stima dei parametri ambientali da essi derivati. Tali metodi infatti sono stati sviluppati sulla base di dati polarimetrici finora acquisiti nelle frequenze abitualmente impiegate dai sistemi SAR satellitari e aviotrasportati, principalmente nelle bande X e L. Per questa analisi vengono usati due set di dati: una serie temporale acquisita nella regione del ghiacciaio Bisgletscher nella valle della Matter nel canton Vallese e un'immagine polarimetrica del villaggio di Münsingen e della campagna circostante, nelle vicinanze di Berna. I risultati di questa analisi mostrano un alto livello di entropia polarimetrica accompagnata da un consistente ritorno in polarizzazione incrociata — HV nella base lineare—. Questi valori sono probabilmente da attribuire alla presenza di meccanismi di scattering depolarizzante causati da mezzi di propagazione inomogenei e casuali quali volumi di vegetazioni o superfici rugose. Tuttavia, è necessario considerare l'effetto della lunghezza d'onda molto corta in relazione alla dimensione delle celle di risoluzione. Questi fattori fanno in modo che diversi scatteratori di diverso tipo si trovino all'interno della stessa cella di risoluzione, contribuendo all'aumento dell'entropia.

CONTENTS

List of Figures	xv
1 Introduction	1
1.1 Motivation	1
1.2 Background	2
1.2.1 Radar Remote Sensing	2
1.2.2 Radar Interferometry (InSAR)	6
1.2.3 Radar Polarimetry (PolSAR)	11
1.2.4 Terrestrial Radar Systems	21
1.3 Research Objectives and Questions	23
1.3.1 Investigation #1: Polarimetric Calibration of the Ku-Band Advanced Polarimetric Radar Interferometer (KAPRI)	24
1.3.2 Investigation #2: Geostatistical Analysis and Mitigation of Atmospheric Phase Screens in Ku-Band Terrestrial Radar Interferometric Observations of an Alpine Glacier	24
1.3.3 Investigation #3: Polarimetric Analysis of Natural Terrain Observed With a Ku-Band Terrestrial Radar	25
1.4 Structure of The Dissertation	26
2 Polarimetric Calibration of KAPRI	43
2.1 Introduction	44
2.1.1 State of the Art	44
2.1.2 KAPRI: Real Aperture Polarimetric FMCW Radar.	45
2.1.3 Contributions of This Paper	46
2.1.4 Outline	46
2.2 Methods and Data	47
2.2.1 KAPRI: FMCW Radar Signal Model	47
2.2.2 Beam Squint Correction	49
2.2.3 Azimuth Processing	51
2.2.4 Antenna Pattern Misalignment	53
2.2.5 Removal of Topographic Phase	54
2.2.6 Polarimetric Calibration	56
2.2.7 Experimental Data	57
2.3 Results.	60
2.3.1 Beam Squint Correction	60
2.3.2 Azimuth Processing	61
2.3.3 Antenna Pattern Misalignment	61
2.3.4 Removal of Topographic Phase	63
2.3.5 Polarimetric Calibration	63
2.4 Discussion	67
2.4.1 Beam Squint Correction	67
2.4.2 Azimuth Processing	67
2.4.3 Antenna Pattern Misalignment	68
2.4.4 Removal of Topographic Phase	68
2.4.5 Polarimetric Calibration	69

2.5	Conclusions.	69
2.5.1	Preprocessing.	70
2.5.2	Calibration	70
3	Geostatistical Analysis and Mitigation of APS in Ku-Band TRI	77
3.1	Introduction	78
3.1.1	Motivation	78
3.1.2	State of the Art	79
3.1.3	Research Gaps	80
3.1.4	Contributions of This Paper	80
3.2	Methods.	81
3.2.1	Differential Radar Interferometry: Signal Model	81
3.2.2	Spatial Correction of APS.	89
3.2.3	Temporal Inversion.	92
3.3	Data	97
3.3.1	Device: KAPRI.	97
3.3.2	Bisgletscher 2015 Campaign.	97
3.3.3	Data Processing.	98
3.4	Results.	99
3.4.1	Spatial Correction of APS.	99
3.4.2	Temporal Inversion.	101
3.5	Discussion	106
3.5.1	Spatial Correction of APS.	106
3.5.2	Temporal Inversion.	107
3.6	Conclusions.	109
4	Polarimetric Analysis of Natural Terrain Observed With a Ku-Band TRI	119
4.1	Introduction	120
4.1.1	Motivation	120
4.1.2	Contributions of This Paper	121
4.2	Methods and Data	121
4.2.1	Radar: KAPRI	121
4.2.2	KAPRI Data Preparation and Calibration	122
4.2.3	Datasets	124
4.2.4	Polarimetric Analysis	125
4.3	Results.	127
4.3.1	Bisgletscher	127
4.3.2	Chutzen	132
4.4	Discussion	139
4.4.1	Depolarization	140
4.4.2	Noise.	147
4.4.3	Mixing of Scattering Processes Due to Multilooking	148
4.4.4	Mixing Within a Resolution Cell	150
4.5	Conclusions.	152
5	Conclusions	165
5.1	Main Findings	165
5.1.1	Chapter 2: <i>Polarimetric Calibration of the Ku-Band Advanced Polarimetric Radar Interferometer (KAPRI)</i>	165
5.1.2	Chapter 3: <i>Geostatistical Analysis and Mitigation of Atmospheric Phase Screens in Ku-Band Terrestrial Radar Interferometric Observations of an Alpine Glacier</i>	166

5.1.3	Chapter 4: <i>Polarimetric Analysis of Natural Terrain Observed With a Ku-Band Terrestrial Radar</i>	169
5.2	Outlook	171
A	Curriculum Vitae	175

LIST OF FIGURES

1.1 Schematic representation of the synthetic aperture principle. L is the physical antenna aperture size, R is the slant range distance from an object represented as a black dot. L_{SA} is the synthetic aperture length, θ_{3dB} is the antenna half-power beamwidth and δ_{az} is the cross-range resolution achievable with the real aperture antenna at a distance R from the scatterer.	3
1.2 Schematic representation of a real aperture radar employing an azimuth scan for lateral resolution: the antenna with a length L – giving it an half-power beamwidth of θ_{3dB} – is rotated around its center with an angular velocity ω . δ_{az} is the cross-range resolution achievable at a distance R from the radar.	4
1.3 Illustration of the effects of the sidelooking image geometry. The slope between points A and B is affected by foreshortening: their projection on the radars line of sight maps the points to A' and B', whose distance is shorter than the true distance on the ground. Hence, in the radar image the slope will appear compressed. The steep slope between D and E will be in layover: in the line of sight projection, the mountain top, which is mapped to point E' is closer than the radar than base of the slope, mapped to D'. Thus in the radar imagery the mountain will appear inverted. Finally, the points on the flat terrain located beyond E will be affected by its shadow.	5
1.4 Schematic representation of propagation of plane waves in a stratified atmosphere affected by turbulent mixing. The red lines represent wavefronts, that is the surfaces of constant phase. The atmospheric stratification is represented by changes in colors, signifying decreases in the atmospheric density with increasing height.	8
1.5 Illustration of the geometry used to describe the Jones vector and the polarization ellipse. \mathbf{E} is a snapshot of the electric field vector on the $z = 0$ plane, whose motion in time appears to describe the contour of an ellipse, a circle or a line, which can all be described with the ellipticity angle τ and the orientation angle ϕ	13
1.6 Illustration of the concept of a partially polarized wave. Three situations are depicted. On top, the polarization ellipse for a fully polarized wave with linear polarization with orientation angle of 45° is shown. Its degree of polarization is 1: looking into the direction of propagation, the electric field vector appears to moves along a line. In the middle, a partially polarized wave with $DoP < 1$ is shown: here the vector does not move along a line anymore but fluctuates in a circular wedge: the three arrows represent probable instantaneous direction of the E-field vector. Finally, the bottom drawing shows a fully unpolarized wave, where the instantaneous electric field can take any direction in the xy plane. This is represented by the many arrows, showing that the electric field vector at one time can take any possible direction with equal probability.	17

- 1.7 Illustration of the resolution grid for an imaging radar system with a short real or synthetic antenna aperture length L_A : the angular resolution δ_{θ} and the range resolution δ_r are constant. However, the cross-range distance resolution δ_{az} –the minimal distance between two point such that one of them is outside of the antenna footprint when the other is in the middle of the beam– increases with increasing slant range r . This means $\delta_{az, far} > \delta_{az, near}$; this produces a grid of trapezoidal resolution cells. Given a maximum δ_{az} , the swath length where the resolution is better than the chosen threshold is limited by the aperture length L_A . An air- or spaceborne SAR system can overcome this limitation because the synthetic aperture length can be increased at will. Therefore, the resolution grid for these systems can be assumed to be composed of squared or rectangular cells. 22
- 2.1 Geometrical description of the displaced phase center with all relevant parameters, as used in subsection 2.2.3. R is the slant range from the radar to the point scatterer, L_{ph} is the phase center displacement, L_{wg} the length of the antenna, L_{arm} is the antenna rotation lever arm, R_0 the range of closest approach and α the additional rotation angle necessary to obtain closest approach when the phase center is not in the midpoint of the antenna but the rotation angle is measured assuming $L_{ph} = 0$ 48
- 2.2 (a) Illustration of the frequency-dependent pointing direction θ_{sq} of the main lobe of the slotted waveguide antennas of KAPRI. The response at different chirp frequencies is represented by the colors of the mainlobes; they correspond to the increasing chirp frequencies as they are represented by the inset plot. The corresponding waveguide wavelengths are displayed underneath the antenna. For the design wavelength λ_g^{design} , the antenna mainlobe points at the antenna broadside. (b) The plots represent the time domain envelope of a point target as a function of chirp time t (y-axis) and slow time $n\tau = \frac{\theta}{\omega}$ (x-axis). The y-axis is proportional to the transmitted frequency, the x-axis to the rotation angle of the antenna. If the antennas mainlobe would not change its direction during the chirp, a beat signal as shown in the bottom would be obtained. It would have a frequency proportional to the range and would cover the slow time extent where the objects stays within the beamwidth. In the case when the mainlobe changes direction with frequency, the response is skewed because the target is only illuminated at the moment when the mechanical and the electrical antenna pointing direction match, causing its response to occupy several azimuth cells. After range compression, obtained with a Fourier transform along the t axis, the frequency-dependent antenna pointing would cause a loss of range resolution because only a fraction of the transmitted bandwidth would be used for each azimuth bin. To correct this effect, the data is interpolated in the time domain in order to reconstruct the full bandwidth by combining the subsequent sub-bandwidths that are obtained at different mechanical pointing angle. This correction requires sufficient azimuth oversampling, which is achieved by slow rotation of the antennas w.r.t the chirp duration. 50
- 2.3 Illustration of the adjustable antenna mount allowing to shift the patterns to bring the H and the V antennas into alignment. The left bracket can be slid towards the front, allowing the antenna to pivot on the right hinge. For small shifts, this movement approximates a rotation around the center of the antenna tower, as depicted by the blue antenna pattern. 54
- 2.4 KAPRI radar during a field test. The antenna arrangement used in this paper is overlaid. The blue and red dots represent the equivalent phase centers for the HH and VV channels from the top receiver. The bottom blue dot on the right represents the one for the lower HH channel, which is used in conjunction with the upper HH phase center to estimate the topographic phase contribution. 55

2.5	Pauli RGB composite ($R = HH - VV $, $G = HV $, $B = HH + VV $) of the imaged scene, geocoded using a digital elevation model with 2-m pixel spacing. Each channel is scaled according to its own dynamic range. The location of corner reflectors is marked by cyan circles, the reflector used for polarimetric calibration is shown in orange. The image is overlaid on a 1:25000 scale Swiss topographic map (Reproduced with the authorization of swisstopo JD100042).	59
2.6	Azimuth-frequency response of the "CR2" TCR: the raw data samples around the reflectors azimuth location were extracted, then filtered in range by Fourier transforming them along the frequency axis, applying an Hamming window about the range location and converting them back into the time domain with an inverse Fourier transform. By doing so, only the portion of the range spectrum close to the reflectors location was kept. Finally, the complex envelope of the data was extracted using a discrete Hilbert transform. This is conceptually equivalent to the plot of Figure 2.2. (a) for the HH channel, (b) for the HH channel after the interpolation described in subsection 2.2.2, (c) for the VV channel, and (d) the same as (b) for the VV channel.	60
2.7	Oversampled phase and amplitude responses for the corner reflector "CR2" at 673 m slant range. (a) HH channel without correction, (b) HH channel with frequency-dependent squint compensation (c) same as (b) with azimuth phase ramp removal. (d) VV channel without correction, (e) VV channel with frequency-dependent squint compensation, (f) same as (e) with azimuth phase ramp removal. (g) Color palette used to represent the above plots. The hue is modulated by the phase, while the brightness corresponds to the gamma-corrected normalized intensity. The phase of each response is referenced to the phase at the peak.	62
2.8	Relative phase response for all reflectors in the calibration array, (a) no azimuth phase correction (b) after azimuth phase correction. Continuous lines: VV channel, dashed lines: HH channel. To display the relative phase variation, the phase at the maximum is subtracted from each plot. The vertical lines indicate the theoretical 3-dB resolution of the antenna θ_{3dB}	63
2.9	Oversampled azimuth power response of a dihedral corner reflector, before (green line) and after the correction of antenna pattern mispointing (orange line). The observed gain is in good agreement with the loss computed using the antenna patterns provided by the manufacturer and the azimuth shift determined using intensity correlation of HH and VV point target responses.	64
2.10	HH-VV phase difference in radar coordinates, (a) before and (b) after the removal of the topographic phase term as described in subsection 2.2.5; (c) calibrated copolar phase difference. The hue of the image is modulated by the covariance phase, the intensity by the magnitude, the saturation by the copolar coherence magnitude. The inset on the bottom left shows the copolar coherence magnitude. The interferometric fringe pattern visible in (a) is removed by the proposed correction, as plotted in (b).	64
2.11	Dependence of the residual copolar phase ($\phi_r + \phi_t$) and amplitude (f) imbalances on the local incidence angle. The mean and RMS imbalances are shown in each plot. The reflector used for the determination of calibration parameters has been excluded from the plot.	65
2.12	Polarization signatures for two trihedral corner reflectors at the locations "CR2" and "CR6" . For both plots, each panel shows: (a) uncalibrated copolar signature, (b) uncalibrated cross-polar signature; (c) calibrated copolar signature, (d): calibrated crosspolar signature. The power of each response is normalized to the corresponding maximum. A distinct change in signature is observed after the calibration; it is mostly due to the removal of the HH-VV phase offset.	66

3.1	Illustration of the computation procedure for the spatio-temporal variogram, used to estimate the space-time covariance of the APS, $\Sigma_{y,atm}$. Assuming separability, the spatial covariance of the APS has the same structure as the covariance of the interferograms and can be estimated as the spatial variogram averaged over all temporal baselines. The temporal variogram corresponds to the mean phase variance of the interferogram grouped by temporal lags.	87
3.2	Schematic description of the two-step spatial APS mitigation and time-series inversion. .	88
3.3	Overview of the area under study. (a) Approximate location of the Bisgletscher in the Canton of Valais, Switzerland. (b) Image of the Bisgletscher as seen from the radar point of view at Domütte, with glacier outline drawn in purple. (c) Geocoded average backscatter power map geocoded in Swiss map coordinates. (d) Locations of radar, glacier and reference location for interferogram referencing, overlaid on 1 : 50000 scale topographic map. Geodata © swisstopo	98
3.4	a Boxplot of the of the Akaike Information Criterion (AIC) values for a selection of models described in Table 3.1. To produce this figure, 400 interferograms were considered. Each of the models discussed was applied to every interferogram, the AIC statistic was computed. The AIC is plotted as a color-coded histogram, the model whose AIC is lower is the one whose performance is best relative to the other models it is compared with. b Boxplot of the R^2 values for the models listed in Table 3.1. The plot is obtained with the same procedure as a.	99
3.5	Spatial and temporal marginal variograms derived from 1535 PS interferograms computed from 100 SLC acquisitions. All possible interferogram up to a maximum temporal baseline of 120 minutes were computed and unwrapped.	100
3.6	Histogram of estimated velocities at non-moving location for different combinations of APS correction and time-series inversion methods. Each column corresponds to a spatial APS correction method: <i>kriged</i> is obtained using regression-Kriging, <i>lm</i> using the stratified APS only while in the column <i>unprocessed</i> no spatial APS correction is applied. Across rows, different temporal covariance models are used for the GLS time series inversion. In <i>APS</i> only the temporal covariance of the APS is considered, in <i>Coh</i> only the covariance of the temporal decorrelation process, while <i>APS + Coh</i> uses both. In <i>OLS</i> no covariance model is used, while in <i>No</i> the interferometric phases are converted in velocities.	101
3.7	Estimated short term coherence γ_0 (3.7a) and time constant τ (3.7b) parameters for the exponential coherence decay model $\gamma(\Delta t) = \gamma_0 e^{-\frac{\Delta t}{\tau}}$. The data was obtained by fitting an exponential model on average coherence maps binned by temporal baseline. The outline of Bisgletscher is shown as a black polygon.	102
3.8	time-series of estimated velocity maps for a subset of times. From left to right: July 14 2:33 CEST , July 26 16:32 CEST and August 2 11:36 CEST. (a) no spatial APS correction and OLS solution for the velocity. (b) spatial APS correction using regression-Kriging combined with OLS inversion. (c) spatial APS correction using regression-Kriging and velocity inversion with full covariance model (APS and decorrelation). The outline of Bisgletscher is shown in black.	104
3.9	Standard deviation maps of velocity estimates for different combinations of APS correction and velocity inversion methods. From left to right: no correction, stratified APS model, regression-Kriging. From top to bottom: velocities estimated from single interferograms, OLS inversion, GLS inversion with the <i>APS+Coh</i> covariance model.	105
3.10	Scatterplot illustrating the correlation between the slant range (r) and height (h) used as regressors for several models of atmospheric stratification listed in Table 3.1.	106

4.1	Typical full-polarimetric antenna arrangement for KAPRI. The upper two antennas are the transmitters in the vertical and horizontal polarizations. Two pairs of vertical and horizontal receiving units are installed on the bottom half of the tower assembly. The two blue dots represent the locations of the equivalent phase centers for the upper and lower HH channel, the red dot the phase center location for the VV channel. The tower assembly is rotated about its center with an angular velocity ω by the motor, producing two-dimensional images resolved by range using a frequency modulated chirp and by angle with the narrow fan beam having beamwidth θ_{3dB}	122
4.2	4.2a 0.25 m resolution orthophoto of the Bisgletscher test site. The ROIs used for the polarimetric analysis are overlaid to the image in dark blue and are assigned a short alphanumeric code. 4.2b shows zooms-in of each ROI, including its full name according to the SWISSNAMES placename inventory and the land cover class from the NOLC04 land use statistics. The alphanumeric codes in 4.2b correspond to the first two characters of the ROI's name followed by an increasing number. (Geodata ©swisstopo).	125
4.3	This figure shows the geographic situation of the Chutzen dataset. 4.3a displays an overview of the area using a 25 cm resolution orthophoto. In 4.3b zoomed-in photographs corresponding to the ROIs used for the polarimetric analysis are shown. The title of each panel gives the ROI's land cover type according to the NOLC04 land cover survey and its name according to the SWISSNAMES Swiss placename inventory (Geodata ©swisstopo).	126
4.4	Temporal and spatial variability of (a) mean α , (b) Cloude-Pottier entropy H , (c) copolar phase difference and (d) copolar coherence for all ROIs in the Bisgletscher data. The vertical lines around each point display ± 1 standard deviation for that data within the ROI, computed over all the pixels in that ROI, the dots the mean and the blue line shows a smoothed trendline.	132
4.5	Temporal and spatial variability of several parameters in the ROIs of the Bisgletscher data. The panels show: (a) magnitude of $\gamma_{(HH-VV)-(HH+VV)}$, (b) backscatter in decibel, (c) normalized backscatter and (d) backscatter versus air temperature measured at the "Zermatt" weather station. The vertical lines around each point display ± 1 standard deviation for that data within the ROI, computed over all the pixels in that ROI. The red, blue and green lines in the backscatter plots encode the polarization.	133
4.6	Cloude-Pottier entropy H (a), (b) mean α , (c) Pauli RGB composite and (d) magnitude of $\gamma_{(HH-VV)-(HH+VV)}$ for the Bisgletscher dataset. The parameters were estimated with a 20×2 boxcar filter.	134
4.7	Cloude-Pottier H - α histogram for the Chutzen dataset. The title of each panel corresponds to the ROI's name as shown in Figure 4.3b.	135
4.8	Histograms of: (a) polarimetric backscatter coefficient, (b) copolar coherence magnitude, (c) copolar coherence phase and (d) coherence magnitude of $\gamma_{(HH-VV)-(HH+VV)}$. The title of each panel indicates the short code of each ROI plotted in Figure 4.3b.	136
4.9	(a) Cloude-Pottier entropy H , (b) mean α , (c) Pauli RGB composite and (d) magnitude of $\gamma_{(HH-VV)-(HH+VV)}$ for the Chutzen dataset. The parameters were estimated with a 20×2 boxcar filter.	138
4.10	Comparison between the entropy estimated by spatial averaging (a), the estimate made using temporal averaging (b) and the estimate obtained using the IDAN filter (c).	151

1

INTRODUCTION

1.1 MOTIVATION

The sensitivity of electromagnetic waves (EM waves) to the structural and electrical properties of media through which they propagate and interact makes them very useful for remote sensing: employing sensors installed on suitable platforms such as satellites or aircraft permits to measure relevant environmental parameters on large swaths of Earth's surface from a distance and over locations that would otherwise be almost inaccessible. Repeating such measurements allows to monitor changes in the environment and to follow the evolution of the underlying processes. Slope instability, volcanic activity, the flow of glaciers, ocean currents, vegetation growth cycles, subsidence in urban areas and urban sprawl are just some examples of the variety of processes in the natural and built environment where remote sensing techniques contribute to improving our understanding of their causes and evolution and where they are employed to provide early warning, potentially preventing loss of human lives and damage to infrastructure and property.

Radar remote sensing is an active remote sensing technique, meaning that the sensor carries its own source of illumination in contrast with aerial or spaceborne cameras or radiometers that rely on the reflection of sunlight on earth's surface or on the variation in thermal emissivity between different surface types. The use of an own source of EM radiation is advantageous in that observations at any time of the day are possible. Secondly, the absorption and scattering of EM waves through the atmosphere at the wavelengths employed by radar sensors is significantly smaller than these at higher frequencies, in the infrared and visible part of the electromagnetic spectrum. Radar observations are thus possible regardless of cloud cover or precipitation. These factors make radar earth observation techniques suitable for all weather, day and night monitoring of large and remote areas.

However, most of the radar remote systems currently employed are carried by airplanes and satellites. While these configurations easily provide large spatial coverage, these platforms are costly and relatively inflexible in acquisition planing. Moreover, they only permit observations at temporal resolutions of hours or days, with the risk of undersampling the faster dynamics of many natural processes. Terrestrial radar systems —also called ground-based radars— are a cost-effective alternative to space and airborne radar sensors for the study of rapidly changing natural phenomena of small spatial extent. These systems can also serve as prototypes and test beds for new sensor technologies and future earth observation mission concepts.

This thesis focuses on KAPRI, a Ku-Band real aperture, polarimetric terrestrial radar based on the Gamma Portable Radar Interferometer II (GPRI-II). The main goal is to investigate the potential of this system to monitor and detect changes in the natural environment with polarimetric and interferometric techniques. To apply these techniques, the data requires internal and external calibration to remove systematic and random effects due to the device itself and to external factors. A significant part of this thesis is dedicated to these data processing and calibration methods.

1.2 BACKGROUND

The following sections provides a brief introduction in radar systems for earth observation. This is followed to three more specific sections giving an extensive background and an overview of the state of the art for the three main aspects of this thesis: radar interferometry, radar polarimetry and terrestrial radar systems.

1.2.1 Radar Remote Sensing

At its core radar (Radio detection and ranging) is a distance-measuring device: it operates by measuring the travel time of electromagnetic waves –usually in the microwave part of the electromagnetic spectrum– emitted by the sensor and scattered back by an object located at a distance. Despite its military origin, it now enjoys widespread civilian use. Air space monitoring, weather forecasting, automotive collision avoidance and environmental remote sensing are only some applications of radar techniques contributing to the safety, sustainability and economic growth in our societies. Most of the radar systems employed in environmental monitoring are imaging devices, i.e they are able to produce two-dimensional maps of the spatial distribution of the terrain’s microwaves reflectivity. The simplest way to obtain two-dimensional resolution is to physically move an antenna with a narrow beam, either by rotating it around its center –as done by airspace surveillance radars and by some terrestrial radar systems– or by displacing the antenna along a –usually linear– path parallel to the scene to be imaged.

The latter solution is normally employed by airborne imaging radars and was historically known by the name of side looking airborne radar (SLAR) [1, 2]. The main limitation of the latter approach is that EM radiation emitted –or received because of the reciprocity theorem for EM waves– by an antenna aperture of finite size is subject to diffraction, which causes the emitted beam to spread with increasing distance from the sensor. Thus, while the nominal distance resolution of an SLAR system is constant, the resolution perpendicular (the *azimuth* or *cross-range* resolution) to the line of sight decreases linearly with range, as illustrated by the drawing in Figure 1.1. An antenna of length L produces a beam with an approximated half power beamwidth θ_{3dB} of:

$$\theta_{3dB} = \frac{\lambda}{L}, \quad (1.1)$$

where λ is the wavelength. The half power beamwidth is the angular separation of two points in the antenna azimuth plane where the received intensity drops by $1/\sqrt{2}$. Therefore, to obtain an azimuth resolution of a few meters or less from a satellite in low earth orbit (LEO) at an altitude of 600 km [3, 4], an antenna with a length of several kilometers is needed. Engineering and financial constraints mean that this requirement is almost impossible to meet with the currently available materials and launch systems. Synthetic aperture radar (SAR) techniques were developed from the 1950s on to overcome this

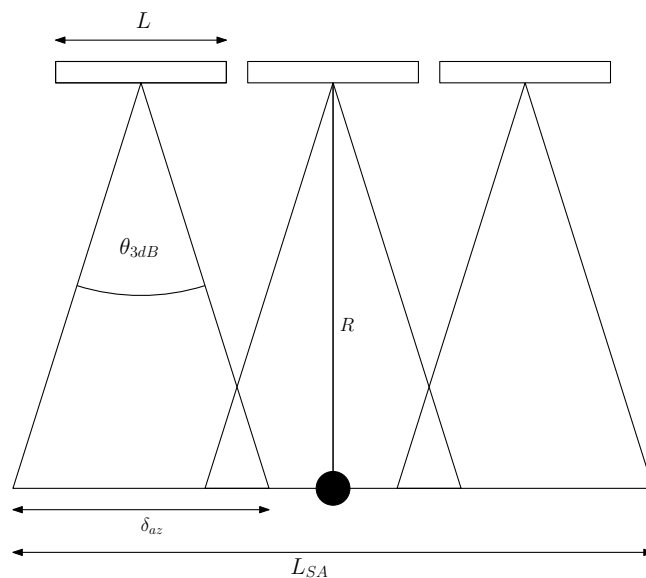


Figure 1.1: Schematic representation of the synthetic aperture principle. L is the physical antenna aperture size, R is the slant range distance from an object represented as a black dot. L_{SA} is the synthetic aperture length, θ_{3dB} is the antenna half-power beamwidth and δ_{az} is the cross-range resolution achievable with the real aperture antenna at a distance R from the scatterer.

limitation [5, 6]. Instead of relying on the physical antenna aperture size, a large antenna aperture is synthesized by coherently combining the echoes recorded at several locations along the sensor trajectory, simulating the effect of an arbitrarily large antenna by illuminating objects with a range of aspect angles. If the synthetic aperture size is made sufficiently large, the cross-range resolution will be almost independent of the slant range distance. In this manner, a SAR system can achieve spatial resolutions of less than a meter from a satellite in low earth orbit. The ability to image large swaths of the earth, at high resolution, remotely and at any weather makes spaceborne SAR system a fundamental tool in modern earth observation.

Terrestrial radars, on the other hand, are normally operated as permanent or semi-permanent installation, consequently they can only image smaller swaths. For cross-range resolutions, they either rotate an antenna with a narrow beam on its center as shown in Figure 1.2 or they move the antenna on a short rail assembly using the displacement to perform aperture synthesis. As the aperture size is rather small compared to the range distance of interest, both solutions do not give range-independent azimuth resolution. The range-resolved, sidelooking geometry of imaging radars, both air- and spaceborne and terrestrial, regardless of the method used to obtain cross-range resolution, produces effects that are rarely seen in angle-resolved, optical images. The term *sidelooking* means that these radar systems observe the scene with a nonzero incidence angle, that is the angle between the terrain's normal and the radar's line of sight, displayed in Figure 1.3. A non-zero incidence angle and hence a sidelooking observation

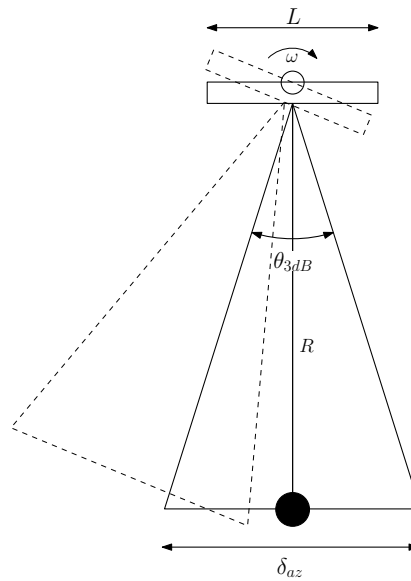


Figure 1.2: Schematic representation of a real aperture radar employing an azimuth scan for lateral resolution: the antenna with a length L – giving it an half-power beamwidth of θ_{3dB} – is rotated around its center with an angular velocity ω . δ_{az} is the cross-range resolution achievable at a distance R from the radar.

geometry is necessary to resolve scatterers by their distances: if the scene is imaged perpendicularly, for example by looking directly underneath the plane in the case of an airborne sensor, the returns from all the objects within the radar’s antenna footprint will be received simultaneously, resulting in a very poor resolution.

Although the sidelooking imaging geometry can be used to overcome this problem, it will make objects appear distorted and very different from their appearance in a conventional optical image. Three main effects can be distinguished [7, 8]:

- When tall objects tilted towards the radar are imaged, they will appear compressed along the range dimension. For example, when a steep mountain face is observed, the base (point A in the illustration) and the top (point B) will appear very close (point A’ and B’) although their distance on the ground could be large. Additionally, as the returns from large swaths of terrain will be falling in the same range resolution cells, these pixels will appear very bright. This effect is named *foreshortening*.
- The extreme case of foreshortening is *layover*: if the slope is steeper than the radar’s incidence angle, the return from the bottom (point D) will reach the radar after the return from the top (point E). Their positions will be inverted in the image: the top of the mountain will “lay over” its base.
- *Radar shadows* are observed when terrain behind tall objects is imaged, a situation often observed in steep mountainous areas. In this case, the object nearest to the sensor will interrupt the propagation path between the farther scatterers and the radar. Only returns from the first object will be received and no energy will be returned from points beyond the first scatterer and. Thus, they will appear dark in the radar image. In the illustration Figure 1.3 radar shadow will affect objects lying behind point E.

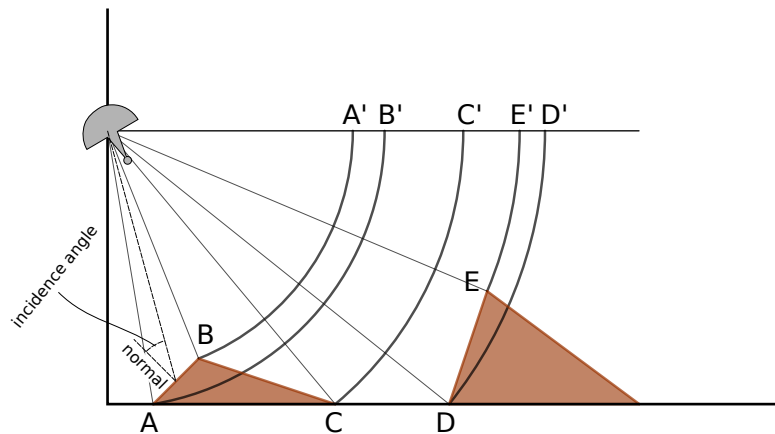


Figure 1.3: Illustration of the effects of the sidelooking image geometry. The slope between points A and B is affected by foreshortening: their projection on the radars line of sight maps the points to A' and B', whose distance is shorter than the true distance on the ground. Hence, in the radar image the slope will appear compressed. The steep slope between D and E will be in layover: in the line of sight projection, the mountain top, which is mapped to point E' is closer than the radar than base of the slope, mapped to D'. Thus in the radar imagery the mountain will appear inverted. Finally, the points on the flat terrain located beyond E will be affected by its shadow.

The all-weather, large coverage capabilities of air- and spaceborne SAR sensors are only one of the reasons for their widespread adoption in remote sensing: while high resolution images of earth's surface can be useful in understanding many natural processes, their scientific utility would be limited, were they simply qualitative depictions of the terrain. Quantitative measurements are necessary in order to develop models and make predictions of scientific value.

Radar measurements deliver quantitative data through their capability to spatially resolve the amplitude, the phase and the polarization state of the waves scattered by the objects on the grounds. In this way, radar images provide complex, vector valued measurements:

1. The amplitude of each pixel is proportional to the strength of the signal scattered by the objects contained in the resolution cell. The reflectivity is influenced by the materials dielectric constant, their shape and – for cells consisting of many scatterers – their spatial distribution and orientations within the cell. The radar reflectivity has been used to infer a variety of geophysical parameters, for example vegetation moisture, total biomass, ice water content or soil roughness [9–16].
2. Thanks to their coherent architecture, SAR systems provide measurement of the absolute phase of each pixel, that is the number of periods the EM waves undergoes in its propagation from the sensor to the scatterer and back. Thus, the phase is proportional to twice the distance plus additional phase delays induced by inhomogeneities in the propagation speed of the medium or by the scatterer's geometric and dielectric characteristics, the so-called intrinsic phase. In this sensitivity lies the value of coherent measurement in SAR remote sensing: by differencing the phases acquired at two different times and/or locations, it is possible to precisely determine the displacement of scatterers between two passes of the sensor or to estimate their height, potentially with a precision orders of magnitude better than the sensors spatial resolution. These techniques are known by *Radar Interferometry* or *Interferometric SAR* (InSAR) and are used for example to derive digital elevation models, reconstruct displacement maps after earthquakes [17–19] and monitor the surface displacement velocity of glaciers [20, 21].

3. By transmitting and receiving signals with orthogonal polarization states, the systems are able to acquire the polarimetric scattering matrix of every pixel. The complex valued scattering matrix gives the scattering phase and amplitude of the scatterers as a function of the polarization state of the transmitted and received waves. The polarization state is modified by the geometrical and dielectric properties of the objects they interacted with; this sensitivity can be employed to infer geophysical parameters such as the properties of snow, soil moisture and roughness, or – in combination with interferometric techniques – to estimate the relative vertical locations of different scatterers within a resolution cell.

The advantages of spaceborne SAR sensors are accompanied by some limitations: the satellites are normally operated in low earth orbits (LEO) at an altitude of approximately 600 km, giving an orbital period of about 90 minutes. As the earth rotates on its axis while the satellites are orbiting, it is only possible to image the same ground track after 10 to 12 days, depending on the orbit altitude. This is a disadvantage when observation of rapid changes is desired, especially so for radar interferometric applications: if the object is displaced by a distance larger than the resolution cell size, interferometric techniques cannot be used to measure its displacement because phase coherence will be lost [22], an issue that will be discussed in detail in a later section. Other barriers to the access to SAR technology are the high cost of designing and launching a satellite and maintaining an adequate ground segment to control and communicate with it, although recent development in commercial SAR satellites are reducing the severity of these issues. Similar issues of cost, complexity and relatively long revisit times also affect airborne SAR systems, however it is foreseen that future developments of UAV technology and cost effective electronics will lead to an increasing adoption of unmanned airborne SAR sensors.

Terrestrial radars –sometimes terrestrial radar interferometers (TRI) or ground based radars (GB-SAR)– [23, 24] are at the other end of the size scale, both in terms of sensor size and in coverage. They are portable, relatively cheap and permit to quickly organize small scale observation campaigns while having large flexibility in acquisition timing, mode and location. Their main drawback is a lower spatial resolution and smaller coverage relatively to air- and spaceborne systems. The lower resolution is determined by the need for portability: they usually synthesize an aperture by moving an antenna on a short rail or directly rely on a physically large antenna [25]. Mechanical and electrical engineering constraints usually limit the size of these –real or synthetic– antenna apertures to a few meters.

1.2.2 Radar Interferometry (InSAR)

Most modern imaging radars use a coherent hardware architecture, i.e they are designed in such a way as to preserve the phase of the electromagnetic waves they transmit and receive [26]. The phase is a measure of how much a monochromatic wave is delayed with respect to a reference wave of the same frequency, normalized to the wavelength. Since sinusoidal waves are periodic they are self-similar and the phase can only be determined up to an integer multiple of 2π . Setting a reference system located at the antenna, after propagating to a target at distance r from the radar, being scattered and propagating again back to the receiver, the wave will have traveled a distance of $2r$. This will give a propagation

phase of

$$\phi_{prop} = 2\pi \frac{(2r)}{\lambda} + 2\pi k, \quad (1.2)$$

where λ is the wavelength. If the propagation distance were the only factor influencing the radar signal's phase, using radars for displacement monitoring would be very straightforward: it would suffice to compute the phase difference between two images acquired at different times to determine the amount of displacement in the line of sight direction—with an ambiguity of 2π —. This is indeed the fundamental concept of the method known as *differential interferometry* [27]¹. Similarly, by differencing the phase acquired simultaneously from two slightly different locations, the position of the scatterers on the plane perpendicular to the line of sight could be estimated, a technique called *single pass interferometry*.

SIGNAL MODEL

However, a number of other effects influence the phase of electromagnetic waves during their travel to the radar to the scatterer and back; they are not contained in the simple model of (1.2). These effects can be summarized compactly in equation (1.3), expressing the signal phase for a scatterer located at distance r from the radar [28–30]:

$$\phi = \phi_{prop} + \phi_{atmo} + \phi_{scat} + \phi_n. \quad (1.3)$$

This phase is sometimes called the *SLC phase* or single look complex phase, as it is obtained directly from the received complex radar signal. Its individual components will be discussed in the following.

- ϕ_{prop} corresponds to the geometrical phase and equals twice the distance between the sensor and the scatterer:

$$\phi_{prop} = 2\pi \frac{(2r)}{\lambda}. \quad (1.4)$$

This is the phase component which is employed in radar interferometry to determine the displacements and/or elevations of the observed objects.

- ϕ_{scat} is the scatterer's intrinsic phase, which is determined by the object's geometrical and dielectric properties.
- ϕ_{atmo} is the atmospheric phase delay; it corresponds to the integral of the refractive index of the propagation medium along the propagation direction. This contribution is due to the spatial and temporal variations in air pressure and water vapor distributions in the atmosphere [28, 31–33]. Ideally, if environmental parameters would be known for each point in space and time, this contribution could be estimated and removed from the data. As this approach is not realistic, the atmospheric phase delay is often simply modeled as a combination of two factors [32, 34, 35], represented schematically in Figure 1.4:

¹The method is often called, DInSAR, although the technique can be applied to any coherent radar data, not only to synthetic aperture measurements.

1. A height-dependent stratified contribution caused by the variation in refraction index depending upon the scatterer's height, as the atmospheric density decreases with increasing elevation. This contribution, known as hydrostatic delay, is approximated with a multiple linear regression model [36–42] or is derived from weather model predictions and weather observations [34, 39, 43–46] or global navigation satellite system (GNSS) observations [47–50]. In Figure 1.4 the hydrostatic delay is represented by increasingly pale rectangles, displaying the decrease in atmospheric density with altitude.
2. A random, spatially and temporally correlated contribution induced by turbulent mixing of water vapor in the troposphere [31, 48, 51]. Because these mixing processes are very complex, they can only be described statistically, usually in terms of spatial and temporal covariances [28, 48, 52]. In Figure 1.4 the turbulence is shown as dark vortexes.

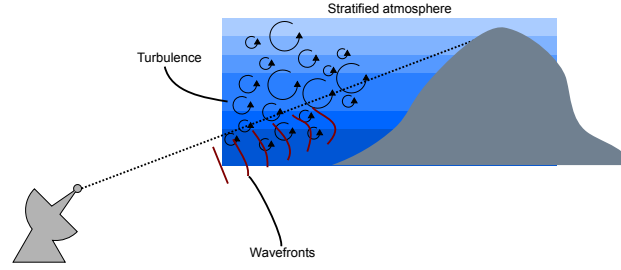


Figure 1.4: Schematic representation of propagation of plane waves in a stratified atmosphere affected by turbulent mixing. The red lines represent wavefronts, that is the surfaces of constant phase. The atmospheric stratification is represented by changes in colors, signifying decreases in the atmospheric density with increasing height.

- Finally, ϕ_n represents a noise contribution, normally attributed to the effect of thermal noise in the radar electronics.

Now, if the acquisition is repeated at a later time and possibly from slightly different radar location and the phase difference is computed, the so called *interferometric phase* is obtained. This can be related to (1.3) and can be written very similarly [28–30, 32, 53, 54]:

$$\Delta\phi = \Delta\phi_{geo} + \Delta\phi_{disp} + \Delta\phi_{atm} + \Delta\phi_{decorr} + \Delta\phi_n + 2\pi k. \quad (1.5)$$

The contribution in the interferometric phase are closely related to the phase component of the SLC phase, but instead of representing factor affecting the propagation and the scattering of the wave at a single instant in time they are related to *difference* of these effects between the two acquisition times. The benefit of operating with interferometric phase differences is that all *systematic*, time invariant effects are removed.

The remaining components of the interferometric phase difference can then be analyzed as follows:

- $\Delta\phi_{geo}$ is the topographic phase contribution, it is only observed in the case when an interferogram is formed between acquisitions acquired from different locations, separated by the *spatial baseline* vector \mathbf{b} . This contribution is proportional to the elevation of the scatterers s , i.e their

locations perpendicular to the line of sight vector [55–57]:

$$\Delta\phi_{geo} \approx \frac{4\pi}{\lambda} \left[\frac{s^2}{2(r_0 - b^{\parallel})} - \frac{b^{\perp} s}{r_0 - b^{\parallel}} \right] \quad (1.6)$$

where the terms b^{\parallel} and b^{\perp} are the parallel and perpendicular projections of the baseline on the line of sight vector. This is the term used in reconstructing digital elevation models [57, 58], ideally in a tandem or single pass configuration, where the signal is received simultaneously from two positions, removing the influence of displacement, atmosphere and decorrelation.

- $\Delta\phi_{disp}$ is the displacement phase; it is proportional to the projection of displacement vector between acquisitions on the line of sight. As the true kinematics of the displacement are not known, a constant displacement rate is often assumed, such that $\Delta\phi_{disp}$ can be written as [59, 60]:

$$\Delta\phi_{disp} = \frac{4\pi}{\lambda} v \Delta T \quad (1.7)$$

where ΔT is the *temporal baseline*, the time elapsed between two acquisitions. This assumption is usually sufficient if enough data is available because the displacement history can be approximated by a series of piecewise displacements with different rates v_i [59, 60]. Otherwise, especially in the case of datasets spanning several years, the model can be expanded by adding seasonal deformation described by sinusoidal waves [61–63] or by considering displacement models including a temperature dependence on the interferometric phase, the latter begin useful to model the thermal expansion of building in urban datasets [64, 65].

- $\Delta\phi_{atm}$ is the differential atmospheric phase, the difference between the phase delays caused by spatially inhomogeneous and varying distributions in the atmospheric propagation speed between the two acquisition times. This term represents a nuisance for repeat pass acquisition; its effect is usually seen in interferograms in the form of the atmospheric phase screen (APS) [28, 51, 66] with a low spatial frequency content. In the most severe cases, this phase contribution can be as large or larger than the displacement signal and may severely limit the precision of displacement estimates. The mathematical model adopted to describe the absolute atmospheric phase delay—the delay for a single acquisition in the SLC phase of (1.3)—can be translated to a similar model for the differential delay affecting interferograms [32, 34]. In this model, the APS is decomposed into a deterministic signal attributed to the difference in atmospheric stratification—described using regression models or derived from external observations as explained above—and in a stochastic component attributed to turbulent mixing in the atmosphere, which is described stochastically through its spatial and temporal covariance functions. Several methods exist to separate the atmospheric phase delay from the displacement, often relying on spatio-temporal filtering on a stack of data. They differ primarily in the way they define a stratification model, which can assume uniform distributions of refraction index or height-dependent variations [36–42] or may use external weather data or weather model predictions [34, 39, 43–46, 67] and GNSS observation of the wet zenith delay [47–50] to estimate the total water vapor content of the atmospheric column. These D-InSAR methods also differ in the statistical model used to describe atmospheric turbulence. Even if the atmospheric phase almost always display some

spatial correlation, the exact form of this correlation is usually not known a priori: while some approaches rely on covariance function derived from Kolmogorov turbulence theory [28, 52], other prefer to derive the spatial statistics of the atmospheric phase disturbances from the data itself [28, 48, 51, 68].

Similarly, most methods assume these phase disturbances to be uncorrelated in time [32, 48]; while this assumption seems to be reasonable for spaceborne InSAR where repeat times of several days are common, this assumption does not necessarily apply to ground-based interferometric studies [69], where the acquisition repeat time can be as small as a few minutes.

Generally, all methods can be seen as spatio-temporal filters operating on a stack of data which exploit the different spatial and temporal correlation properties of the APS and of the deformation signal to mitigate the impact of the latter on the deformation estimation or to separately estimate these two contributions [32, 59, 63, 70–74].

- $\Delta\phi_{decorr}$ is the decorrelation noise which is primarily caused by changes in the complex reflectivity of the objects composing a resolution cells, in other words changes in their radar crosssection and scattering phase [55]. To understand how, it is necessary to consider the statistics of the received SAR signal: usually the wavelength employed by the radar is significantly smaller than the resolution cell size. In that case, the return from a single resolution cell over natural media consists of the complex superposition of scattering contributions from a large quantity of individual scatterers with different reflectivities and scattering phases. Examples of this would be the contributions of individual pebbles on rocky terrain or single leaves and stalks in the case of vegetation. These radar scatterers are named *distributed scatterers* or *extended scatterers* because they are assumed to occupy several resolution cells. For these scatterers, the (pseudo)random combinations within each cell can add in any way from fully constructively to fully destructively, creating a grainy looking image, the so called *speckle*. For these extended scatterers, the phase of a single pixel will be a (pseudo)random quantity, formally a realization of a random variable whose mean is related to the geometrical and dielectric phase of the objects contained in the resolution cell. The displacement or elevation phase for distributed scatterers are then estimated from the interferometric phase by averaging neighboring pixels in the interferogram under the assumption of ergodicity, that is by assuming they represent independent realizations of the same scattering process. However, if the distribution or the dielectric properties of these elementary scatterers within a resolution cell change from an acquisition to the next, the phase difference will have an arbitrary value, being effectively unusable to infer displacements, an effect known as *temporal decorrelation* [22, 75–77].

A similar effect, *volume or baseline decorrelation*, is observed when the cell representing a distributed scatterer—such as a vegetation canopy [75, 78] or an ice volume [79]—is observed at the two ends of spatial baseline, for example in the case of single-pass interferometry for DEM reconstruction. In this case, the scatterers are observed from slightly different incidence angles and so that contributions of elementary scatterers in each cell combine differently at the two ends of the baseline causing baseline decorrelation [22, 80].

These two forms of decorrelation can be avoided if only resolution cells containing a single ob-

ject—or, more precisely, a scatter whose radar reflectivity is dominant in the resolution cell—are analyzed. In this case, the phase contribution is deterministic and is not affected by temporal or baseline decorrelation. Interferometric processing techniques analyzing only these scatterers are known by name of *persistent scatterer interferometry* (PSI) [29, 53, 71, 72]; they proved especially useful for the estimation of terrain displacement in urban areas. The identification of these persistent scatterers (PS): for example by considering the temporal variability of the backscatter in a data stack, with the assumption that a persistent scatterer behaves deterministically and thus its reflectivity is stable in time [71, 72]. Alternatively, the scatter’s spectral phase diversity can be considered as the spectral response of an ideal point scatterer should be flat [72].

- $2\pi k$ represents the phase ambiguity term: as sinusoidal signals are periodic, it is not possible to distinguish a signal delayed by one period by the same signal delayed by any other integer number of periods: the signal is said to be *wrapped*. By assuming spatial or temporal smoothness of the elevation and/or of the displacement, the correct phase ambiguity can be reconstructed from the data using a spatial or temporal phase unwrapping algorithm.

Spatial unwrapping is used in reconstructing digital elevation models from single pass interferograms [81, 82], where the assumption of spatially smoothness is reasonable, at least for terrains with moderate topography. In the case of displacement estimation with differential interferometry, three different approaches are possible:

1. spatial unwrapping of individual interferograms [81, 82] is one option [59], however this approach requires the deformation signal to be spatially smooth and may fail in the case of spatially concentrated and abrupt displacements. Moreover, the deformation time-series thus obtained can show discontinuities [83].
2. Unwrapping in space and time are performed separately and sequentially. Temporal unwrapping ensures continuity in the deformation time-series [71, 84].
3. Phase unwrapping is performed spatio-temporally as a three-dimensional problem, simultaneously enforcing spatial and temporal phase continuity. Using the full spatio-temporal information in a single step helps to increase unwrapping accuracy [85, 86].

For a thorough discussion of different phase unwrapping methods in the context of interferometric time-series, the interested reader is invited to consult the review article in [87].

1.2.3 Radar Polarimetry (PolSAR)

Radar polarimetry is a method to add signal diversity to radar imaging: by measuring the response of the scatterers to EM waves with different polarization states, it enables to infer information on the scatterer’s geometry and dielectric properties. In order to understand the response of objects to polarized waves and how this sensitivity can be used in radar remote sensing; it is instructive to review some basic concepts of polarimetry. Since polarization is usually treated in the context of the propagation of plane electromagnetic waves, it is wise to go a step back and first discuss the plane wave solution to Maxwell’s equations.

WAVE POLARIMETRY

The propagation of electromagnetic waves and their interaction with matter is governed by the four differential equations known as Maxwell's equations [88, 89]:

$$\begin{aligned}\nabla \wedge \mathbf{E} &= -\frac{\partial \mathbf{B}}{\partial t} & \nabla \wedge \mathbf{H} &= \mathbf{J}_T + \frac{\partial \mathbf{D}}{\partial t} \\ \nabla \cdot \mathbf{D} &= \rho & \nabla \cdot \mathbf{B} &= 0\end{aligned}\quad (1.8)$$

The scalar field ρ is the density of free currents, $\mathbf{J}_T = \mathbf{J}_a + \sigma \mathbf{E}$ is the total current density split in a source term and in the electric conduction current governed by the medium's conductivity σ , \mathbf{E} is the electric field, \mathbf{H} is the magnetic field, \mathbf{D} is the electric induction and \mathbf{B} is the magnetic induction field. These fields are related by the following relationship [88]:

$$\mathbf{D} = \epsilon \mathbf{E} + \mathbf{P} \quad \mathbf{B} = \mu (\mathbf{H} + \mathbf{M}) \quad (1.9)$$

where \mathbf{P} is the electric polarization vector, \mathbf{M} is the magnetization, ϵ is the electric permittivity and μ the magnetic permeability. In radar remote sensing, these equations are simplified: linear, source free medias are normally encountered, i.e materials where $\mathbf{P} = 0$, $\mathbf{M} = 0$ and $\mathbf{J}_a = 0$. Furthermore only non-magnetic materials [89] with no free charges are considered, i.e where $\rho = 0$ and $\mu = \mu_0$ since for the situation of interest to radar remote sensing neither free charges as are seen in a plasma [88] nor magnetizable materials are usually encountered. By manipulating Maxwell's equations (1.8), a single vectorial partial differential equation for the electric field is obtained:

$$\Delta \mathbf{E} - \mu \epsilon \frac{\partial^2 \mathbf{E}}{\partial t^2} - \mu \sigma \frac{\partial \mathbf{E}}{\partial t} = 0. \quad (1.10)$$

Almost any well-behaved function of the form $g(\omega t - \mathbf{k} \cdot \mathbf{r})$ is a solution of this equation. For radar polarimetry, where the objects are located far enough from the source of the EM field, assuming a monochromatic plane wave is a valid approximation [90]:

$$\mathbf{E}(\mathbf{r}) = \mathbf{E}_0 e^{-j\mathbf{k} \cdot \mathbf{r}} e^{j\omega t}, \quad (1.11)$$

where the direction of the wavevector \mathbf{k} gives the propagation direction of the wave and its complex magnitude is:

$$k = \omega \mu \epsilon \sqrt{1 - j \frac{\sigma}{\omega \epsilon}} = \beta - j\alpha. \quad (1.12)$$

Any solution of the form (1.11) must satisfy $\mathbf{E} \cdot \mathbf{k} = 0$ to be a plane wave: the electric field has no component in the direction of propagation [88]. Assuming a coordinate systems with $+z$ parallel to \mathbf{k} the component of the electric field vector can be written as:

$$\mathbf{E} = e^{-\alpha z} \begin{bmatrix} E_{0,x} \cos \omega t - kz + \delta_x \\ E_{0,y} \cos \omega t - kz + \delta_y \\ 0 \end{bmatrix}. \quad (1.13)$$

e^{-az} is the attenuation term that can be factored out from the remaining vector, which is the polarization vector or polarization state of the EM wave. The x - and y - components of this vectors are two sinusoids of the same frequency, with different amplitudes $E_{0,x}$ and $E_{0,y}$ and phases δ_x, δ_y .

At a fixed location in space, if the projection of the polarization vector on the xy plane is observed as it varies in time, its end will appear to describe a line, a circle or an ellipse. In fact, all the three cases can be described by an ellipse, the so called *polarization ellipse* [88, 91] which is parameterized by three values: the amplitude A , the ellipticity τ and the orientation angle ϕ , as illustrated in Figure 1.5. The

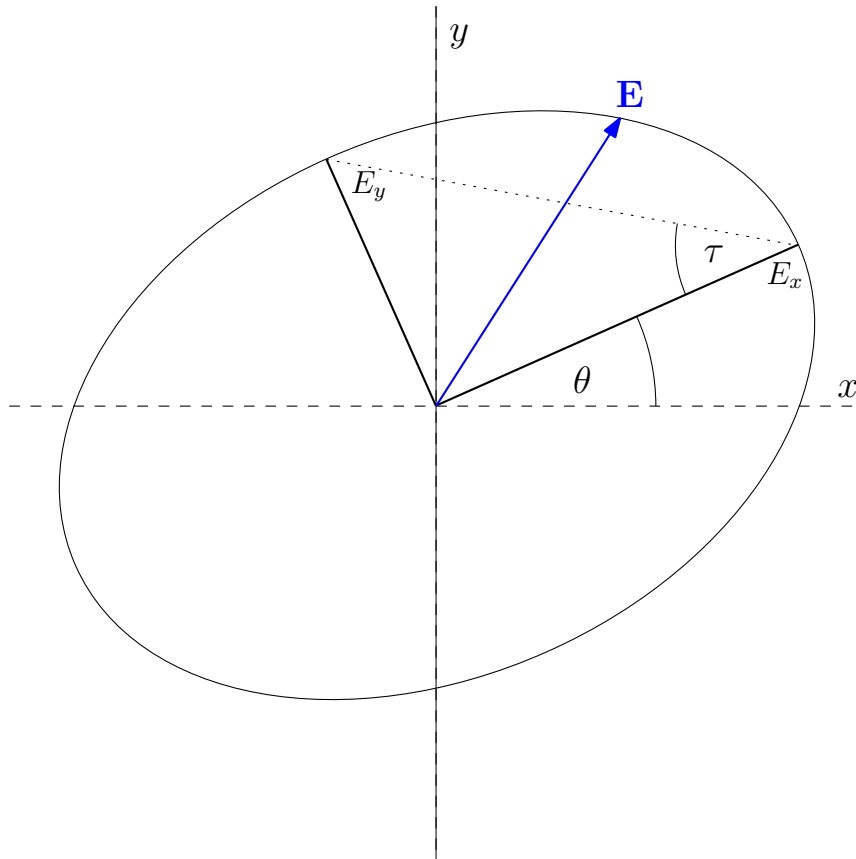


Figure 1.5: Illustration of the geometry used to describe the Jones vector and the polarization ellipse. \mathbf{E} is a snapshot of the electric field vector on the $z = 0$ plane, whose motion in time appears to describe the contour of an ellipse, a circle or a line, which can all be described with the ellipticity angle τ and the orientation angle ϕ .

first parameter, A , describes the total length of the electric field vector, and thus the total intensity of the wave. The second parameter captures the opening of the ellipse described by the tip of the electric field vector as it rotates. At $\tau = 0$ the vector moves along a line, while for an angle of $\tau = \frac{\pi}{2}$ the vector rotates on a circle in counterclockwise sense. Intermediate values describe increasingly round ellipses, while negative ellipticity angle indicate rotation in clockwise direction. Finally, the orientation angle ϕ indicates the orientation of the ellipses semi-major axis with respect to the positive x -axis.

These ellipse parameters are one of the formalism employed to describe the polarization state of plane electromagnetic waves. The *Jones vector* descriptor is a popular alternative based on a two-dimensional complex valued vector describing the amplitude and phase of a plane, monochromatic electromagnetic wave in the plane orthogonal to the direction of propagation, at $z = 0$. The Jones vector is related to the

ellipse parameters [88] in the following way:

$$\mathbf{E} = Ae^{j\alpha} \begin{bmatrix} \cos\phi & -\sin\phi \\ \sin\phi & \cos\phi \end{bmatrix} \begin{bmatrix} \cos\tau \\ j\sin\tau \end{bmatrix}. \quad (1.14)$$

Where $\alpha = \delta_x - \delta_y$ is the absolute phase with respect to the x -axis. The Jones vector can then be defined for an arbitrary orthonormal basis and can be related to the unit horizontal Jones vector $\hat{\mathbf{u}}_H$ in the linear polarization basis (i.e in the basis parallel to the x - and y -axis of the wave coordinate system) by the following transformation [88, 91, 92]:

$$A\mathbf{U}_2(\phi)\mathbf{U}_2(\tau)\mathbf{U}_2(\alpha)\hat{\mathbf{u}}_H \quad (1.15)$$

Where the three matrices $\mathbf{U}_2(\phi), \mathbf{U}_2(\tau), \mathbf{U}_2(\alpha)$ belong to the $SU(2)$ group [92] and are derived from the Pauli matrices [92, 93] σ_i :

$$\begin{aligned} \mathbf{U}_2(\phi) &= e^{-j\phi\sigma_3} \\ \mathbf{U}_2(\tau) &= e^{+j\tau\sigma_2} \\ \mathbf{U}_2(\alpha) &= e^{-j\alpha\sigma_1} \end{aligned} \quad (1.16)$$

Thanks to this base change, it is sufficient to acquire polarimetric radar responses in a polarization basis to reconstruct the response in any desired polarization basis.

A third representation of polarized waves is the Stokes vector, which expresses the wave's polarization state purely in terms of received powers and does not require phase-coherent measurements. It is linked with the ellipse parameters as follows [88, 91, 94]:

$$\mathbf{g} = \begin{bmatrix} g_0 \\ g_1 \\ g_2 \\ g_3 \end{bmatrix} = \begin{bmatrix} A^2 \\ A^2 \cos 2\phi \cos 2\tau \\ A^2 \sin 2\phi \cos 2\tau \\ A^2 \sin 2\tau \end{bmatrix}. \quad (1.17)$$

Notice that the following relationship applies to the component of the Stokes vector [88]:

$$g_0^2 = g_1^2 + g_2^2 + g_3^2; \quad (1.18)$$

this means that the total received power is decomposed in a sum of polarized powers in different polarization states.

This representation is historically relevant: coherent polarimetric radars are relatively recent [88, 94]; non coherent system could only measure the received power but not the phase of the received signal; by receiving the power at a left or right circularly polarized antenna, at a vertically or horizontally unit and at an antenna rotated at either 135° or 45° , the Stokes parameters can be measured from which the Jones vector can be reconstructed. This representation is also important in microwave radiometers and optical imagers, which are almost always incoherent systems since they cannot rely on a controlled, phase locked source of radiation for illumination [91].

Fully Polarized scattering When polarized waves interact with matter, their phase, amplitude and polarization state will be modified. Adopting the Jones vector formalism to describe the electric field of a plane, monochromatic EM wave \mathbf{E}_i incident on an object located at distance r from the origin, the object will scatter an EM wave whose Jones vector \mathbf{E}_s , is expressed with [88, 91, 95, 96]:

$$\mathbf{E}_s = \mathbf{S}\mathbf{E}_i = \frac{e^{-jkr}}{r} \begin{bmatrix} S_{11} & S_{12} \\ S_{21} & S_{22} \end{bmatrix} \mathbf{E}_i. \quad (1.19)$$

The term $\frac{e^{-jkr}}{r}$ describes the effects of propagation on the waves amplitude and phase, while the \mathbf{S} matrix with entries S_{ij} , known as *Jones matrix* or *scattering matrix*, relates the Jones vector—and thus the polarization state—of the transmitted wave with the one of the received wave.

By transmitting and receiving waves with polarization states that form an orthogonal basis for the Jones vector, coherent polarimetric radars are able to measure the scattering matrix \mathbf{S} [88, 91]. Thanks to the change of polarization basis described by the $SU(2)$ matrices in (1.16), if the scattering matrix is measured in any polarization basis, the response of an object to any incoming polarization state can be reconstructed by a change of basis; this method is known as *polarization synthesis* [97–99].

The scattering matrix representation is useful to describe scattering from elementary scatterers whose radar cross section is large enough to permit the assumption that they represent the sole scatterer in a resolution cell; they are so-called *point scatterers* [88]. Example of these scatterers are the trihedral corner reflectors (TCR), that leaves the wave's polarization unaltered or the dihedral reflector with the edge rotated by 45° , which will rotate the wave's polarization state by 90° . Their scattering matrices are:

$$\begin{aligned} \mathbf{S}_{tri} &= \begin{bmatrix} 1 & 0 \\ 0 & 1 \end{bmatrix} \\ \mathbf{S}_{di} &= \begin{bmatrix} 0 & 1 \\ 1 & 0 \end{bmatrix}. \end{aligned} \quad (1.20)$$

Normally, radar polarimetry is concerned with backscattered problems: situations where transmitter and receiver are collocated [91] and only the portion of energy returning directly to the sensor is received. To describe these problems it is useful to use the backscatter alignment (BSA) convention: where the \mathbf{k} vectors for both the transmitted and the received waves are positive when looking away from the antennas: the coordinate system is sensor-centric [91, 100].

Usually, in remote sensing of natural objects only reciprocal scatterers are encountered. These are scatterers whose scattering matrix is unaltered by an exchange in position and polarization states between transmitter and receiver. The assumption of reciprocity is valid for most natural scatterers: the most preeminent exception being the Faraday rotation [101, 102] experienced in spaceborne SAR system, which however is not of any concern for terrestrial radar systems, where the propagation path of the waves is only in the lower troposphere and no free electrons are encountered. For reciprocal backscat-

ter problems the scattering matrix \mathbf{S} in the BSA convention simplifies to:

$$\mathbf{S}_{bs} = \begin{bmatrix} S_{11} & S_{12} \\ S_{12} & S_{22} \end{bmatrix}. \quad (1.21)$$

Thus, any reciprocal backscatter problem can be described with six parameters: the absolute propagation phase $\frac{e^{-jkr}}{r}$, which accounts for the phase delay and the attenuation due to the propagation, and five target parameters, namely two polarimetric phase differences and three amplitudes [88]. Using the linear polarization basis with the horizontal and vertical polarization states as basis vectors and referencing the phases to HH channel, \mathbf{S} can be written as:

$$\frac{e^{-jkr} e^{j\phi_{HH}}}{r} \begin{bmatrix} S_{HH} & S_{HV} e^{j\phi_{HV}-\phi_{HH}} \\ S_{HV} e^{j\phi_{HV}-\phi_{VV}} & S_{VV} e^{j\phi_{VV}-\phi_{HH}} \end{bmatrix}. \quad (1.22)$$

Partially Polarized Waves These five parameters are sufficient to describe scattering from stable, point-like objects. However, many natural objects and surfaces cannot be described by point-like scatterers; they are rather *distributed scatterers* or *extend scatterers* [88], objects whose response to polarized waves is non-stationary in time or space [88]. Temporal fluctuations are caused by motions in the elementary objects composing the distributed scatterers, e.g the effect of winds moving leaves and branches in vegetation or the roughness caused by currents and winds on water and many others. Non-stationarity in space is observed for scatterers composed by large collections of individual objects [103]: in the latter case the scattering of each individual particle is not varying in time, but the coherent combination of many such interactions makes its description in terms of fully polarized waves impractical. The response of these objects may be very sensitive to their relative position with respect to the sensor, such that during the acquisition time due to the varying illumination angles, different polarimetric response are received from the same object [88].

Thus, when these distributed scatterers are illuminated with polarized waves, they will scatter *partially polarized waves*, EM waves whose polarization state fluctuates stochastically [91]. In that case the polarization ellipse cannot be represented by a single set of three parameters as shown earlier, since the ellipse's shape will vary in time or in space; this is shown visually in Figure 1.6. To represent partially polarized waves, it is necessary to employ stochastic descriptions, which require a larger parameter space than the five ellipse parameters. One such description is the wave coherency matrix \mathbf{J} , obtained as the average of the outer product of the Jones vector [89, 91]:

$$\mathbf{J} = E[\mathbf{E}\mathbf{E}^H] \quad (1.23)$$

Where E is the averaging operator, which strictly seen should be computed over the distribution of the process generating the fluctuations of the electric field. From the eigenvalue decomposition of this matrix, the degree of polarization of the wave can be derived:

$$D_p = \frac{\lambda_1 - \lambda_2}{\lambda_1 + \lambda_2} \quad (1.24)$$

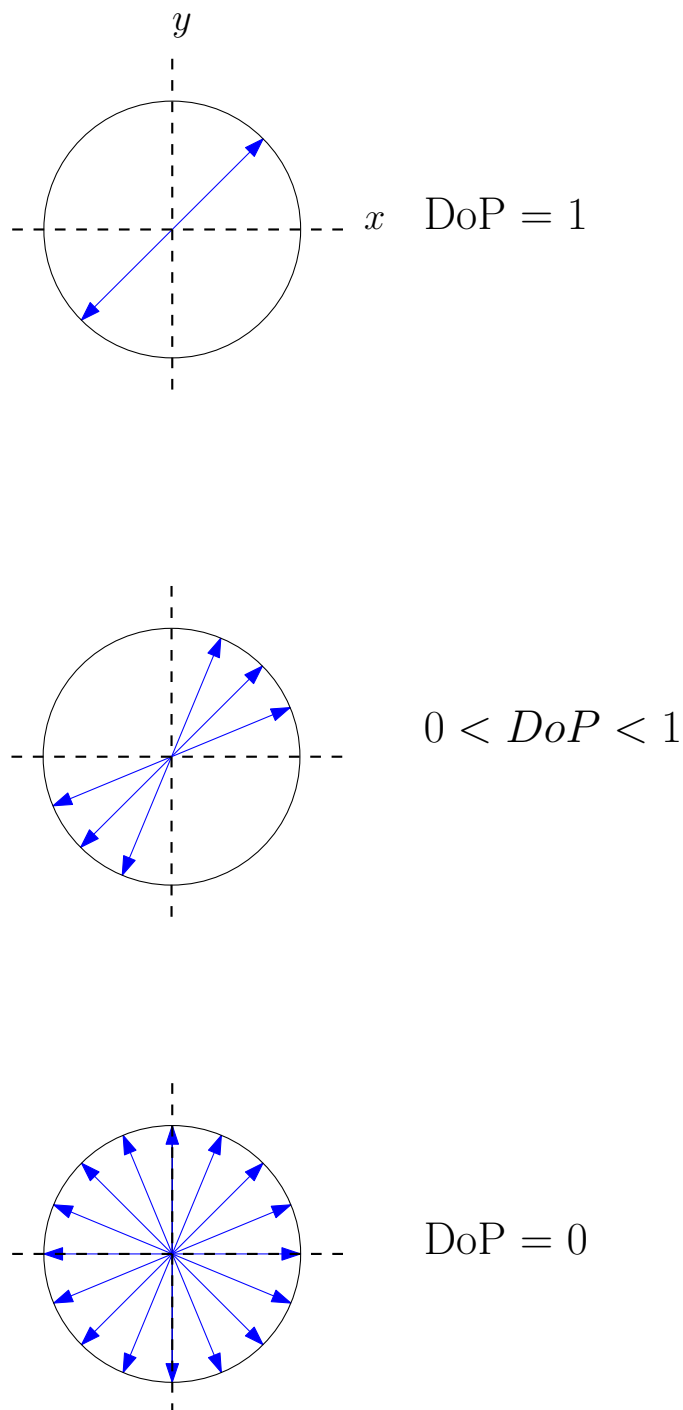


Figure 1.6: Illustration of the concept of a partially polarized wave. Three situations are depicted. On top, the polarization ellipse for a fully polarized wave with linear polarization with orientation angle of 45° is shown. Its degree of polarization is 1: looking into the direction of propagation, the electric field vector appears to move along a line. In the middle, a partially polarized wave with $\text{DoP} < 1$ is shown: here the vector does not move along a line anymore but fluctuates in a circular wedge: the three arrows represent probable instantaneous direction of the E-field vector. Finally, the bottom drawing shows a fully unpolarized wave, where the instantaneous electric field can take any direction in the xy plane. This is represented by the many arrows, showing that the electric field vector at one time can take any possible direction with equal probability.

This parameter is independent on the choice of a basis for the Jones vector and permits to describe a partially polarized waves as a superposition of a fully polarized wave and a noise contribution, whose

polarization state at any moment in time is random. Alternatively, the partially polarized wave can be parameterized as a stochastic mixture of two fully polarized waves of orthogonal polarization states. From the eigenvalue decomposition, the wave entropy H_w can be derived [89, 91]:

$$H_w = - \sum_{i=1}^2 p_i \log_2 p_i \quad (1.25)$$

where p_i are the eigenvalues normalized by their sum. This parameter describes the uncertainty of the wave's polarization state: zero entropy is observed for a fully polarized wave, while an entropy of one is measured for a fully unpolarized wave. The wave coherence matrix is linked to the Stokes parameters representation \mathbf{g} which can be expressed as

$$\mathbf{J} = \frac{1}{2} \begin{bmatrix} g_0 + g_1 & g_2 - jg_3 \\ g_2 + jg_3 & g_0 - g_1 \end{bmatrix} \quad (1.26)$$

However, notice that for partially polarized waves, the relationship of (1.18), $g_0 = g_1^2 + g_2^2 + g_3^2$, no longer holds as an equality and is replaced by an inequality:

$$g_0 \geq g_1^2 + g_2^2 + g_3^2. \quad (1.27)$$

Thus, the for partially polarized waves the total received power can be larger than the polarized power, the additional unpolarized backscatter can be considered "unpolarized noise". Whether the Stokes parameters or the wave coherence matrix are used, it can be shown that partially polarized waves can be parameterized with four quantities: three parameters to describe the polarized part and an additional parameter to quantify the depolarization [91, 104].

Depolarizing Scattering Having studied the properties of partially polarized waves, it is now interesting to investigate their behavior when they interact with a scatterer. Using the definition of the wave coherence matrix of (1.23) and the scattering matrix \mathbf{S} , the wave coherency of the incident wave, \mathbf{J}_i is transformed to \mathbf{J}_s with [91]:

$$\mathbf{J}_s = \mathbf{S} \mathbf{J}_i \mathbf{S}^H, \quad (1.28)$$

or, in terms of Stokes vectors:

$$\mathbf{g}_s = \mathbf{M} \mathbf{g}_i. \quad (1.29)$$

Where the 4×4 matrix \mathbf{M} is the *Mueller matrix*, which relates the Stokes vector of an incoming wave with the Stokes vector of the scattered wave [91]. Any scattering matrix \mathbf{S} can be expressed as a Mueller matrix using the following relationship [103, 105]:

$$\mathbf{M} = \mathbf{A} (\mathbf{S} \otimes \mathbf{S}^H) \mathbf{A}^{-1},$$

$$\mathbf{A} = \begin{bmatrix} 1 & 0 & 0 & 1 \\ 1 & 0 & 0 & -1 \\ 0 & 1 & 1 & 0 \\ 0 & -j & j & 0 \end{bmatrix}. \quad (1.30)$$

Such a Mueller matrix is called a *Pure Mueller Matrix* [105, 106] and does not change the degree of polarization of the incoming wave.

However, an arbitrary Mueller matrix \mathbf{M} does not necessarily correspond to a scattering matrix \mathbf{S} ; these matrices correspond to scatterers that *depolarize* a fully polarized wave, scattering a wave whose degree of polarization is less than one. These depolarizing scatterers are frequently employed in modeling scattering interactions with random media, where the polarization state of the backscattered waves varies over space or time [91].

These depolarizing scattering processes cannot be written as a single pure Mueller matrix, but they can be expressed as a *Sum of Pure Mueller Matrices* (SPM) [105]. SPM appear in the description of the scattering of collections of particles or in the formulation of multiple scattering problems [105].

The advantage of the Stokes vector/Mueller matrix representation is that it permits representing partially polarized waves and their scattering in a fully incoherent way: it only requires to measure the received powers in different polarization states, but does not require measurement of the relative phases between different polarization states. It therefore finds widespread applications in optical polarimetry, where measurement devices are usually non-coherent since the Stokes vector can be measured by inserting different polarizing filters into the system's optical path. Thus, in optical polarimetry, scattering problems are usually modeled using Mueller matrices.

In contrast to optical systems, in radar remote sensing only the coherent polarimetric scattering matrix \mathbf{S} can be measured. Thus, to describe depolarizing scattering processes the scattering coherency or scattering covariance matrix \mathbf{C} or \mathbf{T} is conventionally employed at the place of the Mueller matrix. Both the covariance and coherency matrices—related by a unitary transform—are derived from the second-order statistics of the vectorized scattering matrix \mathbf{k}_P or \mathbf{k}_L , where the vectorization is made using the Pauli or the lexicographic basis matrices respectively [91]:

$$\begin{aligned}\mathbf{C} &= E[\mathbf{k}_L \mathbf{k}_L^H] \\ \mathbf{T} &= E[\mathbf{k}_P \mathbf{k}_P^H]\end{aligned}\tag{1.31}$$

where for reciprocal scattering problems the Pauli scattering vector is $\mathbf{k}_P = [S_{11} + S_{22} \quad S_{11} - S_{22} \quad \sqrt{2}S_{12}]^T$ and the lexicographic vector $\mathbf{k}_L = [S_{11} \quad S_{12} \quad S_{22}]^T$.

Formally—and in analogy to the approach of (1.23) for the wave coherence—the expectation of (1.31) should be computed over the distribution of the fluctuations of the scattering matrix. Since polarimetric radar usually only measure a temporal snapshot of the scattering matrix, this average is normally performed by assuming *ergodicity* and *stationarity* of the measured scattering matrices by averaging the scattering matrices belonging to neighboring pixels, assuming these pixels to be independent realizations of the same distributed or extended scatterer [107].

In a fashion similar to the wave coherency matrix, the scattering coherency matrix is a Hermitian, positive definite matrix, from which a set of stochastic descriptors can be derived. In the backscatter case, the decomposition of \mathbf{T} or \mathbf{C} consists of at the most three nonzero eigenvalues and three eigenvectors, which represent three independent, orthogonal fully polarized scattering vectors. Thus, symmetrical to

the case of partially polarized waves, any depolarizing, reciprocal backscattering process is represented as the sum of three fully polarizing scattering mechanisms—that is, scattering matrices—whose power is given by the eigenvalues:

$$\mathbf{T} = \lambda_1 \mathbf{e}_1 \mathbf{e}_1^H + \lambda_2 \mathbf{e}_2 \mathbf{e}_2^H + \lambda_3 \mathbf{e}_3 \mathbf{e}_3^H. \quad (1.32)$$

From the eigenvalue spectrum of the coherency² an entropy parameter can be derived in analogy to the wave entropy H_w of (1.25) [91, 108]:

$$H = - \sum_{i=1}^3 p_i \log_3 p_i \quad (1.33)$$

where $p_i = \frac{\lambda_i}{\lambda_1 + \lambda_2 + \lambda_3}$ is the *pseudo-probability* of the i -th eigenvalue. A zero entropy implies that the scattering process is not depolarizing; such a scatterer can be represented with a unique scattering matrix associated with the only non-zero eigenvector. Likewise, for low entropy a dominant scattering contribution can be identified and the other two scattering mechanisms can be considered to be noise, while for an entropy of one, any three orthogonal scattering vectors can be used to describe the process [109]. The eigenvectors \mathbf{e}_i obtained from the eigendecomposition of \mathbf{T} can be parameterized as:

$$\mathbf{e}_i = e^{i\phi_i} \begin{bmatrix} \cos \alpha_i \\ \sin \alpha_i \cos \beta_i e^{j\delta_i} \\ \sin \alpha_i \sin \beta_i e^{j\gamma_i} \end{bmatrix}. \quad (1.34)$$

Where ϕ is the absolute propagation phase.

The angle α is the most important parameter of this representation as it describes the type of scattering process: it is a roll-invariant parameter [88, 91, 109], that is it is invariant to rotations of the scatterers in the plane perpendicular to the line of sight. The α parameter is directly related to the scattering type and has been called a basis-invariant polarimetric phase difference [110], which the range of scattering mechanism from isotropic odd-bounce scattering (sphere, surface scattering, trihedral reflections at $\alpha = 0^\circ$) to anisotropic dipole scattering ($\alpha = 45^\circ$ corresponds to a dipole) to dihedral or helix scattering (at $\alpha = 90^\circ$) [91, 100, 111]. The parameter β is related to the orientation of the scatter along the line of sight while the two phases δ and γ are target phases, whose physical interpretation is not as straightforward [112]. By interpreting the eigenvalues as probability of three polarized scattering mechanisms, an average polarized scattering mechanism can be derived [91, 109], whose average α parameter is given by:

$$\bar{\alpha} = p_1 \alpha_1 + p_2 \alpha_2 + p_3 \alpha_3. \quad (1.35)$$

This parametrization defines the average or dominant scattering mechanisms, while the entropy indicates how representative this mechanism is. If the entropy is 1, all three scattering mechanisms are equally probable and α is bound to be 60° . If the entropy is 0, α together with the other parameters shown in (1.34) completely parametrizes the scattering mechanism and the coherency matrix directly corresponds to a scattering matrix and thus represents a non-depolarizing scatterer.

²or covariance matrix, as these two matrices are related by a unitary transformation

POLARIMETRIC RADAR DESIGN AND CALIBRATION

The objective of a coherent polarimetric radar system is the acquisition of the polarimetric scattering matrix \mathbf{S} for every resolution cell it is imaging. This is achieved by transmitting EM waves in two orthogonal polarization states and receiving the backscatter in the same states, measuring all four combinations of transmit and receive polarization. The exact choice of transmit and receive polarizations does not matter in theory, as long as they form an orthogonal basis for the Jones vector. However, vertically and horizontally polarized antennas or left- and right circularly polarized units are the most commonly employed because they are technically easier to build. Ideally, all combinations of transmit and receive polarization states should be measured simultaneously, especially so in the case of acquisitions from moving platform in order to minimize changes in the response due to target motion or because of variations in the observation geometry.

Reception of the two orthogonal states is possible by using a dual polarized antenna or two separate antennas and a system with two receiving channels. Similarly, by employing orthogonally coded sequences [113, 114] it would be possible to simultaneously transmit two polarization states and distinguish the backscatter caused from these two contributions. However, most polarimetric radar systems use the simpler approach of transmitting orthogonal polarization states in subsequent pulses while receiving both orthogonal antennas simultaneously.

Calibration is necessary for all polarimetric radar systems [115]. Any real antenna will not perfectly be able to radiate waves purely in the desired polarization state and there will be always some radiation leaked into the orthogonal state; because of reciprocity this applies to both receiving and transmitting antennas. Secondly the radar electronics and cables can cause additional phase delays and amplitude imbalances between the orthogonal polarization states in their path from the antenna aperture to the radar digitizer or from the signal generator to the antennas. Mathematically, these disturbances can be expressed in the following equation that relates the true scattering matrix \mathbf{S} with the scattering matrix \mathbf{O} observed by the radar [116, 117]:

$$\mathbf{O} = \mathbf{RST} + \mathbf{n}. \quad (1.36)$$

Where \mathbf{T} is the transmission distortion matrix and \mathbf{R} is the receiver distortion, accounting for the amplitude imbalances and differences in phase delays between the two orthogonal polarizations caused by antennas, electronics and cable. Therefore, a complete polarimetric calibration requires the knowledge of sixteen real parameters or eight complex values. Ideally, by using four known targets with orthogonal scattering vectors [118] all sixteen parameters can be estimated. This solution is seldom used in calibrating real systems and simpler techniques resting on various assumptions, such as azimuthal symmetry for distributed targets [116, 119] and tailored to the specific hardware designs are employed [120, 121].

1.2.4 Terrestrial Radar Systems

Most radar remote sensing system currently employed for interferometric and polarimetric applications are spaceborne and airborne SAR systems. These sensors offer excellent spatial resolution and wide coverage but are very costly to acquire and operate; they are usually operated by national and interna-

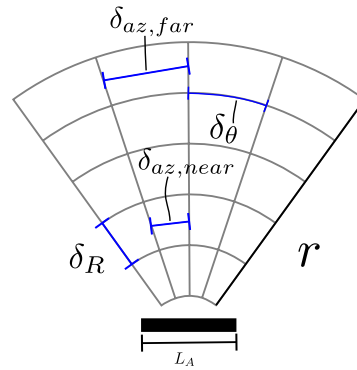


Figure 1.7: Illustration of the resolution grid for an imaging radar system with a short real or synthetic antenna aperture length L_A : the angular resolution δ_{θ} and the range resolution δ_R are constant. However, the cross-range distance resolution δ_{az} —the minimal distance between two point such that one of them is outside of the antenna footprint when the other is in the middle of the beam— increases with increasing slant range r . This means $\delta_{az, far} > \delta_{az, near}$; this produces a grid of trapezoidal resolution cells. Given a maximum δ_{az} , the swath length where the resolution is better than the chosen threshold is limited by the aperture length L_A . An air- or spaceborne SAR system can overcome this limitation because the synthetic aperture length can be increased at will. Therefore, the resolution grid for these systems can be assumed to be composed of squared or rectangular cells.

tional space organizations or large research centers [122–127]. Moreover, these systems only achieve acquisition repeat times of few minutes in the case of airborne SAR devices and to a few days to SAR satellites. Long observations series at high temporal resolution—observations that can improve our understanding of the dynamics of natural processes—are difficult to obtain with these systems.

Terrestrial radar systems³ are a cost-effective alternative to space- and airborne SAR sensors for the monitoring of fast processes of limited spatial extent. Many of these radars are synthetic aperture devices using a small antenna emitting a wide beam. The antenna is translated on a motorized linear rail to synthesize a larger aperture [128–133].

A few alternative SAR systems use a similar synthetic aperture approach but prefer to move the antenna on a circular arm [134–137], which gives a slightly longer synthetic aperture for the same physical assembly size. Historically, the first linear-rail GB-SAR systems were based on a stepped-frequency continuous wave (SFCW) architecture [128, 129, 138], using a vector network analyzer (VNA) as a radio frequency interface [10, 129, 134, 135, 139]. In the SFCW method, the bandwidth necessary for range resolution is obtained by a series of narrowband measurements at different center frequencies: at each frequency the received signal is integrated in time to increase the signal-to-noise ratio [140]. The integration increases the total acquisition time and may affect the aperture synthesis quality for vegetation and other objects affected by winds and other rapid movements or in case of strong variations in the atmospheric propagation speed [38]. In these cases, the scatterer’s response varies randomly across the aperture length, consequently they will be poorly focused in the synthetic aperture image. This issue is largely eliminated by newer system relying on an *ad-hoc* electronic design with significantly shorter acquisition time [41, 132, 141]. These devices are mostly employing the frequency modulated continuous wave (FMCW) [142].

A mechanically large antenna aperture, emitting a physically narrow beam is a common alternative to

³frequently also called *Terrestrial radar interferometers (TRI)* or *Ground-based radar* or *Ground based SAR (GBSAR)*, although the latter name should be reserved for systems employing the synthetic aperture principle

rail-based SAR. In this case, the antenna is rotated around its center with an azimuthal scanner, producing two-dimensional radar images where the lateral resolution is given by the antennas' narrow beamwidth [25, 143]. Compared to a rail-based SAR of the same length, the angular resolution of a real aperture system is half as large, but there is no defocusing due to decorrelation during the acquisition time. Moreover this configuration permits to image a much larger angular extent from a fixed installation while in order to obtain the same angular coverage with a rail-based SAR the entire rail assembly should be mechanically rotated.

Unlike space- and airborne SAR sensors, both rail-based and real aperture TRI do not achieve range-independent azimuth resolution. The images they acquire are in a polar geometry, where the resolution cells are approximately trapezoidal; their width increases linearly with slant range, as illustrated by Figure 1.7: the azimuth distance resolution⁴ worsens with distance. To achieve range-independent azimuth resolution, the synthetic antenna aperture size should increase with increasing slant range distances: this condition cannot be met for the entire range swath using the rail lengths—normally a few meters—typical of rail-based SAR TRIs.

TRIs are used in environmental monitoring and research; some examples of interferometric applications are estimation the surface flow velocity of glaciers [42, 144–148], monitoring of active landslides [38, 149–154], urban subsidence [155], mining-induced subsidence [156], monitoring of dams [157, 158]. A handful of polarimetric TRI were also developed and were used to study the scattering behavior of vegetation canopies or crops [10, 159–162]. The signal diversity given by polarimetric measurements has also been employed to improve the spatial sampling of deformation estimates in urban areas with persistent scatterer methods [41, 163–169].

1.3 RESEARCH OBJECTIVES AND QUESTIONS

Terrestrial radar interferometry is a well-established method for the observation of changes in the natural environment [23, 24]; in the last decade many TRI systems were developed and used for several applications. Many of the common radar remote sensing techniques such as radar polarimetry and radar interferometry can be successfully used with data acquired by such devices. However, they require the data to be free from undesired effects and disturbances. These effect can be systematic, internal biases due to the particular device's design and functioning principle or to natural phenomena other than the parameter of interest that are affecting the measurement. These undesired contributions require data processing strategies specifically tailored to the devices design and to the acquisition conditions; they will be here referred to internal and external calibration respectively.

This thesis is located at the line between science and engineering, considering both the technical aspects of data calibration and device characterization for KAPRI [170]—a fully polarimetric Ku-Band TRI system—and the development and application of interferometric and polarimetric techniques to new datasets acquired with this device. The dissertation is based on three investigations, reflecting different parts of the device's calibration process and different applications.

⁴But not the angular resolution!

1.3.1 Investigation #1: Polarimetric Calibration of the Ku-Band Advanced Polarimetric Radar Interferometer (KAPRI)

This study is focused on the internal calibration of KAPRI, a Ku-Band FMCW polarimetric radar interferometer [170]. The system is based on the Gamma Portable Radar Interferometer (GPRI) II [25, 143], a portable, radar interferometer using $2 - m$ long slotted waveguide antennas [171–174] to provide sufficient azimuth resolution without resorting to aperture synthesis. While the original system only acquired vertically polarized data, KAPRI permits to acquire fully polarimetric data by the addition of horizontally polarized transmitting and receiving antennas. As these units are different in design from the vertically polarized antennas previously employed, the data processing method had to be adapted to the different frequency response of the new units that caused geometrical and phase distortion in the response of point-like scatterers. Moreover, in order to support radar polarimetry, the relative gains and phasing relationships of these antennas had to be characterized and compensated, in order to acquire properly calibrated fully polarimetric datasets. This part of the thesis is primarily concerned with the device's internal calibration and can be summarized concisely with the following questions:

1. *How can the data processing scheme be adapted in order for the radar's phase and frequency response in all polarimetric channels to be free of systematic effects?*
2. *Can the radar's polarimetric distortion parameters be estimated? If so, can they be used, together with the data processing methods mentioned above, to produce properly calibrated polarimetric imagery?*

1.3.2 Investigation #2: Geostatistical Analysis and Mitigation of Atmospheric Phase Screens in Ku-Band Terrestrial Radar Interferometric Observations of an Alpine Glacier

Zero baseline repeat pass radar interferometry is used to estimate displacements in line of sight with an accuracy potentially several times better than the radar's resolution cell size. This is achieved through interferograms, i.e the phase difference between acquisitions at different instants in time: the phase measured by a coherent radar is proportional to the total optical path length between radar and target and back. This quantity corresponds to the integral of the refraction index along the propagation path; assuming a uniform atmosphere it is directly proportional to twice the distance to the scatterer. However, because the atmosphere is a dynamic system, local changes in the air pressure and in the water vapor distribution cause time-varying inhomogeneities in the atmospheric refraction index. These changes are seen in the interferograms as low-spatial frequency *atmospheric phase screens* (APS) whose magnitude can be as large as the displacement signal. Therefore, for correct displacement estimation the data needs phase calibration in order to separate the signal of interest from the atmospheric phase. This calibration is often performed with statistical approaches as these two contributions are known to have different spatio-temporal behaviors [32]:

The atmosphere is assumed to be spatially correlated and uncorrelated in time [32, 48, 175, 176], while the displacement is assumed uncorrelated in space and correlated in time. These differences are normally exploited by combining several acquisitions in a so-called stack and applying spatio-temporal filters on the stack. However, most methods found in the literature are tailored for the more common

spaceborne SAR observation case, where the repeat time of acquisitions is in the order of days, where the acquisition geometry causes the entire atmospheric column to be integrated during the observation and where the geographical extent of the scene is usually very large. The situation in TRI observation can be markedly different: repeat time as short as a few minutes are possible and in many cases only a small vertical extent of the total atmospheric column is interposed between sensor and scene. These factors suggest that the applicability of the commonly employed APS mitigation techniques and especially the assumption on which they rest are not guaranteed to hold for TRI measurement.

In this investigation, different assumptions regarding the statistical nature of atmospheric phase screens in terrestrial radar interferometry are investigated. In particular, three questions are addressed:

1. *Can a multiple regression model be used to explain the phase variance caused by the APS?*
2. *Are the spatio-temporal statistics of the APS in Ku-Band TRI separable? Can the covariance of the APS at any two points in space and time be factored in a purely temporal and a purely spatial covariance?*
3. *Can the regression model and the spatio-temporal statistics be used to extrapolate the APS from a set of scatterers known not to be affected by displacement? Can the temporal covariance model be used to improve the correction of the APS?*

The first aspect relates to an assumption frequently made in TRI data analysis where the APS is assumed to be homogeneous or stratified, situations that can be modeled with multiple linear regression [36–42]. The second point is particularly important: in cases where the displacement is spatially limited to a known area, observations from a set of stable scatterers known not to be displacing can be used to extrapolate the APS at any location using a statistical interpolator such as regression-Kriging [177, 178] exploiting both the stratification model and the spatial correlation structure.

If the spatial statistics do not depend on time a single covariance function can be used for the entire time-series; this can be followed by a separate correction of the effect of the residual, temporally correlated APS in the form of a generalized least squares [179, 180] estimation of the displacement rate, which does not need to consider the spatial correlation induced by the APS because its effect was corrected by the spatial interpolator, reducing the computational cost of the APS compensation.

1.3.3 Investigation #3: Polarimetric Analysis of Natural Terrain Observed With a Ku-Band Terrestrial Radar

This investigation is focused on the polarimetric response of natural surface observed with a Ku-Band polarimetric terrestrial radar. Radar polarimetry has been applied to a variety of environmental monitoring tasks, such as land cover classification, the estimation of vegetation properties and the inversion of structural and dielectric properties of snow and ice. These investigations were mostly performed using two different types of polarimetric radar, widely different in their spatial coverage and imaging capability. On the one side of the spectrum are air- and spaceborne SAR systems, which offer excellent coverage and resolution at high cost and lower temporal resolution, limited by the need of the sensor to overfly again on the same location, making them ideal for large scale investigations of phenomena

whose temporal dynamics are in the order of days at best. On the other extreme are portable polarimetric scatterometers [140, 181–183]: these devices usually have a poor spatial resolution and a small footprint but are relatively cheap and permit frequent acquisitions on a specific target, such as individual trees, crops or parts of a snow pack, making them ideal for controlled experiments or long term monitoring of natural processes of limited spatial extents. Between these two extremes sit polarimetric terrestrial radars, that can achieve a better spatial resolution than scatterometers at a much lower cost than air- and spaceborne SAR systems. However, unlike the latter sensors, which usually operate at wavelength between L- and X-Band, engineering constraints—primarily the limited real or synthetic aperture size—force most of these devices to operate at the higher end of the microwave spectrum, at X- or Ku-band, with wavelengths between 3 cm and 1.5 cm. Because these systems are historically newer compared to air- and spaceborne SAR devices, the polarimetric scattering response of natural surfaces at these wavelengths is not as well characterized as it is for the longer wavelengths employed by the latter.

This investigation aims at improving the understanding the polarimetric scattering behavior of natural surfaces at Ku-band by analyzing two datasets acquired over a glacier and in a mixed use urban and agricultural area. The goal of the analysis can be expressed with these questions:

1. *How do natural surfaces scatter polarized electromagnetic waves at Ku-Band?*
2. *How to explain the high polarimetric entropy observed for most natural surfaces at Ku-Band?*

These questions are important to assess the applicability of the commonly employed polarimetric scattering models –and of the environmental parameter estimation methods derived therefrom– to Ku-band terrestrial radar data, since the majority of these models were developed using air- and spaceborne polarimetric data acquired at longer wavelengths. This study requires an empirical analysis of the polarimetric signatures of common land cover types; as a consequence of the observed overall high polarimetric entropy, the second of the above points needs to be addressed. The second point of interest is to obtain a better understanding of the mechanisms behind the observed high Cloude-Pottier entropy: this question is closely related to the first point as a high entropy means that the polarimetric measurements are less informative. In this case, the data is not useful for classification or to extract environmental parameters.

1.4 STRUCTURE OF THE DISSERTATION

This thesis is based on three studies, whose results were either published or submitted for publication in a peer-reviewed journal. They are presented in the order given by the above outlines in chapter 2, chapter 3 and chapter 4. Finally, in chapter 5 the findings and conclusions of these investigations are discussed.

REFERENCES

- [1] R. Moore, “Active microwave sensing of the Earth's surface—a mini review”, *IEEE Transactions on Antennas and Propagation*, vol. 26, pp. 843–849, 1978. DOI: 10.1109/tap.1978.1141950.

-
- [2] R. Moore and G. Thomann, "Imaging radars for geoscience use", *IEEE Transactions on Geoscience Electronics*, vol. 9, pp. 155–164, 1971. DOI: 10.1109/tge.1971.271488.
- [3] J. Munder and D. Miller, "TerraSAR-X, German X-band remote sensing system", in *Proceeding of the International Conference on Recent Advances in Space Technologies, RAST*, IEEE, 2003. DOI: 10.1109/rast.2003.1303383.
- [4] G. Duchossois and C. Honvault, "The first ESA remote sensing satellite (ERS)–the programme and the system", in *OCEANS 81*, IEEE, 1981. DOI: 10.1109/oceans.1981.1151522.
- [5] C. W. Sherwin, J. P. Ruina, and R. D. Rawcliffe, "Some early developments in synthetic aperture radar systems", *IRE Transactions on Military Electronics*, vol. MIL-6, pp. 111–115, 1962. DOI: 10.1109/iret-mil.1962.5008415.
- [6] L. J. Cutrona and G. O. Hall, "A comparison of techniques for achieving fine azimuth resolution", *IRE Transactions on Military Electronics*, vol. MIL-6, pp. 119–121, 1962. DOI: 10.1109/iret-mil.1962.5008417.
- [7] J. C. Curlander and R. N. Mcdonough, *Synthetic Aperture Radar*. John Wiley & Sons, 12, 1991.
- [8] D. Tilley and K. Bonwit, "Reduction of layover distortion in SAR imagery", *Remote Sensing of Environment*, vol. 27, pp. 211–220, 1989. DOI: 10.1016/0034-4257(89)90083-7.
- [9] B. Bouman, "Crop parameter estimation from ground-based X-band (3-cm wave) radar backscattering data", *Remote Sensing of Environment*, vol. 37, pp. 193–205, 1991. DOI: 10.1016/0034-4257(91)90081-g.
- [10] S. Brown, S. Quegan, K. Morrison, J. Bennett, and G. Cookmartin, "High-resolution measurements of scattering in wheat canopies-implications for crop parameter retrieval", *IEEE Transactions on Geoscience and Remote Sensing*, vol. 41, pp. 1602–1610, 2003. DOI: 10.1109/tgrs.2003.814132.
- [11] M. Boregaud and J. Noll, "Analysis of theoretical surface scattering models for polarimetric microwave remote sensing of bare soils", *International Journal of Remote Sensing*, vol. 15, pp. 2931–2942, 1994. DOI: 10.1080/01431169408954293.
- [12] B. Brisco, R. Brown, K. J., G. Sofko, and M. Mckibben, "The diurnal pattern of microwave backscattering by wheat", *Remote Sensing of Environment*, vol. 34, pp. 37–47, 1990. DOI: 10.1016/0034-4257(90)90082-W.
- [13] C. Albinet, P. Borderies, T. L. Toan, A. Hamadi, T. Koleček, B. Burban, E. Pottier, and P. Dubois-Fernandez, "Overview of three ground based radar experiments for the monitoring of temporal and spatial variability of P-band radar backscattering over temperate and tropical forests", in *Proceedings of the IEEE International Geoscience and Remote Sensing Symposium*, IEEE, 2014. DOI: 10.1109/igarss.2014.6946934.
- [14] F. Ulaby, P. Batlivala, and M. Dobson, "Microwave backscatter dependence on surface roughness, soil moisture, and soil texture: Part I-bare soil", *IEEE Transactions on Geoscience Electronics*, vol. 16, pp. 286–295, 1978. DOI: 10.1109/TGE.1978.294586.

- [15] W. Wagner, C. Pathe, M. Doubkova, D. Sabel, A. Bartsch, S. Hasenauer, G. Blöschl, K. Scipal, J. Martínez-Fernández, and A. Löw, “Temporal stability of soil moisture and radar backscatter observed by the advanced synthetic aperture radar (ASAR)”, *Sensors*, vol. 8, pp. 1174–1197, 2008. DOI: 10.3390/s80201174.
- [16] E. T. Engman and N. Chauhan, “Status of microwave soil moisture measurements with remote sensing”, *Remote Sensing of Environment*, vol. 51, pp. 189–198, 1995. DOI: 10.1016/0034-4257(94)00074-w.
- [17] A. K. Gabriel, R. M. Goldstein, and H. A. Zebker, “Mapping small elevation changes over large areas: Differential radar interferometry”, *Journal of Geophysical Research*, vol. 94, p. 9183, 1989. DOI: 10.1029/JB094iB07p09183.
- [18] H. A. Zebker, P. A. Rosen, R. M. Goldstein, A. Gabriel, and C. L. Werner, “On the derivation of co-seismic displacement fields using differential radar interferometry: The Landers earthquake”, *Journal of Geophysical Research: Solid Earth*, vol. 99, pp. 19617–19634, 1994. DOI: 10.1029/94JB01179.
- [19] J. Biggs, T. Wright, Z. Lu, and B. Parsons, “Multi-interferogram method for measuring interseismic deformation: Denali fault, Alaska”, *Geophysical Journal International*, vol. 170, pp. 1165–1179, 2007. DOI: 10.1111/j.1365-246X.2007.03415.x.
- [20] I. Joughin, R. Kwok, and M. Fahnestock, “Estimation of ice-sheet motion using satellite radar interferometry: Method and error analysis with application to Humboldt Glacier, Greenland”, *Journal of Glaciology*, vol. 42, pp. 564–575, 1996. DOI: 10.1017/S0022143000003543.
- [21] J. J. Mohr, N. Reeh, and S. N. Madsen, “Three-dimensional glacial flow and surface elevation measured with radar interferometry”, *Nature*, vol. 391, pp. 273–276, 1998. DOI: 10.1038/34635.
- [22] H. Zebker and J. Villasenor, “Decorrelation in interferometric radar echoes”, *IEEE Transactions on Geoscience and Remote Sensing*, vol. 30, pp. 950–959, 1992. DOI: 10.1109/36.175330.
- [23] R. Caduff, F. Schlunegger, A. Kos, and A. Wiesmann, “A review of terrestrial radar interferometry for measuring surface change in the geosciences”, *Earth Surface Processes and Landforms*, vol. 40, pp. 208–228, 2015. DOI: 10.1002/esp.3656.
- [24] O. Monserrat, M. Crosetto, and G. Luzi, “A review of ground-based SAR interferometry for deformation measurement”, *ISPRS Journal of Photogrammetry and Remote Sensing*, vol. 93, pp. 40–48, 2014. DOI: 10.1016/j.isprsjprs.2014.04.001.
- [25] C. Werner, T. Strozzi, A. Wiesmann, and U. Wegmüller, “A real-aperture radar for ground-based differential interferometry”, in *Proceedings of the IEEE International Geoscience and Remote Sensing Symposium*, IEEE, 2008, pp. 210–213. DOI: 10.1109/IGARSS.2008.4779320.
- [26] N. R. Gillespie, J. B. Higley, and N. MacKinnon, “The evolution and application of coherent radar systems”, *IRE Transactions on Military Electronics*, vol. MIL-5, pp. 131–139, 1961. DOI: 10.1109/iret-mil.1961.5008331.
- [27] D. Massonnet and K. L. Feigl, “Radar interferometry and its application to changes in the Earth’s surface”, *Reviews of Geophysics*, vol. 36, pp. 441–500, 1998. DOI: 10.1029/97rg03139.

-
- [28] R. F. Hanssen, *Radar Interferometry*, ser. Remote Sensing and Digital Image Processing. Springer Netherlands, 2001, vol. 2, pp. 46–53. DOI: 10.1007/0-306-47633-9.
- [29] M. Crosetto, O. Monserrat, M. Cuevas-González, N. Devanthéry, and B. Crippa, “Persistent scatterer interferometry: A review”, *ISPRS Journal of Photogrammetry and Remote Sensing*, vol. 115, pp. 78–89, 2016. DOI: 10.1016/j.isprsjprs.2015.10.011.
- [30] A. Pepe and F. Calò, “A review of interferometric synthetic aperture RADAR (InSAR) multi-track approaches for the retrieval of Earth’s surface displacements”, *Applied Sciences*, vol. 7, p. 1264, 2017. DOI: 10.3390/app7121264.
- [31] R. N. Treuhaft and G. E. Lanyi, “The effect of the dynamic wet troposphere on radio interferometric measurements”, *Radio Science*, vol. 22, pp. 251–265, 1987. DOI: 10.1029/RS022i002p00251.
- [32] P. S. Agram and M. Simons, “A noise model for InSAR time series”, *Journal of Geophysical Research: Solid Earth*, pp. 1–20, 2015. DOI: 10.1002/2014JB011271.1.
- [33] H. A. Zebker, P. A. Rosen, and S. Hensley, “Atmospheric effects in interferometric synthetic aperture radar surface deformation and topographic maps”, *Journal of Geophysical Research: Solid Earth*, vol. 102, pp. 7547–7563, 1997. DOI: 10.1029/96JB03804.
- [34] R. Jolivet, P. S. Agram, N. Y. Lin, M. Simons, M.-P. Doin, G. Peltzer, and Z. Li, “Improving InSAR geodesy using global atmospheric models”, *Journal of Geophysical Research: Solid Earth*, vol. 119, pp. 2324–2341, 2014. DOI: 10.1002/2013JB010588.
- [35] D. Bekaert, R. Walters, T. Wright, A. Hooper, and D. Parker, “Statistical comparison of InSAR tropospheric correction techniques”, *Remote Sensing of Environment*, vol. 170, pp. 40–47, 2015. DOI: 10.1016/j.rse.2015.08.035.
- [36] L. Pipia, X. Fabregas, A. Aguasca, and C. Lopez-Martinez, “Atmospheric artifact compensation in ground-based DInSAR applications”, *IEEE Geoscience and Remote Sensing Letters*, vol. 5, pp. 88–92, 2008. DOI: 10.1109/LGRS.2007.908364.
- [37] L. Noferini, M. Pieraccini, D. Mecatti, G. Luzi, C. Atzeni, A. Tamburini, and M. Broccolato, “Permanent scatterers analysis for atmospheric correction in ground-based SAR interferometry”, *IEEE Transactions on Geoscience and Remote Sensing*, vol. 43, pp. 1459–1471, 2005. DOI: 10.1109/tgrs.2005.848707.
- [38] G. Luzi, M. Pieraccini, D. Mecatti, L. Noferini, G. Guidi, F. Moia, and C. Atzeni, “Ground-based radar interferometry for landslides monitoring: Atmospheric and instrumental decorrelation sources on experimental data”, *IEEE Transactions on Geoscience and Remote Sensing*, vol. 42, pp. 2454–2466, 2004. DOI: 10.1109/TGRS.2004.836792.
- [39] A. M. Guarnieri, L. Iannini, and D. Giudici, “On the exploitation of meteo information for atmospheric phase screen compensation in GB-SAR interferometry”, in *ESA Living Planet Symposium*, 2010.

- [40] R. Iglesias, X. Fabregas, A. Aguasca, J. J. Mallorqui, C. Lopez-Martinez, J. A. Gili, and J. Corominas, “Atmospheric phase screen compensation in ground-based SAR with a multiple-regression model over mountainous regions”, *IEEE Transactions on Geoscience and Remote Sensing*, vol. 52, pp. 2436–2449, 2014. DOI: 10.1109/TGRS.2013.2261077.
- [41] R. Iglesias, A. Aguasca, X. Fabregas, J. J. Mallorqui, D. Monells, C. Lopez-Martinez, and L. Pipia, “Ground-based polarimetric SAR interferometry for the monitoring of terrain displacement phenomena—part I: Theoretical description”, *IEEE Journal of Selected Topics in Applied Earth Observations and Remote Sensing*, vol. 8, pp. 1–1, 2014. DOI: 10.1109/JSTARS.2014.2360040.
- [42] N. Dematteis, G. Luzi, D. Giordan, F. Zucca, and P. Allasia, “Monitoring alpine glacier surface deformations with GB-SAR”, *Remote Sensing Letters*, vol. 8, pp. 947–956, 2017. DOI: 10.1080/2150704X.2017.1335905.
- [43] Z. Li, J.-P. Muller, P. Cross, P. Albert, J. Fischer, and R. Bennartz, “Assessment of the potential of MERIS near-infrared water vapour products to correct ASAR interferometric measurements”, *International Journal of Remote Sensing*, vol. 27, pp. 349–365, 2006. DOI: 10.1080/01431160500307342.
- [44] R. Jolivet, R. Grandin, C. Lasserre, M.-P. Doin, and G. Peltzer, “Systematic InSAR tropospheric phase delay corrections from global meteorological reanalysis data”, *Geophysical Research Letters*, vol. 38, pp. 1–6, 2011. DOI: 10.1029/2011GL048757.
- [45] J. Jung, D. jin Kim, and S.-E. Park, “Correction of atmospheric phase screen in time series InSAR using WRF model for monitoring volcanic activities”, *IEEE Transactions on Geoscience and Remote Sensing*, vol. 52, pp. 2678–2689, 2014. DOI: 10.1109/TGRS.2013.2264532.
- [46] G. Wadge, P. W. Webley, I. N. James, R. Bingley, A. Dodson, S. Waugh, T. Veneboer, G. Puglisi, M. Mattia, D. Baker, S. C. Edwards, S. J. Edwards, and P. J. Clarke, “Atmospheric models, GPS and InSAR measurements of the tropospheric water vapour field over mount Etna”, *Geophysical Research Letters*, vol. 29, pp. 11–1–11–4, 2002. DOI: 10.1029/2002gl015159.
- [47] M. Bevis, S. Businger, T. A. Herring, C. Rocken, R. A. Anthes, and R. H. Ware, “GPS meteorology: Remote sensing of atmospheric water vapor using the global positioning system”, *Journal of Geophysical Research*, vol. 97, p. 15 787, 1992. DOI: 10.1029/92JD01517.
- [48] T. R. Emardson, M. Simons, and F. H. Webb, “Neutral atmospheric delay in interferometric synthetic aperture radar applications: Statistical description and mitigation”, *Journal of Geophysical Research: Solid Earth*, vol. 108, p. 2231, 2003. DOI: 10.1029/2002jb001781.
- [49] T. R. Emardson, G. Elgered, and J. M. Johansson, “Three months of continuous monitoring of atmospheric water vapor with a network of global positioning system receivers”, *Journal of Geophysical Research: Atmospheres*, vol. 103, pp. 1807–1820, 1998. DOI: 10.1029/97jd03015.
- [50] F. Onn and H. A. Zebker, “Correction for interferometric synthetic aperture radar atmospheric phase artifacts using time series of zenith wet delay observations from a GPS network”, *Journal of Geophysical Research: Solid Earth*, vol. 111, pp. 1–16, 2006. DOI: 10.1029/2005JB004012.

-
- [51] S. Williams, Y. Bock, and P. Fang, “Integrated satellite interferometry: Tropospheric noise, GPS estimates and implications for interferometric synthetic aperture radar products”, *Journal of Geophysical Research: Solid Earth*, vol. 103, pp. 27 051–27 067, 1998. DOI: 10.1029/98JB02794.
- [52] J. M. Boncori and J. Mohr, “Statistical description of tropospheric delay for InSAR: Overview and a new model”, in *2007 IEEE International Geoscience and Remote Sensing Symposium*, IEEE, 2007, pp. 4483–4486. DOI: 10.1109/IGARSS.2007.4423851.
- [53] B. M. Kampes, *Radar interferometry*. Springer Netherlands, 2006. DOI: 10.1007/978-1-4020-4723-7.
- [54] S. Tebaldini and A. M. Guarnieri, “A Cramér Rao like lower bound for parametric phase estimation in multi-pass SAR interferometry”, *Italian Journal of Remote Sensing*, vol. 40, pp. 123–131, 2008. DOI: 10.5721/ItJRS200840211.
- [55] R. Bamler and P. Hartl, “Synthetic aperture radar interferometry”, *Inverse Problems*, vol. 14, R1–R54, 1999. DOI: 10.1088/0266-5611/14/4/001.
- [56] P. Rosen, S. Hensley, I. Joughin, F. Li, S. Madsen, E. Rodriguez, and R. Goldstein, “Synthetic aperture radar interferometry”, *Proceedings of the IEEE*, vol. 88, pp. 333–382, 2000. DOI: 10.1109/5.838084.
- [57] H. A. Zebker and R. M. Goldstein, “Topographic mapping from interferometric synthetic aperture radar observations”, *Journal of Geophysical Research*, vol. 91, p. 4993, 1986. DOI: 10.1029/JB091iB05p04993.
- [58] L. Graham, “Synthetic interferometer radar for topographic mapping”, *Proceedings of the IEEE*, vol. 62, pp. 763–768, 1974. DOI: 10.1109/proc.1974.9516.
- [59] P. Berardino, G. Fornaro, R. Lanari, and E. Sansosti, “A new algorithm for surface deformation monitoring based on small baseline differential SAR interferograms”, *IEEE Transactions on Geoscience and Remote Sensing*, vol. 40, pp. 2375–2383, 2002. DOI: 10.1109/TGRS.2002.803792.
- [60] R. Lanari, F. Casu, M. Manzo, G. Zeni, P. Berardino, M. Manunta, and A. Pepe, “An overview of the small BAseline subset algorithm: A DInSAR technique for surface deformation analysis”, in *Pure and Applied Geophysics*, vol. 164, Springer Nature, 2007, pp. 637–661. DOI: 10.1007/s00024-007-0192-9.
- [61] C. Colesanti, A. Ferretti, F. Novali, C. Prati, and F. Rocca, “SAR monitoring of progressive and seasonal ground deformation using the permanent scatterers technique”, *IEEE Transactions on Geoscience and Remote Sensing*, vol. 41, pp. 1685–1701, 2003. DOI: 10.1109/TGRS.2003.813278.
- [62] F. Rocca, “Modeling interferogram stacks”, *IEEE Transactions on Geoscience and Remote Sensing*, vol. 45, pp. 3289–3299, 2007. DOI: 10.1109/TGRS.2007.902286.
- [63] A. Ferretti, C. Prati, and F. Rocca, “Nonlinear subsidence rate estimation using permanent scatterers in differential SAR interferometry”, *IEEE Transactions on Geoscience and Remote Sensing*, vol. 38, pp. 2202–2212, 2000. DOI: 10.1109/36.868878.

- [64] D. Reale, G. Fornaro, and A. Pauciuolo, “Extension of 4-D SAR imaging to the monitoring of thermally dilating scatterers”, *IEEE Transactions on Geoscience and Remote Sensing*, vol. 51, pp. 5296–5306, 2013. DOI: 10.1109/tgrs.2012.2233205.
- [65] M. A. Siddique, U. Wegmüller, I. Hajnsek, and O. Frey, “Single-look SAR tomography as an add-on to PSI for improved deformation analysis in urban areas”, *IEEE Transactions on Geoscience and Remote Sensing*, vol. 54, pp. 6119–6137, 2016. DOI: 10.1109/tgrs.2016.2581261.
- [66] R. Goldstein, “Atmospheric limitations to repeat-track radar interferometry”, *Geophysical Research Letters*, vol. 22, pp. 2517–2520, 1995. DOI: 10.1029/95GL02475.
- [67] C. Delacourt, P. Briole, and J. A. Achache, “Tropospheric corrections of SAR interferograms with strong topography. application to Etna”, *Geophysical Research Letters*, vol. 25, pp. 2849–2852, 1998. DOI: 10.1029/98gl02112.
- [68] R. B. Lohman and M. Simons, “Some thoughts on the use of InSAR data to constrain models of surface deformation: Noise structure and data downsampling”, *Geochemistry, Geophysics, Geosystems*, vol. 6, 2005. DOI: 10.1029/2004gc000841.
- [69] X Zhou, Y. M. Xu, P Wang, and C Xing, “Research on atmospheric disturbance correction method of ground-based radar interferometry”, *IOP Conference Series: Earth and Environmental Science*, vol. 17, p. 012244, 2014. DOI: 10.1088/1755-1315/17/1/012244.
- [70] A. Ferretti, A. Fumagalli, F. Novali, C. Prati, F. Rocca, and A. Rucci, “A new algorithm for processing interferometric data-stacks: SqueeSAR”, *IEEE Transactions on Geoscience and Remote Sensing*, vol. 49, pp. 3460–3470, 2011. DOI: 10.1109/TGRS.2011.2124465.
- [71] A. Ferretti, C. Prati, and F. Rocca, “Permanent scatterers in SAR interferometry”, *IEEE Transactions on Geoscience and Remote Sensing*, vol. 39, pp. 8–20, 2001. DOI: 10.1109/36.898661.
- [72] C. Werner, U. Wegmüller, T. Strozzi, and A. Wiesmann, “Interferometric point target analysis for deformation mapping”, in *Proceeding of the IEEE International Geoscience and Remote Sensing Symposium*, vol. 7, IEEE, 2003, pp. 4362–4364. DOI: 10.1109/IGARSS.2003.1295516.
- [73] A. Hooper, H. Zebker, P. Segall, and B. Kampes, “A new method for measuring deformation on volcanoes and other natural terrains using InSAR persistent scatterers”, *Geophysical Research Letters*, vol. 31, 2004. DOI: 10.1029/2004gl021737.
- [74] D. A. Schmidt and R. Bürgmann, “Time-dependent land uplift and subsidence in the Santa Clara valley, California, from a large interferometric synthetic aperture radar data set”, *Journal of Geophysical Research: Solid Earth*, vol. 108, p. 2416, 2003. DOI: 10.1029/2002jb002267.
- [75] M. Wei and D. T. Sandwell, “Decorrelation of L-band and C-band interferometry over vegetated areas in California”, *IEEE Transactions on Geoscience and Remote Sensing*, vol. 48, pp. 2942–2952, 2010. DOI: 10.1109/tgrs.2010.2043442.
- [76] G. Nesti, D. Tarchi, and J.-P. Rudant, “Decorrelation of backscattered signal due to soil moisture changes”, in *Proceedings of the IEEE International Geoscience and Remote Sensing Symposium*, IEEE, 1995. DOI: 10.1109/igarss.1995.524098.

-
- [77] X. Luo, J. Askne, G. Smith, and P. Dammert, “Coherence characteristics of radar signals from rough soil - abstract”, *Journal of Electromagnetic Waves and Applications*, vol. 14, pp. 1555–1557, 2000. DOI: 10.1163/156939300x00310.
- [78] R. N. Treuhaft, S. N. Madsen, M. Moghaddam, and J. J. van Zyl, “Vegetation characteristics and underlying topography from interferometric radar”, *Radio Science*, vol. 31, pp. 1449–1485, 1996. DOI: 10.1029/96RS01763.
- [79] H. Zebker and E. W. Hoen, “Penetration depths inferred from interferometric volume decorrelation observed over the Greenland Ice Sheet”, *IEEE Transactions on Geoscience and Remote Sensing*, vol. 38, pp. 2571–2583, 2000. DOI: 10.1109/36.885204.
- [80] F. Gatelli, A. M. Guamieri, F. Parizzi, P. Pasquali, C. Prati, and F. Rocca, “The wavenumber shift in SAR interferometry”, *IEEE Transactions on Geoscience and Remote Sensing*, vol. 32, pp. 855–865, 1994. DOI: 10.1109/36.298013.
- [81] H. A. Zebker and Y. Lu, “Phase unwrapping algorithms for radar interferometry: Residue-cut, least-squares, and synthesis algorithms”, *Journal of the Optical Society of America A*, vol. 15, p. 586, 1998. DOI: 10.1364/josaa.15.000586.
- [82] R. M. Goldstein, H. A. Zebker, and C. L. Werner, “Satellite radar interferometry: Two-dimensional phase unwrapping”, *Radio Science*, vol. 23, pp. 713–720, 1988. DOI: 10.1029/rs023i004p00713.
- [83] F. Hocine, M. Fekir, A. Haddoud, S. Belhadj-aissa, and A. Belhadj-aissa, “A new 2D/3D phase unwrapping strategy of differential interferograms SAR”, *Journal of the Indian Society of Remote Sensing*, vol. 43, pp. 199–212, 2014. DOI: 10.1007/s12524-014-0398-0.
- [84] O. Mora, J. Mallorqui, and A. Broquetas, “Linear and nonlinear terrain deformation maps from a reduced set of interferometric SAR images”, *IEEE Transactions on Geoscience and Remote Sensing*, vol. 41, pp. 2243–2253, 2003. DOI: 10.1109/tgrs.2003.814657.
- [85] A. Hooper and H. A. Zebker, “Phase unwrapping in three dimensions with application to InSAR time series”, *Journal of the Optical Society of America A*, vol. 24, p. 2737, 2007. DOI: 10.1364/josaa.24.002737.
- [86] M. Costantini, F. Malvarosa, F. Minati, L. Pietranera, and G. Milillo, “A three-dimensional phase unwrapping algorithm for processing of multitemporal SAR interferometric measurements”, in *Proceedings of the IEEE International Geoscience and Remote Sensing Symposium*, IEEE, 2002. DOI: 10.1109/igarss.2002.1026239.
- [87] B. Osmanoglu, F. Sunar, S. Wdowinski, and E. Cabral-Cano, “Time series analysis of InSAR data: Methods and trends”, *ISPRS Journal of Photogrammetry and Remote Sensing*, vol. 115, pp. 90–102, 2016. DOI: 10.1016/j.isprsjprs.2015.10.003.
- [88] J.-S. Lee and E. Pottier, *Polarimetric Radar Imaging: From Basics To Applications*. CRC press, 2009. DOI: 10.1201/9781420054989.
- [89] M. Born, E. Wolf, A. B. Bhatia, P. C. Clemmow, D. Gabor, A. R. Stokes, A. M. Taylor, P. A. Wayman, and W. L. Wilcock, *Principles of Optics*. Cambridge University Press, 1999. DOI: 10.1017/cbo9781139644181.

- [90] H. Mott, *Remote Sensing with Polarimetric Radar*. John Wiley & Sons, Inc., 2006. DOI: 10.1002/0470079819.
- [91] S. Cloude, *Polarisation: Applications in Remote Sensing*. Oxford University Press, 2009. DOI: 10.1093/acprof:oso/9780199569731.001.0001.
- [92] J. R. Huynen, “Phenomenological Theory of Radar Targets”, PhD thesis, TU Delft, 1970. DOI: 10.1016/b978-0-12-709650-6.50020-1.
- [93] C. Whitney, “Pauli-algebraic operators in polarization optics”, *Journal of the Optical Society of America*, vol. 61, p. 1207, 1971. DOI: 10.1364/josa.61.001207.
- [94] E. Collett, *Field Guide to Polarization*. SPIE, 2005. DOI: 10.1117/3.626141.
- [95] A. Kostinski and W. Boerner, “On foundations of radar polarimetry”, *IEEE Transactions on Antennas and Propagation*, vol. 34, pp. 1395–1404, 1986. DOI: 10.1109/tap.1986.1143771.
- [96] W.-M. Boerner, W.-L. Yan, A.-Q. Xi, and Y. Yamaguchi, “Basic concepts of radar polarimetry”, in *Direct and Inverse Methods in Radar Polarimetry*, Springer Netherlands, 1992, pp. 155–245. DOI: 10.1007/978-94-010-9243-2_8.
- [97] D. Giuli, “Polarization diversity in radars”, *Proceedings of the IEEE*, vol. 74, pp. 245–269, 1986. DOI: 10.1109/proc.1986.13457.
- [98] S. Cloude, J. Fortuny, J. Lopez-Sanchez, and A. Sieber, “Wide-band polarimetric radar inversion studies for vegetation layers”, *IEEE Transactions on Geoscience and Remote Sensing*, vol. 37, pp. 2430–2441, 1999. DOI: 10.1109/36.789640.
- [99] J. J. van Zyl, H. A. Zebker, and C. Elachi, “Imaging radar polarization signatures: Theory and observation”, *Radio Science*, vol. 22, pp. 529–543, 1987. DOI: 10.1029/RS022i004p00529.
- [100] J. van Zyl and Y. Kim, *Synthetic Aperture Radar Polarimetry*. John Wiley & Sons, Inc., 2011. DOI: 10.1002/9781118116104.
- [101] S. Bickel and R. Bates, “Effects of magneto-ionic propagation on the polarization scattering matrix”, *Proceedings of the IEEE*, vol. 53, pp. 1089–1091, 1965. DOI: 10.1109/proc.1965.4097.
- [102] F. Meyer, “A review of ionospheric effects in low-frequency SAR signals, correction methods, and performance requirements”, in *Proceedings of the IEEE International Geoscience and Remote Sensing Symposium*, IEEE, 2010. DOI: 10.1109/igarss.2010.5654258.
- [103] N. G. Parke, “Optical algebra”, *Journal of Mathematics and Physics*, vol. 28, pp. 131–139, 1949. DOI: 10.1002/sapm1949281131.
- [104] S. Cloude, “A new method for characterizing depolarization effects in radar and optical remote sensing”, in *Proceedings of the IEEE International Geoscience and Remote Sensing Symposium*, IEEE, 2011. DOI: 10.1109/igarss.2011.976677.
- [105] J. W. Hovenier, C. V. D. Mee, and H. Domke, *Transfer of Polarized Light in Planetary Atmospheres*. Springer Netherlands, 2004. DOI: 10.1007/978-1-4020-2856-4.
- [106] J. W. Hovenier, “Structure of a general pure Mueller matrix”, *Applied Optics*, vol. 33, p. 8318, 1994. DOI: 10.1364/ao.33.008318.

-
- [107] F. Weissgerber, E. Colin-Koeniguer, N. Trouve, and J.-M. Nicolas, "A temporal estimation of entropy and its comparison with spatial estimations on PolSAR images", *IEEE Journal of Selected Topics in Applied Earth Observations and Remote Sensing*, vol. 9, pp. 3809–3820, 2016. DOI: 10.1109/jstars.2016.2555243.
- [108] S. Cloude and E. Pottier, "An entropy based classification scheme for land applications of polarimetric SAR", *IEEE Transactions on Geoscience and Remote Sensing*, vol. 35, pp. 68–78, 1997. DOI: 10.1109/36.551935.
- [109] —, "A review of target decomposition theorems in radar polarimetry", *IEEE Transactions on Geoscience and Remote Sensing*, vol. 34, pp. 498–518, 1996. DOI: 10.1109/36.485127.
- [110] D. Turner and I. H. Woodhouse, "An icon-based synoptic visualization of fully polarimetric radar data", *Remote Sensing*, vol. 4, pp. 648–660, 2012. DOI: 10.3390/rs4030648.
- [111] M. Galletti, M. Chandra, E. Pottier, and A. Ghorbani, "Application of the Cloude-Pottier decomposition to weather radar signatures", *Advances in Radio Science*, vol. 3, pp. 413–420, 2005. DOI: 10.5194/ars-3-413-2005.
- [112] R. Touzi, "Target scattering decomposition in terms of roll-invariant target parameters", *IEEE Transactions on Geoscience and Remote Sensing*, vol. 45, pp. 73–84, 2007. DOI: 10.1109/tgrs.2006.886176.
- [113] D. Giuli, L. Facheris, M. Fossi, and A. Rossettini, "Simultaneous scattering matrix measurement through signal coding", in *Proceedings of the IEEE International Conference on Radar*, IEEE, 1990. DOI: 10.1109/radar.1990.201173.
- [114] D. Giuli, M. Fossi, and L. Facheris, "Radar target scattering matrix measurement through orthogonal signals", *IEEE Proceedings F Radar and Signal Processing*, vol. 140, p. 233, 1993. DOI: 10.1049/ip-f-2.1993.0033.
- [115] A. Freeman, "SAR calibration: An overview", *IEEE Transactions on Geoscience and Remote Sensing*, vol. 30, pp. 1107–1121, 1992. DOI: 10.1109/36.193786.
- [116] S. Quegan, "A unified algorithm for phase and cross-talk calibration of polarimetric data-theory and observations", *IEEE Transactions on Geoscience and Remote Sensing*, vol. 32, pp. 89–99, 1994. DOI: 10.1109/36.285192.
- [117] H. A. Zebker, J. J. van Zyl, and D. N. Held, "Imaging radar polarimetry from wave synthesis", *Journal of Geophysical Research*, vol. 92, p. 683, 1987. DOI: 10.1029/jb092ib01p00683.
- [118] M. Whitt, F. Ulaby, P. Polatin, and V. Liepa, "A general polarimetric radar calibration technique", *IEEE Transactions on Antennas and Propagation*, vol. 39, pp. 62–67, 1990. DOI: 10.1109/8.64436.
- [119] K. Sarabandi, "Calibration of a polarimetric synthetic aperture radar using a known distributed target", *IEEE Transactions on Geoscience and Remote Sensing*, vol. 32, pp. 575–582, 1994. DOI: 10.1109/36.297998.
- [120] A. G. Fore, B. D. Chapman, B. P. Hawkins, S. Hensley, C. E. Jones, T. R. Michel, and R. J. Muellerschoen, "UAVSAR polarimetric calibration", *IEEE Transactions on Geoscience and Remote Sensing*, vol. 53, pp. 3481–3491, 2015. DOI: 10.1109/TGRS.2014.2377637.

- [121] K. Sarabandi and F. Ulaby, “A convenient technique for polarimetric calibration of single-antenna radar systems”, *IEEE Transactions on Geoscience and Remote Sensing*, vol. 28, pp. 1022–1033, 1990. DOI: 10.1109/36.62627.
- [122] A. Moreira, G. Krieger, M. Younis, I. Hajnsek, K. Papathanassiou, M. Eineder, and F. D. Zan, “Tandem-L: A mission proposal for monitoring dynamic Earth processes”, in *Proceedings of the IEEE International Geoscience and Remote Sensing Symposium*, IEEE, 2011, pp. 1385–1388. DOI: 10.1109/IGARSS.2011.6049324.
- [123] R. Horn, A. Nottensteiner, A. Reigber, J. Fischer, and R. Scheiber, “F-SAR—DLR’s new multifrequency polarimetric airborne SAR”, in *Proceedings of the IEEE International Geoscience and Remote Sensing Symposium*, IEEE, vol. 2, IEEE, 2009, pp. II-902. DOI: 10.1109/IGARSS.2009.5418244.
- [124] A. Rosenqvist, M. Shimada, and M. Watanabe, “ALOS PALSAR: Technical outline and mission concepts”, in *Proceeding of the International Symposium on Retrieval of Bio- and Geophysical Parameters from SAR Data for Land Applications*, vol. 1, 2004, pp. 1–7.
- [125] R. Horn, “E-SAR - the experimental airborne L/C-band SAR system of DFVLR”, in *Proceedings of the IEEE International Geoscience and Remote Sensing Symposium*, IEEE, vol. 2, IEEE, 1988, pp. 1025–1026. DOI: 10.1109/IGARSS.1988.570511.
- [126] L. C. Morena, K. V. James, and J. Beck, “An introduction to the RADARSAT-2 mission”, *Canadian Journal of Remote Sensing*, vol. 30, pp. 221–234, 2004. DOI: 10.5589/m04-004.
- [127] R. Raney, A. Luscombe, E. Langham, and S. Ahmed, “RADARSAT (SAR imaging)”, *Proceedings of the IEEE*, vol. 79, pp. 839–849, 1991. DOI: 10.1109/5.90162.
- [128] H. Rudolf, D. Leva, D. Tarchi, and A. Sieber, “A mobile and versatile SAR system”, in *Proceedings of the IEEE International Geoscience and Remote Sensing Symposium*, vol. 1, IEEE, 1999, pp. 592–594. DOI: 10.1109/IGARSS.1999.773575.
- [129] D. Leva, G. Nico, D. Tarchi, J. Fortuny-Guasch, and A. Sieber, “Temporal analysis of a landslide by means of a ground-based SAR interferometer”, *IEEE Transactions on Geoscience and Remote Sensing*, vol. 41, pp. 745–752, 2003. DOI: 10.1109/TGRS.2003.808902.
- [130] S. Rödelberger, “Real-time processing of ground based synthetic aperture radar (GB-SAR) measurements”, PhD thesis, TU Darmstadt, 2011.
- [131] A. Aguasca, A. Broquetas, J. Mallorque, and X. Fabregas, “A solid state L to X-band flexible ground-based SAR system for continuous monitoring applications”, in *Proceedings of the IEEE International Geoscience and Remote Sensing Symposium*, vol. 2, IEEE, 2004, pp. 757–760. DOI: 10.1109/IGARSS.2004.1368512.
- [132] S. Rodelsperger, A. Coccia, D. Vicente, and A. Meta, “Introduction to the new Metasensing ground-based SAR: Technical description and data analysis”, in *Proceedings of the IEEE International Geoscience and Remote Sensing Symposium*, IEEE, 2012, pp. 4790–4792. DOI: 10.1109/IGARSS.2012.6352542.

-
- [133] S. Rödelsperger and A. Meta, "MetaSensing's FastGBSAR: Ground based radar for deformation monitoring", in *SAR Image Analysis, Modeling, and Techniques XIV*, SPIE, 2014. DOI: 10.1117/12.2067243.
- [134] H. Lee, S.-J. Cho, and K.-E. Kim, "A ground-based arc-scanning synthetic aperture radar (Arc-SAR) system and focusing algorithms", in *Proceedings of the IEEE International Geoscience and Remote Sensing Symposium*, IEEE, 2010, pp. 3490–3493. DOI: 10.1109/IGARSS.2010.5652569.
- [135] H. Lee, J.-H. Lee, K.-E. Kim, N.-H. Sung, and S.-J. Cho, "Development of a truck-mounted arc-scanning synthetic aperture radar", *IEEE Transactions on Geoscience and Remote Sensing*, vol. 52, pp. 2773–2779, 2014. DOI: 10.1109/TGRS.2013.2265700.
- [136] M. Pieraccini and L. Miccinesi, "ArcSAR: Theory, simulations, and experimental verification", *IEEE Transactions on Microwave Theory and Techniques*, vol. 65, pp. 1–9, 2016. DOI: 10.1109/tmtt.2016.2613926.
- [137] H. Rudolf, D. Leva, D. Tarchi, and A. Sieber, "A parallelogram shaped arm for improving circular SARs", in *Proceedings of the IEEE International Geoscience and Remote Sensing Symposium*, vol. 1, IEEE, 1999, pp. 553–555. DOI: 10.1109/IGARSS.1999.773562.
- [138] S. Rödelsperger, G. Läufer, C. Gerstenecker, and M. Becker, "Monitoring of displacements with ground-based microwave interferometry: IBIS-S and IBIS-L", *Journal of Applied Geodesy*, vol. 4, pp. 41–54, 2010. DOI: 10.1515/jag.2010.005.
- [139] Z.-S. Zhou, W.-M. Boerner, and M. Sato, "Development of a ground-based polarimetric broadband SAR system for noninvasive ground-truth validation in vegetation monitoring", *IEEE Transactions on Geoscience and Remote Sensing*, vol. 42, pp. 1803–1810, 2004. DOI: 10.1109/TGRS.2004.832248.
- [140] A. Wiesmann, C. Werner, C. Mätzler, M. Schneebeli, T. Strozzi, and U. Wegmüller, "Mobile X-to Ku-band scatterometer in support of the CoRe-H2O mission", in *Proceedings of the IEEE International Geoscience and Remote Sensing Symposium*, IEEE, 2008. DOI: 10.1109/igarss.2008.4780073.
- [141] Y. Luo, H. Song, R. Wang, Y. Deng, F. Zhao, and Z. Xu, "Arc FMCW SAR and applications in ground monitoring", *IEEE Transactions on Geoscience and Remote Sensing*, vol. 52, pp. 5989–5998, 2014. DOI: 10.1109/TGRS.2014.2325905.
- [142] A. Stove, "Linear FMCW radar techniques", *IEE Proceedings F Radar and Signal Processing*, vol. 139, p. 343, 1992. DOI: 10.1049/ip-f-2.1992.0048.
- [143] C. L. Werner, A. Wiesmann, T. Strozzi, A. Kos, R. Caduff, and U. Wegmüller, "The GPRI multi-mode differential interferometric radar for ground-based observations", in *Proceedings of the European Conference on Synthetic Aperture Radar*, VDE, 2012, pp. 304–307.
- [144] K. E. Allstadt, D. E. Shean, A. Campbell, M. Fahnestock, and S. D. Malone, "Observations of seasonal and diurnal glacier velocities at Mount Rainier, Washington, using terrestrial radar interferometry", *Cryosphere*, vol. 9, pp. 2219–2235, 2015. DOI: 10.5194/tc-9-2219-2015.

- [145] T. H. Dixon, D. Voytenko, C. Lembke, S. de la Peña, I. Howat, N. Gourmelen, C. Werner, and B. Oddsson, “Emerging technology monitors ice-sea interface at outlet glaciers”, *Eos*, vol. 93, pp. 497–498, 2012. DOI: 10.1029/2012EO480001.
- [146] L. Noferini, D. Mecatti, G. Macaluso, M. Pieraccini, and C. Atzeni, “Monitoring of Belvedere Glacier using a wide angle GB-SAR interferometer”, *Journal of Applied Geophysics*, vol. 68, pp. 289–293, 2009. DOI: 10.1016/j.jappgeo.2009.02.004.
- [147] D. Voytenko, T. H. Dixon, I. M. Howat, N. Gourmelen, C. Lembke, C. L. Werner, S. D. L. Peña, and B. Oddsson, “Multi-year observations of Breiðamerkurjökull, a marine-terminating glacier in southeastern Iceland, using terrestrial radar interferometry”, *Journal of Glaciology*, vol. 61, pp. 42–54, 2015. DOI: 10.3189/2015JøG14J099.
- [148] D. Voytenko, T. H. Dixon, C. Werner, N. Gourmelen, I. M. Howat, P. C. Tinder, and A. Hooper, “Monitoring a glacier in southeastern Iceland with the portable terrestrial radar interferometer”, in *Proceedings of the IEEE International Geoscience and Remote Sensing Symposium*, IEEE, 2012, pp. 3230–3232. DOI: 10.1109/IGARSS.2012.6350736.
- [149] R. Caduff and T. Strozzi, “Terrestrial radar interferometry monitoring during a landslide emergency 2016, Ghirone, Switzerland”, in *Advancing Culture of Living with Landslides*, Springer International Publishing, 2017, pp. 301–309. DOI: 10.1007/978-3-319-53487-9_34.
- [150] L. Kristensen, C. Rivolta, J. Dehls, and L. H. Blikra, “GB InSAR measurement at the Åknes rock-slide, Norway”, *Italian Journal of Engineering Geology and Environment*, vol. 2013, pp. 339–348, 2013. DOI: 10.4408/IJEGE.2013-06.B-32.
- [151] T. Strozzi, R. Delaloye, H. Raetzo, and U. Wegmüller, “Radar interferometric observations of destabilized rock glaciers”, in *Proceedings of Fringe*, 2010, p. 5. DOI: 10.1126/science.170.3962.1090.
- [152] C. D. Ventisette, E. Intrieri, G. Luzi, N. Casagli, R. Fanti, and D. Leva, “Using ground based radar interferometry during emergency: The case of the A3 motorway (Calabria region, Italy) threatened by a landslide”, *Natural Hazards and Earth System Science*, vol. 11, pp. 2483–2495, 2011. DOI: 10.5194/nhess-11-2483-2011.
- [153] B. Lowry, F. Gomez, W. Zhou, M. Mooney, B. Held, and J. Grasmick, “High resolution displacement monitoring of a slow velocity landslide using ground based radar interferometry”, *Engineering Geology*, vol. 166, pp. 160–169, 2013. DOI: 10.1016/j.enggeo.2013.07.007.
- [154] R. Caduff, A. Kos, F. Schlunegger, B. W. McArdeell, and A. Wiesmann, “Terrestrial radar interferometric measurement of hillslope deformation and atmospheric disturbances in the Illgraben debris-flow catchment, Switzerland”, *IEEE Geoscience and Remote Sensing Letters*, vol. 11, pp. 434–438, 2014. DOI: 10.1109/lgrs.2013.2264564.
- [155] C. Werner, B. Lowry, U. Wegmüller, N. Pugh, G. Schrock, and W. Zhou, “Deformation time-series derived from terrestrial radar observations using persistent scatterer interferometry in Seattle, Washington”, in *Proceedings of the IEEE International Geoscience and Remote Sensing Symposium*, IEEE, 2016. DOI: 10.1109/igarss.2016.7730784.

-
- [156] L. Pipia, A. Aguasca, X. Fabregas, J. J. Mallorqui, C. Lopez-Martinez, and J. Marturia, "Mining induced subsidence monitoring in urban areas with a ground-based SAR", in *2007 Urban Remote Sensing Joint Event*, IEEE, 2007. DOI: 10.1109/urs.2007.371881.
- [157] A. D. Pasquale, G. Nico, A. Pitullo, and G. Prezioso, "Monitoring strategies of earth dams by ground-based radar interferometry: How to extract useful information for seismic risk assessment", *Sensors*, vol. 18, p. 244, 2018. DOI: 10.3390/s18010244.
- [158] D. Tarchi, H. Rudolf, G. Luzi, L. Chiarantini, P. Coppo, and A. Sieber, "SAR interferometry for structural changes detection: A demonstration test on a dam", in *Proceedings of the IEEE International Geoscience and Remote Sensing Symposium*, IEEE, 1999. DOI: 10.1109/igarss.1999.772006.
- [159] J. Bennett and K. Morrison, "Development of a ground-based, polarimetric synthetic aperture radar", *Proceedings of the IEEE Aerospace Applications Conference*, vol. 4, 139–146 vol.4, 1996. DOI: 10.1109/AERO.1996.499408.
- [160] J. Bennett, K. Morrison, A. Race, G. Cookmartin, and S. Quegan, "The UK NERC fully portable polarimetric ground-based synthetic aperture radar (GB-SAR)", in *Proceedings of the European Conference on Synthetic Aperture Radar*, IEEE, 2000, pp. 2313–2315. DOI: 10.1109/IGARSS.2000.858393.
- [161] K. Morrison, J. C. Bennett, G. Cookmartin, A. J. McDonald, A. Race, and S. Quegan, "Three-dimensional x-band SAR imaging of a small conifer tree", *International Journal of Remote Sensing*, vol. 22, pp. 705–710, 2001. DOI: 10.1080/01431160010013487.
- [162] K. Morrison, J. Bennett, and S. Solberg, "Ground-based C-band tomographic profiling of a conifer forest stand", *International Journal of Remote Sensing*, vol. 34, pp. 7838–7853, 2013. DOI: 10.1080/01431161.2013.826836.
- [163] R. Iglesias, A. Aguasca, X. Fabregas, J. J. Mallorqui, D. Monells, C. Lopez-Martinez, and L. Pipia, "Ground-based polarimetric SAR interferometry for the monitoring of terrain displacement phenomena—part II: Applications", *IEEE Journal of Selected Topics in Applied Earth Observations and Remote Sensing*, vol. 8, pp. 1–14, 2014. DOI: 10.1109/JSTARS.2014.2366711.
- [164] R. Iglesias, D. Monells, X. Fabregas, J. J. Mallorqui, A. Aguasca, and C. Lopez-Martinez, "Phase quality optimization in polarimetric differential SAR interferometry", *IEEE Transactions on Geoscience and Remote Sensing*, vol. 52, pp. 2875–2888, 2014. DOI: 10.1109/TGRS.2013.2267095.
- [165] L. Pipia, "Polarimetric differential SAR interferometry with ground-based sensors", PhD thesis, Universitat Politècnica de Catalunya, 2009. DOI: 10.803/6951.
- [166] L. Pipia, X. Fabregas, A. Aguasca, and C. Lopez-Martinez, "Polarimetric temporal analysis of urban environments with a ground-based SAR", *IEEE Transactions on Geoscience and Remote Sensing*, vol. 51, pp. 2343–2360, 2013. DOI: 10.1109/TGRS.2012.2211369.
- [167] L. Pipia, X. Fabregas, A. Aguasca, C. Lopez-Martinez, S. Duque, J. J. Mallorqui, and J. Marturia, "Polarimetric differential SAR interferometry: First results with ground-based measurements", *IEEE Geoscience and Remote Sensing Letters*, vol. 6, pp. 167–171, 2009. DOI: 10.1109/LGRS.2008.2009007.

- [168] L. Pipia, X. Fabregas, A. Aguasca, C. Lopez-Martinez, J. J. Mallorqui, and O. Mora, “A subsidence monitoring project using a polarimetric GB-SAR sensor”, *European Space Agency, (Special Publication) ESA SP*, 2007.
- [169] L. Pipia, X. Fabregas, A. Aguasca, C. Lopez-Martinez, J. J. Mallorqui, and O. Moraline, “Polarimetric temporal information for urban deformation map retrieval”, in *Proceedings of the IEEE International Geoscience and Remote Sensing Symposium*, IEEE, 2007, pp. 192–195. DOI: 10.1109/IGARSS.2007.4422762.
- [170] S. Baffelli, O. Frey, C. Werner, and I. Hajnsek, “Polarimetric calibration of the Ku-band advanced polarimetric radar interferometer”, *IEEE Transactions on Geoscience and Remote Sensing*, vol. 56, pp. 1–17, 2018. DOI: 10.1109/tgrs.2017.2778049.
- [171] R. K. Enju and M. B. Perotoni, “Slotted waveguide antenna design using 3D EM simulation”, *Microwave Journal*, 2013.
- [172] M. Grabowski, “Non-resonant slotted waveguide antenna design method”, *High Frequency Electronics Journal*, pp. 32–46, 2012.
- [173] H. M. E. Misilmani, M. Al-Husseini, and K. Y. Kabalan, “Design of slotted waveguide antennas with low sidelobes for high power microwave applications”, *Progress In Electromagnetics Research C*, vol. 56, pp. 15–28, 2015. DOI: 10.2528/pierc14121903.
- [174] J. Ramsay and B. Popovich, “Series-slotted waveguide array antennas”, in *IRE International Convention Record*, vol. 11, Institute of Electrical and Electronics Engineers, 1956, pp. 30–55. DOI: 10.1109/IRECON.1963.1147177.
- [175] P. J. González and J. Fernández, “Error estimation in multitemporal InSAR deformation time series, with application to Lanzarote, Canary Islands”, *Journal of Geophysical Research: Solid Earth*, vol. 116, pp. 1–17, 2011. DOI: 10.1029/2011JB008412.
- [176] Y. Cao, Z. Li, J. Wei, J. Hu, M. Duan, and G. Feng, “Stochastic modeling for time series InSAR: With emphasis on atmospheric effects”, *Journal of Geodesy*, vol. 92, pp. 185–204, 1, 2018. DOI: 10.1007/s00190-017-1055-5.
- [177] D. G. Krige, “A statistical approach to some basic mine valuation problems on the Witwatersrand”, *Journal of the Chemical, Metallurgical and Mining Society of South Africa*, pp. 201–215, 1952. DOI: 10.2307/3006914.
- [178] J. Butt, A. Wieser, and S. Conzett, “Intrinsic random functions for mitigation of atmospheric effects in terrestrial radar interferometry”, *Proceedings of JISDM 2016 Vienna*, vol. 11, pp. 89–98, 2016. DOI: 10.1515/jag-2016-0042.
- [179] R. Snieder and J. Trampert, “Inverse problems in geophysics”, in *Wavefield Inversion*, Springer Vienna, 1999, pp. 119–190. DOI: 10.1007/978-3-7091-2486-4_3.
- [180] A. Tarantola and B. Valette, “Inverse problems - quest for information”, *Journal of Geophysics*, pp. 159–170, 1982.
- [181] F. Ulaby, M. Whitt, and K. Sarabandi, “AVNA-based polarimetric scatterometers”, *IEEE Antennas and Propagation magazine*, vol. 32, pp. 6–17, 1990. DOI: 10.1109/74.80582.

- [182] M. Whitt, F. Ulaby, and K Sarabandi, "Polarimetric scatterometer systems and measurements", *Radar Polarimetry for Geoscience Applications*, vol. 5, pp. 191–217, 1990.
- [183] Y. Kim, T. Jackson, R. Bindlish, H. Lee, and S. Hong, "Monitoring soybean growth using L-, C-, and X-band scatterometer data", *International Journal of Remote Sensing*, vol. 34, pp. 4069–4082, 2013. DOI: 10.1080/01431161.2013.772309.

POLARIMETRIC CALIBRATION OF THE KU-BAND ADVANCED POLARIMETRIC RADAR INTERFEROMETER (KAPRI)

This chapter is a post-print version of a peer reviewed journal article that was published as:

S. Baffelli, O. Frey, C. Werner, and I. Hajnsek, “Polarimetric calibration of the Ku-band advanced polarimetric radar interferometer”, *IEEE Transactions on Geoscience and Remote Sensing*, vol. 56, pp. 1–17, Apr. 2018. DOI: 10.1109/tgrs.2017.2778049

It differs from the published version in formatting and typesetting. A final list of errata is included.

Differential interferometry using ground-based radar systems permits to monitor displacements in natural terrain with high flexibility in location, time of acquisition and revisit time. In combination with polarimetric imaging, discrimination of different scattering mechanisms present in a resolution cell can be obtained simultaneously with the estimation of surface displacement. In this paper we present the pre-processing steps and the calibration procedure required to produce high-quality calibrated polarimetric single-look complex imagery with KAPRI, a new portable Ku-band polarimetric radar interferometer. The processing of KAPRI data into single look complex images is addressed, including the correction of beam squint and of azimuthal phase variations. A polarimetric calibration model adapted to the acquisition mode is presented and used to produce calibrated polarimetric covariance matrix data. The methods are validated by means of a scene containing five trihedral corner reflectors. Data preprocessing is assessed by analyzing the oversampled response of a corner reflector and the polarimetric calibration quality is verified by computing polarimetric signatures and residual calibration parameters.

2.1 INTRODUCTION

Differential radar interferometry [2–5] is widely used to monitor and study changes in the natural and built environment. The ability to measure the line-of-sight component of movements over large areas makes it suitable for many applications. Some examples are the estimation of subsidence rate associated with temporal changes in the water table of aquifers, oil and gas extraction, deep mining and tunnel excavation [6–8], the monitoring of inflation/deflation connected to volcanic activity [9], the mapping of ice sheet and glacier motion [10, 11], the observation of instable slopes in rugged natural terrain and open pit mines [12, 13] and the measurement of seismic displacements [14, 15].

Fully polarimetric radar data provides additional information on the scattering mechanism within each resolution cell, which is employed for classification of the surface cover [16, 17], to extract geophysical parameters such as moisture content [18], to estimate the orientation of the vegetation canopy [19] or the height of fresh snow [20].

The availability of polarimetric information in addition to the interferometric time series allows to combine the scattering matrix and the interferometric coherence to better characterize the natural processes observed with the radar: a salient example being coherence optimization, where the scattering mechanism providing the best coherence and thus the least noisy phase measurement is selected [21, 22].

Spaceborne SAR systems, such as ERS-1 and 2, Envisat/ASAR, TerraSAR-X, Sentinel 1-A/1-B, Radarsat-1 and 2 and ALOS, ALOS 2, Cosmo SkyMed, have been an important data source to build up interferometric time series for displacement measurements — sometimes spanning over many years. These platforms are convenient in that they offer a large coverage in a single pass. However, the revisit time of these system is limited to few hours at best. In many cases, to better understand the dynamics of natural processes and for real-time surveillance and alarming, a denser temporal sampling over longer time spans and other observation geometries are desired than the ones afforded by current spaceborne radar earth observation systems.

2.1.1 State of the Art

Today, several ground-based radar systems are available, operating in C [23–25], X [26, 27] or Ku band [23, 24, 28, 29]. The majority of these systems are based on aperture synthesis, using a moving antenna on a rail. An alternative imaging approach is to scan a fan beam by rotating a large antenna [28, 30]. This imaging method has been called type II in [31]. This configuration has certain advantages over ground-based synthetic aperture systems [32] of comparable rail length:

1. Azimuth samples are acquired independently and do not require focusing, eliminating defocusing and loss of coherence caused by moving targets and atmospheric phase screens during aperture time. These changes may adversely affect the coherence of the scene over the aperture length and will worsen the azimuth resolution. This is especially problematic for the analysis of coherent targets.

2. A large angular section of up to 270° can be imaged in a single pass. This is more difficult to obtain using a rail-based SAR.

An important advantage of rail-based SAR systems is the better azimuth resolution: a SAR using a rail of length L will have an angular resolution of:

$$\theta_{3dB}^{SAR} = \frac{\lambda}{2L}, \quad (2.1)$$

while an antenna with physical aperture size L has an azimuth 3dB resolution of:

$$\theta_{3dB}^{RAR} = \frac{\lambda}{L}. \quad (2.2)$$

The majority of polarimetric ground-based radar systems is based on the aperture synthesis principle. An indoor system is presented in [33] followed by a portable outdoors version [34]. A broadband polarimetric SAR system with two dimensional aperture synthesis is introduced in [35], with measurement results presented in [36]. Another example of a synthetic aperture system is described in [26, 27, 37–39]. Examples of ground-based polarimetric SAR data at X and C band are shown in [25, 40].

A dual polarization, multiband GB-SAR system is used in [41] to produce tomograms of snow covered sea ice. A similar concept is used in [42, 43] to produce tomographic profiles of a snow pack by synthesizing an aperture in the elevation direction.

Excluding non-imaging devices such as ground-based scatterometers, only few real aperture polarimetric ground-based radars exist, one example being the C-band version of the Gamma portable radar interferometer (GPRI) [44].

2.1.2 KAPRI: Real Aperture Polarimetric FMCW Radar

This paper introduces KAPRI, the Ku-band advanced polarimetric radar interferometer (KAPRI)[45]. It is an extension of the GPRI (Gamma Portable Radar Interferometer) [28, 30, 46], a real-aperture radar interferometer operating in Ku-band at 17.2 GHz. It is designed to monitor unstable slopes using zero baseline differential interferometry [3]; two antennas arranged along a spatial baseline and a dual channel receiver permit to acquire digital elevation models.

The GPRI employs 2-m-long, vertically polarized slotted waveguide antennas, giving the system a 3-dB azimuth beamwidth of 0.385° and a 3-dB elevation beamwidth of 35° .

The feature distinguishing KAPRI and GPRI is the addition of horizontally polarized antennas and switches that permit to connect transmitter and receiver to either type of antenna. Together with modifications in the control software, they enable it to acquire a full polarimetric-interferometric dataset by cycling through all the combinations of transmitted and received polarization during the acquisition.

In Table 2.1 the main hardware characteristics of KAPRI are summarized.

Parameter	Value
Modulation	FM-CW (250 μ s to 16ms chirp duration)
Center frequency	17.2GHz
Bandwidth	200MHz
Range resolution	0.95 m 3 dB resolution @ -26 dB peak sidelobe ratio (PSLR)
Azimuth 3dB beamwidth	0.385°
Elevation 3dB beamwidth	35°
Polarization	fully polarimetric, selectable TX and RX polarization

Table 2.1: Summary of main KAPRI parameters.

2.1.3 Contributions of This Paper

The following contributions are made in this paper:

1. Preprocessing methods adapted to KAPRI's hardware are presented, that can be used to generate correct single look complex (SLC) images from the acquired raw data.
2. A polarimetric calibration model adapted to the system design of KAPRI is presented. It includes the correction of effects caused by different designs of vertical and horizontal polarized antennas and the presence of spatial baselines between their phase centers.
3. The proposed processing and calibration approaches are validated by analyzing the response of trihedral corner reflectors in a specifically acquired dataset.

2.1.4 Outline

Section 2.2.1 presents the methods employed to process the raw data into range compressed SLC. This part includes a derivation of the frequency modulated continuous wave (FMCW) signal model and of the acquisition geometry that will be used throughout the rest of this paper. subsection 2.2.2 deals with the correction of frequency-dependent beam squint due to the slotted waveguide antenna design. These two sections describe the parts of the processing that are common to both KAPRI and GPRI. The quality of the processing is evaluated in subsection 2.3.1 by plotting the oversampled phase and amplitude response of trihedral corner reflectors, where significant range resolution improvements are observed by applying the described squint compensation procedure.

After this step, the range compressed, frequency-squint corrected data still show a residual azimuth phase variation, especially in the VV channel where a linear variation of almost 30° is observed for samples inside the antenna beamwidth. This effect is modeled in subsection 2.2.3 as a change in distance between the antennas phase center and the scatterers caused by the rotation of the antenna. A method to correct it is proposed and tested in subsection 2.3.2 on an array of five trihedral corner reflectors.

An azimuthal shift between the HH and the VV channel is observed on the response of point targets along with the phase variation; it is ascribed to misaligned antenna patterns. If left uncorrected, it would cause a reduced power and decreased signal-to-noise-ratio (SNR) for cross-polar measurements.

To remove it, modified antenna mounts that permit to mechanically shifting the antennas mainlobe were manufactured. They are tested in subsection 2.3.3 by analyzing the response of a cross-polarizing dihedral reflector acquired with different antenna mounting settings.

A final step is required before polarimetric calibration: since KAPRI employs separate antennas for each transmit and receive polarization, spatial baselines are obtained between certain combinations of channels. These baselines add a topographic contribution to the polarimetric phase differences. In subsection 2.2.5 a method is derived to estimate this contribution using an interferogram obtained from two identically polarized channel on a baseline and rescaled to the undesired polarimetric baseline. Its validity is verified by analyzing the resulting HH-VV phase difference in subsection 2.3.4.

In subsection 2.2.6 the polarimetric calibration is discussed. A linear distortion model without crosstalk is assumed; the copolar phase and amplitude imbalances are estimated using a trihedral corner reflector, while the imbalance between the crosspolar channel is determined using the HV-VH phase difference over distributed scatterers assuming reciprocity. The plausibility of zero cross-talk is assessed by computing the polarization purity of all the trihedral reflectors in the calibration dataset, showing a purity better than 35 dB at worst.

Finally, in subsection 2.3.5 the quality of data calibration is assessed by computing polarization signatures for the trihedral corner reflectors and by estimating calibration model residuals on the corner reflector array.

2.2 METHODS AND DATA

2.2.1 KAPRI: FMCW Radar Signal Model

A fundamental requirement to generate calibrated polarimetric data is the availability of properly processed SLC images for all elements of the polarimetric scattering matrix. To process them, it is necessary to understand the data acquisition and correct several effects specific to KAPRI. For this purpose a signal model for type II [31] radar data using the deramp-on-receive FMCW architecture [47] is introduced.

Consider a coordinate system having its origin at the location of a radar, as depicted in Figure 2.1. In this system the antenna is mounted on a lever arm of length L_{arm} ; its mainlobe is parallel to the x axis when the pointing angle θ is 0. The radar images a scene with a complex reflectivity distribution $\sigma(x, y)$ by measuring range profiles $\hat{\sigma}(R, \theta)$ for a number of antenna azimuths angles $\theta = \arctan\left(\frac{y}{x}\right)$ by rotating the antenna assembly with angular speed ω . Each profile is measured by transmitting a linearly modulated signal of duration τ with bandwidth B and center frequency f_c :

$$s_t(t) = e^{j2\pi\left(tf_c + \frac{\gamma}{2}t^2\right)}. \quad (2.3)$$

with $\gamma = \frac{B}{\tau}$. The backscattered signal s_r for a scatterer at range R is s_t delayed by $\frac{2R}{c}$ and scaled by σ , the complex reflectivity of the scatterer.

$$s_r(t) = \sigma e^{j2\pi\left(\left(t - \frac{2R}{c}\right)f_c + \frac{\gamma}{2}\left(t - \frac{2R}{c}\right)^2\right)}. \quad (2.4)$$

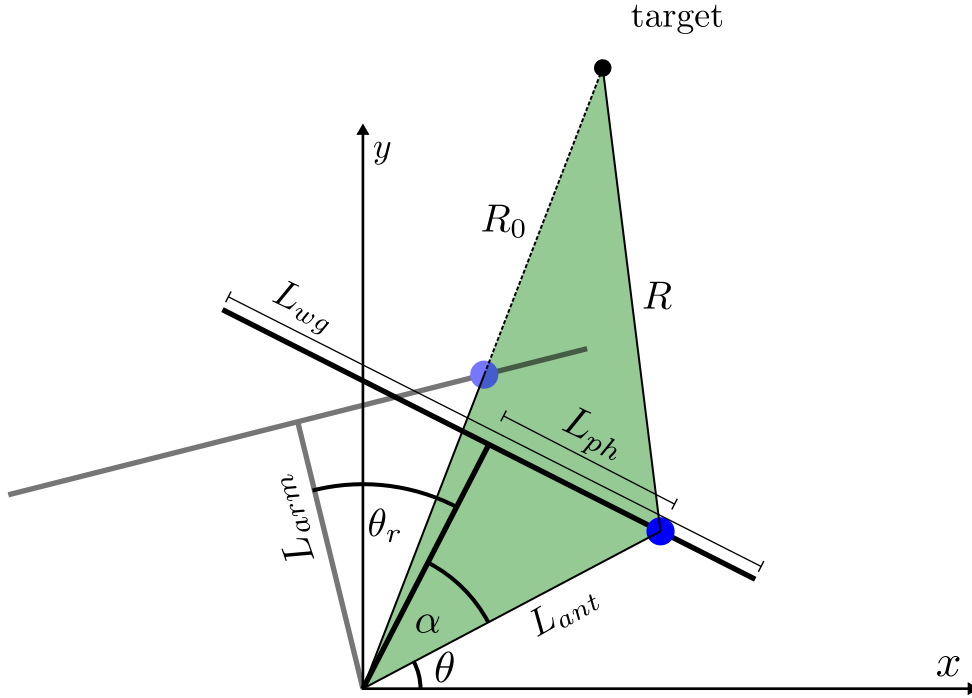


Figure 2.1: Geometrical description of the displaced phase center with all relevant parameters, as used in subsection 2.2.3. R is the slant range from the radar to the point scatterer, L_{ph} is the phase center displacement, L_{wg} the length of the antenna, L_{arm} is the antenna rotation lever arm, R_0 the range of closest approach and α the additional rotation angle necessary to obtain closest approach when the phase center is not in the midpoint of the antenna but the rotation angle is measured assuming $L_{ph} = 0$.

In the radar, s_r is mixed with the transmitted chirp s_t to remove the linear modulation, resulting in a deramped signal s_d which is sampled and stored:

$$s_d(t) = s_t(t)^* s_r(t) = \sigma e^{j4\pi \frac{R}{\lambda}} e^{j2\pi f_b t} e^{-j4\pi \frac{R^2 \gamma}{c^2}}. \quad (2.5)$$

The deramped signal consist of a phase term with beat frequency $f_b = \frac{2R\gamma}{c}$ which is proportional to the slant range R . In addition, the deramped signal contains the following two phase terms:

$e^{j4\pi \frac{R}{\lambda}}$ —where $\lambda = \frac{c}{f_c}$ is the wavelength—is the two way propagation phase, the quantity of interest for interferometric measurements. $e^{-j4\pi \frac{R^2 \gamma}{c^2}}$ is proportional to the squared distance, is named "residual video phase" and has to be compensated for in SAR processing. Although KAPRI is a real-aperture system, an azimuth processing step is required to correct a residual azimuth phase ramp, as described in subsection 2.2.3. However, in this case the variation of $R^2 B$ during the aperture length is much smaller than c^2 and the residual video term can be assumed to be zero.

From (2.5) an by the linearity of the Fourier transform, it follows that the range profile $\hat{\sigma}(R, \theta)$ of a collection of scatterers with complex reflectivity σ_i at ranges R_i can be estimated by the Fourier transform of $s_d(t)$.

Using a bandwidth of 200MHz, the theoretical range resolution for KAPRI is 0.75 m [46]; the effective

range resolution is observed to be lower because a Kaiser window is applied to the data before the Fourier transform to mitigate range sidelobes.

To obtain 2-D images, range profiles are acquired while the antenna is rotated with angular velocity ω . In this case, the deramped signal for a point target at R, θ_t is:

$$s_d(t, \theta) = \sigma e^{j2\pi f_b t} e^{j4\pi \frac{R}{\lambda}} e^{-j4\pi \frac{vR^2}{c^2}} P(\theta - \theta_t), \quad (2.6)$$

where t is the fast time, $\theta = n\omega\tau$ is the azimuth scan angle and $P(\theta)$ describes the two-way antenna pattern with beamwidth:

$$\theta_{3dB} = \frac{\lambda}{L_{wg}}, \quad (2.7)$$

where L_{wg} is the size of the antenna aperture and λ is the wavelength employed. If the rotation speed is chosen such that $\omega\tau \ll \theta_{3dB}$, the acquisition is oversampled in azimuth; several range profiles are samples of the same target. Their average in slow time—called azimuth presum or decimation—produces measurements with an increased signal to noise ratio, assuming all range profile to be affected by a white noise process.

Due to diffraction, the radiation beam emitted by the antenna broadens linearly with increasing distance; consequently the spatial resolution in cross-range δ_{az} increases with distance:

$$\delta_{az} = \frac{R\lambda}{L_{wg}}, \quad (2.8)$$

2.2.2 Beam Squint Correction

To obtain the desired cross-range resolution at the distances of interest a sufficiently narrow antenna beamwidth is required. To do so, KAPRI employs 2 m-long slotted waveguide antennas [48, 49]. They are constructed by cutting slots resonating at the design frequency in a section of rectangular waveguide. When the slots are appropriately spaced the fields emitted by the cuts combine in phase, producing a narrow beam in the desired direction.

Two types of slotted waveguide antenna exist [50]: the resonant and the traveling wave design. The second type has been chosen because it can be operated with a larger bandwidth; achieving a finer range resolution. The main drawback of this antenna design is its frequency-dependent beam squint: when it is operated at frequencies differing from the design value, the phase differences at the slots change; altering the direction of the mainlobe. When a chirped signal is transmitted, the mainlobe direction continuously changes during the pulse. This effect has been used for imaging radars where a mechanical antenna rotation would not be possible [51–54]. In the case of KAPRI the beam squint is undesired: the large angular deviation relative to the beamwidth causes the mainlobe to be centered on a scatterer during a fraction of t_{chirp} only, decreasing the effective transmitted bandwidth and worsening the range resolution.

In dechirped data acquired with sufficient levels of azimuth oversampling, the effect of beam squint is

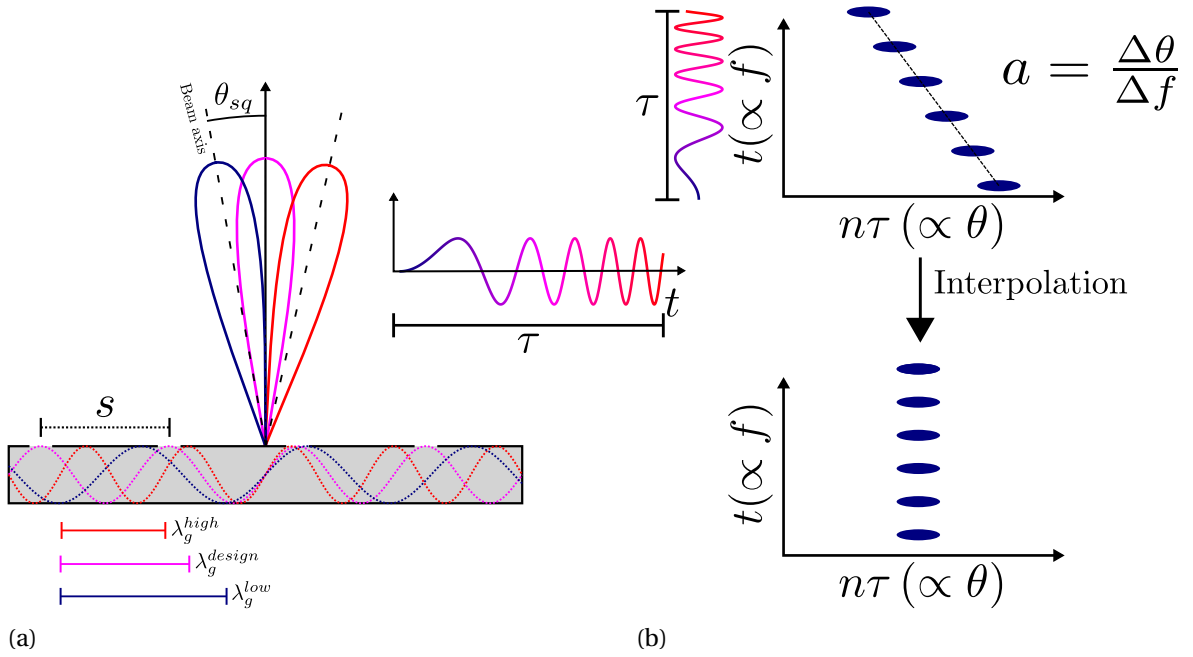


Figure 2.2: (a) Illustration of the frequency-dependent pointing direction θ_{sq} of the main lobe of the slotted waveguide antennas of KAPRI. The response at different chirp frequencies is represented by the colors of the mainlobes; they correspond to the increasing chirp frequencies as they are represented by the inset plot. The corresponding waveguide wavelengths are displayed underneath the antenna. For the design wavelength λ_g^{design} , the antenna mainlobe points at the antenna broadside.

(b) The plots represent the time domain envelope of a point target as a function of chirp time t (y-axis) and slow time $n\tau = \frac{\theta}{\omega}$ (x-axis). The y-axis is proportional to the transmitted frequency, the x-axis to the rotation angle of the antenna. If the antenna's mainlobe would not change its direction during the chirp, a beat signal as shown in the bottom would be obtained. It would have a frequency proportional to the range and would cover the slow time extent where the objects stays within the beamwidth. In the case when the mainlobe changes direction with frequency, the response is skewed because the target is only illuminated at the moment when the mechanical and the electrical antenna pointing direction match, causing its response to occupy several azimuth cells. After range compression, obtained with a Fourier transform along the t axis, the frequency-dependent antenna pointing would cause a loss of range resolution because only a fraction of the transmitted bandwidth would be used for each azimuth bin. To correct this effect, the data is interpolated in the time domain in order to reconstruct the full bandwidth by combining the subsequent sub-bandwidths that are obtained at different mechanical pointing angle. This correction requires sufficient azimuth oversampling, which is achieved by slow rotation of the antennas w.r.t the chirp duration.

visible as skewed point target responses, as illustrated in Figure 2.2. During the chirp, the target is only at the center of the beamwidth when the antenna rotation angle matches the beam squint angle. The availability of raw data oversampled in azimuth is key to mitigate the effect of the beam squint:

For each chirp frequency f , the data at the corresponding fast time $t_f = \frac{f-f_c}{\gamma}$ is shifted by the opposite of the squint angle using a bilinear interpolator. The amount of shift is predicted by:

$$\theta_{sq} = \sin^{-1} \left(\frac{\lambda}{\lambda_{g_{ij}}} + \frac{k\lambda}{s} \right), \quad (2.9)$$

where $\lambda_{g_{ij}}$ is the wavelength for the ij -TE mode of the waveguide, λ is the free space wavelength, s is the element spacing and k is the mode number. In this case, the waveguide mode used is TE_{01} and $k = 0$ is assumed because all the slots must have the same phase [55] to direct the main beam at the antenna broadside.

Instead of using the above expression, a linear approximation for the squint relative to the pointing

direction at the design frequency f_c is used to process KAPRI data:

$$\theta_{sq} - \theta_{sq}^{f_c} = af. \quad (2.10)$$

The equivalent shift to apply at each range line i_r in number of azimuth samples i_θ is given by:

$$i_\theta = \frac{a\gamma}{\omega} i_r \quad (2.11)$$

The linearized expression is necessary because the antenna patterns measurements at different frequencies provided by the manufacturer suggest that the vertically and the horizontally polarized units have different frequency dependent squint behaviors. Because the design information necessary to use the above exact expression for the squint is not available, a data-driven method is used for the correction of the beam squint.

To estimate the squint rate a , the response of a strong point-like target is extracted from the data by windowing it in range and converting it back in the fast time domain with a Fourier transform; its envelope is then extracted with a discrete Hilbert transform. For each frequency the peak is located and stored in a vector from which an estimate of a is obtained by fitting (2.10).

To correct the frequency-dependent beam squint the azimuth sample spacing must be smaller than the antenna beamwidth: this permits to reconstruct the full bandwidth illumination of each scatterer by combining chirp samples acquired at subsequent azimuth positions.

After correcting the beam squint, azimuth presumming can be applied if desired to reduce the data size and increase SNR.

Then, an Hann window is applied to the first and last z samples of the raw data s_d to mitigate the transient signal caused by the abrupt change in frequency due to the repetition of the chirp and the end of each pulse. A Kaiser window is applied to reduce range processing sidelobes that are caused by the finite bandwidth. Finally, a fast time Fourier transform performs the range compression to obtain the SLC image $\hat{\sigma}(R, \theta)$.

Each range line of the SLC is then multiplied by $\sqrt{R^3}$ to compensate for the power spreading loss. In this manner, the intensity of the SLC data is directly proportional to the radar brightness β_0 [56].

2.2.3 Azimuth Processing

In the case of KAPRI, the correction of frequency-dependent squint as described in the preceding section is not sufficient to produce correct SLC data: a strong residual azimuth phase is observed on the response of point-like scatterers, especially in the VV channel. This phase contribution is problematic for two reasons:

1. Because the azimuth samples have differing phases it reduce the amplitude and the SNR after azimuth presumming.
2. Since each polarization displays a different ramp, the coherence magnitude of polarimetric phase differences will be reduced and the resulting coherence phase will be affected by a residual phase

variation. For example, if the HH-VV phase is needed for calibration in the method described in subsection 2.2.6 and the azimuth variation is not taken into account, the additional phase will result in incorrect calibration parameters.

The azimuthal phase variation arises from the rotational acquisition: the antennas are mounted with an offset L_{arm} from their center of rotation, as shown in Figure 2.1. Therefore, during the rotation the distance from the phase center to a scatterer varies with the azimuth position, changing the propagation phase accordingly [57]. If the variation in distance is larger than the range resolution, the target will move through several range cells as a function of azimuth position, in analogy to *range cell migration* in SAR systems. In the case of KAPRI the variation in distance is two orders of magnitude smaller than the range resolution and will only visibly affect the phase of the signal.

To model the change in phase, consider the radar acquisition geometry depicted in Figure 2.1:

The antennas are mounted on a lever arm offset by L_{arm} from the center of rotation. Their phase centers have a horizontal displacement L_{ph} from the lever arm attachment. A point target is considered, located at the range of closest approach R_0 , obtained when the phase center, the target and the lever arm are aligned. For an incremental rotation θ_r from the angle of closest approach, the relative phase variation, is:

$$\phi_{scan} = \frac{4\pi}{\lambda} (R_0 - R(\theta_r)) \quad (2.12)$$

where R is the effective distance between the point target and the phase center, computed with the law of cosines on the green triangle of Figure 2.1 with the included angle θ_r , one side $L_{ant} = \sqrt{L_{arm}^2 + L_{ph}^2}$ and the other $c = L_{ant} + R_0$:

$$R(\theta_r) = \sqrt{c^2 + L_{ant}^2 - 2cL_{ant} \cos(\theta_r - \alpha)}. \quad (2.13)$$

L_{ant} is interpreted as the equivalent lever arm of an antenna without the horizontal phase center shift that would produce the same phase variation as a system with a nonzero L_{ph} .

The function is shifted by the angle $\alpha = \arctan\left(\frac{L_{ph}}{L_{arm}}\right)$ that describes the additional rotation needed for an antenna with nonzero L_{ph} to be at closest approach. This shift is necessary because the azimuth angle is measured assuming a zero L_{ph} : the reading given by the angle encoder does not correspond to the angular position of the phase center.

The complete characterization of the phase ramp requires the knowledge of the antenna phase center displacement L_{ph} . Normally, it is assumed that the phase center is at the midpoint of the antenna. However, when the experimental data was analyzed using this assumption (which implies $L_{ant} = L_{arm}$), (2.13) failed to model the observed azimuth phase variation and possibility of a displaced antenna phase center was included. This displacement is used to describe physical differences in the antennas, which could explain the larger azimuth phase in the VV channel.

L_{ph} is estimated using the measured phase of a point target by minimizing the squared distance with the phase simulated according to (2.13).

$$\hat{L}_{ph} = \underset{(L_{ph}, \phi_{off})}{\operatorname{argmax}} \|\phi_{meas} - \phi_{scan}\|^2, \quad (2.14)$$

where $\phi_{sim} = \phi_{scan} + \phi_{off}$ is the simulated phase with an additional offset that accounts for noise and the intrinsic scattering phase and the system.

When L_{ph} is known, the azimuth phase variation is corrected in the range compressed data $\hat{\sigma}$ by convolution of each range R_i with the phase of (2.13) used as a matched filter:

$$\hat{\sigma}^{corr}(R_i, \theta) = \int_{-\frac{\theta_{int}}{2}}^{\frac{\theta_{int}}{2}} e^{-j \frac{4\pi}{\lambda} R(\theta - \theta', R_i)} \hat{\sigma}(R_i, \theta') d\theta'. \quad (2.15)$$

This expression replaces the azimuth presum described in subsection 2.2.1: the samples are now averaged with an appropriate phase factor; this combines SNR improvement and the correction of the azimuth trend in a single step. Because the model only describes the variation of the phase relative to closest approach R_0 , the absolute phase is preserved; this is very important for interferometry and polarimetry.

The procedure is similar to azimuth focusing of synthetic aperture data, where the cross-range resolution is obtained by the integration of the data in the azimuth-time direction. However, in the case of real aperture systems the resolution is limited by the physical antenna beamwidth and the response of a target occupies a single azimuth sample; unless the data is oversampled. In the first case, integrating the data in azimuth degrades the resolution because samples that do represent the same scatterer are combined.

To correct the phase variation without an excessive increase in azimuth resolution, the integration is limited to a window of size θ_{int} . The optimal trade-off is empirically determined to be 0.6° , slightly larger than θ_{3dB} .

2.2.4 Antenna Pattern Misalignment

By analyzing the response of a strong point-like target a significant azimuth shift between the HH and the VV channels was observed, corresponding to an azimuth pattern mispointing of 0.2° , almost half of the antenna beamwidth. The misalignment is particularly problematic for cross-polar measurements: the transmitting and receiving patterns are not aligned. Using the available pattern information a power loss of approx 2.5 dB compared to the ideal case is predicted. This loss reduces the SNR for the cross-polar channels, leading to noisier measurements.

While the offset between copolar channels can be corrected by coregistration, no *a posteriori* method can compensate the SNR loss in the cross-polar measurements.

To realign the patterns, an adjustable antenna mount was manufactured by replacing one of two hinges where the antennas are fixed on the tower (see Figure 2.3) with an adjustable bracket that allows to slide the antenna back and forth on the one side, obtaining the effect of rotating it around the center. Based on the size of the antenna mounting bracket and on the amount of misalignment, it was determined

that the horizontally polarized antennas need to be shifted by 1.8mm to align the antenna patterns.

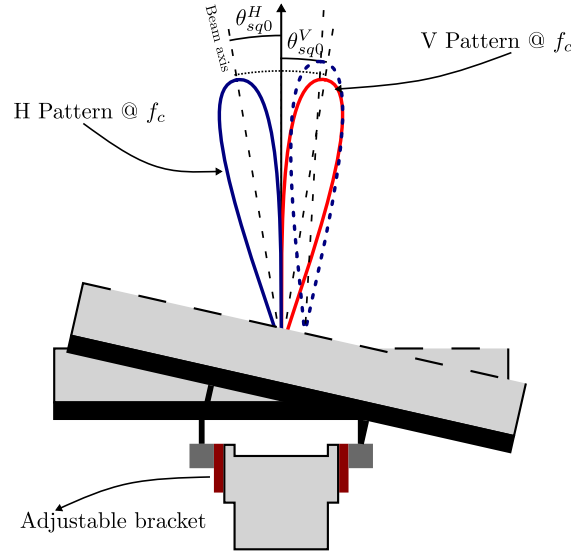


Figure 2.3: Illustration of the adjustable antenna mount allowing to shift the patterns to bring the H and the V antennas into alignment. The left bracket can be slid towards the front, allowing the antenna to pivot on the right hinge. For small shifts, this movement approximates a rotation around the center of the antenna tower, as depicted by the blue antenna pattern.

2.2.5 Removal of Topographic Phase

The next step on the way to calibrated polarimetric data requires a brief review of KAPRI's antenna configuration, depicted in Figure 2.4:

Six antennas are mounted on a supporting structure connected to the rotary scanner. Of these, two are transmitting antennas, one for each polarization. The remaining four are connected in pairs through switches to the receivers; each pair composed of an horizontally and a vertically polarized unit. This configuration permits to acquire full polarimetric dataset by selecting the desired antennas for the transmitter and for each receiver separately. This arrangement ensures a low level of polarimetric crosstalk because only one combination is acquired at each time and the antennas are physically separated. Additionally, the separation of transmitting and receiving antennas increases the transmit-receive isolation, a fundamental requirement for FMCW performance [46, 47, 58]. The disadvantage of this configuration is that certain combinations of channels i and j will be separated by a baseline: These antennas can be replaced by an equivalent antenna located at the midpoint between transmitter and receiver [38]. For the combinations of polarizations i and j where the equivalent phase centers are separated by a baseline \mathbf{b}_{ij}^{eq} , the polarimetric phase difference ϕ_{ij} will contain an interferometric contribution:

$$\phi_{ij} = \phi_{ij}^{pol} + \phi_{ij}^{prop}. \quad (2.16)$$

This term appears as topographic fringes in the polarimetric phase difference. It will complicate calibration by adding an additional phase contribution unrelated to the polarimetric properties of the scatterer.

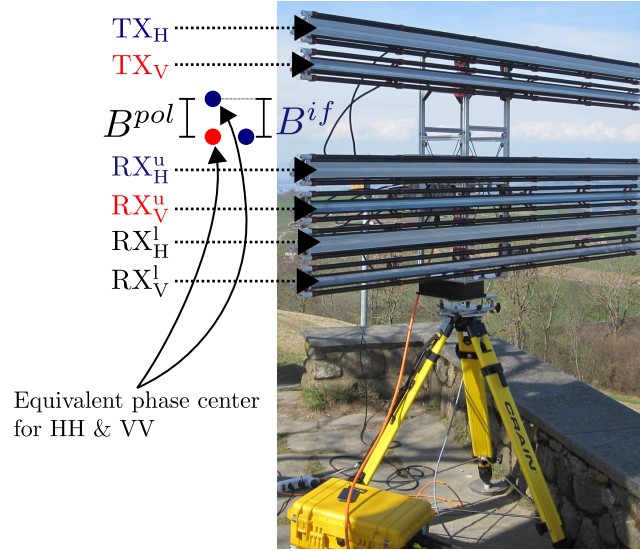


Figure 2.4: KAPRI radar during a field test. The antenna arrangement used in this paper is overlaid. The blue and red dots represent the equivalent phase centers for the HH and VV channels from the top receiver. The bottom blue dot on the right represents the one for the lower HH channel, which is used in conjunction with the upper HH phase center to estimate the topographic phase contribution.

To obtain correct phase differences the topographic contribution can be estimated by considering two additional channel k and l acquired with a non-zero baseline \mathbf{b}_{kl}^{eq} and with the same polarization, where $\phi_{kl}^{pol} = 0$. In this case, the propagation phase difference can be approximated as a function of the local incidence angle and of the perpendicular baseline separating the phase centers:

$$\phi_{kl}^{prop} = \frac{4\pi}{\lambda} b_{kl}^{eq} \sin(\theta_{kl}^l - \alpha_{kl}^{bl}) \quad (2.17)$$

where α_{kl}^{bl} is the baseline angle with respect to the vertical, the look angle θ_l is the angle between the line of sight vector and the vertical, b_{kl}^{eq} is the perpendicular baseline between the equivalent phase centers. Then ϕ_{ij}^{prop} can be estimated from ϕ_{kl} if the look vector elevation angle and the baseline orientation do not significantly change from kl to ij , i.e. if $\theta_{ij}^l - \alpha_{ij}^{bl} \approx \theta_{kl}^l - \alpha_{kl}^{bl}$.

$$\hat{\phi}_{ij}^{prop} = \frac{b_{ij}^{eq}}{b_{kl}^{eq}} \phi_{kl}. \quad (2.18)$$

if the ratio of the baselines is not integer [59] phase unwrapping of ϕ_{kl}^{prop} is required before rescaling.

To correct all combinations that have a non-zero baseline, the measured scattering matrix \mathbf{S} is converted into a covariance matrix \mathbf{C} ; then $\hat{\phi}_{ij}^{prop}$ is subtracted from the phase of every non-diagonal element ij where $b_{ij}^{eq} \neq 0$. The result is a terrain flattened covariance matrix where the phase of off-diagonal elements only contains polarimetric contributions, possibly affected by an offset that needs compensation in the polarimetric calibration.

2.2.6 Polarimetric Calibration

The polarimetric calibration is based on the covariance matrix corrected above; the procedure is based on the linear distortion matrix model [60, 61] relating the observed scattering matrix \mathbf{S}' with the theoretical \mathbf{S} :

$$\mathbf{S}' = \mathbf{RST}. \quad (2.19)$$

The same can be restated for polarimetric covariance matrices $\mathbf{C} = \mathbf{SS}^H$:

$$\mathbf{C}' = \mathbf{DCD}^H \quad (2.20)$$

where \mathbf{D} is the Kronecker product of \mathbf{R} and \mathbf{T} , the matrices that describe the phase and amplitude imbalances and crosstalk in reception and transmission.

In the case of KAPRI, crosstalk calibration is not considered: the radar has a good polarization isolation, largely because only one polarization is acquired at a time by selecting the appropriate combination of transmitting and receiving antennas. The only source of crosstalk is the presence of cross-polarized antenna sidelobes in the direction of the antenna mainlobe. The manufacturer has provided simulated radiation patterns for the horizontally polarized antennas, where the isolation between the co and the cross-polarized pattern in the mainlobe direction is observed to be better than 60 dB. Additionally, by computing the VV-HV ratio of the oversampled response of a trihedral corner reflector, the polarization purity of the system was estimated to be better than 35 dB in the worst case.

Under the assumption of negligible crosstalk, the distortion matrices are:

$$\begin{aligned} \mathbf{R} &= A \begin{bmatrix} 1 & 0 \\ 0 & f/g e^{i\phi_r} \end{bmatrix}, \\ \mathbf{T} &= A \begin{bmatrix} 1 & 0 \\ 0 & f g e^{i\phi_t} \end{bmatrix} \end{aligned} \quad (2.21)$$

where f is the one-way copolar amplitude imbalance relative to the H polarization, and g the amplitude imbalance of the crosspolarized channels. $\phi_t = \phi_{t,h} - \phi_{t,v}$ is the phase offset between the polarizations when transmitting, $\phi_r = \phi_{r,h} - \phi_{r,v}$ is the phase offset in reception and A is the absolute amplitude calibration parameter [62, 63].

The four complex parameters in \mathbf{D} can be estimated using a trihedral corner reflector and a reciprocal scatterer with a significant cross polarized contribution [38, 64].

The copolar amplitude imbalance f is estimated by the ratio of C'_{HHHH} and C'_{VVVV} :

$$f = \left(\frac{C'_{VVVV}}{C'_{HHHH}} \right)^{\frac{1}{4}}. \quad (2.22)$$

The copolar phase imbalance $\phi_r + \phi_t$ is estimated from the phase of C'_{VVHH} :

$$\phi_r + \phi_t = \arg(C'_{VVHH}). \quad (2.23)$$

Both parameters are estimated on the oversampled response of a corner reflector. In [63], a polynomial model for the copolar calibration parameters is used, that links the imbalances to the incidence angle. In that case, the estimate are performed using an array of corner reflectors covering a large range of incidence angles. In the case of this paper, such an array is not available and a simplified calibration model is used, assuming the copolar parameters to be independent of incidence angle.

Because of the difficulty of placing and correctly orienting a cross-polarizing target such as a 45° dihedral, the estimation of g and $\phi_t - \phi_r$ is based on the assumption that most pixels in the data represent reciprocal scatterers:

$$g = \left\langle \frac{C'_{HVHV}}{C'_{VHVH}} \right\rangle^{\frac{1}{4}} \quad (2.24)$$

and

$$\phi_t - \phi_r = \arg(\langle C'_{VVHV} \rangle) \quad (2.25)$$

where the bracket indicates averages over all pixels. Finally, calibrated covariance matrices are obtained by inverting (2.20) using the estimated \mathbf{D} .

If radiometric calibration is desired, the value of A can be determined after imbalance correction from the ratio of the expected and the measured radar cross section (RCS).

$$A = \left(\frac{\sigma_{tri}}{C'_{HHHH} R_{tri}^3} \right)^{\frac{1}{2}} \quad (2.26)$$

where R_{tri} is the slant range to the trihedral corner reflector. This is necessary to remove the range spread loss compensation as performed in section 2.2.

2.2.7 Experimental Data

A dataset for calibration purposes was acquired in September 2016 at an urban-agricultural area near Münsingen, Switzerland. The data was acquired from the top of the "Chutzen" hill approximately 800 m a.s.l, looking down towards a mixture of fields and forests, with the town in the far range region. Six trihedral corner reflectors were placed in the area for the determination of calibration parameters and to assess imaging quality. Three of these reflectors have triangular faces with a length of 40 cm, corresponding to a RCS of $\frac{4}{3}\pi \frac{a^4}{\lambda^2} = 25.5$ dB, while the remaining two are cubic corner reflector with a RCS of 35 dB, at the nominal central frequency of 17.2GHz. Figure 2.5 shows the calibrated Pauli RGB composite of the scene, interpolated in Cartesian coordinates using a 2-m posting digital elevation model (DEM). The location of the reflectors is marked using blue circles and their names according to Table 2.2 are shown next to them.

The dataset was acquired with the horizontally polarized antenna group shifted towards the V group by 1.8 mm to compensate for the pattern misalignment as described in subsection 2.2.4.

A second dataset containing a dihedral reflector was acquired at ETH Höggerberg campus in order to investigate the effect of antenna pattern misalignment on crosspolar acquisitions and to test the suitability of the computed adjustment value as discussed in subsection 2.2.4. This measurement was

held separately because of the logistical problems associated with the transportation and the setup of large dihedral calibration targets.

Name	R_0 [m]	σ_0 [dB]	Type
CR1	74.3	35	cubic
CR2	673.1	25.5	triangular
CR3	824.6	35	cubic
CR4	838.9	25.5	triangular
CR5	1,049	35	cubic
CR6	2,689.3	25.5	triangular

Table 2.2: Summary of TCRs in the calibration dataset: Name of nearest map feature, Distance from the radar, expected radar cross section, type of reflector.

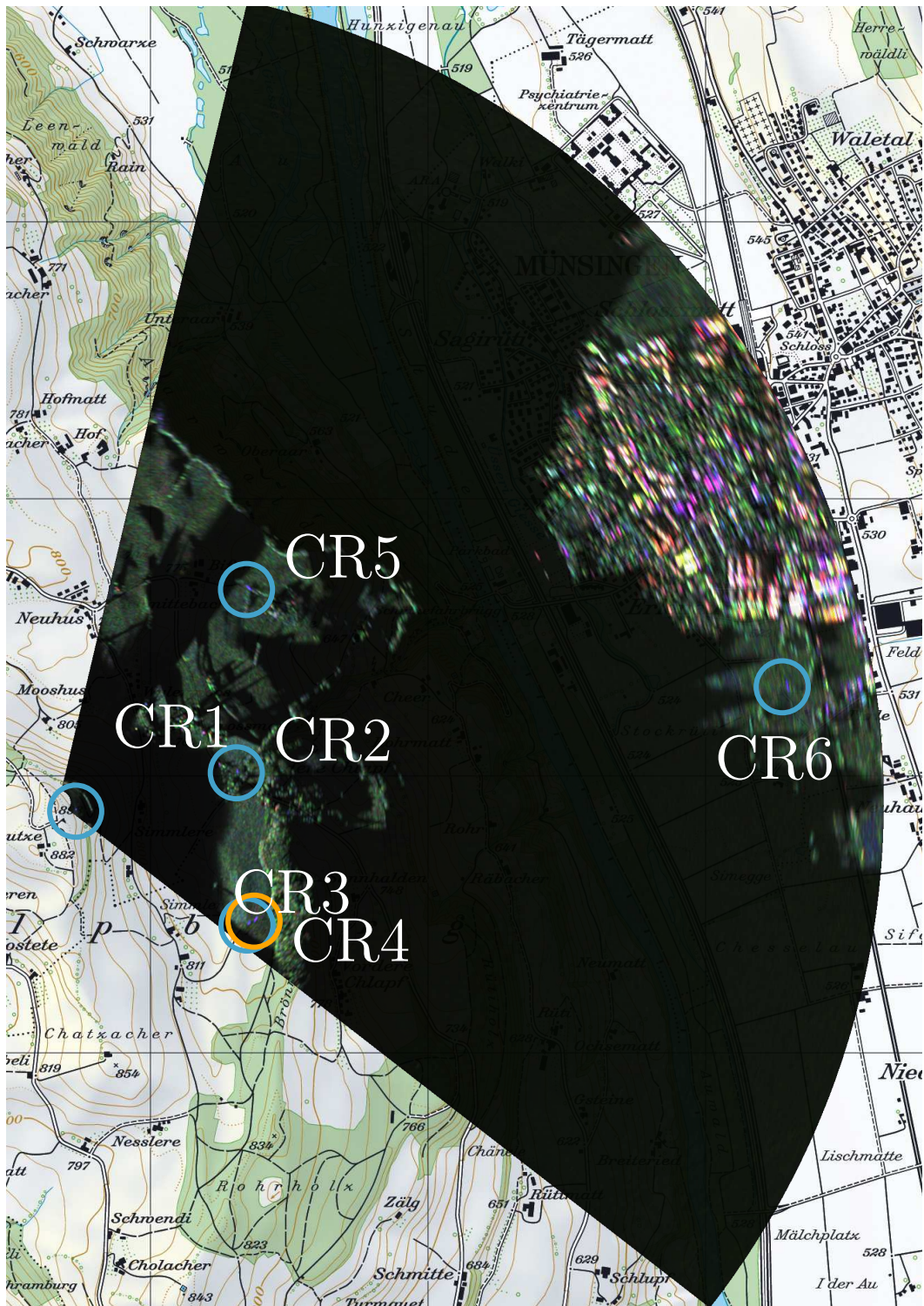


Figure 2.5: Pauli RGB composite ($R = |HH - VV|$, $G = |HV|$, $B = |HH + VV|$) of the imaged scene, geocoded using a digital elevation model with 2-m pixel spacing. Each channel is scaled according to its own dynamic range. The location of corner reflectors is marked by cyan circles, the reflector used for polarimetric calibration is shown in orange. The image is overlaid on a 1:25000 scale Swiss topographic map (Reproduced with the authorization of swisstopo JD100042).

2.3 RESULTS

2.3.1 Beam Squint Correction

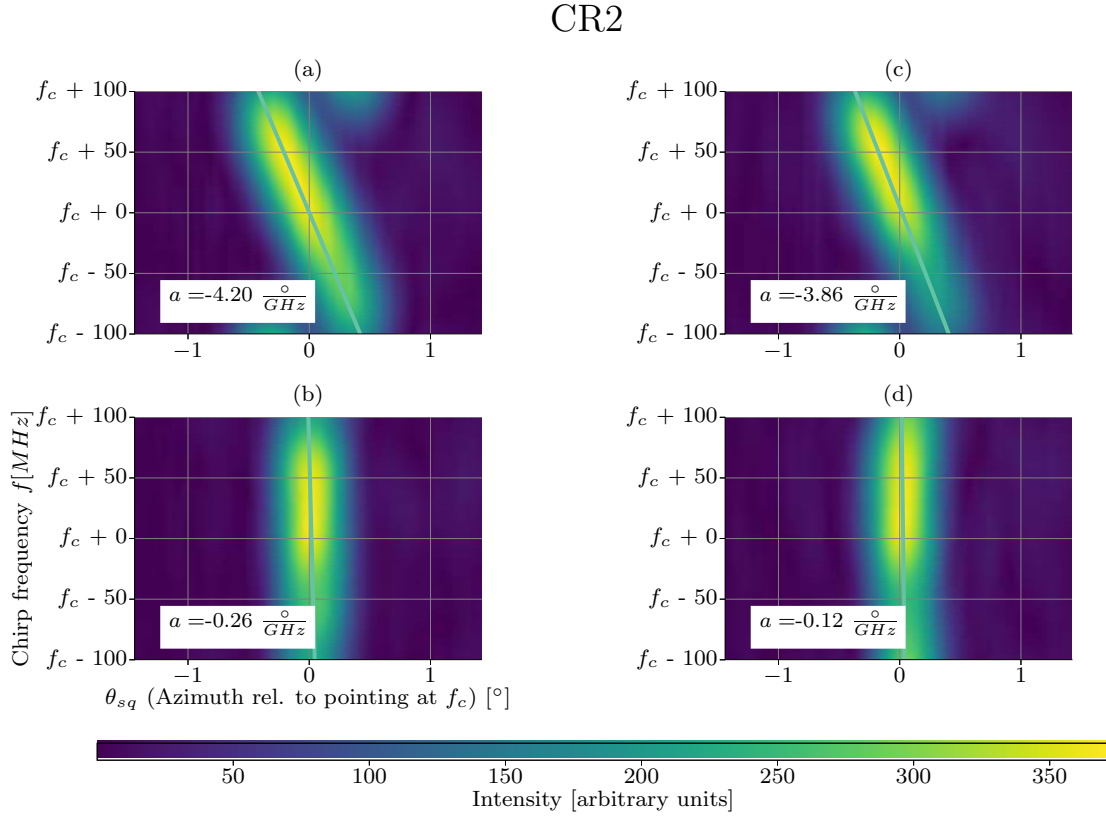


Figure 2.6: Azimuth-frequency response of the "CR2" TCR: the raw data samples around the reflectors azimuth location were extracted, then filtered in range by Fourier transforming them along the frequency axis, applying an Hamming window about the range location and converting them back into the time domain with an inverse Fourier transform. By doing so, only the portion of the range spectrum close to the reflectors location was kept. Finally, the complex envelope of the data was extracted using a discrete Hilbert transform. This is conceptually equivalent to the plot of Figure 2.2. (a) for the HH channel, (b) for the HH channel after the interpolation described in subsection 2.2.2, (c) for the VV channel, and (d) the same as (b) for the VV channel.

Figure 2.6 shows the frequency-azimuth response relative to the pointing at the center frequency for the "CR2" TCR. This plot was generated with the procedure described in subsection 2.2.2 by filtering the range compressed data around the location of the reflector and converting it back to the time domain by an inverse Fourier transform. In Figure 2.6(a) and (c), the procedure was applied to the HH and VV channel data before any squint correction was applied. In Figure 2.6(b) and (d) the same is shown after applying the interpolation described in subsection 2.2.2 using $a = 4.2 \frac{\circ}{\text{GHz}}$ and $a = 3.9 \frac{\circ}{\text{GHz}}$ for the HH and VV channels. In each plot, a line shows the results of the linear model fit described by (2.10), the estimated a parameter is overlaid to the plot.

The same fit procedure is applied to all reflectors for both the HH and the VV data; the results are shown in Table 2.3.

In Figure 2.7(a),(b), (d) and (e), the effect of frequency-dependent squint and the result of its correction

Name	a_{HH}	a_{VV}	residual a_{HH}	residual a_{VV}
CR1	$-3.7 \cdot 10^{-9}$	$-4.1 \cdot 10^{-9}$	$-1.1 \cdot 10^{-10}$	$-8.3 \cdot 10^{-10}$
CR2	$-4.2 \cdot 10^{-9}$	$-3.9 \cdot 10^{-9}$	$-2.6 \cdot 10^{-10}$	$-1.2 \cdot 10^{-10}$
CR3	$-3.9 \cdot 10^{-9}$	$-3.7 \cdot 10^{-9}$	$-4 \cdot 10^{-11}$	$1.4 \cdot 10^{-11}$
CR4	$-4 \cdot 10^{-9}$	$-3.7 \cdot 10^{-9}$	$-7.9 \cdot 10^{-11}$	$-2.8 \cdot 10^{-10}$
CR5	$-4.2 \cdot 10^{-9}$	$-4 \cdot 10^{-9}$	$-2 \cdot 10^{-10}$	$-2.4 \cdot 10^{-10}$
CR6	$-3.9 \cdot 10^{-9}$	$-3.9 \cdot 10^{-9}$	$-1.4 \cdot 10^{-10}$	$-4.2 \cdot 10^{-10}$
mean	$-4 \cdot 10^{-9}$	$-3.9 \cdot 10^{-9}$	$-1.4 \cdot 10^{-10}$	$-3.1 \cdot 10^{-10}$

Table 2.3: Result of fitting the model of (2.10) to each reflector in the calibration array. In the second column, the a parameter for the HH channel is shown, in the third the one for the VV channel. The last two columns show the same parameters re-estimated after applying the squint correction using 4.2 and $3.9 \frac{\circ}{\text{GHz}}$ for a_{HH} and a_{VV} respectively.

are visible for the "CR2" reflector. The plots are generated by oversampling the range compressed data around the reflector in azimuth and range using a cubic order spline approximating a sinc interpolator. In each plot azimuth and range resolutions are estimated numerically by fitting a spline on the response at the corresponding maximum location and computing its 3-dB width. Figure 2.7(a) and (d) show the range compressed data for the HH and VV channels. In Figure 2.7(b) and (e) the same is repeated after applying squint correction before range compression.

2.3.2 Azimuth Processing

The ability of the phase model described in subsection 2.2.3 to explain the observed phase variation on the VV channel response is tested on each reflector in the array: the maximum in range and azimuth was identified and the samples corresponding to the half power beamwidth were extracted at the range of maximum intensity. The unwrapped phase is used to estimate L_{ph} according to (2.14). The resulting model parameters' fit values for the H and V antennas are shown in Table 2.4 alongside with the distance from the radar and the name of the reflector, defined in Table 2.2. Owing to the lack of sufficiently bright cross-polarizing point targets, the equivalent horizontal phase center locations for HV and VH channels were not directly estimated from the data. In the following, their location is assumed to be at the midpoint between L_{ph}^H and L_{ph}^V , the theoretical equivalent phase center for these channels.

The result of applying the correction of (2.15) to the TCR "CR2" at 673 m is displayed in panels (c) and (f) of Figure 2.7.

In Figure 2.8b the phase response in both the HH and VV channels is plotted for all reflectors. To produce the plot, all responses were aligned in azimuth, normalized to the maximum, finally their phase was referenced to the phase at closest approach; this corresponds to the phase of (2.12). This allows an easier comparison of the azimuthal phase variation.

2.3.3 Antenna Pattern Misalignment

To verify the impact of the H-V pattern pointing shift as described in subsection 2.2.4 on the performance of cross-polar measurements, the response of a dihedral reflector with a high cross-polar contribution is analysed for two configurations:

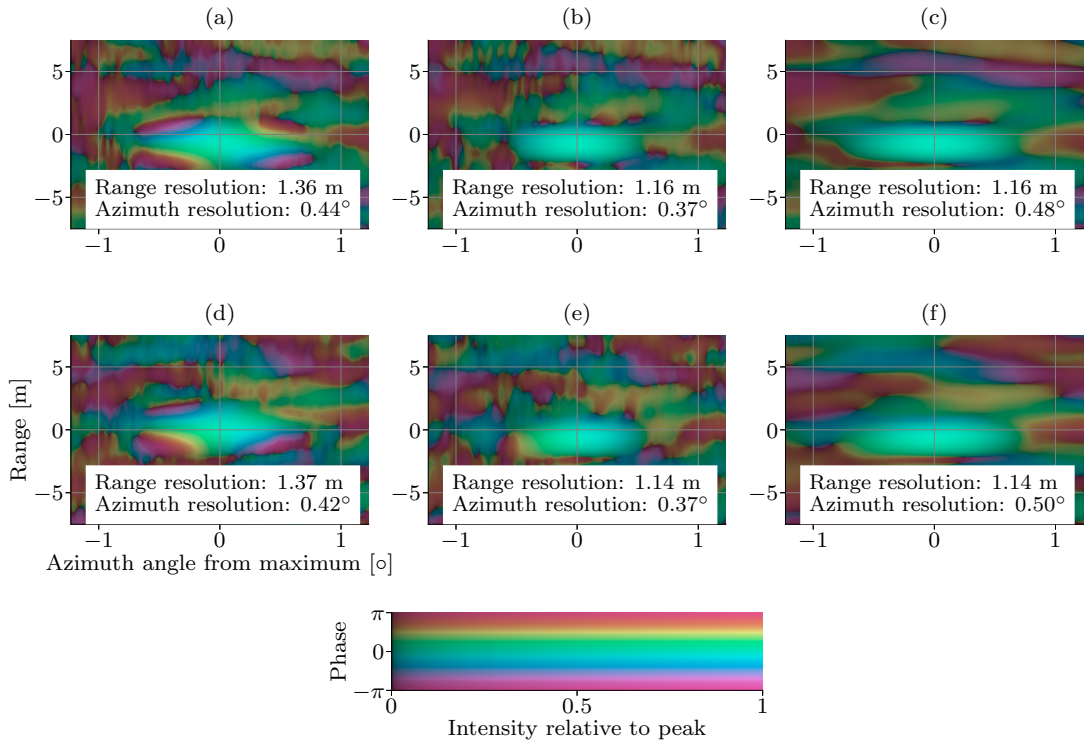


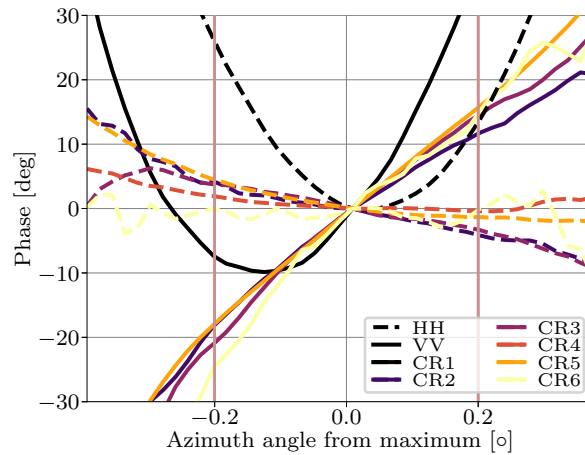
Figure 2.7: Oversampled phase and amplitude responses for the corner reflector "CR2" at 673 m slant range. (a) HH channel without correction, (b) HH channel with frequency-dependent squint compensation (c) same as (b) with azimuth phase ramp removal. (d) VV channel without correction, (e) VV channel with frequency-dependent squint compensation, (f) same as (e) with azimuth phase ramp removal. (g) Color palette used to represent the above plots. The hue is modulated by the phase, while the brightness corresponds to the gamma-corrected normalized intensity. The phase of each response is referenced to the phase at the peak.

Name	$R_0[m]$	$L_{ph}^H[m]$	$L_{ph}^V[m]$
CR1	74.3	0.03	-0.18
CR2	673.1	0.02	-0.1
CR3	824.6	0.03	-0.12
CR4	838.9	0.01	-0.12
CR5	1,049	0.02	-0.12
CR6	2,689.3	0	-0.12

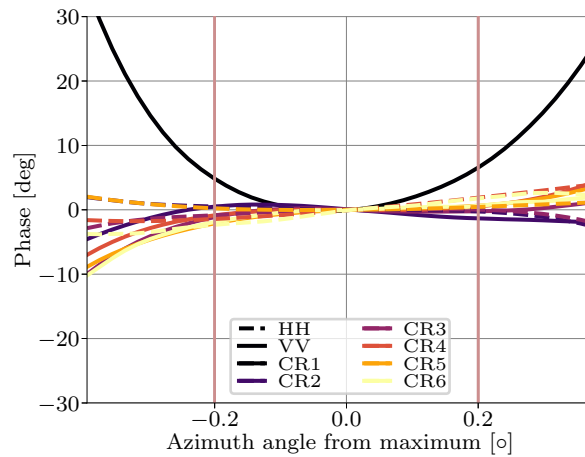
Table 2.4: Result of the phase center displacement fit for six trihedral corner reflectors located at different ranges. In the third column, the estimated phase center displacements for the H antenna are shown, in the fourth the ones for the V unit.

1. the antennas are not mechanically moved; the H and V pattern are not aligned in azimuth.
2. the optimal shift of 1.8 mm, as described in subsection 2.2.4 is applied to the movable antenna hinge to bring the patterns into alignment.

In Figure 2.9, the result of the above experiment is shown as the oversampled, coregistered azimuth response in the HV channel.



(a)



(b)

Figure 2.8: Relative phase response for all reflectors in the calibration array, (a) no azimuth phase correction (b) after azimuth phase correction. Continuous lines: VV channel, dashed lines: HH channel. To display the relative phase variation, the phase at the maximum is subtracted from each plot. The vertical lines indicate the theoretical 3-dB resolution of the antenna θ_{3dB} .

2.3.4 Removal of Topographic Phase

For the analysis of the topographic phase contribution removal, as described subsection 2.2.5, the copolar (HH-VV) phase is chosen because it is the covariance element affected by an interferometric baseline that shows the highest overall coherence, making the effect of the baseline easier to visualize. An excerpt of the copolar phase difference is visualized in Figure 2.10 in radar coordinates; the phase assigned to the hue, the intensity to the corresponding \mathbf{C} matrix element magnitude and by setting the saturation of the image with a sigmoid transformation of the copolar coherence magnitude, estimated using a 5×2 window.

2.3.5 Polarimetric Calibration

The methods described in the preceding sections were applied to prepare SLC images for each channel. For the final polarimetric calibration the procedure of subsection 2.2.6 was used; one reflector in the

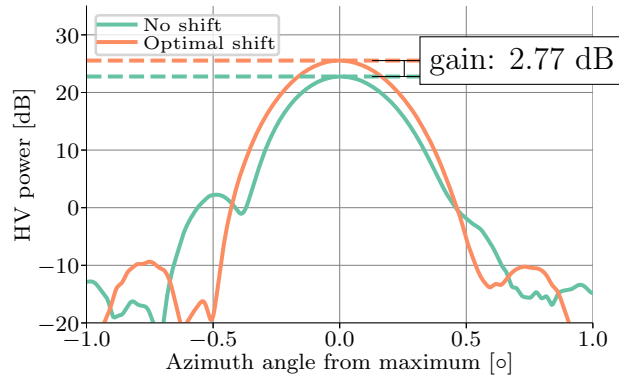


Figure 2.9: Oversampled azimuth power response of a dihedral corner reflector, before (green line) and after the correction of antenna pattern mispointing (orange line). The observed gain is in good agreement with the loss computed using the antenna patterns provided by the manufacturer and the azimuth shift determined using intensity correlation of HH and VV point target responses.

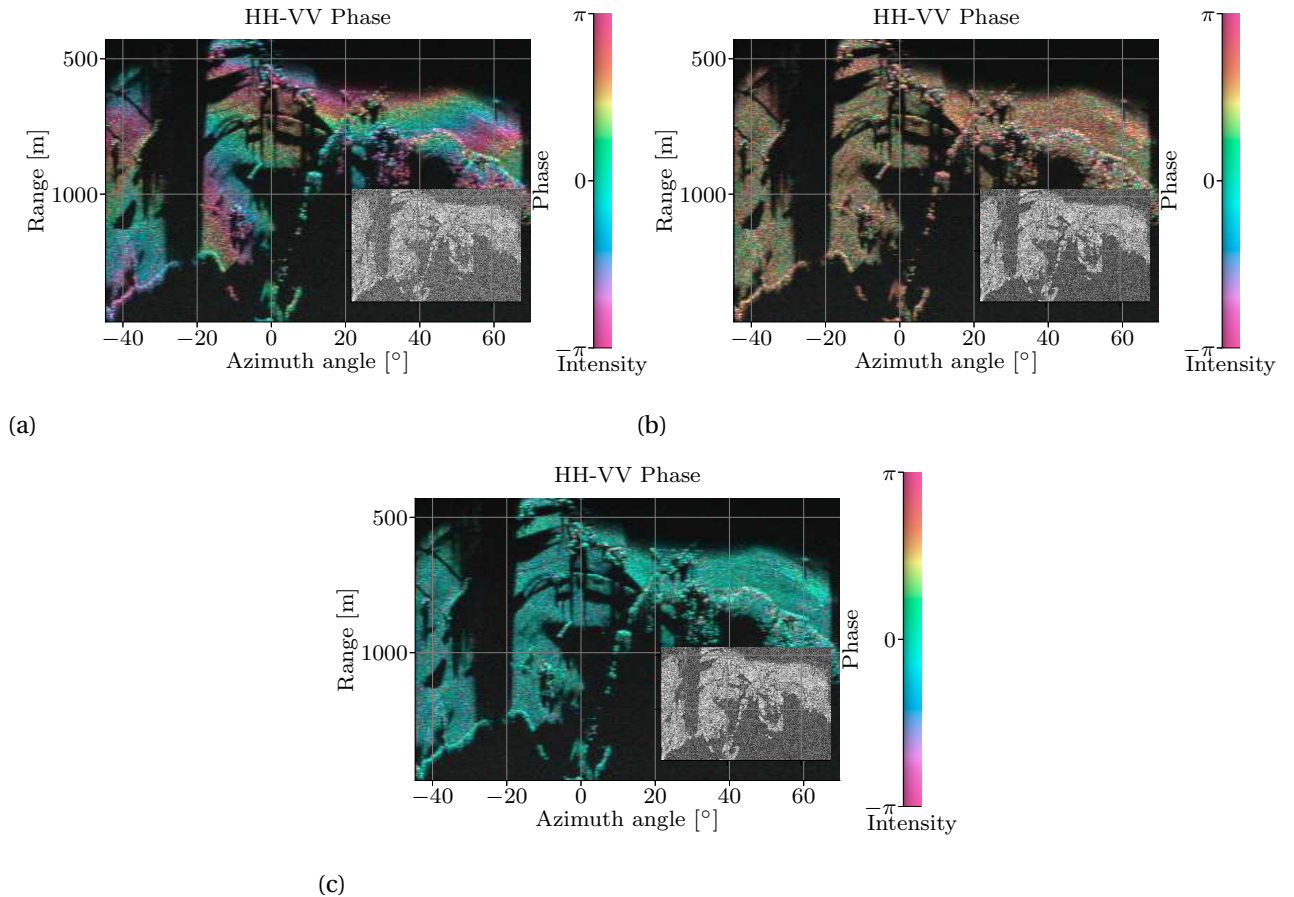


Figure 2.10: HH-VV phase difference in radar coordinates, (a) before and (b) after the removal of the topographic phase term as described in subsection 2.2.5; (c) calibrated copolar phase difference. The hue of the image is modulated by the covariance phase, the intensity by the magnitude, the saturation by the copolar coherence magnitude. The inset on the bottom left shows the copolar coherence magnitude. The interferometric fringe pattern visible in (a) is removed by the proposed correction, as plotted in (b).

scene was used as a calibration target, with the four remaining reflectors used for the assessment of the

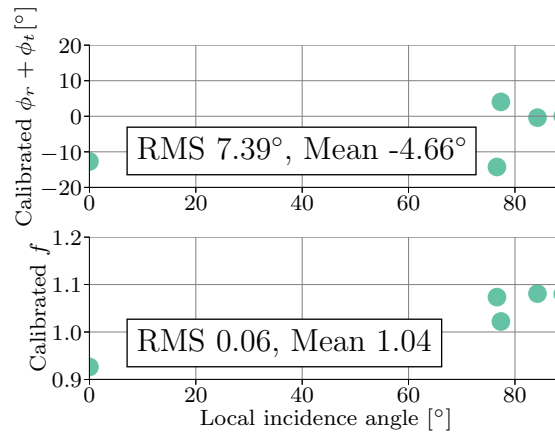


Figure 2.11: Dependence of the residual copolar phase ($\phi_r + \phi_t$) and amplitude (f) imbalances on the local incidence angle. The mean and RMS imbalances are shown in each plot. The reflector used for the determination of calibration parameters has been excluded from the plot.

Name	R_0 [m] Range distance	f	$\phi_r + \phi_t$ [°]	Purity [dB]
CR1	74.3	0.93	-12.71	39.3
CR2	673.1	1.08	-0.39	43.1
CR3	824.6	1.08	0.02	45.1
CR5	1,049	1.02	4.04	39.5
CR6	2,689.3	1.07	-14.27	35.5

Table 2.5: Copolar phase ($\phi_r + \phi_t$), amplitude imbalance (f) and polarization purity (VV/HV ratio) computed on the reflectors using the calibrated dataset. The calibration reflector has been excluded from the table.

calibration performance.

An initial assessment of the data quality is made by computing polarization signatures [65] for two corner reflector located at different ranges. They are plotted in Figure 2.12. A quantitative evaluation of the calibration is obtained by estimating the residual copolar phase and amplitude imbalances f and $\phi_r + \phi_t$ on the trihedrals after the calibration. The results are shown in Table 2.5. In Figure 2.11, the dependence of the residuals on the local incidence angle is plotted; the angle was estimated using a 2-m posting digital elevation model of the scene that was backwards geocoded in the radar geometry.

For visual representation of the calibration results, the HH-VV phase difference in radar coordinates is shown as a color image in Figure 2.10c.

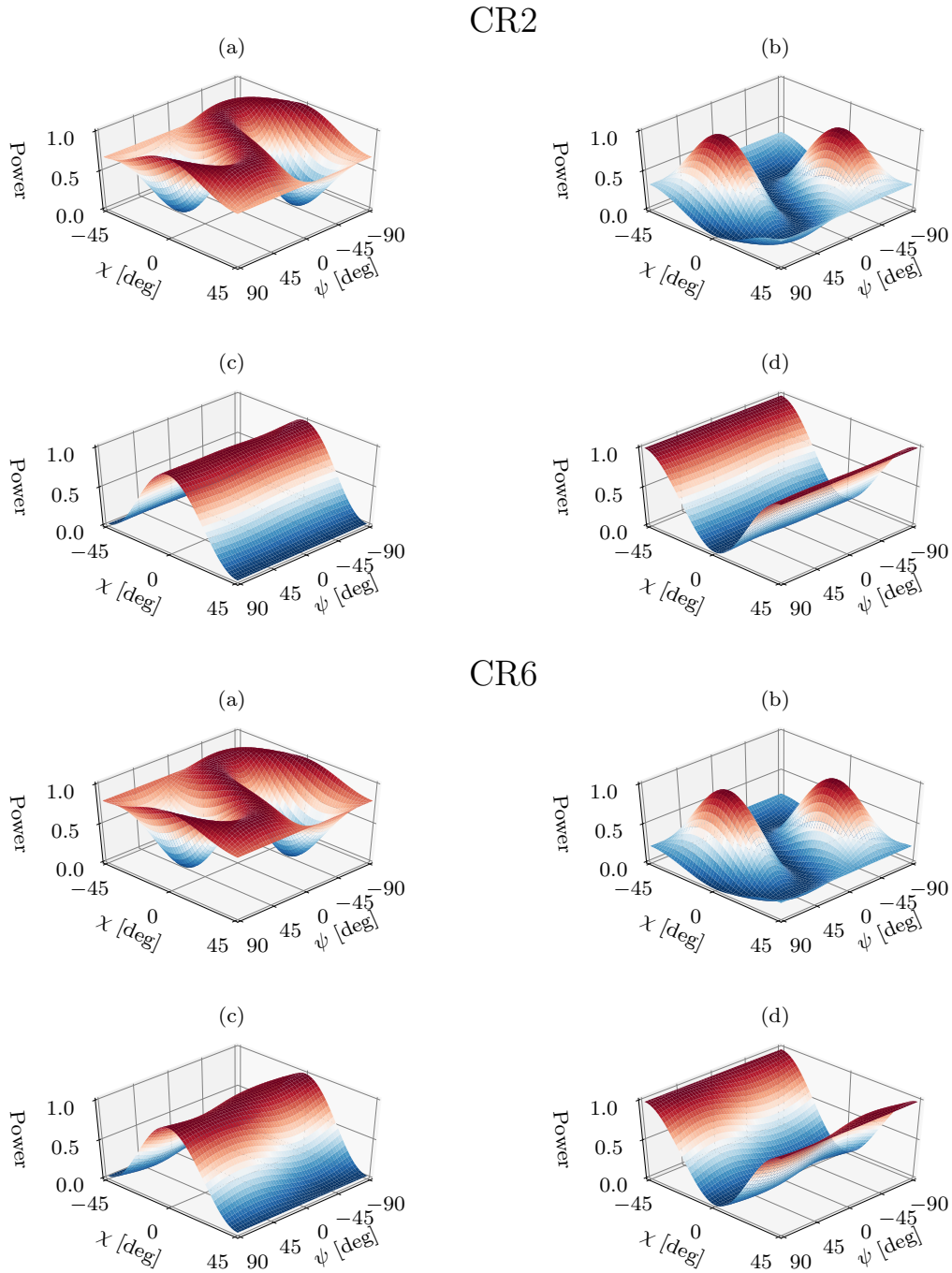


Figure 2.12: Polarization signatures for two trihedral corner reflectors at the locations "CR2" and "CR6" . For both plots, each panel shows: (a) uncalibrated copolar signature, (b) uncalibrated cross-polar signature; (c) calibrated copolar signature, (d): calibrated cross-polar signature. The power of each response is normalized to the corresponding maximum. A distinct change in signature is observed after the calibration; it is mostly due to the removal of the HH-VV phase offset.

2.4 DISCUSSION

2.4.1 Beam Squint Correction

The effect of the frequency squint on the raw data around TCR "CR2" is visible in Figure 2.6 (a) and (c) for the HH and VV channels. As sketched in Figure 2.2 and described in subsection 2.2.2, the data matrix appears skewed: the physical antenna direction and the effective pointing angle of the beam pattern only match for a brief time during each chirp due to the frequency scanning of the antenna. Because of that, if the data is range compressed, only part of the chirp bandwidth illuminates the target at each time, reducing the observed range resolution. This is verified in Figure 2.7 (a) and (c), where the oversampled response of TCR "CR2" after range compression is shown.

The linear squint factor a estimated on all reflectors of the calibration array is given in Table 2.3; the average estimated values of 4 and $3.9 \frac{\circ}{\text{GHz}}$ fit well with the figures suggested by the antenna manufacturer: 4.2 and $3.9 \frac{\circ}{\text{GHz}}$ for the H and V antennas respectively.

Thanks to the oversampled acquisition it is possible to use the proposed interpolation method to realign the samples in azimuth, compensating the effect of the squint by combining subsequent subchirps with different squint angles in a single coherent chirp that covers the entire bandwidth for the whole duration of time when the target is within the antenna beamwidth. This is shown in Figure 2.6 (a) and (c). The result of the interpolation is visible in Figure 2.6 (c) and (d): the spectrum is now aligned in azimuth; as a consequence the range resolution is decreased, as visible in Figure 2.7. Additionally the phase response seems to become more stable. Visually, the phase pattern observed in Figure 2.7(a) and (c) is also removed entirely; however, a residual azimuthal phase can be observed in the VV channel in Figure 2.7(e).

2.4.2 Azimuth Processing

The residual phase ramp observed on the "CR2" reflector in subsection 2.4.1 is not unique to that object:

A linear variation of 30 degrees over the 3dB antenna beamwidth can be observed for all reflectors in the dataset, as plotted in Figure 2.8a. The model of subsection 2.2.3 was developed to explain this variation in terms of the acquisition geometry. The estimated phase center location values \hat{L}_{ph} of Table 2.4 are consistent and display a standard deviation of less than 2 % of the antenna length, suggesting that the model is able to predict most of the phase variation. The estimated phase center shift for the H unit \hat{L}_{ph}^H is less than 5 cm, while the one for the V antenna, \hat{L}_{ph}^V , is -12 cm, almost twice as large and with opposite sign. This difference presumably explains the steeper phase ramp in the VV channel:

the range of θ_r for a scatterer is limited by the narrow antenna beamwidth θ_{3dB} . This should not cause a large phase variation, because evaluating (2.7) around zero should result in small values. However, considering the effect of L_{ph} , the entire function of (2.12) is shifted by α , simulating the effect of a larger θ_r , as it would be obtained with a much bigger antenna beamwidth.

As shown in Figure 2.7 (g), the azimuth phase variation is significantly reduced by the proposed correction method and the azimuth resolution is slightly degraded, although it is still better than 0.6° , the value that is expected by an incoherent average of azimuth samples. This result hints again that most of the phase ramp has been removed by the proposed method.

Similar results are observed for all trihedral reflectors, summarized in Figure 2.8b. The uncorrected HH channel shows a smaller variation, while the VV phase changes by 30° over the antenna beamwidth. The observed phase slopes for the V and H antennas have opposite signs, as it is expected from the estimated phase center locations of Table 2.4.

After the correction, only the reflector "CR1" shows an appreciable residual azimuth phase variation; which is likely explained by its proximity to the radar relative to the antennas far field transition distance, in the order of 500 m. A very similar variation is also observed in the HH channel. Excluding this exception, the residual phase inside the antenna beamwidth is under 5° .

2.4.3 Antenna Pattern Misalignment

Correcting for the estimated pattern alignment results in a gain of approximately 2.5 dB in HV power with respect to the uncompensated reference case, as plotted in Figure 2.9. The estimated gain is very close to the one expected by analyzing the patterns provided by the antenna manufacturer. This results confirms that the 1.8 mm shift setting employed to acquire the calibration data can correctly compensate the cross-polar power loss and the HH-VV misregistration.

2.4.4 Removal of Topographic Phase

The effect of the topographic phase compensation as described in subsection 2.2.5 is displayed in Figure 2.10; three topographic fringes are counted in the unflattened interferogram [Figure 2.10a], corresponding to a total phase variation of 9π . An estimate of this contribution is obtained from the unwrapped and rescaled interferogram between the upper and the lower HH channels. Because they are separated by a spatial baseline and they employ the same polarization [as seen in Figure 2.4], this interferogram provides an estimate of the topographic phase without additional polarimetric phase differences. The estimated topographic phase is then subtracted from the covariance matrix; the resulting flattened copolar phase difference is displayed in Figure 2.10b; no interferometric fringes can be counted. A more quantitative evaluation of the flattening process is obtained computing the correlation coefficient of the copolar phase and $\sin(\theta_l)$, where θ_l is the look vector elevation angle obtained from a DEM. The estimated value is very close to zero, suggesting the correct removal of the topographic phase contribution:

if there would be a linear relationship between these two quantities, as expected from the approximate expression for the topographic phase of (2.17), a significant level of correlation would be observed. This measure cannot exclude residual nonlinear relationships between topography and the copolar phase; an additional visual verification was obtained by plotting their joint histogram; this did not display any discernible functional relationship. Therefore, it can be safely assumed that the flattening process is able to remove the topographic phase contribution. An additional advantage of this correction

is the increased copolar coherence magnitude, as it can be by the inset coherence plot shown in Figure 2.10.

2.4.5 Polarimetric Calibration

An illustration of the effect of the calibration procedure of subsection 2.2.6 is given in Figure 2.12 by the polarization signatures of two reflectors before and after the calibration. The signature of the uncorrected data is distorted, the large variation of the maximum with respect to the orientation angle is reminiscent of the response of a dihedral scatterer, which would show two distinct peaks. After calibration, both signatures show a fair correspondence with the expected polarization signature for trihedral reflectors. The dihedral-like response before the calibration is due to the HH-VV phase imbalance, which shows a significant offset after the removal of the topographic contribution, as it can be seen in Figure 2.10b. By using a trihedral corner reflector or a similar odd-bounce scatterer, this offset is estimated and removed. The effect of copolar phase imbalance correction is shown visually in Figure 2.10c; low entropy odd bounce scattering seems to be dominant in this part of the scene, which is mainly composed of open fields and wooded areas.

Amplitude and phase imbalances are successfully corrected by the proposed method; the mean residual for the amplitude imbalance f is 1.03 with a root mean square deviation of 0.05. A mean of -4.5° is observed for the copolar phase imbalance $\phi_r + \phi_t$, with a root mean square deviation of 7° . Two outliers, "CR1" and "CR6" heavily skew the estimated phase statistics; as shown in Figure 2.11. For "CR1", its placement on the ground together with its closeness to the radar could explain the offset in the copolar phase. The other extreme case is "CR6", that was placed at a large distance from the radar, this could result in a reduced polarization purity due to the larger influence of clutter in the larger resolution cell.

Despite the outliers, no dependence of the residuals with the local incidence angle can be observed. This also suggests the validity of the method proposed in subsection 2.2.6 for the estimation and removal of the topographic contribution from the polarimetric phase differences.

Finally, the assumption of negligible crosstalk for the calibration model seems plausible considering that almost all reflectors exhibit polarization purities above 35 dB.

2.5 CONCLUSIONS

In this paper, two main aspects of the calibration of KAPRI, a new polarimetric portable ground-based FMCW radar were discussed:

1. The preprocessing of raw data into SLC images, taking into account several effects due to the specific hardware design of the system.
2. The polarimetric calibration of data into phase and amplitude calibrated polarimetric covariance matrices.

2.5.1 Preprocessing

The particular antenna design causes a frequency-depending shift of the antenna mainlobe during the chirp that causes a worsened range resolution. It is corrected using a slow time-fast time interpolation procedure; significant range resolution improvement are observed after the correction.

The real aperture, azimuth scanning design results in a motion of the antenna phase center relative to the scatterers, causing an observable azimuth phase ramp in point target responses. The variation is significantly different between the antennas, with almost 30° over the 3 dB beamwidth for the V antenna and much smaller for the H unit. This additional phase will complicate polarimetric calibration if left unaltered; this phase ramp is corrected by a SAR-like azimuth filter that reduces the total phase variation to under 10° .

Because separated transmitting and receiving antennas are used for each polarization, the polarimetric calibration is more intricate due to the presence of an interferometric baseline between channels that adds a topographic phase contribution in the polarimetric phase differences. Using the cross-track interferometric baselines of KAPRI, the topographic contribution can be estimated and subtracted from each element of the covariance matrix affected by it.

2.5.2 Calibration

The resulting flattened covariance matrix is then calibrated by assuming zero crosstalk and estimating copolar imbalances using a trihedral corner reflector assuming the parameters to be independent from the incidence angle. The crosspolar imbalance is estimated using distributed targets under the assumption of reciprocity.

The calibration quality is assessed by estimating residual calibration parameter on a calibrated scene with five trihedral corner reflectors: the mean amplitude imbalance is close to unity while the mean residual phase imbalance is very close to zero, with an RMS of 7° ; no significant variation with incidence angle is observed. These results suggest that the simplified calibration model [63, 64] is suitable to calibrate fully polarimetric KAPRI data.

ERRATA

1. In subsection 2.2.2 ...*data-driven method is be used* should be replaced with *is used*.

REFERENCES

- [1] S. Baffelli, O. Frey, C. Werner, and I. Hajnsek, "Polarimetric calibration of the Ku-band advanced polarimetric radar interferometer", *IEEE Transactions on Geoscience and Remote Sensing*, vol. 56, pp. 1–17, 2018. DOI: 10.1109/tgrs.2017.2778049.
- [2] A. K. Gabriel, R. M. Goldstein, and H. A. Zebker, "Mapping small elevation changes over large areas: Differential radar interferometry", *Journal of Geophysical Research*, vol. 94, p. 9183, 1989. DOI: 10.1029/JB094iB07p09183.

-
- [3] D. Massonnet and T. Rabaute, "Radar interferometry: Limits and potential", *IEEE Transactions on Geoscience and Remote Sensing*, vol. 31, pp. 455–464, 1993. DOI: 10.1109/36.214922.
- [4] P. Rosen, S. Hensley, I. Joughin, F. Li, S. Madsen, E. Rodriguez, and R. Goldstein, "Synthetic aperture radar interferometry", *Proceedings of the IEEE*, vol. 88, pp. 333–382, 2000. DOI: 10.1109/5.838084.
- [5] R. Bamler and P. Hartl, "Synthetic aperture radar interferometry", *Inverse Problems*, vol. 14, R1–R54, 1999. DOI: 10.1088/0266-5611/14/4/001.
- [6] D. L. Galloway, K. W. Hudnut, S. E. Ingebritsen, S. P. Phillips, G. Peltzer, F. Rogez, and P. a. Rosen, "Detection of aquifer system compaction and land subsidence using interferometric synthetic aperture radar, Antelope Valley, Mojave Desert, California", *Water Resources Research*, vol. 34, p. 2573, 1998. DOI: 10.1029/98WR01285.
- [7] T Strozzi, U. Wegmüller, L Tosi, G Bitelli, and V Spreckels, "Land subsidence monitoring with differential SAR interferometry", *Photogrammetric Engineering & Remote Sensing*, vol. 67, pp. 1261–1270, 2001.
- [8] D. L. Galloway and J. Hoffmann, "The application of satellite differential SAR interferometry-derived ground displacements in hydrogeology", *Hydrogeology Journal*, vol. 15, pp. 133–154, 2007. DOI: 10.1007/s10040-006-0121-5.
- [9] D. Massonnet, P. Briole, and A. Arnaud, "Deflation of mount Etna monitored by spaceborne radar interferometry", *Nature*, vol. 375, pp. 567–570, 1995. DOI: 10.1038/375567a0.
- [10] R. M. Goldstein, H. Engelhardt, B. Kamb, and R. M. Frolich, "Satellite radar interferometry for monitoring ice sheet motion: Application to an Antarctic ice stream.", *Science*, vol. 262, pp. 1525–1530, 1993. DOI: 10.1126/science.262.5139.1525.
- [11] J. J. Mohr, N. Reeh, and S. N. Madsen, "Three-dimensional glacial flow and surface elevation measured with radar interferometry", *Nature*, vol. 391, pp. 273–276, 1998. DOI: 10.1038/34635.
- [12] C. Carnec, D. Massonnet, and C. King, "Two examples of the use of SAR interferometry on displacement fields of small spatial extent", *Geophysical Research Letters*, vol. 23, p. 3579, 1996. DOI: 10.1029/96GL03042.
- [13] F. Catani, P. Farina, S. Moretti, G. Nico, and T. Strozzi, "On the application of SAR interferometry to geomorphological studies: Estimation of landform attributes and mass movements", *Geomorphology*, vol. 66, pp. 119–131, 2005. DOI: 10.1016/j.geomorph.2004.08.012.
- [14] D. Massonnet, M. Rossi, C. Carmona, F. Adragna, G. Peltzer, K. Feigl, and T. Rabaute, "The displacement field of the Landers earthquake mapped by radar interferometry", *Nature*, vol. 364, pp. 138–142, 1993. DOI: 10.1038/364138a0.
- [15] H. A. Zebker, P. A. Rosen, R. M. Goldstein, A. Gabriel, and C. L. Werner, "On the derivation of coseismic displacement fields using differential radar interferometry: The Landers earthquake", *Journal of Geophysical Research: Solid Earth*, vol. 99, pp. 19617–19634, 1994. DOI: 10.1029/94JB01179.

- [16] S. Cloude and E. Pottier, "An entropy based classification scheme for land applications of polarimetric SAR", *IEEE Transactions on Geoscience and Remote Sensing*, vol. 35, pp. 68–78, 1997. DOI: 10.1109/36.551935.
- [17] J.-S. Lee, M. Grunes, T. Ainsworth, L.-J. Du, D. Schuler, and S. Cloude, "Unsupervised classification using polarimetric decomposition and the complex Wishart classifier", *IEEE Transactions on Geoscience and Remote Sensing*, vol. 37, pp. 2249–2258, 1999. DOI: 10.1109/36.789621.
- [18] I. Hajnsek, E. Pottier, and S. Cloude, "Inversion of surface parameters from polarimetric SAR", *IEEE Transactions on Geoscience and Remote Sensing*, vol. 41, pp. 727–744, 2003. DOI: 10.1109/TGRS.2003.810702.
- [19] F. T. Ulaby, D. Held, M. C. Donson, K. C. McDonald, and T. B. A. Senior, "Relating polarization phase difference of SAR signals to scene properties", *IEEE Transactions on Geoscience and Remote Sensing*, vol. GE-25, pp. 83–92, 1987. DOI: 10.1109/TGRS.1987.289784.
- [20] S. Leinss, G. Parrella, and I. Hajnsek, "Snow height determination by polarimetric phase differences in X-band SAR data", *IEEE Journal of Selected Topics in Applied Earth Observations and Remote Sensing*, vol. 7, pp. 3794–3810, 2014. DOI: 10.1109/JSTARS.2014.2323199.
- [21] L. Pipia, X. Fabregas, A. Aguasca, C. Lopez-Martinez, S. Duque, J. J. Mallorqui, and J. Marturia, "Polarimetric differential SAR interferometry: First results with ground-based measurements", *IEEE Geoscience and Remote Sensing Letters*, vol. 6, pp. 167–171, 2009. DOI: 10.1109/LGRS.2008.2009007.
- [22] R. Iglesias, D. Monells, X. Fabregas, J. J. Mallorqui, A. Aguasca, and C. Lopez-Martinez, "Phase quality optimization in polarimetric differential SAR interferometry", *IEEE Transactions on Geoscience and Remote Sensing*, vol. 52, pp. 2875–2888, 2014. DOI: 10.1109/TGRS.2013.2267095.
- [23] D. Leva, G. Nico, D. Tarchi, J. Fortuny-Guasch, and A. Sieber, "Temporal analysis of a landslide by means of a ground-based SAR interferometer", *IEEE Transactions on Geoscience and Remote Sensing*, vol. 41, pp. 745–752, 2003. DOI: 10.1109/TGRS.2003.808902.
- [24] H. Rudolf, D. Leva, D. Tarchi, and A. Sieber, "A mobile and versatile SAR system", in *Proceedings of the IEEE International Geoscience and Remote Sensing Symposium*, vol. 1, IEEE, 1999, pp. 592–594. DOI: 10.1109/IGARSS.1999.773575.
- [25] M.-K. Kang, K.-E. Kim, H. Lee, S.-J. Cho, and J.-H. Lee, "Preliminary results of polarimetric characteristics for C-band quad-polarization GB-SAR images using H / A / α polarimetric decomposition theorem", *Korean Journal of Remote Sensing*, vol. 25, pp. 531–546, 2009.
- [26] A. Aguasca, A. Broquetas, J. Mallorqui, and X. Fabregas, "A solid state L to X-band flexible ground-based SAR system for continuous monitoring applications", in *Proceedings of the IEEE International Geoscience and Remote Sensing Symposium*, vol. 2, IEEE, 2004, pp. 757–760. DOI: 10.1109/IGARSS.2004.1368512.
- [27] L. Pipia, X. Fabregas, A. Aguasca, C. Lopez-Martinez, J. J. Mallorqui, and O. Mora, "A subsidence monitoring project using a polarimetric GB-SAR sensor", *European Space Agency, (Special Publication) ESA SP*, 2007.

-
- [28] C. Werner, T. Strozzi, A. Wiesmann, and U. Wegmüller, “A real-aperture radar for ground-based differential interferometry”, in *Proceedings of the IEEE International Geoscience and Remote Sensing Symposium*, IEEE, 2008, pp. 210–213. DOI: 10.1109/IGARSS.2008.4779320.
- [29] S. Rodelsperger, A. Coccia, D. Vicente, and A. Meta, “Introduction to the new Metasensing ground-based SAR: Technical description and data analysis”, in *Proceedings of the IEEE International Geoscience and Remote Sensing Symposium*, IEEE, 2012, pp. 4790–4792. DOI: 10.1109/IGARSS.2012.6352542.
- [30] C. L. Werner, A. Wiesmann, T. Strozzi, A. Kos, R. Caduff, and U. Wegmüller, “The GPRI multi-mode differential interferometric radar for ground-based observations”, in *Proceedings of the European Conference on Synthetic Aperture Radar*, VDE, 2012, pp. 304–307.
- [31] R. Caduff, F. Schlunegger, A. Kos, and A. Wiesmann, “A review of terrestrial radar interferometry for measuring surface change in the geosciences”, *Earth Surface Processes and Landforms*, vol. 40, pp. 208–228, 2015. DOI: 10.1002/esp.3656.
- [32] O. Monserrat, M. Crosetto, and G. Luzi, “A review of ground-based SAR interferometry for deformation measurement”, *ISPRS Journal of Photogrammetry and Remote Sensing*, vol. 93, pp. 40–48, 2014. DOI: 10.1016/j.isprsjprs.2014.04.001.
- [33] J. Bennett and K. Morrison, “Development of a ground-based, polarimetric synthetic aperture radar”, *Proceedings of the IEEE Aerospace Applications Conference*, vol. 4, 139–146 vol.4, 1996. DOI: 10.1109/AERO.1996.499408.
- [34] J. Bennett, K. Morrison, A. Race, G. Cookmartin, and S. Quegan, “The UK NERC fully portable polarimetric ground-based synthetic aperture radar (GB-SAR)”, in *Proceedings of the European Conference on Synthetic Aperture Radar*, IEEE, 2000, pp. 2313–2315. DOI: 10.1109/IGARSS.2000.858393.
- [35] Z.-S. Zhou, W.-M. Boerner, and M. Sato, “Development of a ground-based polarimetric broadband SAR system for noninvasive ground-truth validation in vegetation monitoring”, *IEEE Transactions on Geoscience and Remote Sensing*, vol. 42, pp. 1803–1810, 2004. DOI: 10.1109/TGRS.2004.832248.
- [36] T. Hamasaki, M. Sato, L. Ferro-Famil, and E. Pottier, “Natural objects monitoring using polarimetric interferometric ground-based SAR (GB-SAR) system”, in *Proceedings of the IEEE International Geoscience and Remote Sensing Symposium*, vol. 6, IEEE, 2005, pp. 4092–4095. DOI: 10.1109/IGARSS.2005.1525814.
- [37] R. Iglesias, A. Aguasca, X. Fabregas, J. J. Mallorqui, D. Monells, C. Lopez-Martinez, and L. Pipia, “Ground-based polarimetric SAR interferometry for the monitoring of terrain displacement phenomena—part I: Theoretical description”, *IEEE Journal of Selected Topics in Applied Earth Observations and Remote Sensing*, vol. 8, pp. 1–1, 2014. DOI: 10.1109/JSTARS.2014.2360040.
- [38] L. Pipia, “Polarimetric differential SAR interferometry with ground-based sensors”, PhD thesis, Universitat Politècnica de Catalunya, 2009. DOI: 10.803/6951.

- [39] L. Pipia, X. Fabregas, A. Aguasca, and C. Lopez-Martinez, "Polarimetric temporal analysis of urban environments with a ground-based SAR", *IEEE Transactions on Geoscience and Remote Sensing*, vol. 51, pp. 2343–2360, 2013. DOI: 10.1109/TGRS.2012.2211369.
- [40] M.-K. Kang, K.-E. Kim, H. Lee, S.-J. Cho, and J.-H. Lee, "Preliminary result of polarization property analysis using fully polarimetric GB-SAR images", in *Proceedings of the IEEE International Geoscience and Remote Sensing Symposium*, IEEE, 2010, pp. 4019–4022. DOI: 10.1109/IGARSS.2010.5650762.
- [41] T. G. Yitayew, "High resolution three-dimensional imaging of sea ice using ground-based tomographic SAR data", in *Proceedings of the European Conference on Synthetic Aperture Radar*, 2014, pp. 2–5.
- [42] O. Frey, C. L. Werner, and A. Wiesmann, "Tomographic profiling of the structure of a snow pack at X-/Ku-band using SnowScat in SAR mode", in *Proceedings of the European Radar Conference*, vol. 1, IEEE, 2015, pp. 1–4. DOI: 10.1109/EuRAD.2015.7346227.
- [43] O. Frey, C. L. Werner, R. Caduff, and A. Wiesmann, "A time series of SAR tomographic profiles of a snowpack", *Proceedings of the European Conference on Synthetic Aperture Radar*, pp. 726–730, 2016.
- [44] S. S. Cherukumilli, "GBIR crosstalk reduction of fully polarimetric data from Blue Springs Dam", Master Thesis, University of Missouri – Columbia, 2012.
- [45] S. Baffelli, O. Frey, and I. Hajnsek, "System characterization and polarimetric calibration of the Ku-band advanced polarimetric interferometer", in *Proceedings of the European Conference on Synthetic Aperture Radar*, 2016, pp. 2–5.
- [46] T. Strozzi, C. Werner, A. Wiesmann, and U. Wegmüller, "Topography mapping with a portable real-aperture radar interferometer", *IEEE Geoscience and Remote Sensing Letters*, vol. 9, pp. 277–281, 2011. DOI: 10.1109/LGRS.2011.2166751.
- [47] A. Stove, "Linear FMCW radar techniques", *IEE Proceedings F Radar and Signal Processing*, vol. 139, p. 343, 1992. DOI: 10.1049/ip-f-2.1992.0048.
- [48] J. N. Hines, V. H. Rumsey, and C. H. Walter, "Traveling-Wave Slot Antennas", *Proceedings of the IRE*, vol. 41, pp. 1624–1631, 1953. DOI: 10.1109/JRPROC.1953.274190.
- [49] C. Granet, G. L. James, and A. Ross Forsyth, "Aperture Antennas: Waveguides and Horns", in *Modern Antenna Handbook*, John Wiley & Sons, Ltd, 2007, pp. 97–156. DOI: 10.1002/9780470294154.ch3.
- [50] R. K. Enjiu and M. B. Perotoni, "Slotted waveguide antenna design using 3D EM simulation", *Microwave Journal*, 2013.
- [51] S.-T. Yang and H. Ling, "Combining a frequency-scanned antenna and a short-pulse radar for 2-D imaging", in *Proceedings of the IEEE International Symposium on Antennas and Propagation*, IEEE, 2014, pp. 137–138. DOI: 10.1109/APS.2014.6904400.

-
- [52] —, “Range-azimuth tracking of humans using a microstrip leaky wave antenna”, in *Proceedings of the IEEE International Symposium on Antennas and Propagation*, IEEE, 2012, pp. 1–2. DOI: 10.1109/AP.2012.6347963.
- [53] W. Mayer, M. Wetzel, and W. Menzel, “A novel direct-imaging radar sensor with frequency scanned antenna”, in *IEEE MTT-S International Microwave Symposium Digest, 2003*, vol. 3, IEEE, 2003, pp. 1941–1944. DOI: 10.1109/MWSYM.2003.1210538.
- [54] Y Alvarez, R. Cambolor, C Garcia, J. Laviada, C Vazquez, S Ver-Hoeye, G. Hotopan, M Fernandez, A. Hadarig, A. Arboleya, and F Las-Heras, “Submillimeter-Wave Frequency Scanning System for Imaging Applications”, *IEEE Transactions on Antennas and Propagation*, vol. 61, pp. 5689–5696, 2013. DOI: 10.1109/TAP.2013.2275747.
- [55] J. D. Kraus, *Antennas*, Second. McGraw-Hill, 1988.
- [56] R. Raney, T. Freeman, R. Hawkins, and R. Bamler, “A plea for radar brightness”, in *Proceedings of the IEEE International Geoscience and Remote Sensing Symposium*, vol. 2, IEEE, 1994, pp. 1090–1092. DOI: 10.1109/IGARSS.1994.399352.
- [57] H. Lee, J.-H. Lee, K.-E. Kim, N.-H. Sung, and S.-J. Cho, “Development of a truck-mounted arc-scanning synthetic aperture radar”, *IEEE Transactions on Geoscience and Remote Sensing*, vol. 52, pp. 2773–2779, 2014. DOI: 10.1109/TGRS.2013.2265700.
- [58] P. Beasley, A. Stove, B. Reits, and B. As, “Solving the problems of a single antenna frequency modulated CW radar”, in *IEEE International Conference on Radar*, IEEE, 1990, pp. 391–395. DOI: 10.1109/RADAR.1990.201197.
- [59] D. Massonnet, H. Vadon, and M. Rossi, “Reduction of the need for phase unwrapping in radar interferometry”, *IEEE Transactions on Geoscience and Remote Sensing*, vol. 34, pp. 489–497, 1996. DOI: 10.1109/36.485126.
- [60] K. Sarabandi and F. Ulaby, “A convenient technique for polarimetric calibration of single-antenna radar systems”, *IEEE Transactions on Geoscience and Remote Sensing*, vol. 28, pp. 1022–1033, 1990. DOI: 10.1109/36.62627.
- [61] K. Sarabandi, L. Pierce, and F. Ulaby, “Calibration of a polarimetric imaging SAR”, *IEEE Transactions on Geoscience and Remote Sensing*, vol. 30, pp. 540–549, 1992. DOI: 10.1109/36.142932.
- [62] T. Ainsworth, L. Ferro-Famil, and J.-S. Lee, “Orientation angle preserving a posteriori polarimetric SAR calibration”, *IEEE Transactions on Geoscience and Remote Sensing*, vol. 44, pp. 994–1003, 2006. DOI: 10.1109/TGRS.2005.862508.
- [63] A. G. Fore, B. D. Chapman, B. P. Hawkins, S. Hensley, C. E. Jones, T. R. Michel, and R. J. Muellerschoen, “UAVSAR polarimetric calibration”, *IEEE Transactions on Geoscience and Remote Sensing*, vol. 53, pp. 3481–3491, 2015. DOI: 10.1109/TGRS.2014.2377637.
- [64] K. Sarabandi, F. Ulaby, and M. Tassoudji, “Calibration of polarimetric radar systems with good polarization isolation”, *IEEE Transactions on Geoscience and Remote Sensing*, vol. 28, pp. 70–75, 1990. DOI: 10.1109/36.45747.

- [65] J. J. van Zyl, H. A. Zebker, and C. Elachi, “Imaging radar polarization signatures: Theory and observation”, *Radio Science*, vol. 22, pp. 529–543, 1987. DOI: 10.1029/RS022i004p00529.

3

GEOSTATISTICAL ANALYSIS AND MITIGATION OF ATMOSPHERIC PHASE SCREENS IN KU-BAND TERRESTRIAL RADAR INTERFEROMETRIC OBSERVATIONS OF AN ALPINE GLACIER

This chapter has been submitted for review to the peer-reviewed journal *IEEE Transactions on Geoscience and Remote Sensing* as:

S. Baffelli, O. Frey, and I. Hajnsek, “Geostatistical analysis and mitigation of atmospheric phase screens in Ku-band terrestrial radar interferometric observations of an alpine glacier”, *IEEE Transactions on Geoscience and Remote Sensing*, 2018, submission ID TGRS-2018-01579

Terrestrial Radar Interferometry (TRI) can measure displacements at high temporal resolution and potentially with high accuracy. An application of this technique is the observation of surface flow velocity of steep, fast flowing glaciers. For these observation scenarios, the main factor limiting the accuracy of TRI observations is the spatial and temporal variability in the distribution of atmospheric water vapor content, causing a phase delay (Atmospheric Phase Screen, (APS)) of a magnitude comparable to the displacement signal. This contribution presents a geostatistical analysis of the spatial and temporal behavior of the APS in Ku-Band terrestrial radar interferometry. The analysis bases on the assumption of a separable spatio-temporal covariance structure, which is tested empirically using variogram analysis. From this analysis, spatial and temporal APS statistics are derived and used in a two-step procedure combining regression-Kriging with generalized least squares (GLS) estimation to estimate a velocity time-series. The performance of this method is evaluated by cross-validation, using observation of stable scatterers. This analysis shows a significant reduction in residual phase variance compared to the commonly employed approach, combining linear models of APS stratification and interferogram stacking.

3.1 INTRODUCTION

3.1.1 Motivation

Avalanching glaciers [2] could pose a hazard to alpine valleys because dry calving events at the terminus can trigger other processes such as floods, snow avalanches and debris flows, sometimes with severe consequences. The 1956 disaster at the Mattmark dam construction site, the 1962 and 1967 Mount Huascaran avalanches and the 2002 Kazbek massif debris flow are examples of the consequences of these rupture events.

Recent advances in the understanding of glacier failures [3] suggest the possibility of early detection of developing glacier failures for two classes of avalanching glaciers. In the case of steep, unbalanced cold glaciers, such as in the Weisshorn hanging glacier [2, 4, 5], mechanical instabilities in the ice are the main mechanisms leading to break-off events, where the rupture happens within the ice mass. A log-periodic oscillation of the surface velocity superimposed to a power-law acceleration is observed in these cases [5]. This behavior may reveal useful to predict break-off times if frequent observations of the surface velocity are available. In the second class of steep, temperate glaciers, sliding is the main source of instability conducive to break offs. Here, sub-glacial water pressure can reduce basal friction, causing a major portion of the tongue to become unstable [6] and eventually to break off, such as in the case of the Allalingsletscher responsible for the 1956 Mattmark disaster. In this latter type of glacier, the surface velocity increases during *active phases*, notably in summer [3]. However, these patterns only rarely correlate with break-off events; surface velocity measurements alone are not sufficient and must be combined with other methods such as seismic measurements [7]. For both glacier types, reliable and precise measures of surface velocities are necessary to monitor them and improve the understanding of their dynamics. In this sense, area-wide estimates at high temporal resolution and over long periods of time are particularly useful.

Remote sensing techniques [8–10] are frequently employed for glacier flow measurement, using visible and infrared images [11–13] or coherent [14–18] and incoherent [16, 19] methods with spaceborne and terrestrial [20–24] synthetic aperture radar (SAR) data. In this context terrestrial radar interferometry [20–24] (TRI) is complimentary to the more established space- and airborne SAR observations. While the spatial coverage of the former is normally smaller, these systems offer great flexibility in the acquisition geometry and timing, both of which are necessary for the surveillance and study of the fast dynamics of alpine glaciers. Moreover, one strength of radar data is independence from external illumination and the ability to image through fog and clouds, permitting continuous observations during the night and with cloud cover. These advantages are accompanied by relatively complex data processing requirements and by problems specific to the coherent nature of radar images.

Among coherent techniques, the most useful for glacier monitoring is differential radar interferometry (D-InSAR)[25], which is based on the sensitivity of the phase of microwaves to the length of the propagation path from the sensor to the observed surface. By computing the phase difference between measurements at subsequent times, D-InSAR permits estimating displacements with high precision; theoretically only limited by the wavelength employed.

Temporal variations in the spatial distribution of the atmospheric water vapor content causing time-varying heterogeneity in the propagation speed of light are one of the largest source of errors in displacement estimation with differential radar interferometry—both in the spaceborne and in the terrestrial case—. These nuisances are known as Atmospheric Phase Screen (APS)[26–28]. Because of these nuisances, precise estimation of displacements with D-InSAR requires phase calibration of the data in order to remove—or at least mitigate—the phase contribution of the APS.

While the modeling and correction of the APS in the spaceborne SAR case is an established field of research, the relative novelty of TRIs and the limited availability of this type of data leave several open questions. The different acquisition geometries and the shorter revisit times possible with TRI suggest the necessity of reassessing the applicability of the APS models and correction methods employed in spaceborne D-InSAR to these situations.

3.1.2 State of the Art

The atmosphere is a complex and dynamic environment: temporal variations of temperature, pressure and water vapor content [29] and their heterogeneous spatial distribution cause variability in the atmospheric refraction index that cause the appearance of the APS in differential radar interferometry.

Additional information is sometimes employed to reconstruct the refractivity distribution at the time of the acquisitions and hence correct the phase delays in interferometric observations. These external observations can be in the form of weather model outputs [30], of wet zenith delays maps derived from global navigation satellite system (GNSS) observations [26, 31–33] or from spaceborne microwaves radiometers and imaging spectrometers [34–37]. These solutions are primarily applicable to spaceborne InSAR: In the TRI case the spatial extent of the scene can be much smaller than the resolutions of the mentioned data products and the observation geometry very different. In terrestrial radar interferometry only a small portion of the atmospheric air column is observed, while the auxiliary data acquired from space would give the total phase delay through the entire height of the troposphere. Similar concepts employing automatic weather station data (AWS) exist for TRI [38, 39]. Unfortunately, AWS observations are often not available during a TRI monitoring campaign. Another difficulty with these approaches is that they can only correct large scale phase variation and cannot compensate local phase trends of high spatial frequency which tend to make the interpretation of deformation maps very difficult.

These limitations suffered by external observations motivates the development of APS correction approaches based only on the statistical behavior of the APS and which operate solely on the radar data. In most cases, these methods base on a hybrid statistical model of the atmospheric phase screen, factorizing it [40, 41] in a deterministic component of low spatial frequency attributed to vertical stratification [30, 39, 42–48], often strongly correlated with the terrain relief, and in a random contribution attributed to turbulent mixing of water vapor in the troposphere. Since the turbulent component shows a dynamic and complex behavior that is not easily modeled in a closed form, the random component is described through structure functions or covariance functions [28, 29, 31], which sometimes are derived from turbulence theory [29, 49]. The turbulent contribution is frequently assumed to show spatial

correlation but uncorrelated in time [40, 50, 51]. Thanks to this assumption, the APS is often separated from other nuisances and from the deformation using time series analysis applied on a set of scatterers whose phase response is stable in time, the so called persistent scatterers [52]. The point-wise estimates of the APS are then extrapolated to a regular grid covering the area of interest using geostatistical interpolators such as Kriging [50, 53], which account for its spatially correlated nature. The extrapolated APS can then be subtracted from the interferometric phases, which then undergo further processing to obtain displacement estimates [54, 55].

3.1.3 Research Gaps

The applicability of the statistical assumptions used in spaceborne D-InSAR to TRI is doubtful, considering the different acquisition repeat rate and the smaller spatial coverage of the data. Additionally, the acquisition geometry in TRI is very different from the one in spaceborne SAR. In the former case, the radar signal only travels through a small vertical portion of the troposphere, while in the latter the entire atmospheric air column is traversed. These differences may reflect on the validity of both the deterministic models of stratified APS and of the statistical model of turbulence employed spaceborne InSAR.

In the case of stratification, the smaller scene size and the shorter vertical propagation path in TRI data may reduce the visibility of the effect of atmospheric layering. Regarding the turbulent APS, the statistical assumptions of temporal uncorrelatedness does necessarily apply to the shorter revisit times frequently employed in TRI.

3.1.4 Contributions of This Paper

This work presents a geostatistical analysis of the atmospheric phase screen [26–28] (APS) affecting Ku-Band TRI data with the aim of studying the research gaps discussed above. To do so, the study starts from an APS model similar to the one customarily employed in In-SAR studies, assuming a combination of turbulent and stratified atmosphere. Using this mathematical setup, several issues are investigated:

1. The performance of several models for APS stratification is assessed statistically by measuring their ability to describe the phase variance observed at a set of persistent scatterers (PS). These points are chosen at locations known to be only affected by atmospheric disturbances.
2. The assumption of spatially correlated, temporal uncorrelated statistics, which is commonly used to model the APS in spaceborne InSAR data is replaced by a separable spatio-temporal covariance model. The suitability of this model is tested with variogram analysis.
3. The performance of APS correction using a regression-Kriging interpolator accounting for stratification effects and a spatial covariance model of turbulence is evaluated. Its performance is measured by computing the residual phase variance at a set of non-moving persistent scatterers (PS).

4. A time-series inversion approach employing the temporal covariance model is presented. Its performance in mitigating the residual APS observed after regression-Kriging correction is assessed.

3.2 METHODS

3.2.1 Differential Radar Interferometry: Signal Model

Differential radar interferometry [56, 57] uses the phase coherency exhibited by radar images: the phase of a scatterer acquired by a coherent radar contains a contribution proportional to the line-of-sight distance from the sensor to the object. Therefore, the phase difference computed from a pair of images taken at different locations and/or times contains a contribution proportional to the displacements and/or heights of the scatterers composing the scene.

More formally, consider a radar placed at a fixed location where the origin $\mathbf{0}$ of a Cartesian coordinate system is set. Consider a scatterer located at \mathbf{s} at time t_k ; its phase measured by the above radar is:

$$\phi(t_k) = \frac{4\pi}{\lambda} R(t_k) + \phi_{scat}(t_k) + \phi_{atm}(t_k) \quad (3.1)$$

where $R = |\mathbf{s}|$ is the distance between scatterer and sensor and ϕ_{scat} is the scattering phase, which depends on dielectric properties, shape of the object and to a radar-specific phase offset due to delays in the electronics and cables, finally ϕ_{atm} is the excess phase delay caused by the atmosphere.

For a scatterer moving with velocity $v = \frac{\Delta R}{t_{l+m} - t_l}$ along the line of sight in a period of duration Δt between times t_l and t_{l+m} , the *interferometric phase* or *interferometric phase difference* is:

$$\begin{aligned} \Delta\phi &= \frac{4\pi}{\lambda} \Delta R + 2\pi n + \epsilon_{atm} + \epsilon_{decorr} \\ &= \frac{4\pi}{\lambda} \Delta t v + 2\pi n + \epsilon_{atm} + \epsilon_{decorr} \end{aligned} \quad (3.2)$$

where Δt is often called the *temporal baseline*; the term $2\pi n$ indicates that phase measurements are ambiguous modulo the wavelength, $\epsilon_{atm} = \phi_{atm}(t_{l+m}) - \phi_{atm}(t_l)$ represents the additional differential phase delay due to changes in atmospheric refraction index and ϵ_{decorr} describes the noise-like phase error due to thermal noise in the radar and to changes ϕ_{scat} due to variations the scatterer's properties.

Equation (3.2) shows that the interferometric phase difference is sensitive to the displacement ΔR but also to changes in the dielectric properties of the imaged objects and to changes in the propagation medium. In differential interferometry, the objective is the estimation of the displacement ΔR (or the velocity v) from noisy phase observations; therefore all terms but the displacement are considered nuisances. To improve the displacement estimation robustness—and possibly to estimate an object's displacement history—, multiple phase measurements at different times are often used. Thus, the model describing a single interferometric phase observation of (3.2) is extended to multiple observations as follows: Given a vector \mathbf{y} of PN radar phases $y(i, l)$ (single look complex or SLC data) acquired at N times t_k and P locations \mathbf{s}_i , estimate the (PN) -element vector \mathbf{v} of surface velocities $v(i, l)$ at times

$t_l = \frac{t_k + t_{k+1}}{2}$ with $0 < k < N$ between subsequent acquisitions and at locations \mathbf{s}_i with $0 < i < P$ [58, 59]. In analogy to (3.2), it is convenient to replace the SLC phase vector \mathbf{y} with the PM vector of interferometric phases \mathbf{z} :

$$\mathbf{z} = \bar{\mathbf{A}}\mathbf{y} \quad (3.3)$$

where \mathbf{z} is a PM vector of phase differences at P locations and M times, where M is the number of interferograms, limited to at most $\frac{N+1}{2}$ unique pairs. The incidence matrix $\bar{\mathbf{A}} = \mathbf{I}_P \otimes \mathbf{A}$ a $MP \times NP$ block-diagonal incidence matrix used to compute the interferometric phases from the SLC phase vector. Each of its blocks \mathbf{A} indicates which of the N acquisitions are paired to form interferograms in \mathbf{z} : entries A_{mk} and A_{ml} are -1 and 1 for the m -th interferogram between the l -th and the k -th acquisition. For example, given $N = 4$ SLC images, the matrix

$$\mathbf{A} = \begin{bmatrix} 1 & -1 & 0 & 0 \\ 0 & 1 & -1 & 0 \\ 0 & 0 & 1 & -1 \end{bmatrix} \quad (3.4)$$

is used to compute the three unique interferograms between successive acquisitions. The (PN) -element vector of velocities \mathbf{v} can be related to the vector of interferometric phases [29, 40, 58, 59] in analogy with (3.2):

$$\mathbf{z} = \bar{\mathbf{B}}\mathbf{v} + \epsilon_z \quad (3.5)$$

where $\bar{\mathbf{B}} = \mathbf{I}_P \otimes \mathbf{B}$ and \mathbf{B} is a $M \times N$ matrix of the time spans between the acquisition times of the SLC images used to compute \mathbf{z} . Its construction from the interferogram incidence matrix \mathbf{A} is described in [58]. As an example, using the incidence matrix \mathbf{A} of equation (3.4) and assuming regularly spaced acquisitions with Δt seconds separation, \mathbf{B} will be:

$$\mathbf{B} = \begin{bmatrix} \Delta t & 0 & 0 & 0 \\ 0 & \Delta t & 0 & 0 \\ 0 & 0 & \Delta t & 0 \end{bmatrix}. \quad (3.6)$$

Finally, ϵ_z is a term subsuming all the noise-like contributions, assumed to be a zero-mean Gaussian random process with a $PM \times PM$ covariance matrix $\Sigma_z =$: the nuisance terms are allowed to be correlated both in time and space.

As the noise is assumed to be drawn from a multivariate Gaussian distribution of known covariance, the generalized least squares (GLS) solution of equation (3.5) is the minimum variance, unbiased estimator for \mathbf{v} [60, 61]:

$$\hat{\mathbf{v}} = (\bar{\mathbf{B}}^T \Sigma_z^{-1} \bar{\mathbf{B}})^{-1} \bar{\mathbf{B}}^T \Sigma_z^{-1} \mathbf{z}. \quad (3.7)$$

In many cases, acquisitions too distant in time cannot be used to form interferograms because they would show too high a level of phase noise caused by temporal decorrelation and will be affected by excessive phase wrapping. In this case, \mathbf{A} will only consist of those rows where the temporal baseline is shorter than a given threshold, thus $M < \frac{(N)(N-1)}{2}$ and the rank of \mathbf{B} is deficient. In this case the problem is underdetermined and there is no unique solution for \mathbf{v} . An example of this situation is shown in equation (3.6), where only three interferograms are available to estimate four parameters.

The problem of decorrelation can be mitigated by adopting approaches based on persistent scatterers (PS), where only observations at highly coherent scatterers [50, 52, 62] unaffected by temporal decorrelation are used for the inversion. These methods are of limited use when the surface flow velocity of glaciers is studied, since the continuously changing surface features and the rapid motion make the detection of PS very unlikely. As an alternative, the rank of (3.5) can be increased by using a simplified velocity model, described by a vector \mathbf{p} with a smaller number of parameters $d < PN$ [58]:

$$\mathbf{v} = \mathbf{M}\mathbf{p} \quad (3.8)$$

For example, assuming constant velocity v_0 over time, the model for the i -th pixel is:

$$\mathbf{v}_i = \begin{bmatrix} v_0 \\ \vdots \\ v_0 \end{bmatrix} = \mathbf{I}_{N,1} v_0 = \mathbf{M}_i \mathbf{p} \quad (3.9)$$

and \mathbf{M} is the block-diagonal matrix $\mathbf{I}_{N,1} \otimes \mathbf{I}_{N,P}$. Generally, \mathbf{M} can be any $PN \times d$ matrix describing a simplified spatial and temporal displacement model and possibly imposing spatio-temporal smoothness constraints. Thus, the problem is rewritten as:

$$\mathbf{z} = \bar{\mathbf{B}}\mathbf{M}\mathbf{p} + \epsilon_z = \bar{\mathbf{G}}\mathbf{p} + \epsilon_z. \quad (3.10)$$

Where the *design matrix* $\bar{\mathbf{G}}$ is written with a bar to indicate that it is the design matrix for the whole set of P pixels in the set of all M interferograms. For simplicity $\bar{\mathbf{G}}$ is assumed to be a block matrix with P blocks \mathbf{G} —the same velocity model is assumed for each pixel and no spatial constraints are set—. The GLS estimate of \mathbf{p} is obtained with:

$$\hat{\mathbf{p}} = (\bar{\mathbf{G}}^T \Sigma_z^{-1} \bar{\mathbf{G}})^{-1} \bar{\mathbf{G}}^T \Sigma_z^{-1} \mathbf{z}. \quad (3.11)$$

The variance of the estimates is given by:

$$\text{var}(\hat{\mathbf{p}}) = \bar{\mathbf{G}}^T \Sigma_z^{-1} \bar{\mathbf{G}}. \quad (3.12)$$

Without further assumptions, the covariance matrix of the nuisance, Σ_z must only be positive semidefinite. However, as the APS is known to be spatially correlated and can potentially show temporal correlations, its inversion can be computationally very costly [40].

However, by making certain assumptions that will be discussed later, the spatially correlated contributions in Σ_z can be estimated and removed before the least-squares inversion, reducing the spatial correlation in Σ_z and making the inversion computationally easier. Whether the full inversion is attempted or the latter approach is used, knowledge of the covariance matrix of the interferogram network is required for the inversion and to provide uncertainty estimates for the derived parameter. As the interferometric phases \mathbf{z} are derived from the SLC phases via (3.3), the interferogram covariance is related to the covariance of the SLC phase vector \mathbf{y} [40]:

$$\Sigma_z = \bar{\mathbf{A}} \Sigma_y \bar{\mathbf{A}}^T. \quad (3.13)$$

ϵ_y is [29, 40]:

$$\epsilon_y = \epsilon_{y,atm} + \epsilon_{y,decorr}, \quad (3.14)$$

where $\epsilon_{y,atm}$ is the phase contribution from the atmospheric phase screen and $\epsilon_{y,decorr}$ represents the phase noise due to the effect of temporal decorrelation in each acquisition: these two terms are assumed to be mutually uncorrelated because they are produced by different physical mechanisms. When discussing the SLC phase, the noise terms must be seen as deviations from the noise-free SLC phases consisting only of the propagation term and the intrinsic scattering phase as in (3.1)[40]. These equations are only a tool to model the covariance of the interferometric phases. By linearity, the same decomposition applies to the covariance matrix of the interferometric phase vector Σ_z :

$$\Sigma_z = \Sigma_{z,atm} + \Sigma_{z,decorr}. \quad (3.15)$$

The following sections are dedicated to the individual covariance terms.

COVARIANCE OF DECORRELATION PHASE NOISE

$\Sigma_{z,decorr}$ models the effect of thermal noise in the measurement system and random changes in reflectivity on the stability of the observed interferometric phases. This is usually quantified through the magnitude of the interferometric phase coherence, γ [63] derived from spatial or temporal multilooking by assuming ergodicity [64]. The coherence magnitude is used to estimate the interferometric phase variance through the Cramer-Rao lower bound [65]. The phase variance for a interferogram pixel located at \mathbf{s}_i at time $t_l = \frac{t_o + t_p}{2}$, derived from acquisitions at times t_o and t_p is:

$$\text{Var} [z_{i,o,p}] \geq \frac{\sqrt{1 - \gamma_{i,o,p}^2}}{\gamma_{i,o,p} \sqrt{2L}}. \quad (3.16)$$

where the notation $\gamma_{i,o,p}$ indicates the coherence estimate at pixel i from acquisitions o and p .

In the case of interferograms with zero spatial baseline, the decorrelation noise is spatially uncorrelated and $\Sigma_{z,decorr}$ is a block-diagonal matrix, where each $M \times M$ block represents the covariance of the decorrelation process for an individual pixel [40]. The temporal covariance $\Sigma_{z,decorr}(i)$ for the i -th pixel can be modeled in several ways:

- A diagonal matrix, assuming independent, Gaussian noise contributions for each interferogram [29]. The variances can be estimated using a coherence estimator and (3.16) or directly by using a spatial estimator of the phase variance [40].
- A similar model accounts for the interaction between interferograms due to shared SLC acquisitions [31, 66]. Assuming independent Gaussian noise to affect every interferogram, the entry corresponding to the covariance between the lm -th and the np -th interferograms, the covariance is written as:

$$\sigma_{decorr,lm} \sigma_{decorr,np} c_{lm,nq} \quad (3.17)$$

where $\sigma_{decorr,np}$ is the phase standard deviation in the interferogram between t_n and t_q and the factor $c_{lm,nq}$ is used to weigh noise variances in the individual interferograms to account for com-

mon SLC acquisitions:

$$c_{lm,np} = \begin{cases} 1 & l = n, m = q \\ -0.5 & l = q \text{ or } m = n \\ 0.5 & l = n \text{ or } m = q \\ 0 & \text{otherwise} \end{cases} . \quad (3.18)$$

Despite resulting in a non-diagonal interferogram covariance matrix, this model does not assume the underlying decorrelation process to be correlated in time.

- A block-diagonal matrix under the Brownian decorrelation hypothesis: assuming each scatterer inside a resolution cell to move randomly with uniform probability at all time instants [40, 63, 67] results in an exponential decay in coherence between acquisitions:

$$\gamma(\Delta T) = \gamma_0 e^{-\frac{\Delta T}{\tau}} . \quad (3.19)$$

Unlike the previous model, here the decorrelation process is assumed to be temporally correlated and two interferograms are correlated if they cover a common time span, even if they do not share any master or slave images. The construction of $\Sigma_{z,decorr}$ is described in detail in [40]. The Brownian motion model does not apply to all types of terrain; it was found to be applicable to urban areas [67]. In many cases the coherence shows more complex patterns such as seasonal trends or variations correlated with weather conditions.

COVARIANCE OF ATMOSPHERIC PHASE SCREEN

The term $\epsilon_{y,atm}$ models the phase delay caused by the inhomogeneous distribution of atmospheric water vapor in the scene [26–28]. Its effect can not be appreciated in the SLC phase, only in interferograms: temporal changes in the spatial distribution of atmospheric delay $\epsilon_{y,atm}$ between acquisitions are revealed in the interferometric phase difference as low spatial frequency atmospheric phase screens.

Part of the spatial phase trends can be approximated using linear models by assuming homogeneous or layered distributions of atmospheric water vapor [30, 39, 42–48]. These models are often not sufficient to capture the full APS phase variability and must be augmented with a statistical description. Thus, the APS is written as the superposition of these terms [40, 41]:

$$\epsilon_{y,atm} = \epsilon_{y,atm, strat} + \epsilon_{y,atm, turb} . \quad (3.20)$$

where $\epsilon_{y,atm, strat}$ is the *stratified* APS and $\epsilon_{y,atm, turb}$ is the *turbulent* APS, due to turbulent mixing in the troposphere [29, 31], which is modeled statistically as a zero mean random process with covariance matrix $\Sigma_{y,atm}$.

More precisely, the random process generating the APS can be described through a covariance matrix $\Sigma_{y,atm}$ if and only if its covariance function C is *stationary* in space and time. This means that C depends only on spatial temporal separations $\mathbf{d} = \mathbf{s}_1 - \mathbf{s}_2$ and $t = t_1 - t_2$ and not on the locations themselves [68].

This assumption is frequently accompanied by the one of *isotropy* in space, where C does not depend on the direction of \mathbf{d} but only on its magnitude $d = |\mathbf{d}|$.

In spaceborne InSAR studies, the APS covariance is further simplified by assuming lack of temporal correlation [40], thus:

$$C(d, t) = C_s(d) \delta(t). \quad (3.21)$$

Where $\delta(t)$ is the Dirac delta function. The assumption of uncorrelatedness in time is justifiable because in spaceborne InSAR the acquisition repetition times are in the order of days, where it reasonable to expect that the turbulent behavior in troposphere changed completely. This assumption is a particular case of the more general property of *separability*, where C is factorized in temporal and spatial covariances:

$$C(d, t) = C_t(t) C_s(d). \quad (3.22)$$

Separability implies that the spatial statistics are not a function of time; this assumption is theoretically not entirely corrected. For example, it is not respected by Taylor's hypothesis for atmospheric turbulence [27, 28, 32, 33, 68–70]. In Taylor's hypothesis, it is assumed that local atmospheric eddies are advected by the mean wind \mathbf{v} ; so that the temporal covariance function can be written as:

$$C_t(\mathbf{d}, t) = C_s(\mathbf{d} - \mathbf{v}t). \quad (3.23)$$

Despite its limitations, separability is very useful as it greatly simplifies fitting statistical models; more practically, it radically reduces the size of covariance matrices since spatio-temporal interactions are not allowed. To see why, consider the APS covariance matrix of the SLC phase vector— the discretization of the covariance function of (3.22)—. In the stationary, separable case, this matrix can be written as a Kronecker product of a $P \times P$ spatial covariance matrix $\Sigma_{y,atm,s}$ and of a $N \times N$ temporal covariance matrix $\Sigma_{y,atm,t}$ [40, 71]. :

$$\Sigma_{y,atm} = \Sigma_{y,atm,s} \otimes \Sigma_{y,atm,t}. \quad (3.24)$$

Using (3.13) the APS covariance matrix of the interferogram vector is:

$$\begin{aligned} \Sigma_{z,atm} &= \bar{\mathbf{A}} \Sigma_{y,atm} \bar{\mathbf{A}}^T = \\ &(\mathbf{I} \otimes \mathbf{A}) (\Sigma_{y,atm,s} \otimes \Sigma_{y,atm,t}) (\mathbf{A}^T \otimes \mathbf{I}^T) = \\ &= \Sigma_{y,atm,s} \otimes (\mathbf{A} \Sigma_{y,atm,t} \mathbf{A}^T) \end{aligned} \quad (3.25)$$

where the last step follows from the mixed product property of the Kronecker product.

In summary the considerations made above, together with the assumption of spatio-temporal separability lead to the following APS model:

1. Assuming the APS in the SLC phase vector to have a separable covariance, the APS in the interferogram vector has separable covariance as well. The estimation and correction of the spatially and temporally correlated components can be performed separately.
2. The turbulent APS contribution in the interferogram phase vector has the same spatial covariance matrix as the *unobservable* APS in the SLC phase vector. The covariance does not depend on the

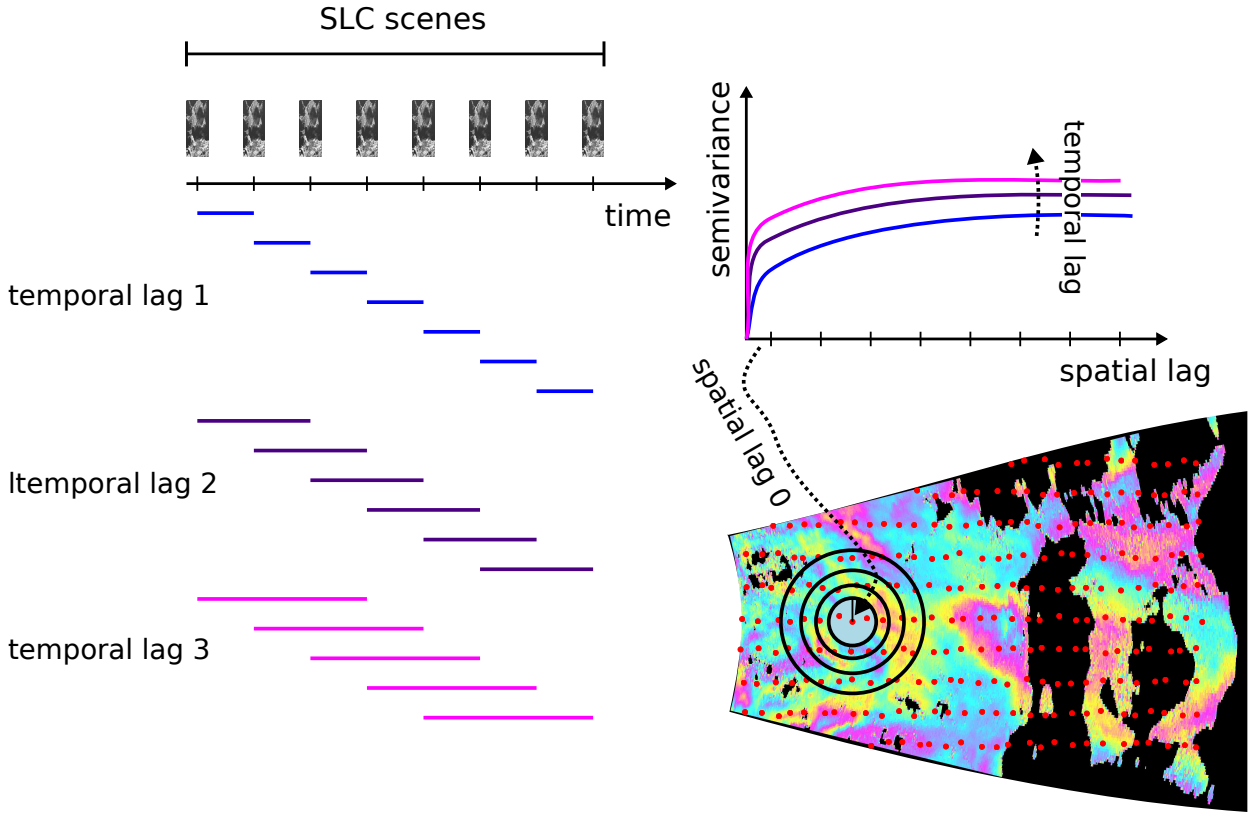


Figure 3.1: Illustration of the computation procedure for the spatio-temporal variogram, used to estimate the space-time covariance of the APS, $\Sigma_{y,atm}$. Assuming separability, the spatial covariance of the APS has the same structure as the covariance of the interferograms and can be estimated as the spatial variogram averaged over all temporal baselines. The temporal variogram corresponds to the mean phase variance of the interferogram grouped by temporal lags.

acquisition times.

3. If a linear model is used to describe the stratified APS in the SLC phase, the stratified APS observed in an interferogram can be described by a functionally identical model with different model parameters.

INVERSION STRATEGY

To summarize the findings of the previous sections, ϵ_z , the noise affecting the interferograms is assumed to be a zero-mean Gaussian random vector with covariance:

$$\Sigma_z = \Sigma_{y,atm,s} \otimes (\mathbf{A}\Sigma_{y,atm,t}\mathbf{A}^T) + \Sigma_{z,decorr} \quad (3.26)$$

where $\Sigma_{y,atm,s}$ is the $P \times P$ matrix of the spatial APS covariance, $\Sigma_{y,atm,t}$ the $N \times N$ matrix of the temporal APS covariance and $\Sigma_{z,decorr}$ is the $PM \times PM$ diagonal or block diagonal matrix of the decorrelation phase noise. Additionally, each interferogram is affected by a stratified APS predicted by a linear model.

The following procedure is used to estimate the APS affecting the interferogram vector and to reconstruct \mathbf{p} :

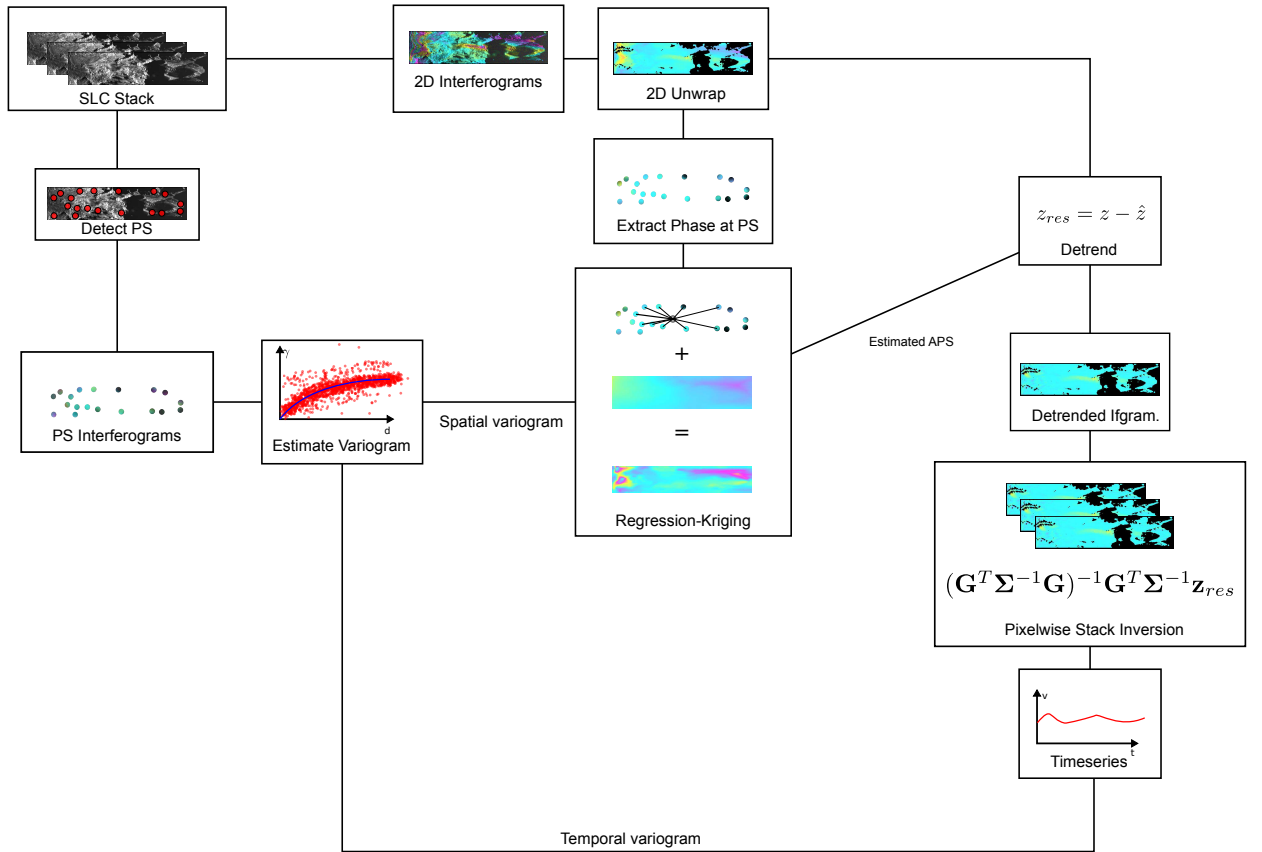


Figure 3.2: Schematic description of the two-step spatial APS mitigation and time-series inversion.

- For each interferogram l at time t_l an estimate $\hat{\epsilon}_{z,atm}(t_l)$ of the spatially correlated APS is obtained by regression-Kriging interpolation of the interferometric phases observed on a set of persistent scatterers (PS) whose phase should not be affected by displacements. These estimates are subtracted from the interferogram vector \mathbf{z} , reducing the spatial correlation in the residual interferogram vector \mathbf{z}_{res} to an extent where it can be assumed to be negligible.
- The generalized least squared inversion for \mathbf{p} can then be performed on the residual interferogram vector \mathbf{z}_{res} independently for each pixel, provided that the design matrix $\bar{\mathbf{G}}$ can be written as a block-diagonal matrix with P blocks and assuming each pixel i to be affected by a spatially uncorrelated, temporal correlated APS and decorrelation noise contribution, which is assumed to have a covariance matrix:

$$\begin{aligned} \Sigma_{z,res}(i) = \Sigma_{z,t}(i) = \\ \mathbf{I} \otimes (\mathbf{A}\Sigma_{y,atm,t}\mathbf{A}^T) + \Sigma_{z,decorr}(i). \end{aligned} \quad (3.27)$$

The correction of the spatially correlated contribution $\epsilon_{y,atm,s}$ will be described in detail in subsection 3.2.2, while the pixel-wise GLS inversion to obtain estimates of the displacement parameters is discussed in subsection 3.2.3.

A block diagram showing the general principle of the employed APS correction and inversion scheme is shown in Figure 3.2. The next sections will be devoted to the discussion of the various steps used in this approach.

3.2.2 Spatial Correction of APS

REGRESSION-KRIGING

According to the model setup, the interferometric phase $z(i, l)$ at time t_l and any location \mathbf{s}_i is written as the superposition of displacement phase and stratified and turbulent APS:

$$\begin{aligned} z(i, l) &= z_{disp}(i, l) + \epsilon_{z,atm}(i, l) \\ &= z_{disp}(i, l) + \epsilon_{z,atm, strat}(i, l) + \epsilon_{z,atm, turb}(i, l) \\ &= z_{disp}(i, l) + \mathbf{X}\beta(l) + \epsilon_{z,atm, turb}(i, l) \end{aligned} \quad (3.28)$$

where \mathbf{X} is a matrix of regressors, which are either functions of the coordinates \mathbf{s}_i or measurement of auxiliary variables at the same positions. $\beta(l)$ is the vector of unknown stratified APS parameters at time t_l and $\epsilon_{z,atm, turb}$ is the turbulent APS.

The parameter vector $\hat{\beta}(l)$ of the stratified APS model can be estimated given prior information on the distribution of displacement throughout the scene, which is easily inferred in the case of TRI monitoring of fast moving alpine glaciers: the area undergoing displacement is of limited spatial extent and often surrounded by features such as mountain flanks and rocks that are effectively immobile relative to the flow of the glacier—which can be in the order of meters per days in the case studied in this paper—

To estimate $\hat{\beta}$ a subset S of persistent scatterers (PS) from the P pixels in the interferogram is used; it is assumed that their phase at any time only consist of the stratified and turbulent APS contributions, with spatial covariance $\Sigma_{z,atm,s}^{PS}$. The best linear unbiased estimator of $\beta(l)$ is given by the GLS estimator [72–74]:

$$\hat{\beta}(l) = \left(\mathbf{X} \Sigma_{z,atm,s}^{PS} \mathbf{X}^T \right)^{-1} \mathbf{X}^T \Sigma_{z,atm,s}^{PS} \mathbf{z}(j, l). \quad (3.29)$$

where \mathbf{X} is the matrix of regressors at locations $\mathbf{s}_j, j \in \mathbf{S}$, $\mathbf{z}(j, l)$ the vector of PS phases and $\Sigma_{z,atm,s}^{PS}$ is the spatial covariance of the APS between the PS locations. Using $\hat{\beta}$ the stratified APS contribution at any pixel i in the interferogram can be predicted:

$$\hat{\epsilon}_{z,atm, strat}(i, l) = \mathbf{X}(i, l) \hat{\beta}(l). \quad (3.30)$$

However using (3.30) does not give predictions for the turbulent component of the APS, which is often the dominant source of phase variability in the interferograms. Due to the spatial correlation of the APS, it is reasonable to assume that the turbulent APS at a \mathbf{s}_i close to a PS observation $\mathbf{s}_j, j \in \mathbf{S}$ is similar to the residual (measured phase minus GLS prediction) of (3.29) at that PS:

$$\epsilon_{res}^{PS}(j, l) = z(j, l) - \mathbf{X}(j, l) \hat{\beta}(l). \quad (3.31)$$

The similarity should decrease with increasing distance from the PS as the spatial correlation drops. At time l , the turbulent APS at \mathbf{s}_i can be approximated as a weighted average of the GLS residuals ϵ_{res}^{PS} at the available PS $\mathbf{s}_j, j \in \mathbf{S}$,

$$\hat{\epsilon}_{z,atm, turb}(i, l) = \mathbf{w}(l) \epsilon_{res}^{PS}(l) \quad (3.32)$$

where \mathbf{w} is a weight vector which is a function of the distances between \mathbf{s}_i and $\mathbf{s}_j, j \in \mathbf{S}$. Under these conditions, the minimum variance, unbiased estimator for the turbulent APS is given by the Kriging equation [53, 72]:

$$\hat{\epsilon}_{z,atm,turb}(i, l) = \mathbf{v}^T \Sigma_{res}^{PS^{-1}} \epsilon_{res}^{PS} \quad (3.33)$$

where \mathbf{v} is the vector of spatial APS covariances between $z(i, l)$ and $z(j, l), j \in \mathbf{S}$ and Σ_{res}^{PS} is the covariance matrix of the regression residuals at the PS. The predictor of the combined deterministic and turbulent APS at any point \mathbf{s}_i is then the *regression Kriging* estimator:

$$\hat{\epsilon}_{z,atm,s}(i, l) = \mathbf{x}(i, l) \hat{\beta}(l) + \mathbf{v}^T \Sigma_{res}^{PS^{-1}} \epsilon_{res}^{PS} \quad (3.34)$$

A similar approach is presented in [75], where intrinsic random functions (IRF-k)[76] are used to predict the spatially correlated APS contribution from observations at a set of PS locations. This method is similar to regression Kriging [77, 78], with the difference that in the form presented in [75] external regressors cannot be employed [78].

In practice, to speedup the inversion of $\Sigma_{res}^{PS^{-1}}$, only the K closest PS to any prediction point \mathbf{s}_i are used, since the farther an observation is located to a reconstruction point, the smaller its weight will be. Furthermore, when the APS is extrapolated to the entire interferogram, the Kriging prediction is computed on a grid whose spacing is larger than the interferogram pixel spacing and the gaps are filled using a distance-weighted bilinear interpolator.

STRATIFIED APS MODEL

The choice of a model for the stratified APS component according to (3.30) deserves separate consideration. Homogeneity and isotropy of the atmospheric refraction index distribution are commonly assumed in the case of terrestrial interferometry, where the scene is often of limited size [42]. These assumptions predict an APS proportional to the range distance from the radar [23, 42–44, 47]. To account for spatial inhomogeneities in water vapor distribution, other authors propose polynomial models of higher order, usually restricted to second order [43].

In situations with large variations in terrain height, the assumption of homogeneous atmospheric refraction index is not suitable; in these cases atmospheric layering is modeled as a height dependent component added to the above homogeneous model [45–47].

An alternative approach is to use weather parameters [38, 39] to model variations of the atmospheric refraction index. However, given the large vertical extents expected when monitoring steep alpine glaciers, from which significant vertical temperature and water vapor gradients can be expected and which are not included in the models, and because no precise weather data is available, these models are not considered in this study. The models described in this section are summarized in Table 3.1. The selection of a stratified APS model best fitting the measurement data is made according to an automatic procedure:

The interferometric phases as the PS for a large set of interferograms are used to compute ordinary least squares fit for each interferogram and model. The relative performance of the models considered is

evaluated comparing the distribution of the Akaike Information Criterion (AIC)[80] and of R^2 for the models considered over the set of interferograms. It must be remembered that the model fit used in model comparison are obtained with ordinary least squares (OLS) rather than with the optimal minimum variance GLS estimator of (3.29). This approximate shortcut seems reasonable since the purpose of this analysis is comparison of the relative performance of several models.

SPATIAL COVARIANCE MODEL

Computing the regression-Kriging prediction according to (3.34) requires knowledge of \mathbf{v} , which is derived from covariance of the APS between any two points in space $\mathbf{s}_i, \mathbf{s}_j$. Theoretical considerations from turbulence theory [29, 32, 33, 49, 70, 81] and data derived from GNSS or spaceborne SAR observations [28, 31, 49] are often employed to derive APS spatial structure functions [82]—variograms, correlograms or periodograms—from which the covariance can be determined or approximated. Nonetheless, the validity of these covariance models in the TRI case is uncertain, given the small number of studies available, the large variability in acquisition setups and scene choice and also due to the fact that the imaging geometry specific to TRI is very different to the one in spaceborne InSAR studies. However, thanks to the assumption of spatio-temporal separability and isotropy, the spatial covariance function can be estimated from the data using a variogram estimator:

$$\gamma_s(d) = \frac{1}{2|N(d)|M_{PS}} \sum_{l=0}^{M_{PS}} \sum_{(i,j) \in N(d)} |z(j,l) - z(i,l)|^2 \quad (3.35)$$

where the sum index l runs over M_{PS} interferograms at different temporal baselines. For each interferogram each the mean square phase difference between all PS with spatial separation d , given by the index set $N(d)$ is computed.

Since z is the interferometric phase difference at a fixed location, the empirical spatial variogram estimator corresponds to the mean squared *double phase difference*—single difference in time and double difference in space—over the set of all interferograms.

To reduce the estimation bias caused by the stratified component of the APS in z [83] the variogram γ_s is estimated using on OLS estimation residuals of the stratified model [72]. From this empirical spatial variogram γ_s , a variogram model is fitted using a nonlinear fitting procedure; the variogram model is used to obtain an approximation $\hat{\mathbf{v}}$ of the covariance between observations and test points, which can be used for the Kriging predictor. If a bounded spatial variogram model $\gamma_{s,m}$ can be fit to the empirical variogram estimate, the value of the spatial covariance function at any spatial lag is computed with [74]:

$$C_s(d) = \gamma_{s,m}(\infty) - \gamma_{s,m}(d). \quad (3.36)$$

Where $\gamma_{s,m}(\infty)$ is the variogram sill, the value that the variogram attains at infinite spatial separation between samples, which corresponds to the phase variance of the interferograms.

If spatial statistics of the APS are estimated from the data, it is advisable to strive for a spatially homogeneous distribution of PS, such that a homogenous distribution of lags d between PS locations is achieved, ensuring a reliable estimate of the spatial variogram. The imaging geometry particular to TRI

should also be considered; both in real aperture systems and in SAR system using an antenna assembly on a rail. In these cases, the images are acquired on a regularly spaced polar grid (r, θ) . For this type of sampling, care must be taken when variograms are estimated; the spatial lag d must be determined using the distance formula for polar coordinates. A simpler approach is to first geocode the data using a digital elevation model, and then to compute variograms in 3D Cartesian coordinates, where the true distance between points can be computed. This is especially important in scenes with large variations in elevation, because distances in the slant-range azimuth grid could substantially differ from the true distances between points. This difference can hinder fair comparisons of empirical variograms with theoretical structure functions derived from turbulence theory.

3.2.3 Temporal Inversion

TEMPORAL COVARIANCE MODEL

Even after removing the APS estimate from the interferogram vector, considerable phase variability in time is observed in the residual interferometric phases [84, 85]:

$$z_{res}(i, l) = z(i, l) - \hat{\epsilon}_{z,atm,s}(i, l) \quad (3.37)$$

where $\hat{\epsilon}_{z,atm,s}$ is the regression-Kriging prediction of the spatially correlated APS, whose estimation is detailed in subsection 3.2.2.

Caudff [84] reported residual phase variations after correcting the APS by interpolating the spatially low-pass filtered phase observations of stable areas, a method similar to the Kriging interpolation proposed in subsection 3.2.2 but which does not use the spatial covariance structure of the APS in the prediction. In that case, the residual phases were observed to correlate with variation in the solar radiation.

Similar observations were made by Butt in [75], where after interpolating the APS observed at a set of PS using Intrinsic Random Function Kriging (IRF-K), a significant residual phase error was observed, especially for areas with a low density of PS. This was explained through the short correlation length of the APS in space and its high temporal frequency.

Under the separable covariance model described in subsection 3.2.1, the residual APS in $z_{res}(i, l)$ is a realization of a Gaussian random process $\epsilon_{z,atm,t}$ with no spatial correlation and a temporal correlation matrix $\Sigma_{z,t}$, approximately the sum of a block diagonal matrix of APS and of a block diagonal or diagonal matrix of noise contributions due to temporal decorrelation, as described in (3.27):

$$\Sigma_{z,res} \approx \mathbf{I} \otimes \Sigma_{z,atm,t} + \Sigma_{z,decorr,t}. \quad (3.38)$$

This formulation is not exact because of the sparse distribution of the PS across the scene and the approximated covariance obtained from the variogram; a residual spatial correlation of the APS can be expected. The residual error will increase with increasing distance from the PS; however for the sake of simplicity this aspect has not been considered in this analysis.

If the noise in the corrected interferogram vector $\Sigma_{z,res}$ is assumed to be spatially uncorrelated, it is only necessary to consider the temporal correlation of APS and decorrelation in the solution of (3.5).

In this case, the temporal covariance structure is described a block-diagonal matrix $\Sigma_{z,res}$, the sum of the temporal APS covariance and of the decorrelation covariance (see (3.38)). Since $\Sigma_{z,res}$ is a block-diagonal matrix, i.e the noise in \mathbf{z}_{res} is not correlated across pixels, the problem of (3.5) can be solved separately for each of the P pixels since \mathbf{G} is a block-diagonal matrix of compatible size and shape, i.e the displacement model does not include spatial dependence across different locations.

The APS covariance $\Sigma_{z,atm,t}$ is estimated through $\Sigma_{y,atm,t}$ using an experimental temporal variogram, computed as the variance of the interferometric phases grouped by temporal baselines ΔT , as illustrated in Figure 3.1:

$$\gamma_t(\Delta T) = \frac{1}{2|N(\Delta T)|N_{PS}} \sum_{l=0}^{N_{PS}} \sum_{i \in N(\Delta T)} |z(l, i)|^2 \quad (3.39)$$

where $N(\Delta T)$ is the set of all interferograms with temporal baseline ΔT and z is the unwrapped interferometric phase. Thus the estimation of the temporal covariance of the APS requires to compute interferograms with all possible temporal baselines up to a reasonably long lag, even if only a subset of baseline can be effectively employed for the inversion. This requirement is not as stringent as it may seem, since only the interferometric phases at the PS are required, which can be computed efficiently.

Similarly, the decorrelation covariance $\Sigma_{z,decorr}$ can be derived from the SLC covariance matrix $\Sigma_{y,decorr}$ [86] and the incidence matrix \mathbf{A} . In this paper the approach suggested in [40] is used to generate covariance matrices for the decorrelation signal, assuming a Brownian decorrelation process:

- The interferometric coherence between two SLCs pixels $y(i, t_l)$ and $y(i, t_l + \Delta T)$ separated by a time ΔT is modeled with an exponential decay $\gamma(\Delta T) = \gamma_0 e^{-\Delta T/\tau}$. The observed coherence as a function of temporal baseline ΔT is computed by averaging interferograms with the same ΔT , giving $\hat{\gamma}(\Delta T)$. The parameters γ_0 and τ are estimated by minimizing $|\hat{\gamma}(\Delta T) - \gamma(\Delta T)|$ [67].
- The model parameters are used to generate the coherence matrix of the SLC vector, Γ . Then Γ is converted into the (incorrectly scaled) covariance matrix of the interferograms \mathbf{z} using \mathbf{A} . For a pixel i :

$$\Omega_{z,i} = \frac{1}{2} \mathbf{A} \Gamma_i \mathbf{A}^T. \quad (3.40)$$

- Finally, Ω_z is rescaled to a covariance matrix using the observed interferometric coherences and the expression for the interferometric phase standard deviation of (3.16). For the i -th pixel, the new matrix is:

$$\Sigma_{z,decorr,i} = \mathbf{D} \Omega_{z,i} \mathbf{D} \quad (3.41)$$

where \mathbf{D} is a diagonal matrix with the j -th entry corresponding to $\frac{\text{Var}[z_{j,i}]}{\Omega_{z,ij}}$.

To improve the robustness of the estimated decorrelation covariance matrix and to reduce computational load, γ_0 and τ are binned in 30 classes and an average covariance matrix for each class is used in the inversion instead of computing a single value for each pixel.

PIXEL-WISE GLS INVERSION

Thanks to the spatial correction of the APS described in subsection 3.2.2 the problem can be solved for each pixel individually using \mathbf{z}_{res} instead of \mathbf{z} to yield the estimate $\hat{\mathbf{p}}$ for all times $t_l, l = 1 \dots M$ at each

location \mathbf{s}_i :

$$\hat{\mathbf{p}}(i) = \left(\mathbf{G}^T \Sigma_{z,res}(i)^{-1} \mathbf{G} \right)^{-1} \Sigma_{z,t}(i)^{-1} \mathbf{G} \mathbf{z}_{res}. \quad (3.42)$$

where $\Sigma_{z,res}(i)$ indicates the i -th block of \mathbf{z}_{res} corresponding to the i -th pixel.

The feasibility and robustness of the inversion described by (3.42) are heavily influenced by the interplay of the available interferograms, controlled \mathbf{A} and by the employed displacement model, chosen by \mathbf{p} through the design of \mathbf{M} . In selecting \mathbf{A} for high repeat rate observations of fast-moving terrain, one must balance between computational and storage costs associated with computing and unwrapping all the possible interferometric pairs and the unreliable phase information provided by interferograms with large temporal baselines, that are prone to low coherence and phase wrapping. A conservative choice is to combine only consecutive SLC images (known as *interferogram chain*) so that the master of the l -th interferogram appears as the slave of the $l + 1$ -th interferogram. In this configuration, $N - 1$ unique interferograms are produced [21, 24, 87, 88]. An interferogram chain is convenient in combination with a model assuming a constant velocity for each pixel, i.e $\mathbf{p} = \mathbf{v}$ with \mathbf{v} a $P \times 1$ vector. In that case, phase contributions that appear only once in a master SLC and in a slave SLC cancel each other in the GLS solution, leaving only the contributions from interferograms at the beginning and end of the stack [66]. However, assuming a single velocity for the entire time-series negates the purpose of high repeat-rate TRI monitoring, variations in displacement velocity are lost. On the other hand, an interferogram chain is not advisable in combination with a model aiming at estimating the full history of N velocities for each pixel, i.e $\mathbf{M} = \mathbf{I}_{PN,PN}$ with \mathbf{v} a PN -vector. This formulation likely results in unreliable estimates, as a just one noise interferometric phase observation is available for each degree of freedom in the model.

Redundancy in the form of a simpler displacement model and of more interferometric pairs can improve estimation robustness. Optimally, all possible measurements, here $\frac{N(N-1)}{2}$ interferometric pairs, should be used; this permits to obtain maximum likelihood estimates for $(N - 1)$ unwrapped phases [67, 86, 89] as if they were computed from a single master acquisition. These ML-estimate can then be converted into a displacement history with $N - 1$ times relative to one "virtual" master. This method is technically not feasible in the case presented in this work, because the number of interferograms to compute and store would be too large due to the quantity of available images; additionally decorrelation and the fast flow of the glacier would make most of the constructed interferograms too noisy and very challenging to unwrap. With a wavelength of $17 \cdot 10^{-3}$ m and assuming a maximum velocity of $2 \frac{\text{m}}{\text{day}}$ in the fastest parts of the glacier, phase wraps in the interferometric phase can be expected for SLC pairs with a temporal separation of approximately 6 min. Since the data is acquired with a repeat rate of 150s, this would permit to form wrap-free interferograms between the l -th and the $l + 1$ -th and $l + 2$ -th SLC at the most. However, such large displacement velocities are not expected to be routinely observed; therefore a maximum temporal baseline of 500s seconds has been used. This choice should not result in displacement-induced phase wraps except for the most severe surges in glacier velocity. A displacement model forcing a constant velocity for a duration t_s longer than the SLC repeat rate is used, such that the interferograms can be divided into *stacks* where the velocity for each pixel is assumed constant.

In this case, \mathbf{M} is:

$$\mathbf{M} = \mathbf{I}_P \otimes \begin{bmatrix} \left[\begin{array}{cccc} 1 & 0 & \dots & 0 \end{array} \right]_{\times N_s} \\ \left[\begin{array}{cccc} 0 & 1 & \dots & 0 \end{array} \right]_{\times N_s} \\ \vdots \\ \left[\begin{array}{cccc} 0 & \dots & 0 & 1 \end{array} \right]_{\times N_s} \end{bmatrix} \quad (3.43)$$

where N_s is the number of (equally spaced) interferograms in each stack. The GLS solution obtained with this model is a modified form of interferogram stacking [31, 33, 90], where a constant velocity for each pixel is assumed for the entire duration covered by the interferograms. In the modified model N_s velocities are estimated, using the parameter to control the balance between reliable estimates and temporal resolution. In this study $N_s = 16$ was empirically selected, corresponding to about 30 minutes.

Name	Trend	Comments	References
Unprocessed	$\phi = \beta_0$	No atmospheric trend is modeled; included for performance comparison.	-
Linear	$\phi = \beta_0 + \beta_1 r$	Assumes homogeneous, isotropic atmospheric refraction index. This model is applicable with little topography and small height extents, where no stratification is expected.	[42–44]
Quadratic Range	$\phi = \beta_0 + \beta_1 r + \beta_2 r^2$	Models inhomogeneities of refraction index as a linear trend in range.	[23, 43]
Height dependent I	$\phi = \beta_0 + \beta_1 r + \beta_2 r h$	Assumes an horizontally isotropic and homogeneous troposphere with vertical layers [79], resulting in an exponential dependence of refraction index with height, which is approximated to the first order..	[45, 46]
Height dependent II	$\phi = \beta_0 + \beta_1 r + \beta_2 h^2$	Similar assumptions as <i>Height Dependent I</i> , here the horizontal and vertical components of refraction are considered to be separable.	[47]
Quadratic 2D Range	$\phi = \beta_0 + \beta_1 r + \beta_2 \theta + \beta_3 \theta r + \beta_4 r^2 + \beta_5 \theta^2$	Includes a lateral component to model inhomogeneity of the atmospheric conditions due to the wide field of view of the real aperture radar imaging geometry. This model is purely empirical.	
Quadratic 2D Height	$\phi = \beta_0 + \beta_1 h + \beta_2 \theta + \beta_3 \theta r + \beta_4 h^2 + \beta_5 \theta^2$	Analogous to "Quadratic 2D Range" but replacing the r with the h .	

Table 3.1: Summary of stratified APS models employed in terrestrial radar interferometry.

3.3 DATA

3.3.1 Device: KAPRI

The data used in this work was acquired with KAPRI [91, 92] (Ku Band Advanced Polarimetric Radar Interferometer), a fully polarimetric version of GPRI-II [93]; a Ku-Band portable terrestrial radar interferometer. Using a 2 m long slotted waveguide array, an angular resolution of 0.385° is achieved, corresponding to a ground cross-range resolution of 7 m at a distance of 1 km. Range resolution is based on the dechirp-on-receive frequency modulated continuous wave (FMCW) architecture [94]. With a bandwidth of 200 MHz, a nominal distance resolution of 0.75 m is achieved. However, since a windowing filter is used to suppress processing sidelobes in the DFT-based range compression, the effective range resolution is slightly larger at about 0.9 m.

3.3.2 Bisgletscher 2015 Campaign

A series of KAPRI data spanning the period between July to late August 2015 was acquired from the Domhütte mountain hut, at an altitude of 2940 m, looking at the Bisgletscher on the opposite side of the valley (see Figure 3.3), covering a range of distances between 4000 and 8000 m. At these distances, GPRI data have a cross-range resolution between 30 m and 60 m and a range resolution of approximately 0.9 m. A SLC image was acquired every 150 s; the repeat time is chosen to minimize temporal decorrelation and to avoid phase wrapping due to the rapid motion of the glaciers surface, estimated using time-lapse camera to be as large as $2 \frac{\text{m}}{\text{day}}$.

The dataset does not uniformly cover the duration of the measurement campaign due to a combination of technical and logistical limitations:

1. The radar installation used the Domhüttes electrical power supply, consisting of solar panels supplemented by a small hydroelectric plant. During times of high activity at the hut and of decreased water flow to the hydro plant, the radar had to be disconnected from the supply. A buffer battery permitted acquisition for approximately 6 hours during these cut-offs. Despite these measures, the alternative supply was not sufficient to ensure continuous operation during periods of longer power cut-offs.
2. Nearly 200 GB of SLC data was produced every day. To provide data download and control the radar was connected to a Wi-Fi link provided by the PermaSense/X-Sense project [95]. However, this link is designed to connect a low-power sensor network, which is expected to produce a much lower daily data volume, downloading the entire radar data over this link was not possible. Therefore, the SLC images were stored locally on a network attached storage (NAS) system connected to the radar via an Ethernet connection. This proved insufficient because only an $100 \frac{\text{MB}}{\text{s}}$ Ethernet cable was available locally; therefore the maximum daily data amount that could be transferred from the radars own storage to the NAS was still smaller than the predicted daily amount. To avoid running out of storage space on the computer controlling the radar, acquisitions were only carried out for 12 hours a day, while the remaining time was dedicated to copying the data to the NAS system.

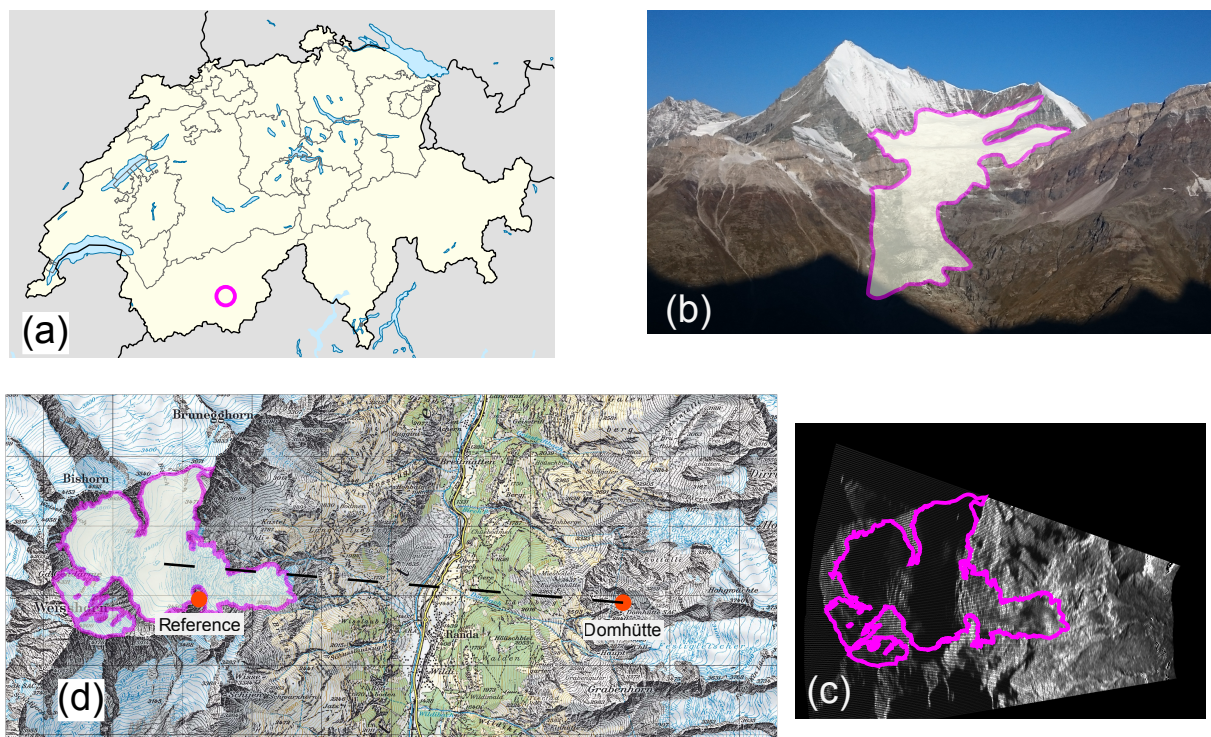


Figure 3.3: Overview of the area under study. (a) Approximate location of the Bisgletscher in the Canton of Valais, Switzerland. (b) Image of the Bisgletscher as seen from the radar point of view at Domütte, with glacier outline drawn in purple. (c) Geocoded average backscatter power map geocoded in Swiss map coordinates. (d) Locations of radar, glacier and reference location for interferogram referencing, overlaid on 1 : 50000 scale topographic map. Geodata © swisstopo

From the acquired data, a subset of data is sampled for the analysis of the APS: 10 timestamps are chosen randomly from the set of all acquisition timestamps. For each of these timestamps, all the SLC closer than one hour are extracted and used for the subsequent analysis. The random sampling is used to guarantee that different atmospheric conditions are represented in the study: they are presumably influenced by the weather and the time of the day.

3.3.3 Data Processing

The acquired SLCs were coregistered to a common master acquisition by amplitude cross correlation, to minimize loss of coherence. Interferograms are formed by complex multiplication, followed by 5×2 multilooking. A larger multilooking factor is used in range in order to minimize the loss of azimuth resolution, which by virtue of the acquisition geometry increases linearly with slant range distance. The interferograms were unwrapped using the minimum cost flow unwrapping algorithm and referenced to a reference point corresponding to a stable rock face close to the glacier, as visible in Figure 3.3.

The persistent scatterers used to derive spatial and temporal statistics were detected using the intensity mean to standard deviation ratio [50] on an SLC stack of 50 acquisitions and by removing the PS found in areas known to be moving. The initial list of candidate PS was reduced to an approximately homoge-

neous spatial PS density using the method described by [96], using the interferometric coherence with respect to the first SLC in the stack as a quality measure.

The processing chain is automated using the Nextflow [97] dataflow engine, that allows a reproducible analysis of the time-series.

3.4 RESULTS

3.4.1 Spatial Correction of APS

STRATIFIED APS MODEL

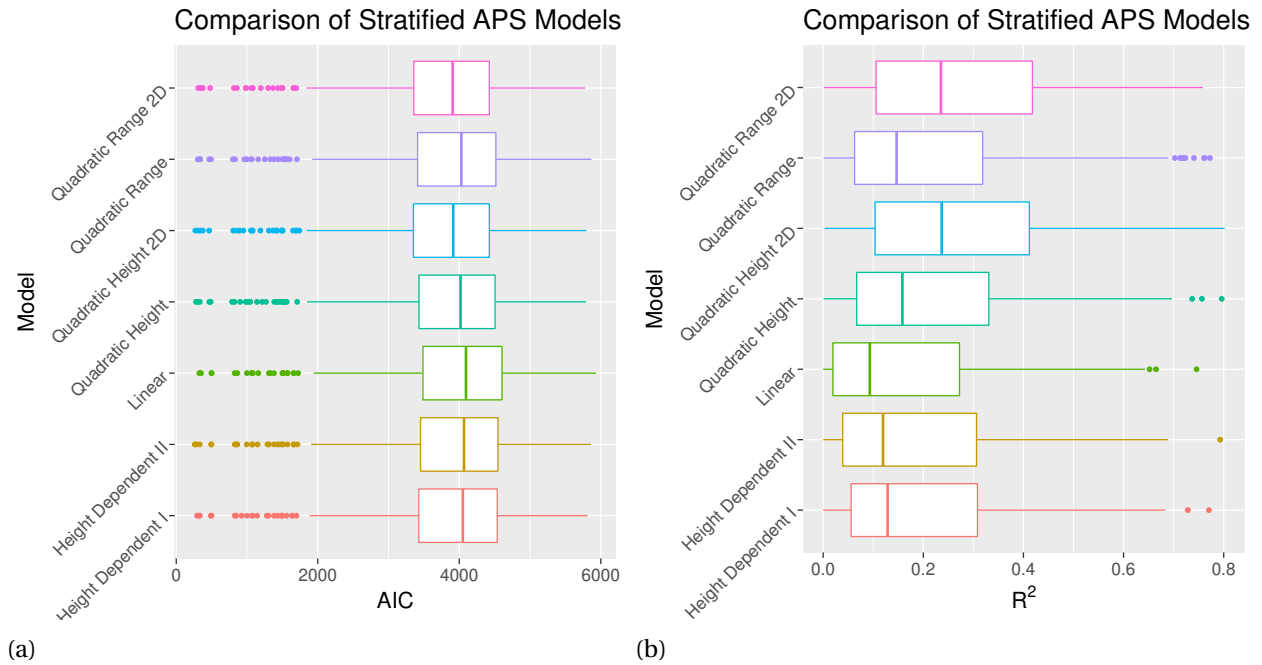


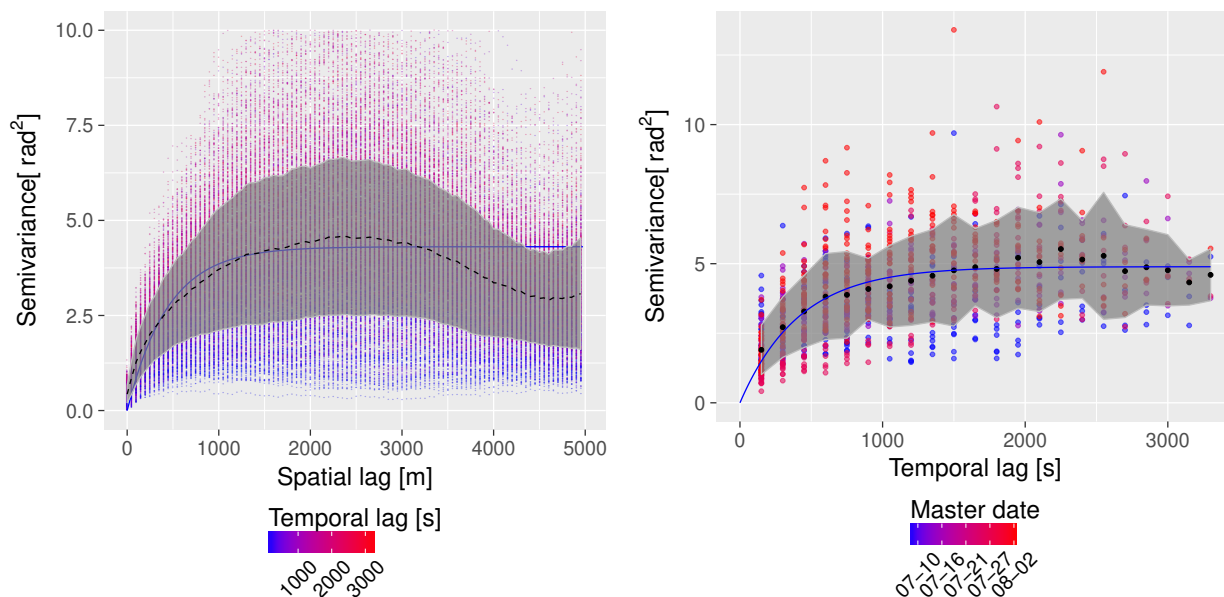
Figure 3.4: a Boxplot of the of the Akaike Information Criterion (AIC) values for a selection of models described in Table 3.1. To produce this figure, 400 interferograms were considered. Each of the models discussed was applied to every interferogram, the AIC statistic was computed. The AIC is plotted as a color-coded histogram, the model whose AIC is lower is the one whose performance is best relative to the other models it is compared with. b Boxplot of the R^2 values for the models listed in Table 3.1. The plot is obtained with the same procedure as a.

As discussed in subsection 3.2.2, the phase contribution of the atmospheric phase screen in the interferograms is modeled as the sum of a deterministic delay predicted by an atmospheric stratification model and a turbulent atmospheric delay contribution, modeled as a Gaussian random variable.

In order to select the best performing linear model for the stratified APS phase $\epsilon_{z,atm,strat}$, a statistical model comparison on a large number of interferograms is made. For each interferogram l at time t_l in the network, an ordinary least squares (OLS) estimate for $\beta(t_l)$ is computed for every linear model to be compared among those described in Table 3.1. The model fit parameters $\beta(t_l)$ alongside summary statistics, such as the sum of residuals, the R^2 value and the Akaike Information Criterion (AIC)[80] are stored for each model run. The results of the numerical evaluation are displayed in Figure 3.4a as

a boxplot of AIC values divided by model; each model is assigned a different color in the bar plot. A statistical summary of R^2 values is shown in Figure 3.4b using a similar visualization.

COVARIANCE MODEL FOR TURBULENT APS



(a) Spatial marginal variogram. Each dot corresponds to the empirical spatial variogram for one PS interferogram, its color indicates the temporal baseline of that interferogram. The black line is the mean variogram, surrounded by a gray ribbon showing the standard deviation of the individual variograms, while the blue line shows the fitted exponential variogram used to compute the Kriging predictions.

(b) Empirical temporal variogram, computed as the phase variance of PS interferograms with increasing temporal baselines. The color of the dots encodes the master date of the master SLC used in computing that interferogram, the black dots show the mean variogram over the set of all interferograms and the gray ribbon its standard deviation. The blue line shows an exponential variogram model fit, which is used to generate temporal covariance matrices used in the inversion.

Figure 3.5: Spatial and temporal marginal variograms derived from 1535 PS interferograms computed from 100 SLC acquisitions. All possible interferogram up to a maximum temporal baseline of 120 minutes were computed and unwrapped.

The spatial correction of the APS contribution is performed by predicting the unobserved APS at the locations of interest \mathbf{s} according to the regression-Kriging equation (3.34). The estimated APS is then subtracted from the interferogram as in (3.37). The prediction at a point \mathbf{s}_i requires the spatial covariance of the APS between this point and the PS used as observations. As the true APS covariance is not known, it is replaced with a covariance model derived from an experimental variogram, as illustrated by (3.36). The variogram is computed by averaging individual spatial variograms obtained from a number of interferograms, according to (3.35). These interferograms are generated using 100 SLC acquisitions, from which all PS interferograms with a maximum temporal baseline of 120 minutes are formed.

The spatial variograms obtained from each interferogram are plotted as dots in Figure 3.5a, their color encodes the temporal baseline. Assuming the validity of the separable covariance, there should be no variation in spatial covariance between interferograms; this is tested empirically by plotting the standard deviation of the spatial variograms across realizations, shown in Figure 3.5a as the gray ribbon around the averaged variogram, plotted as a dashed black line. An exponential variogram model, shown

as a blue line, is fitted to the average.

REGRESSION-KRIGING

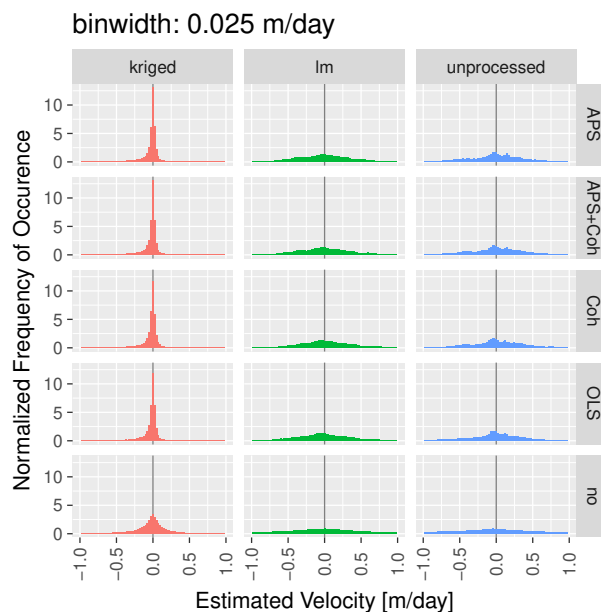


Figure 3.6: Histogram of estimated velocities at non-moving location for different combinations of APS correction and time-series inversion methods.

Each column corresponds to a spatial APS correction method: *kriged* is obtained using regression-Kriging, *lm* using the stratified APS only while in the column *unprocessed* no spatial APS correction is applied. Across rows, different temporal covariance models are used for the GLS time series inversion. In *APS* only the temporal covariance of the APS is considered, in *Coh* only the covariance of the temporal decorrelation process, while *APS + Coh* uses both. In *OLS* no covariance model is used, while in *No* the interferometric phases are converted in velocities.

The performance of the regression-Kriging spatial APS estimation is assessed by cross validation. A second set of PS located on stable areas around the glacier, independent of those used to compute the RK prediction was detected. The phases of each interferogram and the residual phase after removal of the APS estimates at these points were extracted, converted into velocities and stored.

The results of cross validation as displayed as histograms in the *no* row of Figure 3.6, where they are compared with uncorrected interferometric phases at the same locations, shown in the column *unprocessed* and with interferometric phases corrected by subtracting the stratified APS contribution in the column labeled *LM*.

The interferometric phases observed outside of the glacier should correspond to the APS only, because on rocks no displacement is expected at the time scales of the interferograms. Therefore, the distribution of the estimated velocities of stable targets can be used as a proxy for the APS correction quality.

3.4.2 Temporal Inversion

As explained in subsection 3.2.3, it is assumed that the APS correction using regression-Kriging removes the spatial correlation of pixels; only the temporal correlation of pixels along the stack, attributed to the

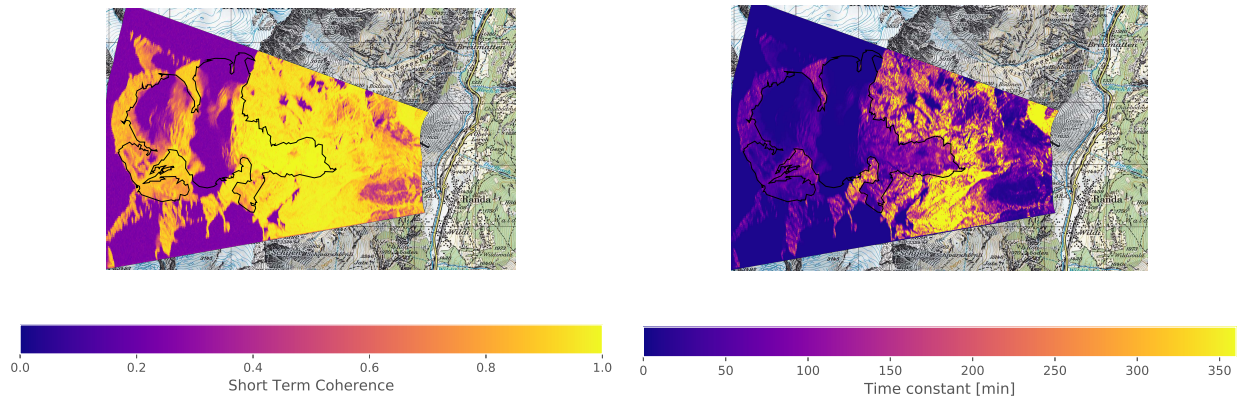
residual APS, described by $\Sigma_{z,atm,t}$, and the decorrelation, described by $\Sigma_{z,decorr}$, must be considered in the GLS inversion, which can be now performed pixel by pixel.

TEMPORAL COVARIANCE MODEL

The Brownian coherence decay model parameters τ and γ_0 were computed using a subset of the interferograms. These estimates are useful to quantify the rapidity of the decorrelation process and are used to construct the covariance matrix $\Sigma_{z,decorr}$ as described in subsection 3.2.3.

The estimates of γ_0 and τ are plotted as geocoded maps overlaid on a topographic map in Figure 3.7. The second component of the temporal covariance is the covariance of the APS; assuming spatio-temporal separability of the APS statistics $\Sigma_{y,atm,t}$ is estimated from a temporal variogram using a set of PS interferograms with increasing temporal baselines. Using this method, the variogram at lag t corresponds to the phase variance computed for all interferogram with temporal baseline t , as illustrated in Figure 3.1.

The resulting temporal variogram is plotted in Figure 3.5b along with a fitted exponential variogram model.



(a) Estimated short term coherence γ_0 .

(b) Estimated time constant τ in minutes.

Figure 3.7: Estimated short term coherence γ_0 (3.7a) and time constant τ (3.7b) parameters for the exponential coherence decay model $\gamma(\Delta t) = \gamma_0 e^{-\frac{\Delta t}{\tau}}$. The data was obtained by fitting an exponential model on average coherence maps binned by temporal baseline. The outline of Bisgletscher is shown as a black polygon.

PIXEL-WISE GLS INVERSION

The pixel-wise GLS inversion performance is tested by the same cross-validation procedure described in subsection 3.4.1. The phases at the same set of points described above are extracted, converted in displacement velocities and plotted in Figure 3.6, in the row named *OLS*, *Coh*, *APS+Coh*, *APS* that represent four inversion approaches using different temporal covariance matrices:

- OLS: Ordinary least squares inversion, the temporal covariance matrix is set to the identity matrix.
- Coh: GLS inversion, temporal covariance only includes the Brownian decorrelation model.
- APS: GLS inversion, temporal covariance only includes APS.

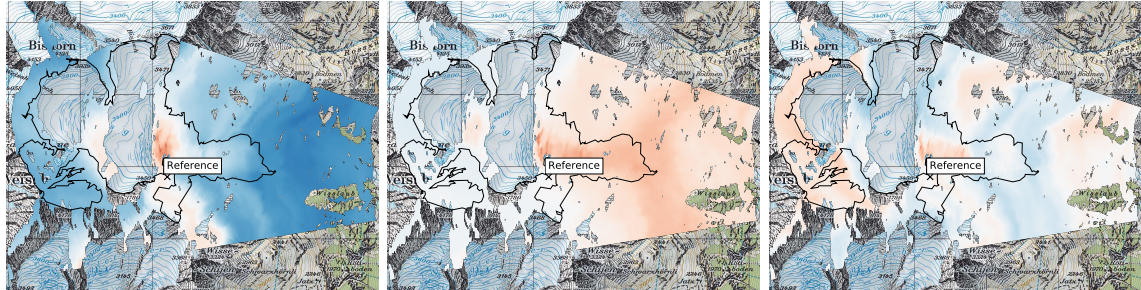
- APS+Coh: GLS inversion, temporal covariance according to (3.38).

The same plots are repeated across three columns (*Kriged*, *LM*, *unprocessed*), showing the combined effect of different spatial APS removal techniques and temporal covariance models.

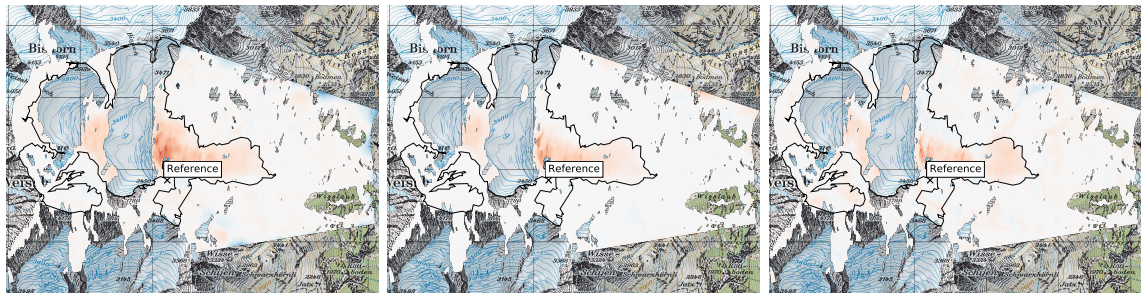
The average velocity at the non-moving location is expected to be close to zero with a small variance, as they are derived from the interferometric phases of parts of the scene that do not displace significantly at the timescales of the interferograms. A larger variance indicates a larger uncorrected APS contribution or a higher level of decorrelation, causing more phase noise.

A visual representation of the estimated velocity maps is shown in Figure 3.8 for a small selection of times. Three maps obtained without spatial APS correction and using a pixel-wise OLS inversion are displayed in Figure 3.8a. The same maps obtained with regression-Kriging and a OLS inversion are shown in Figure 3.8b. Finally, in Figure 3.8c regression-Kriging is combined with GLS using a temporal covariance considering both APS and decorrelation.

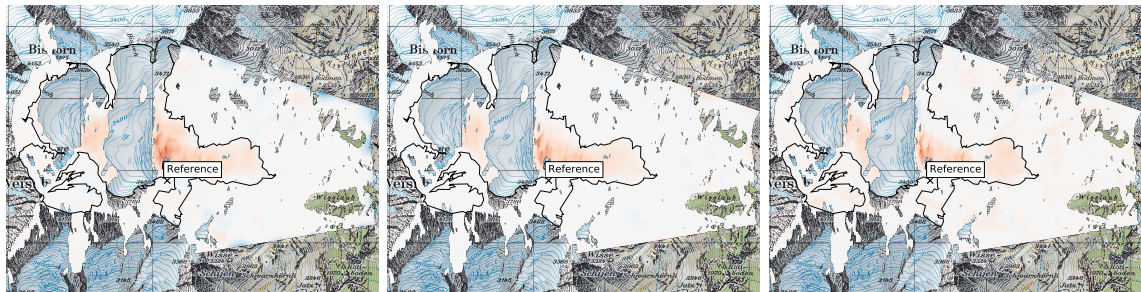
To inspect the spatial distribution of APS correction quality, standard deviation maps of the velocity estimates were produced for all combinations of spatial APS correction and inversion approached described above. These maps were prepared by computing the standard deviation of the velocity vector at every pixel and projecting the result in map coordinates. They are shown in Figure 3.9.



(a) No Spatial APS correction and OLS inversion.



(b) Spatial APS correction using regression-Kriging and OLS inversion.



(c) Spatial APS correction using regression-Kriging and GLS inversion with full covariance model.

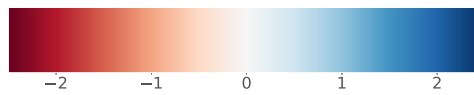
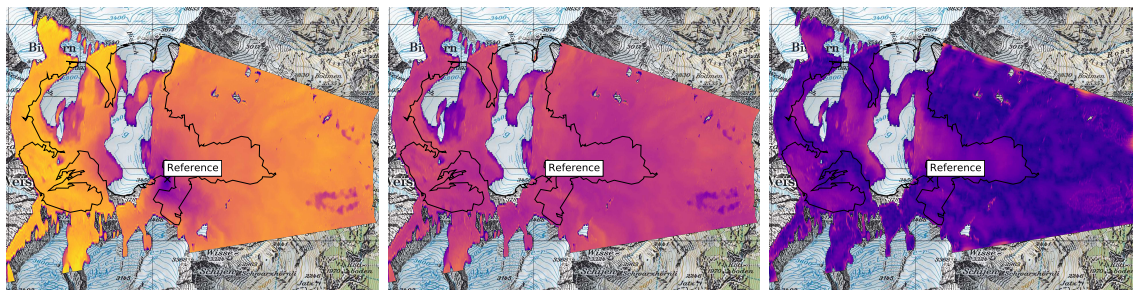
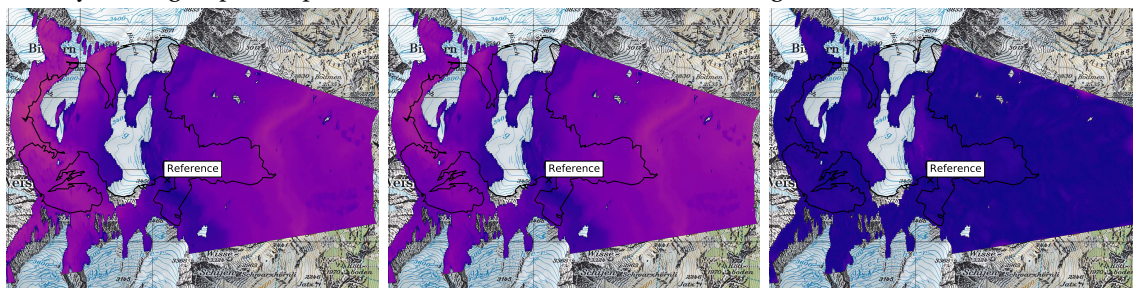
Line of Sight Velocity [m/day]

Figure 3.8: time-series of estimated velocity maps for a subset of times. From left to right: July 14 2:33 CEST , July 26 16:32 CEST and August 2 11:36 CEST. (a) no spatial APS correction and OLS solution for the velocity. (b) spatial APS correction using regression-Kriging combined with OLS inversion. (c) spatial APS correction using regression-Kriging and velocity inversion with full covariance model (APS and decorrelation). The outline of Bisgletscher is shown in black.



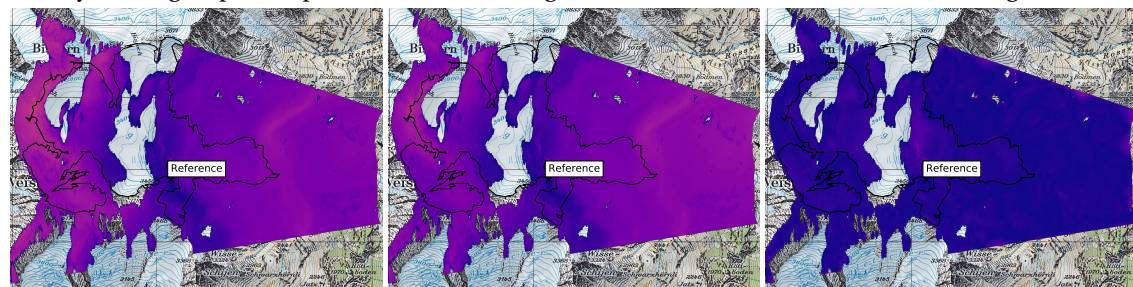
(a) No Spatial APS correction. (b) Spatial APS correction with stratified model. (c) Spatial APS correction using regression-Kriging.

The velocity in this group of maps was estimated from individual interferograms.



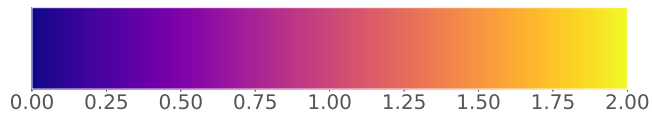
(d) (e) (f)

The velocity in this group of maps was estimated using OLS inversion on the corrected interferograms.



(g) (h) (i)

The velocity in this group of maps was estimated with GLS inversion and a temporal covariance model considering APS and decorrelation.



Standard deviation of the estimates LOS velocity [m/day]

Figure 3.9: Standard deviation maps of velocity estimates for different combinations of APS correction and velocity inversion methods. From left to right: no correction, stratified APS model, regression-Kriging. From top to bottom: velocities estimated from single interferograms, OLS inversion, GLS inversion with the *APS+Coh* covariance model.

3.5 DISCUSSION

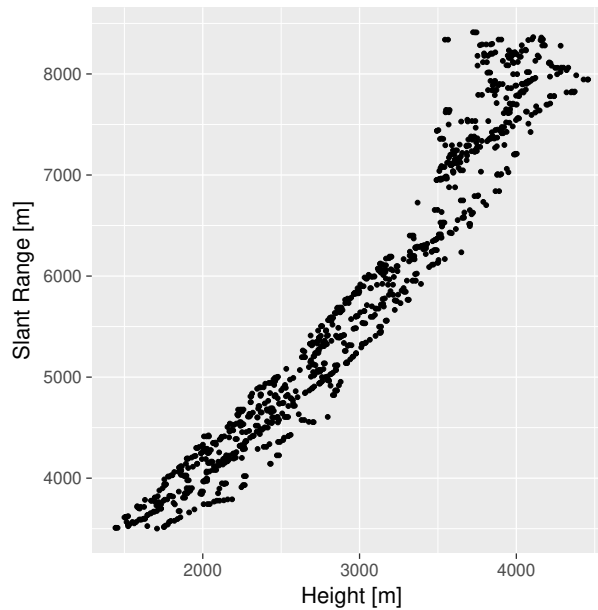


Figure 3.10: Scatterplot illustrating the correlation between the slant range (r) and height (h) used as regressors for several models of atmospheric stratification listed in Table 3.1.

3.5.1 Spatial Correction of APS

STRATIFIED APS MODEL

The stratified APS contribution is predicted by a linear model; however it was difficult to decide *a priori* which of the models listed in Table 3.1 would be the most suitable for the situation analyzed in this work. A statistical comparison of models on a group of interferograms was run, as described in subsection 3.4.1. Figure 3.4a displays a statistical summary of the Akaike Information Criterion (AIC) values, while Figure 3.4b shows a similar summary of R^2 values.

The AIC values are only meaningful in the relative sense: among the investigated model, the one with the lowest AIC will have the best fit quality, in the maximum likelihood sense [80]. As shown by the boxplots of 3.4a, all models have a very similar distribution of the AIC values over the interferograms considered for the analysis, with the "Quadratic Height 2D" model showing the best AIC and the higher R^2 in Figure 3.4b. It appears that the very similar distributions of the AIC statistics across models could be due to multicollinearity between the slant range distance and height variables in the linear regression, which is explained by the observation geometry shown in Figure 3.3: an increase in distance from the radar corresponds to an increasing average elevation. The presence of multicollinearity is verified empirically in Figure 3.10 by plotting r against h for the points used in the regression. The possibility of multicollinearity seems realistic considering the correlation of r and h . In this case, either regressor can be included in the stratified APS model but not both simultaneously; the 2D model including height and azimuth angle was chosen for regression-Kriging as it showed the highest R^2 in Figure 3.4b.

COVARIANCE MODEL FOR TURBULENT APS

In Figure 3.5a, the individual spatial variograms obtained from a number of PS interferograms are shown as dots colored by temporal baseline. Under the separable covariance model, increases in the temporal baseline can only scale or offset the spatial variogram but not modify its shape [98]. Thus, the average of individual spatial variograms is used to derive the spatial variogram model for the APS. Generally, all variograms seem to display a similar behavior with an initial increase at short spatial lags followed by a region of higher semivariance and larger variation in middle and then settling to a lower semivariance. Only a moderate variation in variogram shapes and few outliers are observed across the interferograms: these results suggest that the proposed separable covariance model is a sufficient approximation of the APS covariance.

The choice of an exponential variogram model appears appropriate, given the reasonably good fit of the model to the spatial variogram.

REGRESSION-KRIGING

The performance of APS prediction and removal using regression-Kriging is evaluated in Figure 3.6 in the row named *no* by plotting the histogram of velocity estimates obtained from corrected interferogram pixels on stable areas, as described in subsection 3.2.2. A reduction in phase variance is visible in comparison to the unprocessed interferograms (column *unprocessed*) and to the interferograms corrected by only subtracting an estimate of the stratified APS (column *lm*). The latter result is consistent with the poor performance of stratified APS model, as no mode was capable to explain the phase variance of the APS, observed in the R^2 plot of Figure 3.4b. Thus, most of the observed phase variation it should likely be attributed to the turbulent APS.

An evaluation of the spatial distribution of the APS correction performance is made by computing the temporal standard deviation of the estimated velocities, shown in Figure 3.9, subplots 3.9a, 3.9b and 3.9c. If no spatial APS correction is applied (Figure 3.9a) and individual interferograms are inverted to estimate velocities, a very high variance in the entire the scene is observed, with a minimum in the vicinity of the reference point. This is because referencing the phase results in some APS mitigation by virtue of the spatial correlation of the APS. If a linear model of stratification is used to correct the APS before estimating velocities from single interferograms, the overall variance is reduced, as it can be appreciated in Figure 3.9b; however areas of high standard deviation are still observed. Finally, if regression-Kriging is used, the standard deviation is much lower overall, however an area of high variance is still observed in proximity of the glacier. A part of this variance is likely due to variations in glacier's surface speed over the course of time, while the remaining variation is probably the inherent regression-Kriging prediction variance, which increases with increasing distance between observations and reconstruction locations. In the case of the glacier the average distance between pixels on the glacier surface and the nearest PS is larger than in the rest of the scene. A similar pattern is seen in theoretical variance maps produced by the regression-Kriging procedure.

3.5.2 Temporal Inversion

TEMPORAL COVARIANCE MODEL

The temporally correlated noise in the interferogram phase vector is modeled as the sum of a residual APS plus the phase noise due to decorrelation. The latter is described with a Brownian motion model, attributed to random motion of many scatterers in each resolution cell, resulting in an exponential decay of the interferometric coherence γ .

The estimated exponential decay parameters are displayed in Figure 3.7; a very wide spread of the decorrelation time constant τ is noticeable in Figure 3.7b, probably due to the variety of surfaces types, from rocks to forests and glaciated areas.

The main area of interest is the surface of the glacier, outlined by the polygon, where a time constant between 5 min and 2 hr is observed. This signifies usable phase information up to temporal baselines of approximately 1 hour for the slower decorrelating areas, assuming a minimum coherence threshold of 0.6. However, given the high probability of displacements producing phase wraps, it is generally not advisable to include interferograms with such long temporal baselines in the inversion.

On the other hand, the spatial variability in the short-term coherence γ_0 , which roughly corresponds to the mean coherence at the shortest temporal baseline of 150s, is lower (see Figure 3.7a). Areas that show a low short-term coherence correspond chiefly to vegetation and regions of low backscatter intensity, while the estimate over the glaciers tongue displays high coherence, suggesting the suitability of the chosen repeat time of 150s for this study. The other component of the temporal covariance matrix is represented by the temporally correlated contribution of the APS, which is estimated by an empirical variogram, as discussed in subsection 3.2.3. The experimental variogram is displayed in Figure 3.5b together with an exponential variogram model fit; it appears that the semivariance rapidly increases and settles after about 500 seconds. This result suggests that the APS is not significantly correlated in time at the timescales of the acquisition rate of 2.5 min. Specific experiments—for example by observing a single location at high repeat rate—would be necessary to determine the decorrelation time of the APS.

PIXEL-WISE GLS INVERSION

When both components of the temporal covariance matrix are estimated, the inversion for the estimated velocity is performed according to (3.42). An assessment of inversion quality is made with the same cross-validation method employed to evaluate spatial APS removal, shown in Figure 3.6.

All temporal inversion approaches result in a lower variance of residual velocities for stable areas compared to the inversion of the velocity performed on individual interferograms. The differences in performance among various temporal covariance models appear not to be significant, with both cases considering either the decorrelation or the APS only showing a very similar residual distribution as the OLS inversion. A possible reason could be the poor fit of the Brownian coherence decay model to the PS that were used for cross-validation. It seems reasonable that these pixels correspond to persistent scatterers and not collections of randomly moving scatterers, that are usually considered the source of exponential coherence loss. Similarly, including the APS covariance model seems not to significantly reduce the estimation variance; this could be due to the short temporal range, as observed in Figure 3.5b: after 500s the semivariance already attains a value very close to the sill, implying that the APS between

temporally close acquisitions is not significantly correlated: to notice significant correlation a closer temporal sampling would be required. Thus, in this case including the temporal APS covariance model in the pixel-wise inversion does not significantly change the estimation performance and the covariance model could be reduced to the one used for spaceborne InSAR [40], where the APS is assumed uncorrelated in time.

An analysis of the general pattern of the estimated 2D velocity fields can be made considering the plots in Figure 3.8. In Figure 3.8a the velocity maps were generated directly from uncorrected interferograms, by converting the phases into daily displacement velocities. While these maps seem to capture the main spatial patterns of motion, with the highest velocities observed at the glacier tongue and near the upper and lower icefalls, a significant overestimation of displacements on areas located outside of the glacier, which should not appreciably move during the timespan covered by the acquisitions, is observed. This overestimation is presumably caused by the uncompensated APS and can lead to misinterpretations of the velocity maps. A reduction of apparent velocity outside of the glacier area (shown in black) is observed in Figure 3.8c, obtained by estimating and removing the APS using regression Kriging and then applying the pixel-wise GLS inversion with the *APS+Coherence* covariance model.

The spatial distribution of correction and estimation quality is shown in Figure 3.9 in the second and third row, where the temporal standard deviation of velocity estimates for several combinations of APS correction and covariance models used for the GLS inversion is shown. As already seen in the velocity histograms in Figure 3.6, there seems to be very little difference in estimation variance between the solution obtained combining regression-Kriging and an OLS inversion (3.9f) and the GLS solution considering the temporal correlation due to the APS and to the decorrelation signal (3.9i). This result is to be expected given the short correlation time of the APS, as observed by the means of the temporal variogram in Figure 3.5b.

3.6 CONCLUSIONS

This paper is a study of the atmospheric phase screens (APS) in Ku-Band terrestrial radar interferometry. The APS is one of the most important factor affecting the precision of displacement estimates in radar interferometry. While for spaceborne SAR interferometry a vast literature of approaches for APS modeling and mitigation is available, only few studies are dedicated to the APS in terrestrial radar interferometry.

This study contributes to close this research gap by addressing several aspects of the modeling and correction of APS for terrestrial radar interferometry. To do so, this paper proposes an expansion of the traditional APS model tailored to TRI. The former model—a combination of a stratified atmospheric contribution and of a temporally uncorrelated, spatially correlated stochastic term describing turbulence—is modified by allowing the APS to be correlated in time to account for the short revisit times. To reduce its complexity, the covariance structure of the turbulent component is assumed to be stationary in space and time and separable. Under this assumption, covariance model parameters are fitted by performing marginal spatial and temporal variogram analysis on a large set of interferograms acquired at different times.

This framework is the foundation of a method for APS correction based on an interferogram stack, from which a set of persistent scatterers (PS) known not to undergo displacement is first determined. The interferometric phase observations at these PS — assumed to contain solely an APS contribution— are used to extrapolate the APS to a regular grid covering the interferograms using regression-Kriging, which accounts for both a model of atmospheric stratification and for the spatial correlation of the atmospheric turbulence. Since separable spatio-temporal statistics are assumed, the interpolation is performed using a single covariance function for the entire stack. By this method, a phase calibrated stack is obtained, where the residual nuisances, namely unmodeled APS and decorrelation are assumed to be spatially uncorrelated. In this manner, a pixel-wise generalized least squares estimator using the temporal covariance model can be applied to the phase-calibrated stack to estimate displacement rates, reducing the computational load since spatial correlations are assumed to be removed by the Kriging-based APS phase calibration step.

The proposed approach is tested using a Ku-Band radar dataset over the Bisgletscher glacier, southwestern Swiss Alps. Regression analysis using a set of persistent scatterers (PS) located on stable areas shows that stratification models have a poor ability to explain a significant portion of the phase variance caused by the APS, highlighting the importance of statistical description of the turbulent APS. Variogram analysis suggest that a separable spatio-temporal covariance model is a sufficient approximation for the case considered in the study and that the APS only shows a weak correlation in time. The spatial covariance function derived from this analysis is used for the regression-Kriging APS phase calibration, whose performance is evaluated by estimating the residual velocities at locations known not to be affected by displacements. This analysis shows a significant reduction in phase variance after the regression-Kriging based phase calibration. The same performance analysis is repeated with the output of the time-series inversion applied on the stack of calibrated interferograms. The results show an additional reduction in residual phase variance, at the cost of a coarser temporal resolution caused by the choice of a simplified displacement model.

REFERENCES

- [1] S. Baffelli, O. Frey, and I. Hajnsek, “Geostatistical analysis and mitigation of atmospheric phase screens in Ku-band terrestrial radar interferometric observations of an alpine glacier”, *IEEE Transactions on Geoscience and Remote Sensing*, 2018, submission ID TGRS-2018-01579.
- [2] A. Pralong and M. Funk, “On the instability of avalanching glaciers”, *Journal of Glaciology*, vol. 52, pp. 31–48, 2006. DOI: 10.3189/172756506781828980.
- [3] J. Faillettaz, M. Funk, and C. Vincent, “Avalanching glacier instabilities: Review on processes and early warning perspectives”, *Reviews of Geophysics*, vol. 53, pp. 203–224, 2015. DOI: 10.1002/2014rg000466.
- [4] A. Flotron, “Movement studies on a hanging glacier in relation with an ice avalanche”, *Journal of Glaciology*, vol. 19, pp. 671–672, 1977. DOI: 10.1017/s0022143000029592.

-
- [5] J. Faillettaz, A. Pralong, M. Funk, and N. Deichmann, "Evidence of log-periodic oscillations and increasing icequake activity during the breaking-off of large ice masses", en, *Journal of Glaciology*, vol. 54, pp. 725–737, 2008. DOI: 10.3189/002214308786570845.
- [6] H. Röthlisberger, "Sliding phenomena in a steep section of Balmhorngletscher, Switzerland", *Journal of Geophysical Research*, vol. 92, p. 8999, 1987. DOI: 10.1029/jb092ib09p08999.
- [7] P. D. Canassy, J. Faillettaz, F. Walter, and M. Huss, "Seismic activity and surface motion of a steep temperate glacier: A study on Triftgletscher, Switzerland", *Journal of Glaciology*, vol. 58, pp. 513–528, 2012. DOI: 10.3189/2012JOG11J104.
- [8] G. Luzi, M. Pieraccini, D. Mecatti, L. Noferini, G. Macaluso, A. Tamburini, and C. Atzeni, "Monitoring of an alpine glacier by means of ground-based SAR interferometry", *IEEE Geoscience and Remote Sensing Letters*, vol. 4, pp. 495–499, 2007. DOI: 10.1109/lgrs.2007.898282.
- [9] A. Kääb, R. Wessels, W. Haeberli, C. Huggel, J. S. Kargel, and S. J. S. Khalsa, "Rapid ASTER imaging facilitates timely assessment of glacier hazards and disasters", *Eos, Transactions American Geophysical Union*, vol. 84, p. 117, 2003. DOI: 10.1029/2003EO130001.
- [10] A. Kääb, C. Huggel, L. Fischer, S. Guex, F. Paul, I. Roer, N. Salzmann, S. Schlaefli, K. Schmutz, D. Schneider, T. Strozzi, and Y. Weidmann, "Remote sensing of glacier- and permafrost-related hazards in high mountains: An overview", *Natural Hazards and Earth System Sciences*, vol. 5, pp. 527–554, 2005. DOI: 10.5194/nhess-5-527-2005.
- [11] E. Berthier, H. Vadon, D. Baratoux, Y. Arnaud, C. Vincent, K. Feigl, F. Rémy, and B. Legrésy, "Surface motion of mountain glaciers derived from satellite optical imagery", *Remote Sensing of Environment*, vol. 95, pp. 14–28, 2005. DOI: 10.1016/j.rse.2004.11.005.
- [12] A. Kääb, "Monitoring high-mountain terrain deformation from repeated air- and spaceborne optical data: Examples using digital aerial imagery and ASTER data", *ISPRS Journal of Photogrammetry and Remote Sensing*, vol. 57, pp. 39–52, 2002. DOI: 10.1016/S0924-2716(02)00114-4.
- [13] T. A. Scambos, M. J. Dutkiewicz, J. C. Wilson, and R. A. Bindshadler, "Application of image cross-correlation to the measurement of glacier velocity using satellite image data", *Remote Sensing of Environment*, vol. 42, pp. 177–186, 1992. DOI: 10.1016/0034-4257(92)90101-o.
- [14] R. M. Goldstein, H. Engelhardt, B. Kamb, and R. M. Frolich, "Satellite radar interferometry for monitoring ice sheet motion: Application to an Antarctic ice stream.", *Science*, vol. 262, pp. 1525–1530, 1993. DOI: 10.1126/science.262.5139.1525.
- [15] A. Gray, N. Short, K. Mattar, and K. Jezek, "Velocities and flux of the Filchner ice shelf and its tributaries determined from speckle tracking interferometry", *Canadian Journal of Remote Sensing*, vol. 27, pp. 193–206, 2001. DOI: 10.1080/07038992.2001.10854936.
- [16] T. Strozzi, A. Luckman, T. Murray, U. Wegmüller, and C. Werner, "Glacier motion estimation using SAR offset-tracking procedures", *IEEE Transactions on Geoscience and Remote Sensing*, vol. 40, pp. 2384–2391, 2002. DOI: 10.1109/TGRS.2002.805079.

- [17] I. Joughin, R. Kwok, and M. Fahnestock, “Estimation of ice-sheet motion using satellite radar interferometry: Method and error analysis with application to Humboldt Glacier, Greenland”, *Journal of Glaciology*, vol. 42, pp. 564–575, 1996. DOI: 10.1017/S0022143000003543.
- [18] B. T. Rabus and D. R. Fatland, “Comparison of SAR-interferometric and surveyed velocities on a mountain glacier: Black Rapids Glacier, Alaska, U.S.A.”, *Journal of Glaciology*, vol. 46, pp. 119–128, 2000. DOI: 10.3189/172756500781833214.
- [19] R. Michel and E. Rignot, “Flow of Glaciar Moreno, Argentina, from repeat-pass Shuttle Imaging Radar images: Comparison of the phase correlation method with radar interferometry”, *Journal of Glaciology*, vol. 45, pp. 93–100, 1999. DOI: 10.1017/S0022143000003075.
- [20] K. E. Allstadt, D. E. Shean, A. Campbell, M. Fahnestock, and S. D. Malone, “Observations of seasonal and diurnal glacier velocities at Mount Rainier, Washington, using terrestrial radar interferometry”, *Cryosphere*, vol. 9, pp. 2219–2235, 2015. DOI: 10.5194/tc-9-2219-2015.
- [21] D. Voytenko, T. H. Dixon, I. M. Howat, N. Gourmelen, C. Lembke, C. L. Werner, S. D. L. Peña, and B. Oddsson, “Multi-year observations of Breiðamerkurjökull, a marine-terminating glacier in southeastern Iceland, using terrestrial radar interferometry”, *Journal of Glaciology*, vol. 61, pp. 42–54, 2015. DOI: 10.3189/2015JOG14J099.
- [22] T. H. Dixon, D. Voytenko, C. Lembke, S. de la Peña, I. Howat, N. Gourmelen, C. Werner, and B. Oddsson, “Emerging technology monitors ice-sea interface at outlet glaciers”, *Eos*, vol. 93, pp. 497–498, 2012. DOI: 10.1029/2012EO480001.
- [23] L. Noferini, D. Mecatti, G. Macaluso, M. Pieraccini, and C. Atzeni, “Monitoring of Belvedere Glacier using a wide angle GB-SAR interferometer”, *Journal of Applied Geophysics*, vol. 68, pp. 289–293, 2009. DOI: 10.1016/j.jappgeo.2009.02.004.
- [24] D. Mecatti, L. Noferini, G. Macaluso, M. Pieraccini, G. Luzi, C. Atzeni, and A. Tamburini, “Remote sensing of glacier by ground-based radar interferometry”, in *Proceedings of the IEEE International Geoscience and Remote Sensing Symposium*, IEEE, 2007, pp. 4501–4504. DOI: 10.1109/IGARSS.2007.4423856.
- [25] D. Massonnet and K. L. Feigl, “Radar interferometry and its application to changes in the Earth’s surface”, *Reviews of Geophysics*, vol. 36, pp. 441–500, 1998. DOI: 10.1029/97rg03139.
- [26] M. Bevis, S. Businger, T. A. Herring, C. Rocken, R. A. Anthes, and R. H. Ware, “GPS meteorology: Remote sensing of atmospheric water vapor using the global positioning system”, *Journal of Geophysical Research*, vol. 97, p. 15 787, 1992. DOI: 10.1029/92JD01517.
- [27] R. F. Hanssen, “Atmospheric heterogeneities in ERS tandem SAR interferometry”, Delft University, Tech. Rep., 1998.
- [28] R. N. Treuhaft and G. E. Lanyi, “The effect of the dynamic wet troposphere on radio interferometric measurements”, *Radio Science*, vol. 22, pp. 251–265, 1987. DOI: 10.1029/RS022i002p00251.
- [29] R. F. Hanssen, *Radar Interferometry*, ser. Remote Sensing and Digital Image Processing. Springer Netherlands, 2001, vol. 2, pp. 46–53. DOI: 10.1007/0-306-47633-9.

-
- [30] J. Jung, D. jin Kim, and S.-E. Park, "Correction of atmospheric phase screen in time series InSAR using WRF model for monitoring volcanic activities", *IEEE Transactions on Geoscience and Remote Sensing*, vol. 52, pp. 2678–2689, 2014. DOI: 10.1109/TGRS.2013.2264532.
- [31] T. R. Emardson, M. Simons, and F. H. Webb, "Neutral atmospheric delay in interferometric synthetic aperture radar applications: Statistical description and mitigation", *Journal of Geophysical Research: Solid Earth*, vol. 108, p. 2231, 2003. DOI: 10.1029/2002jb001781.
- [32] F. Onn and H. A. Zebker, "Correction for interferometric synthetic aperture radar atmospheric phase artifacts using time series of zenith wet delay observations from a GPS network", *Journal of Geophysical Research: Solid Earth*, vol. 111, pp. 1–16, 2006. DOI: 10.1029/2005JB004012.
- [33] S. Williams, Y. Bock, and P. Fang, "Integrated satellite interferometry: Tropospheric noise, GPS estimates and implications for interferometric synthetic aperture radar products", *Journal of Geophysical Research: Solid Earth*, vol. 103, pp. 27 051–27 067, 1998. DOI: 10.1029/98JB02794.
- [34] P. Basili, S. Bonafoni, V. Mattioli, P. Ciotti, and N. Pierdicca, "Mapping the atmospheric water vapor by integrating microwave radiometer and GPS measurements", *IEEE Transactions on Geoscience and Remote Sensing*, vol. 42, pp. 1657–1665, 2004. DOI: 10.1109/tgrs.2004.830943.
- [35] Z. Li, J.-P. Muller, P. Cross, P. Albert, J. Fischer, and R. Bennartz, "Assessment of the potential of MERIS near-infrared water vapour products to correct ASAR interferometric measurements", *International Journal of Remote Sensing*, vol. 27, pp. 349–365, 2006. DOI: 10.1080/01431160500307342.
- [36] Z. W. Li, W. B. Xu, G. C. Feng, J. Hu, C. C. Wang, X. L. Ding, and J. J. Zhu, "Correcting atmospheric effects on InSAR with MERIS water vapour data and elevation-dependent interpolation model", *Geophysical Journal International*, vol. 189, pp. 898–910, 2012. DOI: 10.1111/j.1365-246x.2012.05432.x.
- [37] Z. Li, E. J. Fielding, P. Cross, and R. Preusker, "Advanced InSAR atmospheric correction: MERIS/MODIS combination and stacked water vapour models", *International Journal of Remote Sensing*, vol. 30, pp. 3343–3363, 2009. DOI: 10.1080/01431160802562172.
- [38] L. Iannini and A. Monti Guarnieri, "Atmospheric phase screen in ground-based radar: Statistics and compensation", *IEEE Geoscience and Remote Sensing Letters*, vol. 8, pp. 537–541, 2011. DOI: 10.1109/LGRS.2010.2090647.
- [39] A. M. Guarnieri, L. Iannini, and D. Giudici, "On the exploitation of meteo information for atmospheric phase screen compensation in GB-SAR interferometry", in *ESA Living Planet Symposium*, 2010.
- [40] P. S. Agram and M. Simons, "A noise model for InSAR time series", *Journal of Geophysical Research : Solid Earth*, pp. 1–20, 2015. DOI: 10.1002/2014JB011271.1.
- [41] R. Jolivet, P. S. Agram, N. Y. Lin, M. Simons, M.-P. Doin, G. Peltzer, and Z. Li, "Improving InSAR geodesy using global atmospheric models", *Journal of Geophysical Research: Solid Earth*, vol. 119, pp. 2324–2341, 2014. DOI: 10.1002/2013JB010588.

- [42] L. Pipia, X. Fabregas, A. Aguasca, and C. Lopez-Martinez, “Atmospheric artifact compensation in ground-based DInSAR applications”, *IEEE Geoscience and Remote Sensing Letters*, vol. 5, pp. 88–92, 2008. DOI: 10.1109/LGRS.2007.908364.
- [43] L. Noferini, M. Pieraccini, D. Mecatti, G. Luzi, C. Atzeni, A. Tamburini, and M. Broccolato, “Permanent scatterers analysis for atmospheric correction in ground-based SAR interferometry”, *IEEE Transactions on Geoscience and Remote Sensing*, vol. 43, pp. 1459–1471, 2005. DOI: 10.1109/tgrs.2005.848707.
- [44] G. Luzi, M. Pieraccini, D. Mecatti, L. Noferini, G. Guidi, F. Moia, and C. Atzeni, “Ground-based radar interferometry for landslides monitoring: Atmospheric and instrumental decorrelation sources on experimental data”, *IEEE Transactions on Geoscience and Remote Sensing*, vol. 42, pp. 2454–2466, 2004. DOI: 10.1109/TGRS.2004.836792.
- [45] R. Iglesias, X. Fabregas, A. Aguasca, J. J. Mallorqui, C. Lopez-Martinez, J. A. Gili, and J. Corominas, “Atmospheric phase screen compensation in ground-based SAR with a multiple-regression model over mountainous regions”, *IEEE Transactions on Geoscience and Remote Sensing*, vol. 52, pp. 2436–2449, 2014. DOI: 10.1109/TGRS.2013.2261077.
- [46] R. Iglesias, A. Aguasca, X. Fabregas, J. J. Mallorqui, D. Monells, C. Lopez-Martinez, and L. Pipia, “Ground-based polarimetric SAR interferometry for the monitoring of terrain displacement phenomena—part I: Theoretical description”, *IEEE Journal of Selected Topics in Applied Earth Observations and Remote Sensing*, vol. 8, pp. 1–1, 2014. DOI: 10.1109/JSTARS.2014.2360040.
- [47] N. Dematteis, G. Luzi, D. Giordan, F. Zucca, and P. Allasia, “Monitoring alpine glacier surface deformations with GB-SAR”, *Remote Sensing Letters*, vol. 8, pp. 947–956, 2017. DOI: 10.1080/2150704X.2017.1335905.
- [48] P. Webley, G. Wadge, and I. James, “Determining radio wave delay by non-hydrostatic atmospheric modelling of water vapour over mountains”, *Physics and Chemistry of the Earth, Parts A/B/C*, vol. 29, pp. 139–148, 2004. DOI: 10.1016/j.pce.2004.01.013.
- [49] J. M. Boncori and J. Mohr, “Statistical description of tropospheric delay for InSAR: Overview and a new model”, in *2007 IEEE International Geoscience and Remote Sensing Symposium*, IEEE, 2007, pp. 4483–4486. DOI: 10.1109/IGARSS.2007.4423851.
- [50] A. Ferretti, C. Prati, and F. Rocca, “Permanent scatterers in SAR interferometry”, *IEEE Transactions on Geoscience and Remote Sensing*, vol. 39, pp. 8–20, 2001. DOI: 10.1109/36.898661.
- [51] C. Werner, U. Wegmüller, T. Strozzi, and A. Wiesmann, “Interferometric point target analysis for deformation mapping”, in *Proceeding of the IEEE International Geoscience and Remote Sensing Symposium*, vol. 7, IEEE, 2003, pp. 4362–4364. DOI: 10.1109/IGARSS.2003.1295516.
- [52] M. Crosetto, O. Monserrat, M. Cuevas-González, N. Devanthéry, and B. Crippa, “Persistent scatterer interferometry: A review”, *ISPRS Journal of Photogrammetry and Remote Sensing*, vol. 115, pp. 78–89, 2016. DOI: 10.1016/j.isprsjprs.2015.10.011.

-
- [53] D. G. Krige, "A statistical approach to some basic mine valuation problems on the Witwatersrand", *Journal of the Chemical, Metallurgical and Mining Society of South Africa*, pp. 201–215, 1952. DOI: 10.2307/3006914.
- [54] A. Ferretti, C. Prati, and F. Rocca, "Nonlinear subsidence rate estimation using permanent scatterers in differential SAR interferometry", *IEEE Transactions on Geoscience and Remote Sensing*, vol. 38, pp. 2202–2212, 2000. DOI: 10.1109/36.868878.
- [55] A. Hooper, H. Zebker, P. Segall, and B. Kampes, "A new method for measuring deformation on volcanoes and other natural terrains using InSAR persistent scatterers", *Geophysical Research Letters*, vol. 31, 2004. DOI: 10.1029/2004gl021737.
- [56] D. Massonnet and T. Rabaute, "Radar interferometry: Limits and potential", *IEEE Transactions on Geoscience and Remote Sensing*, vol. 31, pp. 455–464, 1993. DOI: 10.1109/36.214922.
- [57] P. Rosen, S. Hensley, I. Joughin, F. Li, S. Madsen, E. Rodriguez, and R. Goldstein, "Synthetic aperture radar interferometry", *Proceedings of the IEEE*, vol. 88, pp. 333–382, 2000. DOI: 10.1109/5.838084.
- [58] P. Berardino, G. Fornaro, R. Lanari, and E. Sansosti, "A new algorithm for surface deformation monitoring based on small baseline differential SAR interferograms", *IEEE Transactions on Geoscience and Remote Sensing*, vol. 40, pp. 2375–2383, 2002. DOI: 10.1109/TGRS.2002.803792.
- [59] R. Lanari, F. Casu, M. Manzo, G. Zeni, P. Berardino, M. Manunta, and A. Pepe, "An overview of the small BAseline subset algorithm: A DInSAR technique for surface deformation analysis", in *Pure and Applied Geophysics*, vol. 164, Springer Nature, 2007, pp. 637–661. DOI: 10.1007/s00024-007-0192-9.
- [60] R. Snieder and J. Trampert, "Inverse problems in geophysics", in *Wavefield Inversion*, Springer Vienna, 1999, pp. 119–190. DOI: 10.1007/978-3-7091-2486-4_3.
- [61] A. Tarantola and B. Valette, "Inverse problems - quest for information", *Journal of Geophysics*, pp. 159–170, 1982.
- [62] B. M. Kampes, *Radar interferometry*. Springer Netherlands, 2006. DOI: 10.1007/978-1-4020-4723-7.
- [63] H. Zebker and J. Villasenor, "Decorrelation in interferometric radar echoes", *IEEE Transactions on Geoscience and Remote Sensing*, vol. 30, pp. 950–959, 1992. DOI: 10.1109/36.175330.
- [64] R. Touzi, A. Lopes, J. Bruniquel, and P. Vachon, "Coherence estimation for SAR imagery", *IEEE Transactions on Geoscience and Remote Sensing*, vol. 37, pp. 135–149, 1999. DOI: 10.1109/36.739146.
- [65] E. Rodriguez and J. Martin, "Theory and design of interferometric synthetic aperture radars", *IEEE Proceedings F Radar and Signal Processing*, vol. 139, p. 147, 1992. DOI: 10.1049/ip-f-2.1992.0018.
- [66] J. Biggs, T. Wright, Z. Lu, and B. Parsons, "Multi-interferogram method for measuring interseismic deformation: Denali fault, Alaska", *Geophysical Journal International*, vol. 170, pp. 1165–1179, 2007. DOI: 10.1111/j.1365-246X.2007.03415.x.

- [67] F. Rocca, “Modeling interferogram stacks”, *IEEE Transactions on Geoscience and Remote Sensing*, vol. 45, pp. 3289–3299, 2007. DOI: 10.1109/TGRS.2007.902286.
- [68] T. Gneiting, M. Genton, and P. Guttorp, “Geostatistical Space-Time Models, Stationarity, Separability, and Full Symmetry”, in *Statistical Methods for Spatio-Temporal Systems*, Chapman and Hall, 2006, pp. 151–175. DOI: 10.1201/9781420011050.ch4.
- [69] V. K. Gupta and E. Waymire, “On Taylor’s hypothesis and dissipation in rainfall”, *Journal of Geophysical Research*, vol. 92, p. 9657, 1987. DOI: 10.1029/JD092iD08p09657.
- [70] R. F. Hanssen, “High-resolution water vapor mapping from interferometric radar measurements”, *Science*, vol. 283, pp. 1297–1299, 1999. DOI: 10.1126/science.283.5406.1297.
- [71] M. G. Genton, “Separable approximations of space-time covariance matrices”, *Environmetrics*, vol. 18, pp. 681–695, 2007. DOI: 10.1002/env.854.
- [72] R. S. Bivand, E. J. Pebesma, and V. Gómez-Rubio, “Applied spatial data analysis with R”, in *Use R*, vol. 1, Springer New York, 2013, p. 378. DOI: 10.1007/978-0-387-78171-6.
- [73] W. H. Greene, “The generalized regression model and heteroscedasticity”, in *Econometric Analysis*, 7th ed. Pearson, 2010, ch. 9.
- [74] H. Wackernagel, *Multivariate Geostatistics*. Springer, 2003. DOI: 10.1007/978-3-662-05294-5.
- [75] J. Butt, A. Wieser, and S. Conzett, “Intrinsic random functions for mitigation of atmospheric effects in terrestrial radar interferometry”, *Proceedings of JISDM 2016 Vienna*, vol. 11, pp. 89–98, 2016. DOI: 10.1515/jag-2016-0042.
- [76] G. Matheron, *The Intrinsic Random Functions and Their Applications*, 1973. DOI: 10.2307/1425829.
- [77] K. G. van den Boogaart and A. Brenning, “Why universal Kriging is better than IRFk-Kriging : Estimation of variograms in the presence of trend”, *Journal of Earth System Science*, pp. 1–15, 2001.
- [78] R. Christensen, “The equivalence of predictions from universal Kriging and intrinsic random-function Kriging”, *Mathematical Geology*, vol. 22, pp. 655–664, 1990. DOI: 10.1007/BF00890514.
- [79] N. Blaunstein and C. Christodoulou, *Radio Propagation and Adaptive Antennas for Wireless Communication Links*, ser. Wiley Series in Microwave and Optical Engineering. John Wiley & Sons, Inc., 2006, vol. 8, ch. 6. DOI: 10.1002/0470069996.
- [80] H. Akaike, “A new look at the statistical model identification”, *IEEE Transactions on Automatic Control*, vol. 19, pp. 716–723, 1974. DOI: 10.1109/tac.1974.1100705.
- [81] H. A. Zebker, P. A. Rosen, and S. Hensley, “Atmospheric effects in interferometric synthetic aperture radar surface deformation and topographic maps”, *Journal of Geophysical Research: Solid Earth*, vol. 102, pp. 7547–7563, 1997. DOI: 10.1029/96JB03804.
- [82] P. Legendre and L. Legendre, “Spatial analysis”, in *Numerical ecology 2nd English Edition*, Elsevier, Ed. 1998, pp. 712–738.

-
- [83] N. Bliznyuk, R. J. Carroll, M. G. Genton, and Y. Wang, "Variogram estimation in the presence of trend", *Statistics and Its Interface*, vol. 5, pp. 159–168, 2012. DOI: 10.4310/SII.2012.v5.n2.a2.
- [84] R. Caduff, A. Kos, F. Schlunegger, B. W. McArdell, and A. Wiesmann, "Terrestrial radar interferometric measurement of hillslope deformation and atmospheric disturbances in the Illgraben debris-flow catchment, Switzerland", *IEEE Geoscience and Remote Sensing Letters*, vol. 11, pp. 434–438, 2014. DOI: 10.1109/lgrs.2013.2264564.
- [85] L. Kristensen, C. Rivolta, J. Dehls, and L. H. Blikra, "GB InSAR measurement at the Åknes rockslide, Norway", *Italian Journal of Engineering Geology and Environment*, vol. 2013, pp. 339–348, 2013. DOI: 10.4408/IJEGE.2013-06.B-32.
- [86] S. Tebaldini and A. Monti, "Methods and performances for multi-pass SAR interferometry", in *Geoscience and Remote Sensing New Achievements*, InTech, 2010, pp. 329–357. DOI: 10.5772/9112.
- [87] R. Caduff, F. Schlunegger, A. Kos, and A. Wiesmann, "A review of terrestrial radar interferometry for measuring surface change in the geosciences", *Earth Surface Processes and Landforms*, vol. 40, pp. 208–228, 2015. DOI: 10.1002/esp.3656.
- [88] P. Riesen, T. Strozzi, A. Bauder, A. Wiesmann, and M. Funk, "Short-term surface ice motion variations measured with a ground-based portable real aperture radar interferometer", *Journal of Glaciology*, vol. 57, pp. 53–60, 2011. DOI: 10.3189/002214311795306718.
- [89] S. Samiei-Esfahany, J. E. Martins, F. van Leijen, and R. F. Hanssen, "Phase estimation for distributed scatterers in InSAR stacks using integer least squares estimation", *IEEE Transactions on Geoscience and Remote Sensing*, vol. 54, pp. 5671–5687, 2016. DOI: 10.1109/tgrs.2016.2566604.
- [90] T. Strozzi, U. Wegmüller, C. Werner, and A. Wiesmann, "Measurement of slow uniform surface displacement with mm/year accuracy", in *Proceedings of the IEEE International Geoscience and Remote Sensing Symposium*, vol. 00, IEEE, 2000, pp. 4–6. DOI: 10.1109/igarss.2000.858368.
- [91] S. Baffelli, O. Frey, and I. Hajnsek, "System characterization and polarimetric calibration of the Ku-band advanced polarimetric interferometer", in *Proceedings of the European Conference on Synthetic Aperture Radar*, 2016, pp. 2–5.
- [92] S. Baffelli, O. Frey, C. Werner, and I. Hajnsek, "Polarimetric calibration of the Ku-band advanced polarimetric radar interferometer", *IEEE Transactions on Geoscience and Remote Sensing*, vol. 56, pp. 1–17, 2018. DOI: 10.1109/tgrs.2017.2778049.
- [93] C. L. Werner, A. Wiesmann, T. Strozzi, A. Kos, R. Caduff, and U. Wegmüller, "The GPRI multi-mode differential interferometric radar for ground-based observations", in *Proceedings of the European Conference on Synthetic Aperture Radar*, VDE, 2012, pp. 304–307.
- [94] A. Stove, "Linear FMCW radar techniques", *IEE Proceedings F Radar and Signal Processing*, vol. 139, p. 343, 1992. DOI: 10.1049/ip-f-2.1992.0048.
- [95] J. Beutel, B. Buchli, F. Ferrari, M. Keller, M. Zimmerling, and L. Thiele, "X-SENSE: Sensing in extreme environments", in *Design, Automation & Test in Europe*, IEEE, 2011, pp. 1–6. DOI: 10.1109/DATE.2011.5763236.

- [96] U. Wegmüller, O. Frey, and C. L. Werner, “Point density reduction in persistent scatterer interferometry”, in *Proceedings of the European Conference on Synthetic Aperture Radar*, 2012, pp. 673–676.
- [97] P. Di Tommaso, M. Chatzou, E. W. Floden, P. P. Barja, E. Palumbo, and C. Notredame, “Nextflow enables reproducible computational workflows”, *Nature Biotechnology*, vol. 35, pp. 316–319, 2017. DOI: 10.1038/nbt.3820.
- [98] D. Myers, “Estimating and modeling space-time variograms”, in *Proceedings of the joint meeting of The 6th International Symposium On Spatial Accuracy Assessment In Natural Resources and Environmental Sciences and The 15th Annual Conference of The International Environmetrics Society*, 2004.

4

POLARIMETRIC ANALYSIS OF NATURAL TERRAIN OBSERVED WITH A KU-BAND TERRESTRIAL RADAR

This chapter has been submitted for review to the peer-reviewed journal *IEEE Journal Of Selected Topics In Applied Remote Sensing* as:

S. Baffelli, O. Frey, and I. Hajnsek, "Polarimetric analysis of natural terrain observed with a Ku-band terrestrial radar", *IEEE Journal of Selected Topics in Applied Earth Observation and Remote Sensing*, 2018, submission ID JSTARS-2018-00992

Terrestrial Radar Interferometers (TRI) are complimentary to spaceborne SAR systems for deformation monitoring in natural terrain: they permit shorter revisit times and greater flexibility in acquisition mode and timing. The additional diversity offered by polarimetric data can also be beneficial for TRI observations because polarized waves are sensitive to the dielectric and geometrical properties of the scatterers; thus polarimetric data may permit to distinguish different scattering mechanisms in a resolution cell while at the same time estimating terrain displacements.

However, the polarimetric scattering signatures of natural surfaces at Ku-Band are not as well characterized as the ones at longer wavelengths, owing to relative rarity of full polarimetric systems operating in Ku-Band. The latter is frequently employed in TRI to obtain a fine azimuth resolution while limiting the physical size of the system.

This paper aims at assessing the potential of polarimetric measurements in Ku-Band TRI through an empirical study of polarimetric scattering signatures of natural surfaces using two datasets acquired over a glacier and in an agricultural scene.

The main finding of this analysis is that the Cloude-Pottier entropy is high for all land cover types; it is only observed to be less than 0.5 for very bright scatterers such as buildings and individual rocks. This behavior is explained through a combination of depolarizing scattering from natural surfaces and the effect of the wavelength to resolution cell size ratio, causing the presence of several different scatterers in a resolution cell.

4.1 INTRODUCTION

4.1.1 Motivation

Polarimetric modes are an interesting add-on to imaging radars: the sensitivity of polarized electromagnetic waves to the geometric and dielectric properties of the objects with which they interact permits distinguishing scattering mechanisms within a resolution cell, to characterize their scattering behavior and potentially to estimate environmental parameters. Example applications of polarimetric radar data are land cover classification [2, 3], the estimation of soil moisture and the reconstruction of snow and vegetation properties and structures [4–12].

While polarimetric data acquired from air- [13–16] and spaceborne sensors [17, 18] has been studied and employed in the last three decades [19], there exists only few polarimetric terrestrial radar interferometers [20–33].

Terrestrial radar interferometers are a mature technology which found applications in the monitoring of unstable slopes [34–39], glaciers [40–50], snow [51, 52] and subsidence in urban areas [25, 53, 54]. A thorough review of these systems and their application is presented in [35, 55]. Compared to air- and spaceborne SAR, these systems are relatively inexpensive and permit greater flexibility in the acquisition modality and schedule; they are very suitable for the monitoring of small, fast changes in difficult terrain.

Some polarimetric TRI systems are documented in the literature; RISKSAR [20–27] an X-Band full polarimetric SAR mounted on a motorized rail is the most exhaustive examples: the polarimetric data was employed to improve the spatial density of persistent scatterers in urban areas and to optimize the temporal phase stability of the selected pixels. A rail-based system operating in C-Band is presented in [28]; a polarimetric analysis of an urban scene acquired with it is shown in [31, 32]. In [29, 30] another system operating from L- to X-band is introduced, which is used in different configurations to produce polarimetric imagery and study the scattering behavior of trees and tree stands [11, 12], crops [56] and the effect of changes in soil moisture [57].

The polarimetric TRI cited above are operated between L- and X- band at wavelengths between 30 cm and 3 cm, the same wavelengths employed in the majority of air- and spaceborne polarimetric SAR systems. In contrast to these devices, KAPRI [58] —the real-aperture polarimetric TRI at the center of this paper— is designed for operations in Ku-Band, at a wavelength of 17 mm. The choice of a shorter wavelength is imposed by two aspects: Firstly, KAPRI is a real-aperture radar; this design requires a short wavelength to achieve a good azimuth resolution while keeping the antenna's size small enough for easy transportation and installation. Secondly, a short wavelength is beneficial for zero-baseline differential interferometry as it increases the sensitivity to deformation for short repeat-time observations.

However, since KAPRI uses a wavelength relatively unexplored in SAR polarimetry —both in the TRI and in the space- and airborne case—, an assessment of Ku-band polarimetry is necessary to understand the applicability of the common polarimetric scattering models and the method derived thereof to the acquisition scenarios — in terms of repeat time, geometry, resolutions and wavelength— encountered in Ku-Band polarimetric terrestrial radar interferometry.

4.1.2 Contributions of This Paper

This paper presents a polarimetric analysis of two datasets acquired with KAPRI, a Ku-Band terrestrial radar interferometer. One dataset covers the Bisgletscher glacier and the surrounding alpine terrain, in the southwestern Swiss Alps, while the other dataset covers urban and agricultural terrain near the city of Bern.

In both datasets a high Cloude-Pottier entropy parameter H and high crosspolar backscatter power are observed for the majority of the land cover types. Four different interpretations for these observations are proposed:

in the first hypothesis, the entropy is attributed to the presence of depolarizing scattering mechanisms. Likely physical mechanism for depolarization are found by relating the observed parameters with the terrain types using land cover classification data, aerial photographs and, in the case of one polarimetric time-series dataset, with temperature measurement from a nearby automatic weather station (AWS).

Other than physical scattering interactions, three alternative hypotheses for the high entropy are presented and tested. They are: 1. the effect of measurement noise, 2. target mixing caused by spatial averaging 3. mixing of the responses of several scatterers in the resolution cell.

The results of the analyses performed in this paper suggest that a combination of depolarizing scattering from natural surfaces together with the short wavelength and large resolution cell size are the likely cause of the observed entropy.

4.2 METHODS AND DATA

4.2.1 Radar: KAPRI

KAPRI (Ku-Band Advanced Polarimetric Radar Interferometer) [58] is a Ku-Band polarimetric real aperture radar developed on the base of the GPRI-II radar [59]. GPRI was originally designed as a terrestrial radar interferometer (TRI) for slope instability monitoring using differential interferometry. While the latter employs vertically polarized antennas, KAPRI was modified by the manufacturer by adding a group of horizontally polarized antennas and switching circuitry to acquire polarimetric datasets.

Before analyzing the polarimetric signatures of different terrain types, it is necessary to prepare the acquired raw data by accurately processing it into SLC (single-look complex) images and to apply polarimetric calibration to it, so that the estimated signatures match the true polarimetric response of the observed targets. To understand the processing and calibration principles employed for KAPRI data, it is instructive to first consider the main hardware characteristics of this device.

KAPRI operates at 17.2 GHz, corresponding to a wavelength of 0.17 m. Distance resolution is obtained using a 200 MHz chirp, processed with the deramp-on-receive FMCW architecture [60], giving a range resolution of 0.75 m. Resolution orthogonal to the line of sight is obtained by scanning a 2 m-long slotted waveguide antenna having a beamwidth of 0.385° with an azimuthal drive: this is shown schematically

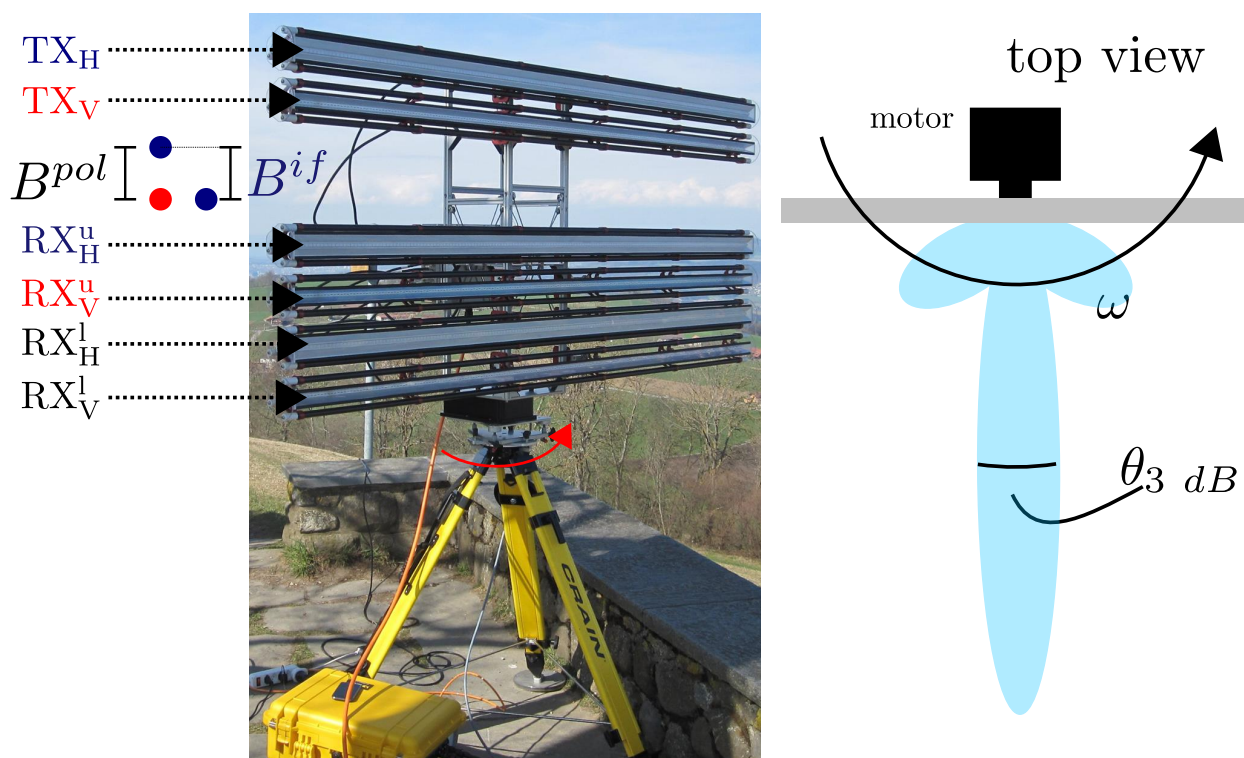


Figure 4.1: Typical full-polarimetric antenna arrangement for KAPRI. The upper two antennas are the transmitters in the vertical and horizontal polarizations. Two pairs of vertical and horizontal receiving units are installed on the bottom half of the tower assembly. The two blue dots represent the locations of the equivalent phase centers for the upper and lower HH channel, the red dot the phase center location for the VV channel. The tower assembly is rotated about its center with an angular velocity ω by the motor, producing two-dimensional images resolved by range using a frequency modulated chirp and by angle with the narrow fan beam having beamwidth θ_{3dB} .

in Figure 4.1. In this configuration images are acquired on a polar grid, with trapezoidal resolution cells whose cross-range size increases linearly with distance from the radar: the ground resolution in cross-range is 8 m at a distance of 1 km.

The hardware characteristics of KAPRI are summarized in Table 4.1.

4.2.2 KAPRI Data Preparation and Calibration

For a correct polarimetric analysis it is very important that radar data is processed and calibrated in order to be free of systematic biases. The methods employed for this purpose are described in detail in another publication [58]. The following paragraphs provide a short overview of the procedure for the benefit of the reader.

KAPRI is based on a dechirp-on-receive FMCW architecture, where the system transmits a chirped continuous wave signal; the backscatter signal received by the antenna is then mixed with the transmitted chirp, producing a modulated signal whose beat frequency is proportional to range. This beat signal is digitized and range profiles are reconstructed using a Fourier transform [58, 61]. To obtain two-dimensional images, a series of range profiles at different antenna azimuth angles are acquired, resolving the scatterers by their range and by their angle thanks to a narrow fan beam emitted by a slotted waveguide antenna, as illustrated in Figure 4.1. However, during the chirped the relative phasing

Parameter	Value
Modulation	FM-CW (250 μ s to 16 ms chirp duration)
Center frequency	17.2 GHz
Bandwidth	200 MHz
Range resolution	0.95 m 3 dB resolution –26 dB peak sidelobe ratio (PSLR)
Azimuth 3 dB beamwidth	0.385°
Elevation 3 dB beamwidth	35°
Polarization	fully polarimetric, selectable TX and RX polarization
Polarimetric Isolation	better than 30 dB
Residual copolar phase imbalance	less than 10°

Table 4.1: This table summarizes the most important hardware parameters of KAPRI.

of the radiation emitted at the antenna's slot change, causing an antenna mainlobe squint [62] leading to the degradation of range and azimuth resolution. To correct this effect, the raw data acquired in the chirp frequency-azimuth angle domain (often called fast time and slow time respectively) is processed with a frequency-azimuth interpolation to correct for the squint before the range Fourier transform, producing squint-free SLC (single look complex) data. After squint compensation and range compression the SLC data must be corrected with an azimuth matched filter to remove the azimuth phase ramp caused by the eccentric motion of the antenna's phase centers as the antenna are mounted offset from the motor's center of rotation. This correction is done according to the procedure detailed in a previous publication [58].

The four polarimetric SLC channels are coregistered by interpolation using the HH channel as a reference. Coregistration is necessary to correct the 0.18° antenna mainlobe pointing difference between the horizontally and the vertically polarized antennas. However, the pattern misalignment reduces the signal-to-noise ratio (SNR) for HV channel by 1.8 dB with respect to the SNR for the copolar channels because the transmit and receive patterns do not fully overlap.

KAPRI uses separate transmitting and receiving antennas for the H and the V polarizations to minimize polarimetric crosstalk. The antennas are installed vertically spaced on a metal truss attached to the azimuth drive, as shown in Figure 4.1. Because of the spatial separation of the equivalent polarimetric antenna phase centers —as shown by the diagram in Figure 4.1 where the equivalent phase center locations for the HH and VV for the upper receiver are displayed as blue and red dots respectively—the entries of scattering matrix \mathbf{S} acquired in this configurations will have a different absolute phase. Therefore, phase differences computed from channels whose phase centers are not at the same height will contain a phase contribution proportional to the terrain topography and to the baseline, that is the separation of the channels. A method to remove this contribution from a single look polarimetric covariance matrix \mathbf{C} was presented in [58]. The method was latter modified to operate on scattering matrices: the absolute topographic phase is estimated using two channels with the same polarization located at two ends of a baseline; then unwrapped, rescaled to the baseline between each channel's phase center and the reference phase center placed at the location of the top transmitting antenna and subtracted from the channel's phase.

After removal of the topographic phase, the polarimetric and radiometric calibration parameters deter-

mined using the dataset and procedure described in a previous publication [58] are applied to \mathbf{S} .

Finally, radiometric normalization is applied by dividing the entries of the scattering matrix \mathbf{S} with the pixel area factor, determined using an external digital elevation model geocoded in radar azimuth-range coordinates [63, 64]. This last procedure generates a scattering matrix where the intensities of the pixels correspond to the equivalent normalized radar cross-section σ_0 .

4.2.3 Datasets

The polarimetric analysis presented in this work is made with two datasets acquired in 2015 and 2016 in two regions of Switzerland. The first data was taken in the summer months of 2015 during a glacier monitoring project in the Mattertal, an Alpine valley in the Southwestern Swiss Alps, canton of Valais. The second dataset was acquired in September 2016 during a calibration experiment at the "Chutzen" location, on the top of the "Belpberg" hill, near the town of Münsingen, Canton of Bern, Switzerland. Details of these two datasets are discussed individually in the next subsections.

BISGLETSCHER DATASET

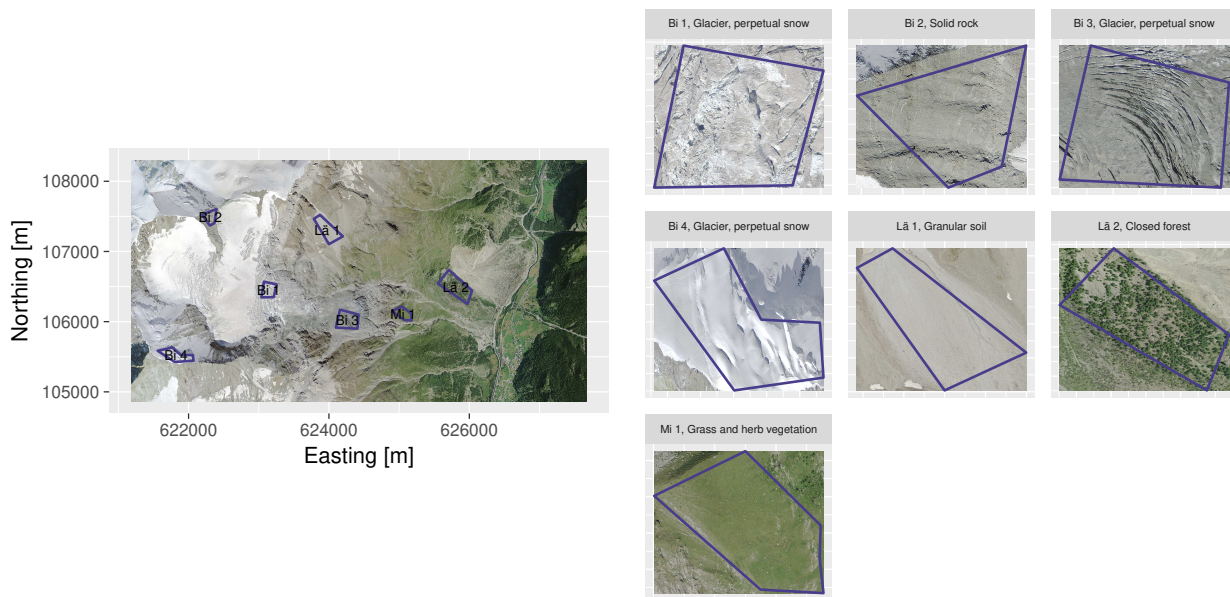
The data was acquired during a project to monitor the flow velocity of the Bisgletscher [65] glacier in the Mattertal valley, Canton of Valais, Southwestern Swiss Alps. The device was installed in the proximity of the Domütte mountain hut, where the electrical power supply for the hut and a Wireless LAN communication and control link used by the PermaSense/X-Sense project [66] were available.

From its location at the hut, KAPRI was overlooking the Bisgletscher on the other flank of the valley at distances between 3000m and 8000m, where the terrain is covered by glaciers, rocks, scree, short vegetation and sparse forests at lower altitudes. An overview of the scene is given by the aerial photograph of Figure 4.2a.

The campaign was carried out in the summer months of 2015, between the second half of July and September with acquisitions spaced 2.5 min from each other. Because of data transmission and storage limitations, acquisition were only made for 12 hr each day.

Only a subset of the whole time-series could be analyzed: processing the entire dataset would have exceeded our current storage and computation capabilities. Therefore, the week between July 10 and July 17, 2015 was chosen. For each of these days, 10 acquisition times (6:00, 7:00, 8:00, 9:00, 10:00, 12:00, 14:00, 15:00, 16:00, 18:00 UTC) were used.

An averaging window of 20 pixels in range and 2 in azimuth is used to estimate the polarimetric covariance matrices used to extract polarimetric parameters; the choice of a rectangular window with such a high aspect ratio is dictated by the polar acquisition geometry: if too many azimuth pixels are used in the averaging, the angular resolution would be severely degraded and pixels representing widely different targets on the ground would have been averaged together; however enough independent samples are necessary for a robust estimate of the second order statistics. This choice gives a multilooked resolution cell size of 20×50 meters at a slant range of 6000m in the center of the scene.



(a) Overview map for Bisgletscher

(b) Excerpts for Bisgletscher ROIs

Figure 4.2: 4.2a 0.25m resolution orthophoto of the Bisgletscher test site. The ROIs used for the polarimetric analysis are overlaid to the image in dark blue and are assigned a short alphanumeric code. 4.2b shows zooms-in of each ROI, including its full name according to the SWISSNAMES placename inventory and the land cover class from the NOLC04 land use statistics. The alphanumeric codes in 4.2b correspond to the first two characters of the ROI's name followed by an increasing number. (Geodata ©swisstopo).

CHUTZEN DATASET

Unlike the Bisgletscher dataset where a long time-series has been acquired, only one fully polarimetric acquisition is available from the Chutzen site.

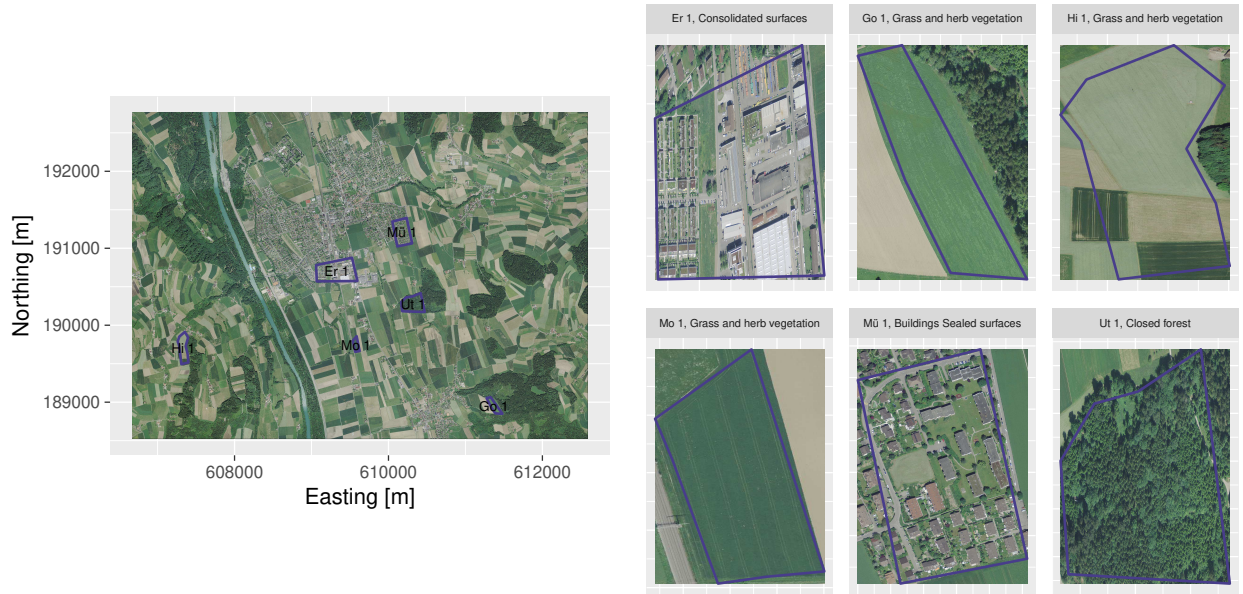
The name of the dataset is taken from the hill above the town of Münsingen and the in the vicinity of Bern, Switzerland where KAPRI was installed. The data covers slant range distances between 50m and 3km. An aerial photograph of the scene is shown in Figure 4.3a.

This measurement was taken for calibration and validation purposes; to this end five trihedral corner reflectors (TCR) —of which three have triangular faces with 40cm side length and two have cubic faces with the same size— were placed at distances between 70m and 3km from the radar. More details on these issues, the acquisition campaign and the polarimetric calibration are found in [58].

4.2.4 Polarimetric Analysis

To study the polarimetric signatures of different terrain types, a number of standard polarimetric parameters are derived from the polarimetric covariance and coherency matrix \mathbf{T} and \mathbf{C} :

- Backscatter coefficients $\sigma_{HH}^0, \sigma_{HV}^0, \sigma_{VH}^0$



(a) Overview map for Chutzen

(b) Excerpts for Chutzen ROIs

Figure 4.3: This figure shows the geographic situation of the Chutzen dataset. 4.3a displays an overview of the area using a 25cm resolution orthophoto. In 4.3b zoomed in photographs corresponding to the ROIs used for the polarimetric analysis are shown. The title of each panel gives the ROI's land cover type according to the NOLC04 land cover survey and its name according to the *SWISSNAMES* Swiss placename inventory (Geodata ©swisstopo).

- Normalized backscatter: polarimetric channels divided by the total backscatter power (span).

$$r_i = \frac{\sigma_0^i}{\sum_{j=HH,VV,HV,VH} \sigma_0^j}. \quad (4.1)$$

- Cloude-Pottier decomposition parameters [67]: entropy H , anisotropy A , mean α angle.
- Copolar coherence: phase and magnitude of the complex $HH-VV$ correlation coefficient γ_{HHVV} .
- $\gamma_{(HH-VV)-(HH+VV)}$: coherence magnitude between the first two components of the Pauli scattering vector, corresponding to the normalized T_{12} entry of the polarimetric coherency matrix.

The Cloude-Pottier parameters provide a measure of the type and uniqueness of polarimetric scattering mechanism observed in a pixel; this information is independent of the total backscatter power. The entropy H is particularly important: a high entropy indicates the presence of several scattering mechanisms in a pixel and a higher degree of scattering randomness.

The polarimetric backscatter coefficients are interesting from several applications; they have been linked to variations in environmental parameters: vegetation parameters such as water content [68], snow properties [69–72], soil moisture and roughness [73–75] to cite some examples.

The normalized backscatter is included because it permits to remove the dependence of the parameters on the total backscattered power, allowing for a better interpretation of the relative contributions of polarimetric channels.

$\gamma_{(HH-VV)-(HH+VV)}$ is the coherence between the $HH + VV$ and $HH - VV$ components of the Pauli scattering vector; corresponding to the normalized T_{12} element of the polarimetric coherency matrix \mathbf{T} . This parameter is an indicator for the presence or absence of rotational and azimuthal scattering symmetries [76]; in [4] it was shown that this coherence is correlated with the surface roughness through the X-Bragg (extended-Bragg) scattering model.

The copolar ($HH - VV$) coherence phase and magnitude have been linked with several physical quantities; for example the depth of fresh snow [6], the anisotropy of ice and snow particles [77], properties of snow and firn [78] and several properties of the vegetation cover [5].

Because the two datasets are different in temporal sampling—Bisgletscher data being a time-series and Chutzen a single snapshot in time—the results of the polarimetric analysis are displayed differently. In the former case, both the spatial and the temporal variability of the parameters needs to be addressed, while in the latter only their spatial distribution within the ROIs and in the scene are of interest. For this reason, results for the two datasets are discussed separately in the next section.

Data processing is automated with Nextflow [79], a scientific workflow management system, to ensure consistent and reproducible analyses.

For each dataset a number of polygonal region of interest (ROIs) are selected over the extent of the data, each representing different terrain features. These ROIs are drawn in a GIS software on a 0.25m orthophoto (SWISSIMAGE 25 by Swisstopo) of the investigated area, ensuring that each polygon only consist of one land cover type (Ice, Rock, Forest, Scree, etc); the land cover type according to the NOLC04 [80] land cover statistic is then automatically added to the polygons and each ROI is assigned a name taken from the nearest feature in the *SWISSNAMES* geographic name inventory provided by Swisstopo (Federal Office For Topography and Cartography).

Finally, these polygons are converted to range-azimuth coordinates using a geocoding lookup table generated with an external DEM.

The shape of the ROIs is shown in the map of Figure 4.2a and Figure 4.3a where they are assigned a short alphanumeric code; detailed excerpts of the aerial photograph showing individual ROIs with their land cover class and full name are displayed in Figure 4.2b and Figure 4.3b.

4.3 RESULTS

The results of the polarimetric analysis are described individually for the two datasets in the following subsections. First, the variability of the parameters within the ROIs, between land cover types and—in the case of the Bisgletscher time-series—are addressed. This discussion is followed by an analysis of parameter maps covering the spatial extent of the whole dataset, to assess the presence of large-scale patterns that could have been overseen in the relatively small ROIs.

4.3.1 Bisgletscher

ROI-BY-ROI ANALYSIS

An assessment of the variability of the selected parameters in time and within the ROIs is made by plotting them as a time-series. Dots are used to mark the mean value inside each ROI at any time, vertical bars show ± 1 standard deviations from the mean. A smoothed mean line is superimposed to the plot to facilitate the detection of temporal trends. Each panel of the plot shows the time-series for an individual ROI, with the title giving the code corresponding to the codes shown in Figure 4.2a; These short codes are derived from the first three characters of the name shown in each panel of Figure 4.2b and a sequential number.

In the following sections, a detailed description of these time-series is provided; the description is made ROI-by-ROI: all parameters for a particular ROI are commented together to facilitate later interpretations of the observed variations.

- "Bi 1" is classified as "Glacier, Perpetual Snow" in the land cover map; this is verified by visual inspection of the map shown in Figure 4.2b. The polygon is located on the lower icefall of Bisgletscher.

The mean entropy in the ROI (Figure 4.4b) decreases in the course of time, dropping from 0.75 to 0.6. Its spatial variability is rather large and tends to increase over time. The mean α angle (Figure 4.4a) drops as well, starting from 50° and decreasing to about 35° ; always showing a small spatial variability. The values of entropy and α place "Bisgletscher 1" between the *Zone 6: Medium Entropy Surface Scattering* and *Zone 4: Medium Entropy Multiple Scattering* zones of the classification scheme suggested by Cloude and Pottier.

The copolar coherence magnitude (Figure 4.4d) shows an increase very similar to the decrease in entropy; going from 0.75 in average to 0.85; the copolar phase difference is very stable in space and time and stays at about 45° .

The $\gamma_{(HH-VV)-(HH+VV)}$ coherence likewise shows a similar increase but with a relatively high spatial variance.

The backscatter power (Figure 4.5b) shows a large spatial variation; the mean copolar backscatter increases in time, from -35 dB to -30 dB; the crosspolarized backscatter does not vary as strongly in time and only slightly drops. The normalized backscatter (Figure 4.5c) better shows this behavior: at first the backscatter is dominated by the crosspolarized signal, after July, 12th the copolar backscatter increases and peaks on July 17.

These variations are not significantly correlated with the air temperature as observed at the "Zermatt" automatic weather station (AWS) (see Figure 4.5d).

- "Bi 2" is assigned the land cover class "Solid Rock", it is located on a rocky mountain face. The orthophoto shown in Figure 4.2b confirms the classification.

The entropy H varies very little within the ROI, its mean is stable at around 0.8 showing a slight dip on July 17. This behavior is seen in the mean α angle as well, whose spatial variance is small; its mean drops from 50° to about 45° . In the Cloude-Pottier classification this would signify a move

between *Zone 5: Medium Entropy Vegetation Scattering* and *Zone 4: Medium Entropy Multiple Scattering*.

The copolar coherence magnitude displays again an increase from 0.5 to 0.6 on July 17; its spatial variance however is rather large. The copolar phase difference shows a small spatial variance and remains stable over time.

$\gamma_{(HH-VV)-(HH+VV)}$ shows a large spatial variance and again a slight increase towards the end of the time-series.

The backscatter power is dominated by crosspolarized backscatter and has a small spatial variance; it periodically drops over the course of a day and shows a larger drop towards July 17. The backscatter ratio on the other hand is stable, showing a dominant *HV* component; the second most important contribution is *HH*, which is at least 2 dB larger than *VV*. All three backscatter coefficients show a correlation with the air temperature measured at the automatic weather station.

- "Bi 3" is marked as "Glacier, Perpetual Snow" in the land cover classification; the ROI is located on the lower tongue of Bisgleschter. The aerial photograph shows several crevasses in this region: they may not correspond to the glacier's surface at the time of acquisition since the glacier is constantly flowing and breaking off.

The mean entropy is about 0.75 with a drop of 0.1 over the course of July 17th. Its spatial variability remains always small. The α angle displays a similar pattern; its mean dropping from 50° to 45° , indicating a change between *Zone 6: Medium Entropy Surface Scattering* and *Zone 5: Medium Entropy Vegetation Scattering*.

The copolar coherence magnitude is stable at about 0.7 for most of the time and shows an increase of 0.2 on July 17. Its spatial variance is always large at 0.2. The coherence phase on the other hand is stable with low variance at around 50° .

$\gamma_{(HH-VV)-(HH+VV)}$ shows a behavior similar to the copolar coherence magnitude.

The backscatter is predominantly cross polarized with a large spatial variance of 20 dB, diurnal patterns are seen: the radar cross section decreases slightly over the course of each day. The power ratio is stable and confirms the main contribution to be from the *HV* channel, with a slight decrease on July 17. The copolar channels are equal in power. All channels correlate similarly with air temperature measured at the Zermatt weather station.

- "Bi 4" is classified as "Glacier, perpetual snow"; it is located on a small hanging glacier on the flanks of Weisshorn at an elevation of approx. 4000 m.

The mean entropy in this ROI is 0.75 with small spatial variability; a slight decrease is observed on July 16 followed by an increase over the course of July 17. The α angle has a small spatial variance; its mean shows some oscillations in time, for example on July 13 and on July 17; similar to the oscillations observed for *H*. In all cases, the observed values are assigned *Zone 6: Medium Entropy Surface Scattering* in the Cloude-Pottier classification scheme.

The average copolar coherence magnitude never drops below 0.6, albeit with a large spatial variability. Small cyclical variations in the course of each day are observed. The copolar phase shows little intra-ROI variability, its mean starts at -50° , increasing to -40° on July 17.

$\gamma_{(HH-VV)-(HH+VV)}$ again shows a similar pattern.

The backscatter is predominantly crosspolarized; the copolar channels have very similar values and are in average at least 5 dB weaker than HV ; they show a larger spatial variance than the crosspolar backscatter. The power ratio shows a global increase in HV power, albeit with periodical diurnal decreases.

The backscatter coefficients are not strongly correlated with air temperature.

- "Lä 1" is assigned "Granular Soil" in the land cover classification; this is confirmed by the aerial photograph: the ROI contains only glacial till.

High entropy with low spatial variability is observed in this region: the mean entropy is always higher than 0.75. α is 0.55° in average until July 17th, when it drops to approximately 45° . These values of H and α would imply a Cloude-Pottier classification in the *Zone 6: Medium Entropy Surface Scattering*.

The copolar coherence magnitude is stable at 0.6 with a large spatial standard deviation of 0.25; it increases on July 17 to slightly above 0.75. The copolar phase shows a pattern similar to these observed in the other ROIs and is stable in time at around -50° .

The coherence $\gamma_{(HH-VV)-(HH+VV)}$ is at 0.5 with large spatial variance and follows the same temporal pattern as the copolar coherence.

The backscatter is predominantly crosspolarized, HV is 5 dB stronger than the copolar backscatter until July 17, where it drops significantly, almost reaching the level of the copolar backscatter. The decrease in crosspolarized power is well visible in the backscatter power ratio plot. All channels show a decrease during the course of every day; but the ratios within the days are stable except for July 17th.

The backscatter does not strongly correlate with temperature.

- The land cover type for "Lä 2" is "Closed Forest"; the aerial photograph shows a sparse forest next to the Randa rockslide, growing on scree with individual large boulders.

The entropy is high at 0.75 and shows little spatial and temporal variability; α displays a similar pattern; its mean is at 55° , slightly decreasing on July 17. These observations correspond to *Zone 6: Medium Entropy Surface Scattering* in the Cloude-Pottier scheme.

The backscatter is strongly crosspolarized; its spatial variability is small and diurnal variations can be seen. The backscatter ratio is constant over time with a slight drop on July 17. All polarimetric channels are strongly correlated with air temperature.

- "Mi 1" is marked as "Grass and Herb vegetation", the aerial photograph shows a surface covered in short grass with some exposed slabs of rock.

The entropy of this ROI is high at 0.75 with very little temporal or spatial variability. α likewise does not vary significantly and is always at 55° in average. These values correspond to *Zone 6: Medium Entropy Surface Scattering* in the Cloude-Pottier segmentation of the H - α plane.

The copolar coherence magnitude is 0.5 in average, with a spatial variance of 0.3. Some intraday variation is observed. The copolar phase difference is low at about -15° and does not show temporal patterns.

$\gamma_{(HH-VV)-(HH+VV)}$ is around 0.3 with large spatial variance and slightly increases towards the end of the time-series.

Once more the HV channel is stronger than the copolar channel by about 5 dB; likewise the VV channel is stronger than the HH channel. All channels show a small spatial variability; diurnal decreases in backscatter can be observed for most days. The normalized backscatter ratio on the other hand is very stable.

All polarimetric channels correlate negatively with the air temperature.

SPATIAL DISTRIBUTION OF PARAMETERS

The results of the polarimetric analysis show that —except for the backscatter— the parameters do not considerably vary over time for most of the ROIs. Therefore, by selecting one date and plotting their spatial variation as maps, it is possible to analyze their large scale behavior over the entire scene.

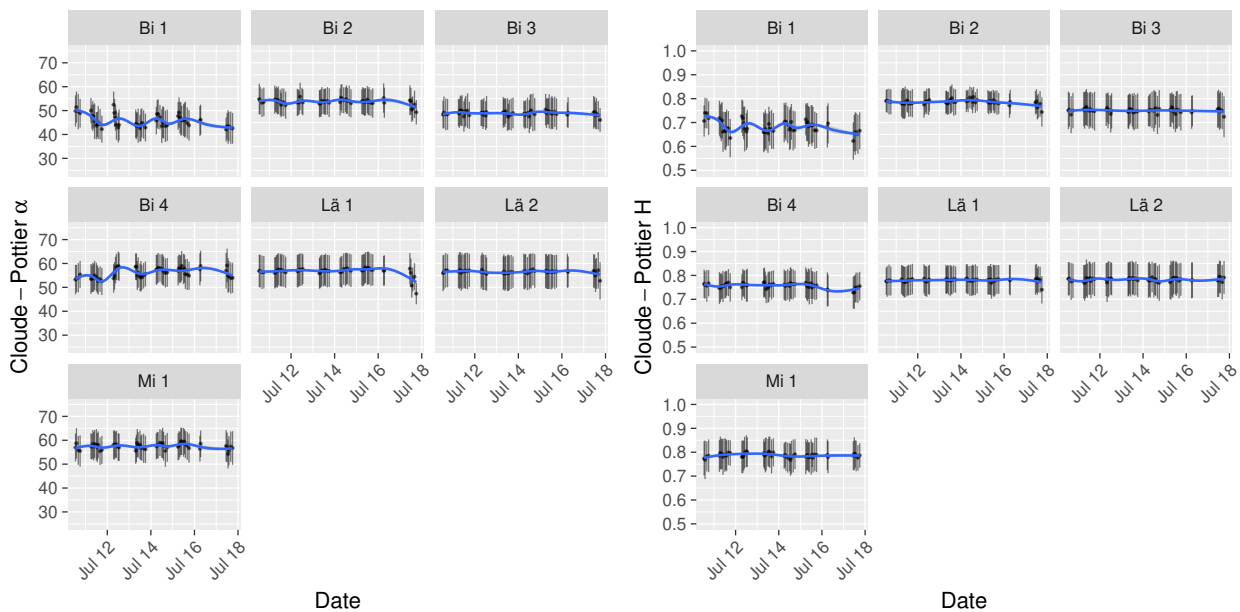
These plots should help to assess whether the selected ROIs are representative and if there are spatial trends at scales larger than those captured by the ROIs. For this analysis an acquisition on July 14 is used.

In the entropy map (Figure 4.6a) the difference between areas located in radar shadow and the rest of the scene is visible; the locations of shadow are seen in the Pauli RGB composite in Figure 4.6c as the dark areas in the upper part of the image.

Except for this, no large trends can be distinguished; the entropy appears to be between 0.6 and 1.0 over the entire scene. Very few areas where the entropy is low and spatially smooth can be identified. A region of lower entropy is visible in the center of the scene; this part corresponds to the glacier which appears dark blue in the Pauli RGB composite. The α angle is high throughout the image and only shows an area of lower values in the center, in correspondence with the glacier. Except for the radar shadow, no areas where α is higher than 60° are observed.

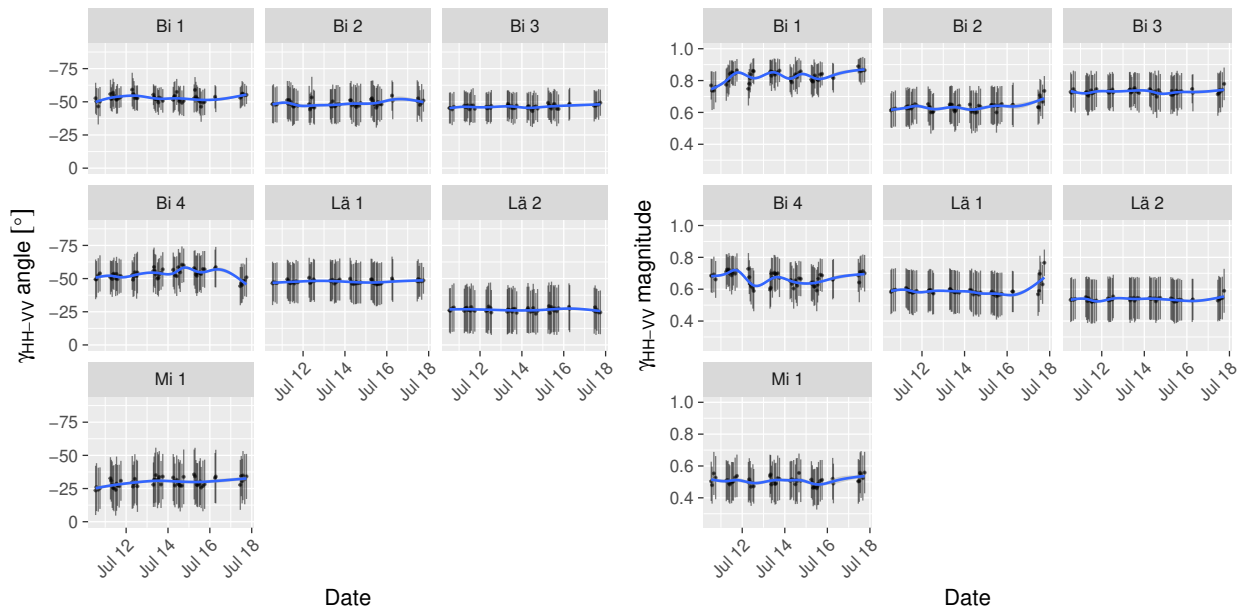
Outside of the glacier, where surface scattering appears dominant (blue-violet in the Pauli RGB composite), HV backscatter (green color in the Pauli RGB) is predominant, which is consistent with the observation of dominant HV backscatter made in subsection 4.3.1.

Finally, subplot 4.6d display the magnitude of $\gamma_{(HH-VV)-(HH+VV)}$, the coherence between the first two component of the Pauli scattering vector, corresponding to the normalized T_{12} entry of the polarimetric coherence matrix. This parameter is an indicator for the presence of rotational and azimuthal scattering symmetries [76] and is shown to correlate with surface roughness [4].



(a) Cloud Pottier mean α

(b) Cloud Pottier entropy H



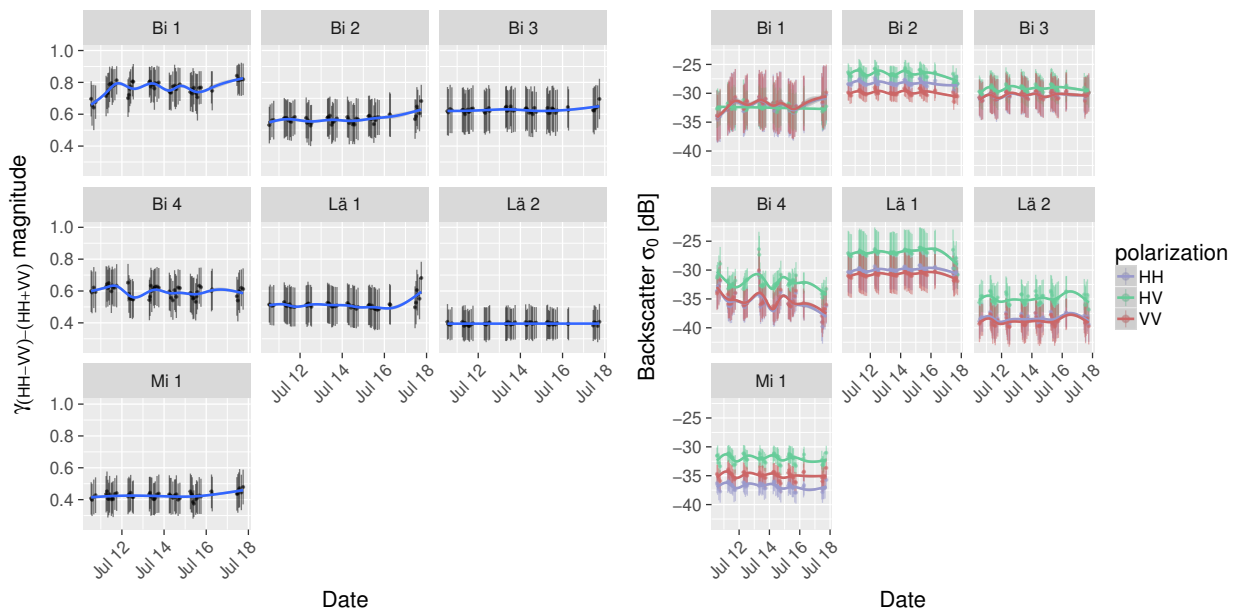
(c) Copolar coherence phase.

(d) Copolar coherence magnitude.

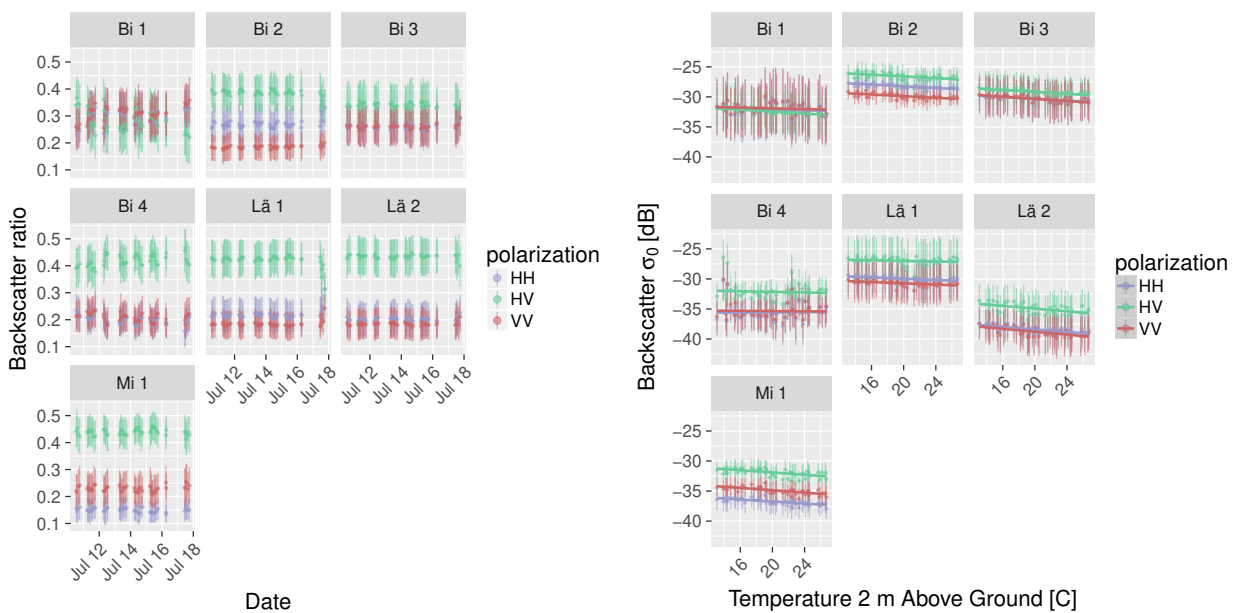
Figure 4.4: Temporal and spatial variability of (a) mean α , (b) Cloud-Pottier entropy H , (c) copolar phase difference and (d) copolar coherence for all ROIs in the Bisgletscher data. The vertical lines around each point display ± 1 standard deviation for that data within the ROI, computed over all the pixels in that ROI, the dots the mean and the blue line shows a smoothed trendline.

The highest values of $\gamma_{(HH-VV)-(HH+VV)}$ are observed in correspondence of the glacier, in the middle of the scene; they appear to correlate with areas appearing blue in the Pauli RGB composite and where the entropy and α show the lowest values.

4.3.2 Chutzen

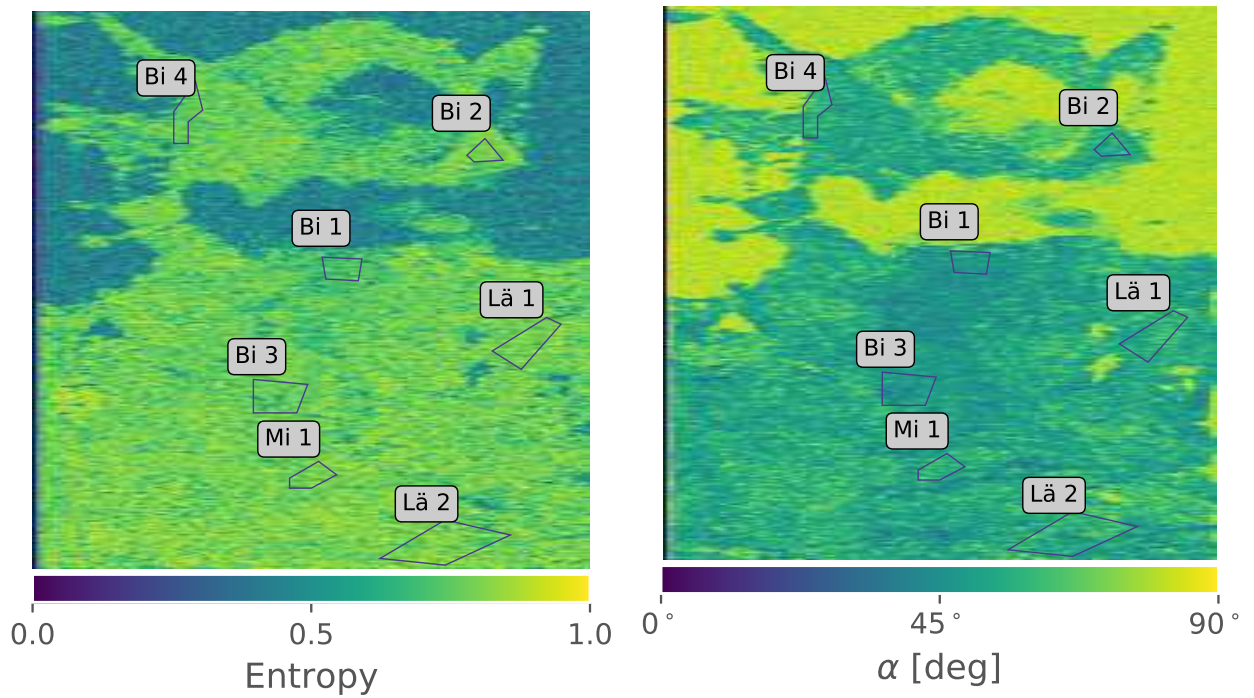


(a) $\gamma_{(HH-VV)-(HH+VV)}$: coherence magnitude between the first two components of the Pauli scattering vector, Bisgletscher dataset. (b) Spatio-temporal variability of backscatter in dB.

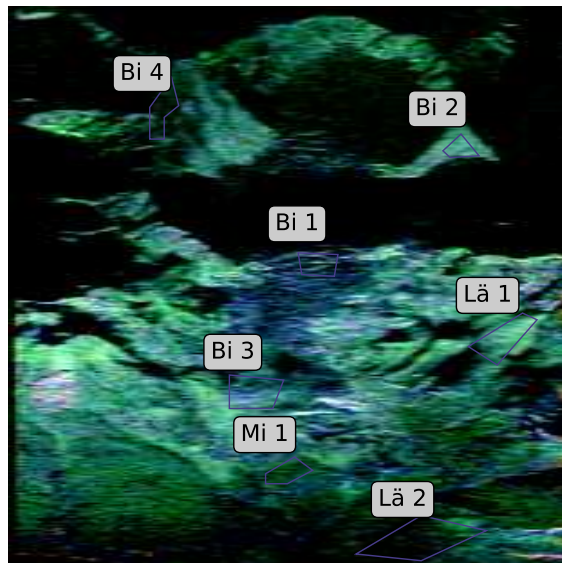


(c) Spatio-temporal variability of normalized backscatter. (d) Backscatter against air temperature as measured by the "Zermatt" automatic weather station.

Figure 4.5: Temporal and spatial variability of several parameters in the ROIs of the Bisgletscher data. The panels show: (a) magnitude of $\gamma_{(HH-VV)-(HH+VV)}$, (b) backscatter in decibel, (c) normalized backscatter and (d) backscatter versus air temperature measured at the "Zermatt" weather station. The vertical lines around each point display ± 1 standard deviation for that data within the ROI, computed over all the pixels in that ROI. The red, blue and green lines in the backscatter plots encode the polarization.



(a) Cloud-Pottier Entropy.

(b) Mean α .

(c) Pauli RGB composite.

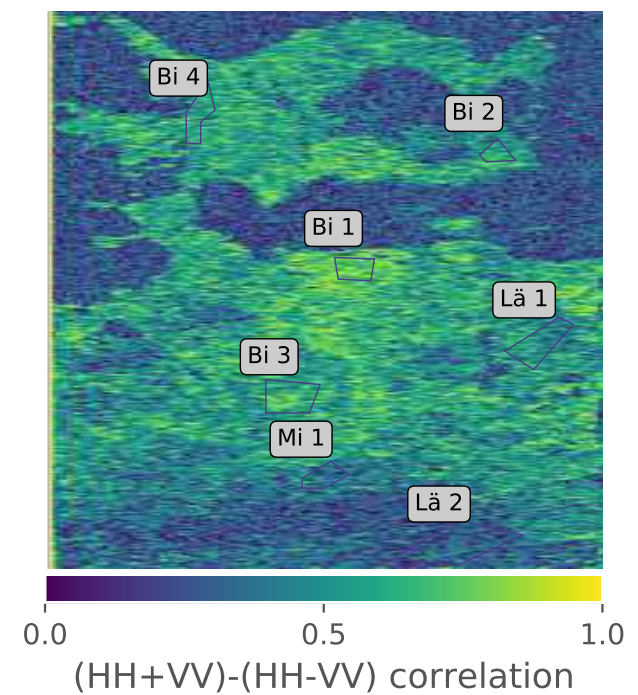
(d) Magnitude of $\gamma_{(HH+VV)-(HH-VV)}$.

Figure 4.6: Cloud-Pottier entropy H (a), (b) mean α , (c) Pauli RGB composite and (d) magnitude of $\gamma_{(HH+VV)-(HH-VV)}$ for the Bisgletscher dataset. The parameters were estimated with a 20×2 boxcar filter.

ROI-BY-ROI ANALYSIS

Since no time-series is available for the "Chutzen" dataset, the ROI-wise analysis will be performed on 2D histograms of the Cloud-Pottier parameters and on histograms of the polarimetric backscatter, of

the copolar coherence and of $\gamma_{(HH-VV)-(HH+VV)}$.

The H - α histogram grouped by ROI are shown in Figure 4.7; the histograms of the polarimetric backscatter in Figure 4.8a, the histogram of $\gamma_{(HH-VV)-(HH+VV)}$ in Figure 4.8d and those of the copolar coherence magnitude and phase in Figure 4.8b and Figure 4.8c.

- The land cover map classified "Er 1" as "Consolidated Surfaces". This is confirmed by the aerial photograph in Figure 4.3b showing an urban settlement and some industrial buildings. The 2D Cloude-Pottier histogram of Figure 4.7 displays a large variance in both α and entropy. The mean entropy is about 0.75 and the mean α angle 50° .

$\gamma_{(HH-VV)-(HH+VV)}$ shows a large variance too, with a median about 0.5.

The copolar coherence has a similar distribution, the copolar phase shows a wide distribution with a negative skew.

The backscatter distribution is broad and all polarizations have a very similar distribution.

- "Go 1" 's land cover type is "Grass and Herbs"; in the aerial photograph two different crops are visible; however at the time of the radar acquisition the crops may have been different.

The median entropy is 0.75, the median α 35° and the distribution is concentrated. These values would place the scattering in the ROI in *Zone 6: Medium Entropy Surface Scattering* of the Cloude-Pottier classification.

$\gamma_{(HH-VV)-(HH+VV)}$ is concentrated around 0.15, the copolar coherence is concentrated with a mean of around 0.75 and the copolar phase difference shows a narrow distribution around 0.

The distribution of backscatter is very narrow; the mean VV backscatter is 2 dB higher than the VH backscatter, the mean crosspolar backscatter is between them.

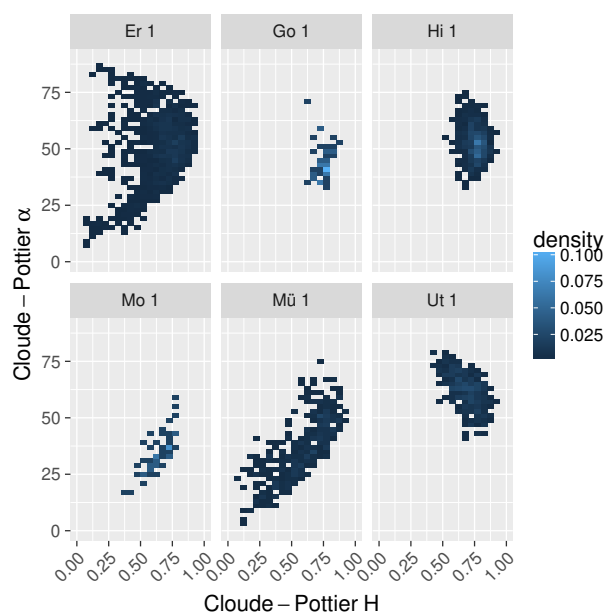
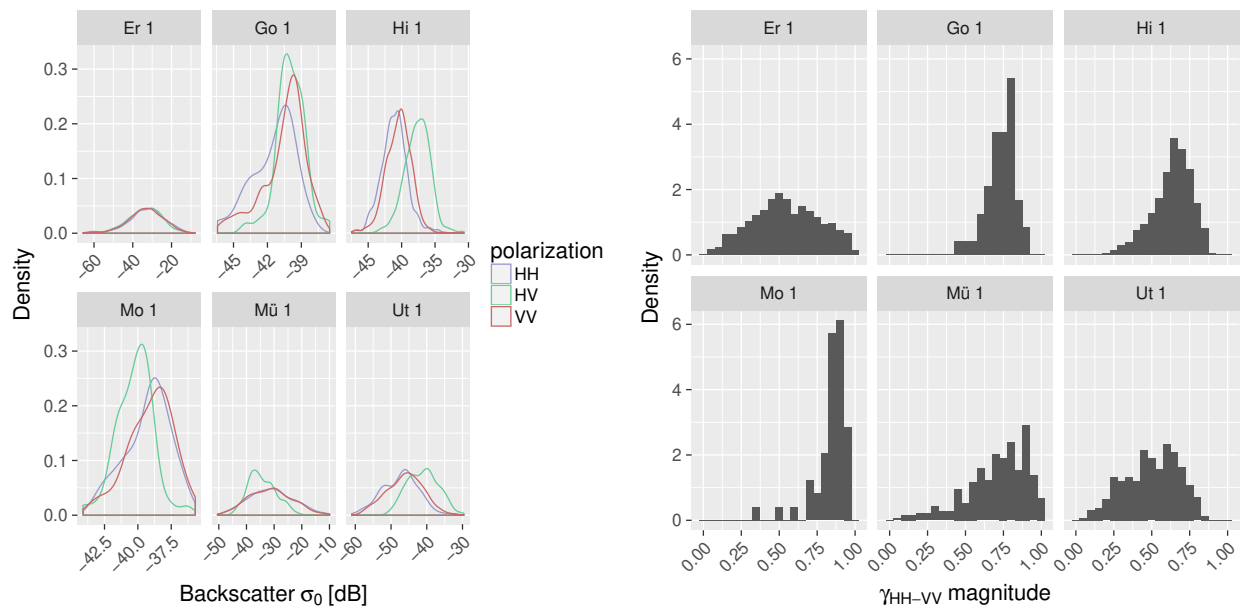
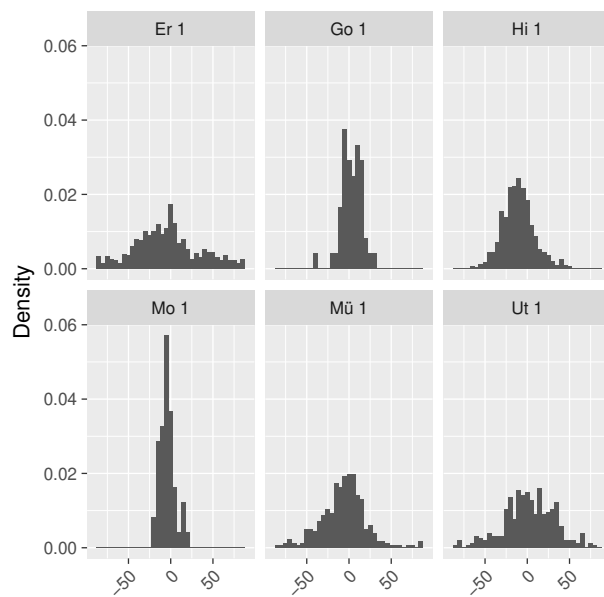


Figure 4.7: Cloude-Pottier H - α histogram for the Chutzen dataset. The title of each panel corresponds to the ROI's name as shown in Figure 4.3b.

(a) Polarimetric backscatter σ_0 .

(b) Copolar coherence magnitude.



(c) Copolar coherence phase.

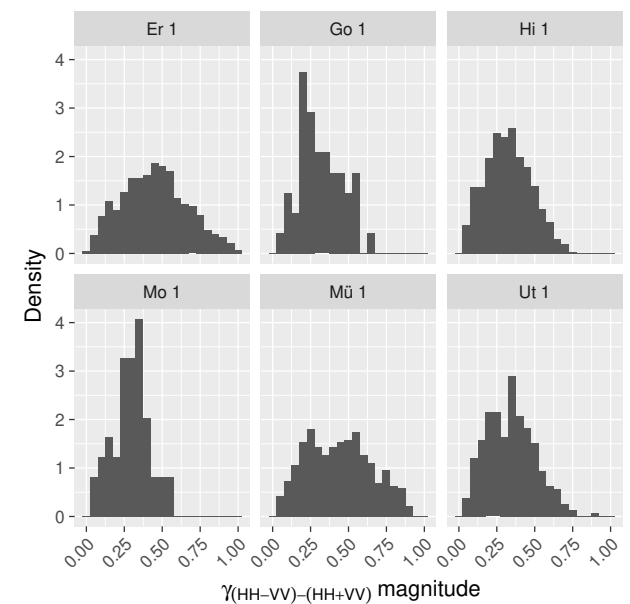
(d) $\gamma_{(HH-VV)-(HH+VV)}$ correlation coefficient

Figure 4.8: Histograms of: (a) polarimetric backscatter coefficient, (b) copolar coherence magnitude, (c) copolar coherence phase and (d) coherence magnitude of $\gamma_{(HH-VV)-(HH+VV)}$. The title of each panel indicates the short code of each ROI plotted in Figure 4.3b.

- "Hi 1" has the same classification and appearance as "Go 1".

The median entropy is 0.75 with a distribution skewed towards higher values; the median α is 55° with some outliers at higher α angles. The distribution is generally wider than in the previous case. Considering the median values of H and α , the Cloude-Pottier classification would assign *Zone 4: Medium Entropy Multiple Scattering* to this ROI.

The median $\gamma_{(HH-VV)-(HH+VV)}$ is 0.3 with a heavily right tailed distribution, the copolar coher-

ence distribution is skewed towards high values, with a median around 0.6 while the copolar phase difference has a narrow distribution with a negative median.

The VV backscatter is slightly larger than VV , the median HV backscatter is larger than both.

- "Mo 1" is again classified "Grass and Herb Vegetation"; the aerial photograph shows a cultivated field with a single type of crop. However, once again it must be reminded that these images are not necessarily representative of the state of the crops at the time of the radar acquisition and can only provide a general idea of the land cover type expected in each of the ROIs.

The median H is 0.75; the distribution appears skewed towards lower entropy, with outliers as low as 0.3. The median α is 30, some outliers at lower values are seen as well. According to the median values, this region should be classified as *Zone 6: Medium Entropy Surface Scattering* in the Cloude-Pottier scheme.

The median $\gamma_{(HH-VV)-(HH+VV)}$ is 0.3; its distribution tends towards lower values; no pixels above 0.55 are seen, the copolar magnitude distribution is very concentrated at around 0.8. The copolar phase difference distribution is very narrow around 0.

The backscatter is predominantly copolarized, the median VV is slightly larger than HH . The crosspolar backscatter shows a smaller dispersion, its median value however is smaller than the copolar channels.

- "Mü 1"'s land cover is "Buildings, Sealed surfaces". Inspection of orthophotos shows a residential area with regularly arranged houses surrounded by gardens with several individual trees.

The Cloude-Pottier histogram displays a very wide distribution with α predominantly concentrated in the lower half; however a clear center cannot be identified. Low entropy and low α outliers can be observed.

$\gamma_{(HH-VV)-(HH+VV)}$ shows a similarly wide distribution, a mean value cannot be discerned. Similar patterns are observed for the copolar coherence; the distribution appears skewed towards higher values while the phase distribution is wide with a negative median.

The distributions of HH and VV are almost identical, the median HV is 5 dB lower; its distribution is more concentrated than the one of the copolar channels.

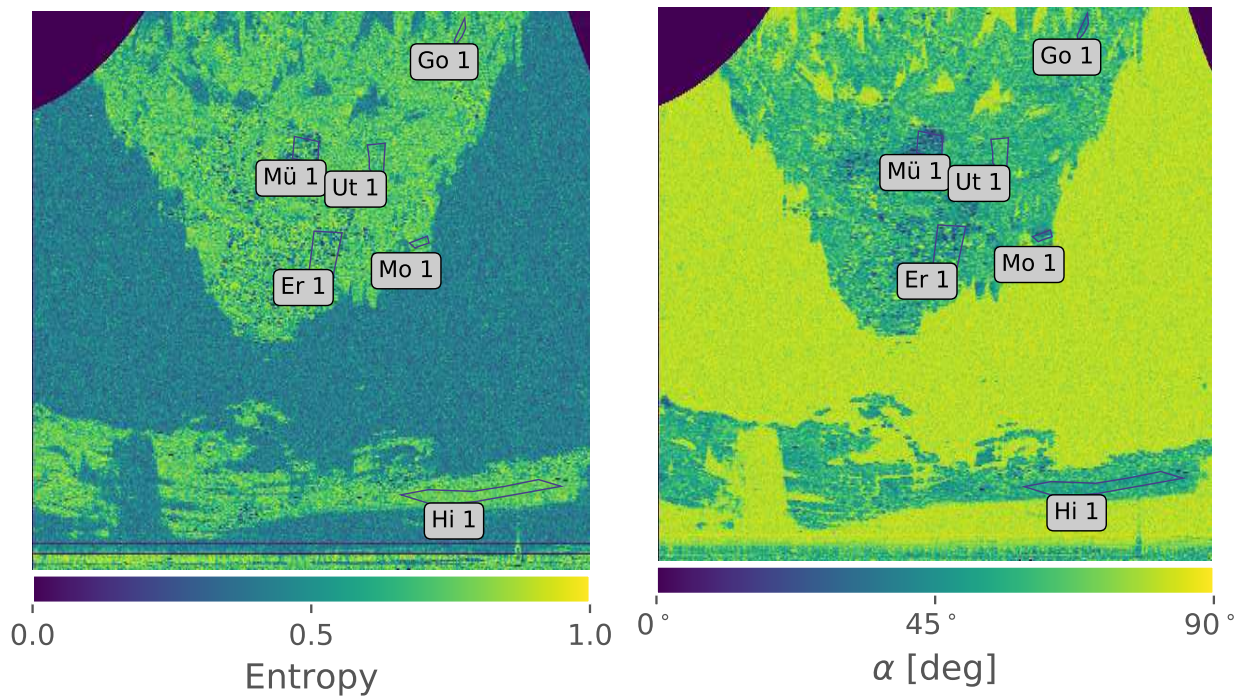
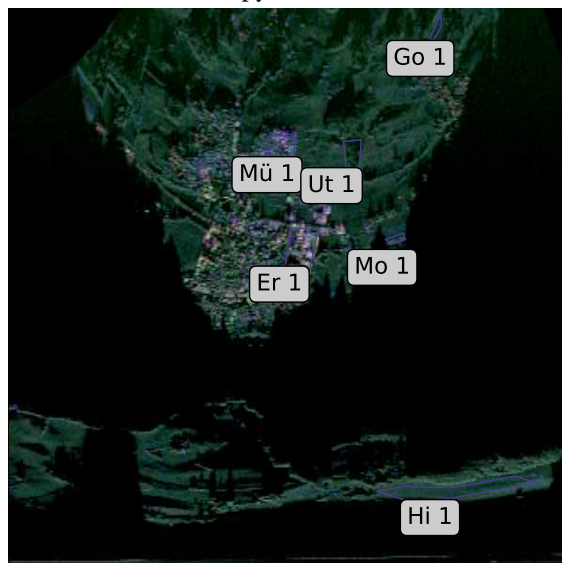
- "Ut 1"'s land cover class is recorded as "Closed Forest"; the classification is verified by checking the orthophoto that shows a mostly dense forest.

The median H is slightly below 0.75; α is 60° ; the distribution is concentrated in the right-upper half of the Cloude-Pottier plane, placing the ROI in the *Zone 4: Medium Entropy Multiple Scattering* region.

$\gamma_{(HH-VV)-(HH+VV)}$ shows a median value of 0.3, its distribution however is quite wide; the copolar phase shows a similar wide distribution. The copolar phase difference distribution is very wide and centered around 0.

The backscatter is predominantly crosspolarized; its median is close to 10 dB stronger than the copolar channels. The distributions show a very similar shape for all channels.

SPATIAL DISTRIBUTION OF PARAMETERS

(a) Cloude-Pottier entropy H .(b) Cloude-Pottier mean α angle.

(c) Pauli RGB.

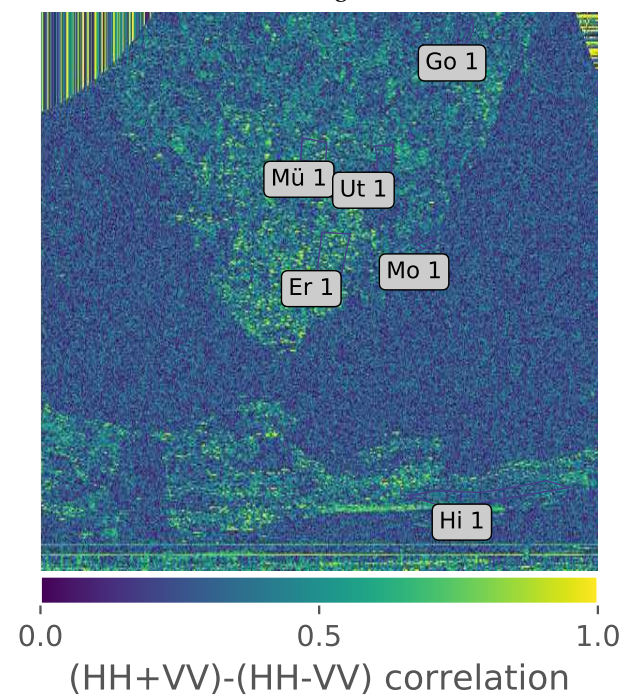
(d) Magnitude of $\gamma_{(HH-VV)-(HH+VV)}$.

Figure 4.9: (a) Cloude-Pottier entropy H , (b) mean α , (c) Pauli RGB composite and (d) magnitude of $\gamma_{(HH-VV)-(HH+VV)}$ for the Chutzen dataset. The parameters were estimated with a 20×2 boxcar filter.

The entropy estimated in the Chutzen dataset is shown in Figure 4.9a; it is generally lower than the

one observed in the Bisgletscher data and is spatially more granular: several low-entropy points can be observed in "Mü 1" and "Erl 1" as well to the immediate top right of "Hi 1". As observed for the other dataset, several areas of low entropy correspond to locations in radar shadows, visible in the Pauli RGB composite of Figure 4.9c.

The mean α angle is lower than in the Bisgletscher data as well at about 45° , as seen in Figure 4.9b. Pixels of very low α are seen, many corresponding to the pixels of low entropy observed previously. Likewise, pixels with α close to 90° are observed too, corresponding to low-entropy pixels. All these points match with very bright features in the Pauli RGB composite; on the aerial photograph they correspond to individual buildings.

The map of $\gamma_{(HH-VV)-(HH+VV)}$ is displayed in Figure 4.9d; a correlation with the entropy is visible: points of low entropy appear to have a very high coherence value, while in the rest of the scene the coherence is low.

4.4 DISCUSSION

The most important results of the polarimetric analysis is the observation of an overall high entropy as displayed by the Bisgletscher entropy map in Figure 4.6a and in Figure 4.9a for Chutzen. In the latter case the entropy is observed to be lower than 0.5 for individual buildings of large scattering cross section in the urban areas.

The α angle is rarely lower than 45° for any of the ROIs; both parameters do not show large temporal variation in the Bisgletscher time-series plot (see Figure 4.4a and in Figure 4.4b).

These values indicate that the dominant scattering mechanism in both scenes is in the range between Zone 4: Medium Entropy Multiple Scattering and Zone 6: Medium Entropy Surface Scattering of the Cloude-Pottier classification.

A considerable amount of crosspolarized backscatter is observed for most of the ROIs in addition to the high entropy—see Figure 4.5 for Bisgletscher, and the histogram in Figure 4.8a for Chutzen—. This is visible in the Pauli RGB composites: large portions of both images appear green.

This combination of high entropy and crosspolarized backscatter points at the presence of depolarizing scattering mechanism [76].

This is realistic considering the dominant land cover types encountered in both areas—ice, gravel, vegetation canopies—whose scattering behavior at Ku-band can presumably be well approximated by random media.

However, other mechanisms not related to the scattering media are also known to increase the observed entropy [81]. Thus, four hypotheses ought to be considered for the analysis of the polarimetric signatures:

1. The dominance of depolarizing scattering mechanisms
2. A significant noise contribution.

3. Mixing of heterogeneous pixels in the multilooking process.
4. Mixing of many polarized scattering processes in a resolution cell.

In the next section the way these effect can increase entropy estimates is discussed and their likeliness is assessed.

4.4.1 Depolarization

Depolarization in the theory of scattering entropy [76] is the situation where electromagnetic waves scattered from targets illuminated by fully polarized waves are partially polarized, i.e when they contain a stochastic contribution. This means that the polarization vector of the backscattered wave fluctuates stochastically. Such a scattering process can not be described by the scattering matrix \mathbf{S} , statistical parameters are needed to characterize these types of scattering interactions.

Coherent polarimetric radars only measure the fully polarized component of the backscattered signal i.e the scattering matrix \mathbf{S} , thus in a strict sense they cannot directly observe depolarization. However, it is possible to use the scattering matrix data to estimate statistical descriptors for depolarizing scattering mechanism. To do so, it is necessary to assume *ergodicity* of the scattering process; i.e assuming that different samples of \mathbf{S} acquired at different locations or times represent independent samples of the same scattering process [76]. In coherent SAR polarimetry this is done by computing the polarimetric coherence or covariance matrices \mathbf{T} or \mathbf{C} from \mathbf{S} and averaging the result in space assuming that adjacent pixels belong to the same *distributed target* or *extended target*, i.e a scatterer whose spatial extent is larger than a single resolution cell. This is usually assumed to hold for natural surfaces, for example vegetation or soils.

At least three physical mechanisms creating depolarization in (low-frequency) polarimetric radar data are found in the literature [67]:

- The first is caused by Rayleigh scattering from a volume of anisotropic spheroidal particles with random locations and orientations [67, 76]. The field scattered by each individual particle is fully polarized, but the coherency matrix obtained as the average over the distribution of these particles will have more than one nonzero eigenvalue and will thus behave as a depolarizer. Shape and orientation of the particles influence the amount of depolarization: a cloud of random isotropic spheres will not produce depolarization while a cloud of random dipoles is the strongest depolarizer [76, 82]. The amount of depolarization is also influenced by the ratio of wavelength to particle size and to the resolution cell size: using a system able to perfectly resolve each scatterer no depolarization will be observed; as the wavelength to cell size ratio increases, depolarization will be increasingly observed due to the averaging effect of a coarser resolution.
- A second way in which scattering interactions can generate depolarization is through multiple scattering in a cloud of spheroidal particles [83–85], where in addition to the direct backscatter from each individual element, the model considers interactions between scatterers up to an order n . When multiple scattering interactions are modeled, a cloud of symmetric, spherical particles results in depolarization. Generally, the level of depolarization increases rapidly as higher order interactions are considered [76].

- A third mechanism generating depolarization is surface scattering from a rough surface [4, 76]: depolarization is caused to the average of polarized scattering —predicted by the Bragg (or Small Perturbation Method, SPM) surface scattering model [86]— over a distribution of surface facet orientation, the so-called Extended Bragg or X-Bragg scattering. Its applicability for high frequency polarimetric radar applications is not clear: the X-Bragg is a low frequency approximation, which is considered valid for surfaces whose root-mean -square (RMS) height s [87] is small compared to the wavelength; the limit is usually taken to be at $ks < 0.3$ where k is the wavenumber. At Ku-Band, the latter is 367 m^{-1} , while for agricultural soils a RMS roughness between 0.3 cm and 4 cm is reported [73, 88, 89]. With these parameters, it seems that the X-Bragg model could still be realistic, at least for the smoother soils.

The results for the two datasets analyzed in the previous section will be discussed individually in the following subsections, trying to explain the observed parameters in terms of land cover types and surface properties with reference to the depolarizing mechanism just described.

BISGLETSCHER

In the following list the time-series plots shown in subsection 4.3.1 will be interpreted ROI-by-ROI with the help of the orthophotos of Figure 4.2b and the land cover classification data, linking the observations to land cover types and changes in environmental parameters at the light of the depolarizing scattering mechanisms mentioned above.

- "Bi 1" is classified as glacier in the land cover map; it is located in the middle of the lower icefall of Bisgletscher. The ice surface appears covered in crevasses. In this ROI the mean entropy is observed to be between 0.75 and 0.65 with a slight downward trend; its spatial variation at any time is relatively high. The α angle shows a similar decrease from 50° towards 35° . These parameters correspond to mechanisms between *Zone 5: Medium Entropy Vegetation Scattering* and *Zone 4: Medium Entropy Multiple Scattering* of the Cloude-Pottier classification scheme. In this classification scheme the α angle was explained with the dominance of dipole-like scatterers such as needles and branches, while the entropy is attributed to a wide, random distribution of the scatterer's orientation angles. However, the penetration depth of Ku-Band EM radiation in wet ice —as it can be encountered on a glacier's surface in summer— is almost zero, thus scattering from anisotropic ice crystals from within the ice volume appears to be unlikely under these conditions, while significant penetration can be expected for dry conditions [90–92]. The high copolar coherence magnitude signals that the presence of volume scattering is debatable: polarimetric coherencies for a random volume are expected to be much lower, around $1/3$ [93].

Medium entropy surface scattering, appears to be a more convincing explanation for the observed values of α and H especially at the light of the observed high copolar coherence magnitude, low copolar phase dispersion; the low level of crosspolarized backscatter and the similar magnitude of the HH and VV backscatter coefficients. The increase in $\gamma_{(HH-VV)-(HH+VV)}$, together with decreasing values of H and of the crosspolar scattering power could be related with decreasing surface roughness [4].

- "Bi 2" is entirely located on a steep mountain face; in the aerial photograph the rock appears entirely snow-free; to confirm that it was the case during the acquisition times, low-resolution automatic camera photos acquired from the radar's location were inspected as well as webcam photos located near the "Längenflueberg 1" ROI, showing no appearance of snow during the timespan analyzed. This should explain the temporal and spatial stability of the polarimetric parameters. In this case the dominant scattering mechanism would probably be medium entropy surface scattering. Given the high crosspolar power and the entropy, the surface would probably be very rough; this may explain the lower $\gamma_{(HH-VV)-(HH+VV)}$ compared to "Bisgletscher 1" [4].

An alternative explanation for the observed entropy and α would be the presence of many individual even bounce scattering processes in a resolution cell, for example between individual boulders much smaller than the pixel's size; this corresponds to *Zone 4: Medium Entropy Multiple Scattering* in the Cloude-Pottier classification. This hypothesis is supported by the observation of a stronger HH component compared to the VV power, a signature typical for even-bounce scattering.

This ROI shows one of the highest entropy observed: this could perhaps be attributed to the presence of several scattering mechanism at the same time.

The observed diurnal variations in the backscatter power are presumably related to changes in moisture driven by changing level of solar irradiation [69, 71, 94, 95]; however owing to the lack of better ground measurement a conclusive interpretation cannot be made.

- "Bi 3" is classified as glacier in the land cover map; the aerial photograph shows that the polygon is mostly covered in crevasses and that the ice is gray; presumably covered in debris. This factor, together with the short wavelength make significant penetration in the ice volume appears unlikely: at Ku-Band a penetration depth in the order of meters is observed at best with very dry snow and ice [96, 97]. This in turn would imply that volume scattering from the glacier ice should be excluded as an explanation for the observed high entropy and HV backscatter; this is supported by the relatively high copolar coherence magnitude, which is not expected of a random volume.

Medium entropy scattering from the rough surface would be a more plausible mechanism generating the observed levels of entropy and α ; the lower relative HV contribution compared to "Bi 2" and the slightly higher $\gamma_{(HH-VV)-(HH+VV)}$ would suggest a less rough surface.

The diurnal variations in backscatter power are probably related to change in the ice surface water content, which in turn are correlated with solar radiation, which drives changes in air temperature as well.

- "Bi 4" is located on a small hanging glacier on the flanks of Weisshorn; the observed values of entropy and α at around 0.75 and 55° respectively suggest the classification in the *Zone 4: Medium Entropy Multiple Scattering* of the Cloude-Pottier classification. Considering that the snow surface appears smooth in the aerial photograph and given the high altitude of this ROI, scattering contribution from the ice volume is more likely than in the lower ROIs; this hypothesis would be supported by the dominance of crosspolarized backscatter and by the lower copolar magnitude and its wider distribution compared to the previous ROIs on the Bisgletscher. The lower value

of $\gamma_{(HH-VV)-(HH+VV)}$ compared to the previous glacier ROIs could be another piece of evidence in favor of this explanation: a random volume is rotationally invariant [98]; thus a lower coherence is expected. The diurnal backscatter fluctuations are presumably connected to changes in the snow wetness; however the backscatter seems to only marginally correlate with temperature. However, the weather station used for the comparison is located in Zermatt, much lower on the valley; it is likely that the ice in "Bi 4" is at lower temperature than measured at the weather station. It is plausible that backscatter variations are related to icefalls and new crevasses opening on the surface of the hanging glacier. However, due to the lack of ground truth, this interpretation cannot be tested.

- "Lä 1" is considered "Granular Soil" in the land cover classification; this is confirmed by the aerial photographs, which show that the entire ROI contains only glacial till. The entropy in this ROI is stable and high at around 0.75, the α angle in average 55° ; these values again would suggest a classification in *Zone 4: Medium Entropy Multiple Scattering*. As no vegetation is present, the two most likely mechanisms generating high entropy here would multiple scattering from a dense packing of individual boulders [2] or surface scattering from a very rough surface. The low value of $\gamma_{(HH-VV)-(HH+VV)}$ could indicate an azimuthally symmetric scattering process, as would be expected from a random medium; this would be the case for both mechanisms described above. The higher level of *HH* backscatter compared to *VV* would suggest the dominance of even-bounce scattering, as already remarked in "Bisgletscher 2"; the difference in backscatter coefficients could explain the lower copolar coherence.

Diurnal variations in backscatter are again observed; they presumably relate to changes in soil moisture [73, 75] driven by solar radiation; however given the lack of ground measurement these conclusions are speculative at best.

- "Lä 2" is classified as "Closed Forest"; aerial photographs show a sparse forest growing on scree. *H* is high at 0.75 and α is around 55° . In this case, given the surface cover, the classification in *Zone 4: Medium Entropy Multiple Scattering* seems the most reasonable: vegetation scattering, either from the canopy volume or dihedral interactions under the canopy followed from propagation in the vegetation volume contribute significantly to the scattering in this ROI. Evidence for the dominance of even bounce scattering is the *HH* component being larger than *VV* and by the copolar phase difference being lower with a lower magnitude. This interpretation is supported by the very low value of $\gamma_{(HH-VV)-(HH+VV)}$ that would suggest an azimuthally symmetric medium as it is expected from a vegetation volume; the low copolar coherence and its wide distribution are also suggesting increased scattering randomness.

Once again daily variations in the backscatter are observed; they could be related to changes in vegetation water content [68, 99–101]. These variations correlate with temperature, but this correlation could be due to a common third factor such as variation in solar radiation drying the vegetation or to precipitation which is in turn likely correlated with changes in air temperature.

- "Mi 1" consists entirely of short grass; the observed values of *H* and α would suggest a classification between *Zone 5: Medium Entropy Vegetation Scattering* and *Zone 4: Medium Entropy Multiple Scattering*; the most likely mechanism being scattering from a distribution of

anisotropic scatterers with a dominant orientation; this is reasonable considering the low level of $\gamma_{(HH-VV)-(HH+VV)}$; suggesting an azimuthally symmetric distributed medium with a certain degree of randomness, which would cause higher entropy and a larger amount of HV backscatter. The higher level of VV compared to HH and the low copolar phase difference point to predominantly vertically oriented structures, such as it is expected from blades of grass; the considerable amount of HV backscatter suggest secondary scattering mechanisms; either rough soil or a certain randomness in the vegetation orientation distribution, which could explain the low $\gamma_{(HH-VV)-(HH+VV)}$ and copolar coherence.

Regular diurnal variations in the total backscatter power are observed again; the most likely driver for these changes being soil moisture and vegetation water content.

Since most parameters except for the total backscatter power do not significantly change over the course of time, analyzing a single date should give a good idea of its spatial variability. In this case July 14, 06:00 UTC was selected. In the plot of Figure 4.4b the entropy is never below 0.5 in average all for any of the ROIs. This observation also applies to the scene as a whole: the areas of lower entropy being mostly located in proximity of the glacier and on individual pixels where a very strong scatterer is found. Similarly, the glacier is the area displaying the lowest α angle, suggesting the dominance of surface scattering, which appears blue in the Pauli RGB composite. At the same locations $\gamma_{(HH-VV)-(HH+VV)}$ attains its highest value, which indicates a smoother surface; these observations would suggest a dominance of lower entropy surface scattering, presumably because the glacier's surface is wet during summer.

Crosspolar backscatter dominates in most of the scene, seeing as predominance of green in the Pauli RGB composite. One exception is the region at the left of "Bi 3", where a set of pixels with low entropy are seen, presumably dihedral scattering from highly reflective objects, seen as individual bright red pixel in the pauli composite. Comparison with aerial photographs show the presence of several avalanche protection structures where low-entropy dihedral scattering appears likely.

CHUTZEN

Similarly as observed for the "Bisgletscher" dataset, a high average entropy is seen for distributed target, as displayed in Figure 4.9a. Individual pixels display an entropy closer to zero: they correspond to bright scatterers like single buildings, as it can be seen in the Pauli RGB composite of Figure 4.9c. Other than these exceptions, most of the scene would be again classified in the *Medium Entropy Scattering* region according to scheme proposed by Cloude and Pottier. Unlike the Bisgletscher dataset, more variability in α is observed in Figure 4.9b.

In an attempt to understand the possible physical mechanisms at the root of the observed parameters, the analysis made for the Bisgletscher observations will be repeated for the Chutzen dataset. Since only one acquisition is available for the latter, instead of the time-series analysis discussing both spatial and temporal patterns, the distribution of the parameters within each ROI will be discussed with the help of histograms.

- The land cover classification for "Er 1" is "Consolidated Surfaces". The very wide distribution of the Cloude-Pottier parameters, of the backscatter and of $\gamma_{(HH-VV)-(HH+VV)}$ do not permit to

assign a single unambiguous scattering mechanism to the pixels in this ROI. This appears reasonable considering the variety of building types and orientations observed in the photo of Figure 4.3b.

The low entropy pixels observed inside this ROI in Figure 4.9a presumably correspond to strong scattering from individual buildings, which are seen as the bright points in the RGB composite (Figure 4.9c). From the map of the mean α angle it appears that these interactions are either direct scattering from edges or triple scattering in corners—seen as the points of low α —or odd-bounce scattering between the ground and the buildings—seen as the points where α is close to 90° —.

- "Go 1" consists of a single field and is classified as "Grass and Herb Vegetation". The Cloude-Pottier histogram is concentrated at the edge of *Zone 4: Medium Entropy Multiple Scattering*. This classification is compatible with the observed distribution of backscatter: in the Cloude-Pottier classification vegetation is assumed to scatter as a cloud of anisotropic, randomly oriented dipoles. The higher VV contribution and the high copolar coherence magnitude suggest a dominance of vertical structures such as stalks and blades of grass, the significant HV contribution and the high entropy could then be explained through a wide distribution of dipole orientation angles around the predominantly vertical orientation or by the presence of secondary scattering mechanisms, for example the combination of predominantly vertical stalks under a random canopy [102].

$\gamma_{(HH-VV)-(HH+VV)}$ is part of the evidence pointing at vegetation scattering: lower values are indicative of azimuthal symmetry, which is observed in vegetation volumes [76].

Another cause for the higher VV backscatter could be the effect of Bragg scattering, perhaps from regular tilling rows the fields, exposed after the harvest [103]. The concentration of copolar phase difference close to zero, and the low $\gamma_{(HH-VV)-(HH+VV)}$ support this interpretation; the latter parameter being considered to be an indicator of soil roughness. In this case the high HV contribution and the entropy are due to secondary scattering from short vegetation or to increasingly random distribution of soil facets [4].

- "Hi 1" has the same land cover classification as "Go 1": "Grass and Herb Vegetation", confirmed by Figure 4.3b. The median values of H and α would classify the ROI in *Zone 4: Medium Entropy Multiple Scattering*. The crosspolar power is significantly stronger than the copolar one; compared to the previous case the lack of a preferential orientation in the vegetation could explain the smaller difference between HH and VV and the larger crosspolar power. The low value of $\gamma_{(HH-VV)-(HH+VV)}$ indicate again the presence of scattering symmetries, typical of natural surfaces.

As discussed for "Go 1" medium entropy surface scattering from a rough soil, presumably rougher than in the previous ROI, could cause the higher entropy and the wider distribution of copolar phase differences.

- "Mo 1" is classified as the "Grass and Herb Vegetation". The values of H and α suggest a *Zone 6: Medium Entropy Surface Scattering* classification in the Cloude-Pottier plane. In this case the

median copolar backscatter is higher than the crosspolar and α is lower; this suggests that surface scattering from a relatively smooth surface could be the most likely mechanism in this ROI. This is supported by the low $\gamma_{(HH-VV)-(HH+VV)}$ and the high copolar coherence magnitude and very narrow, zero-mean copolar phase difference distribution, typical of surface scattering from smooth surfaces.

Given the date of acquisition, this appears plausible since many summer crops would have been harvested by mid September. However, the lack of ground truth data does not permit clear conclusions.

- "Mü 1" is located on a residential area. The distribution of α and H is very wide and does not allow the assignment of a single scattering mechanism to the pixels in this ROI; this is seen in the very broad histogram of backscatter as well. Likely the ROI contains a mixture of many scattering types, from low entropy scattering by buildings to vegetation scatter from trees and gardens. An interesting observation is a peak in the HV power approximately 5 dB lower than the copolar peak: this could be related to the weaker secondary scattering from vegetated surfaces, whose radar cross section is smaller than the highly reflective buildings.
- "Ut 1" covers a forest; the Cloude-Pottier parameters indicate a classification in *Zone 4: Medium Entropy Multiple Scattering*: however double bounces followed by propagation in the vegetation volume seems rather unlikely considering the very shallow incidence angle, at which penetration into the forest appears difficult, and the very similar HH and VV powers. Most of the scattering is from the vegetation canopy, which appears either as a very rough surface or as a random volume, depending on the penetration depth. $\gamma_{(HH-VV)-(HH+VV)}$ is observed to be low, suggesting an azimuthally symmetrical volume, as it would be expected from vegetation canopies. The low copolar coherence magnitude is typical of random volumes, as is the wide distribution of copolar phase differences [104].

In the case of the Chutzen dataset, the entropy appears to be slightly lower than observed for the Bisgletscher data: this may be due to the small slant range distance of the scene, leading to a reduced noise level. Some points with very low entropy can be seen in near range and at the middle of the scene: they correspond to individual houses or to the trihedral corner reflectors. These are visible in the α map as well, as it is very close to zero for odd-bounce scattering. In the case of built-up areas the main interaction can be expected to be either direct scattering from the edges of buildings or double-bounce scattering between the walls and the ground.

The relatively high entropy and α observed in the rest of the scene suggest that the main dominant scattering mechanism corresponds to *Zone 4: Medium Entropy Multiple Scattering*; this is compatible with the observed $\gamma_{(HH-VV)-(HH+VV)}$, which is low except at locations of very low entropy. Since the land cover class of most of the scene is either pasture, farmland or forest, it is reasonable to expect medium entropy surface scattering to be the most dominant contribution: these surfaces are presumably azimuthally symmetrical, as it can be expected for most natural surfaces.

4.4.2 Noise

Noise in the radar device and antennas can increase the entropy of low-entropy scatterers: Suppose all polarimetric channels of the radar to be equally affected by noise with standard deviation σ_n ; moreover assume that the observed scatterer is not depolarizing and can be represented by a scattering matrix \mathbf{S} . Then, the estimated coherency matrix $\hat{\mathbf{T}}$ is:

$$\hat{\mathbf{T}} = \mathbf{T} + \mathbf{I}\sigma_n. \quad (4.2)$$

Since the target is not depolarizing, \mathbf{T} is a singular matrix and the entropy of \mathbf{T} is 0. However, the entropy of the observed coherency matrix $\hat{\mathbf{T}}$ is:

$$H(\hat{\mathbf{T}}) = \frac{2}{SNR+3} \log_3 \left(\frac{1}{SNR+3} \right) - \frac{SNR+1}{SNR+3} \log_3 \left(\frac{SNR+1}{SNR+3} \right) \quad (4.3)$$

where the signal-to-noise ratio (SNR) is defined as the ratio of the sole nonzero eigenvalue of \mathbf{T} and of the noise standard deviation σ_n . This function is monotonously decreasing in the SNR; the entropy will approach zero for infinite SNR; this shows that assuming *equal* noise power in all polarizations would cause an increase in estimated entropy. This entropy however is not directly caused by depolarization in the imaged targets.

In the case of unequal noise powers, when different channels experience other levels of noise, this is not longer true: now the entropy depends on the relative noise powers. Therefore, if a depolarizing target is observed a large imbalance in noise power may even lower the estimated entropy by biasing one of the eigenvalues of $\hat{\mathbf{T}}$. A formula for the entropy in this situation –where each channel is affected by different noise levels– cannot be provided since there are no closed-form methods to compute the eigenvalue spectrum of sums of Hermitian matrices.

The effect of measurement noise on the observed entropy was assessed by estimating the noise equivalent radar cross section (noise equivalent σ_0 or NESZ) from 50 acquisitions in the Bisgletscher dataset, using the pixels located in areas of radar shadow. The result of this analysis show that the crosspolar channels — HV and VH — have a NESZ 10 dB larger than the copolar channels.

Thus, it is reasonable to conclude that in the case of KAPRI polarized noise — or colored noise, where the polarimetric channels are affected by different noise powers— is not the main factor increasing the entropy. This can be seen by considering of the entropy maps the Pauli RGB composites: in areas affected by radar shadow, for example immediately on top of the "Bi 1" ROI, the entropy is appreciably lower, closer to 0.6.

A simulation, was performed by generating 1000 realizations of multivariate colored Gaussian noise with the HV power 10 dB stronger than both VV and HH , adding these to a deterministic, zero-entropy scattering vector, from which \mathbf{T} was estimated an averaged over the realizations of the noise. The result of this simulation was an entropy of 0.6; very close to the entropy estimated in areas affected radar shadows.

Since the entropy in non-shadow areas is higher, it can be concluded that noise alone is not sufficient to explain the observed values of H .

4.4.3 Mixing of Scattering Processes Due to Multilooking

The spatial averaging or *multilooking* needed to estimate the coherency matrix \mathbf{T} from the measured scattering matrix data can also contribute to increased entropy [81, 105] values:

Assume that N pixels within a spatial averaging window represent N different non-depolarizing scatterers, i.e. their true entropy is 0 because they represent deterministic scattering processes, each of which can be described by a scattering matrix \mathbf{S}_i .

Each of these coherency matrices \mathbf{T}_i will have only one nonzero eigenvalue and will have entropy $H = 0$. However, the entropy estimated by spatial averaging these N matrices will be nonzero since it will be the average of N different rank one coherency matrices \mathbf{T}_i . Thus, spatial averaging may inflate the estimates of the entropy.

The problem can be expected to be particularly severe at high resolution, where every pixel can correspond to scatterers with widely different orientations, shapes and dielectric constants.

To minimize the biasing effect of multilooking, several adaptive multilooking techniques were proposed [106–111]; they try to preserve spatial resolution and avoid mixing pixels belonging to different scattering types.

Another way to avoid the mixing of different scattering types caused by spatial multilooking is to estimate the coherency matrix by averaging pixels in time [25, 81, 112], which is only possible when time-series data is available.

The biasing effect of spatial mixing on the estimation of H is investigated by comparing the estimated obtained with the latter method to these obtained with two different spatial filters:

- H_{boxcar} : A 20×2 boxcar filter.
- H_{IDAN} : IDAN (Intensity driven adaptive neighborhood) region Growing Filter [111] with a maximum region size of 40 pixels.
- $H_{temporal}$: A temporal average of covariance matrices [25, 81].

The temporal average $H_{temporal}$ does not precisely correspond to the one proposed in [81]: in the latter, the elements of the scattering matrix are acquired in multiple passes; covariance matrices are then built from the stacked channels. In that case, temporal decorrelation directly affects $H_{temporal}$. However in the data used for this paper all channels of \mathbf{S} are acquired simultaneously and the covariance/coherence matrix are estimated from the average of single-look matrices obtained from scattering matrices measured at different instants of time, removing the direct effect of temporal decorrelation¹.

In order to obtain approximately the same number of looks as employed in the two spatial averages, similarly 40 acquisitions are used to estimate the $H_{temporal}$ and the region size for the IDAN filter is likewise set to 40 pixels.

¹Although not its indirect effect through changes in the imaged scene that may increase the entropy.

A comparison of entropy estimate for the Bisgletscher dataset is displayed in Figure 4.10: In Figure 4.10a H_{boxcar} is shown, Figure 4.10c displays H_{IDAN} for the same dataset and Figure 4.10b displays the temporal estimate $H_{temporal}$. This comparison is not possible for the Chutzen dataset because only one acquisition is available.

The entropy obtained with the IDAN filter H_{IDAN} is slightly lower than the entropy estimated with the boxcar average H_{boxcar} . However the contrast between different areas/land cover types is not significantly improved. On the contrary, H_{IDAN} appears grainier and spatially less smooth. The difference between the glacier and the surrounding rocks seems to be lower in H_{IDAN} than in H_{boxcar} , where near "Bi 3" the difference is visible and reflected by the change between green and blue in the Pauli RGB composite. The lower entropy contrast of the IDAN filter may be due to the fact that only the total backscatter power and not the polarimetric information is used to test the similarity of pixels that are deemed to belong to the same region and are averaged together. Thus, in some cases the IDAN filter might not be able to reduce spatial mixing; for example at the edges where two different scattering types with similar total backscatter power meet.

The temporal entropy $H_{temporal}$ is much lower than both H_{boxcar} and H_{IDAN} in correspondence of the glacier: the glacier's outline can be seen as it contrasts with the surrounding rocks left of the "Bi 3" ROI.

However, this observation is not sufficient to prove that spatial mixing is the only factor causing of high entropy: the glacier's high flow velocity —up to $2 \frac{\text{m}}{\text{day}}$ — and weather-driven changes in the ice surface are likely to cause changes in the scattering response, thereby increasing $H_{temporal}$.

The entropy of rocky areas next to the "Lä" ROIs may be underestimated by $H_{temporal}$. The dominance of HV backscatter would suggest the presence of depolarizing scattering: it is unlikely that orientation effects [112] that can produce significant HV backscatter are seen on such a large scale in natural terrain.

Thus, if the presence of depolarizing scattering is assumed; the temporal stability of the scattering response for individual pixels could explain the discrepancy between $H_{temporal}$ and the spatial entropy estimates.

As an example, if the X-Bragg scattering model [4] is used to explain the scattering for a certain pixel and if its surface properties and roughness do not change over time —as it likely the case for rough, dry soil over the course of a few hours— then the observed scattering matrix will remain the same up to a noise contribution and temporal estimation of the entropy will give low values, effectively hiding the depolarization.

Ergodicity does not apply in this case: averaging the coherency matrix for a single pixel over time is not equivalent to the average of coherency matrices of individual scattering facets over the distribution of orientation angles, which are used to model the depolarization in the extended Bragg scattering model.

The same arguments applies to volume scattering: if dielectric properties, shape and orientation of particles in a random volume do not change in time, the entropy estimated with temporal averaging will

be very low even though the scattering process is depolarizing in a strict sense, when the entropy is computed over the distribution of the particles [76]. This situation is unlikely to be observed: for vegetated areas as "Mi 1"; the effect of wind and changes in vegetation water content are presumably strong enough to change the scattering properties of vegetation from acquisition to acquisition, producing a high $H_{temporal}$.

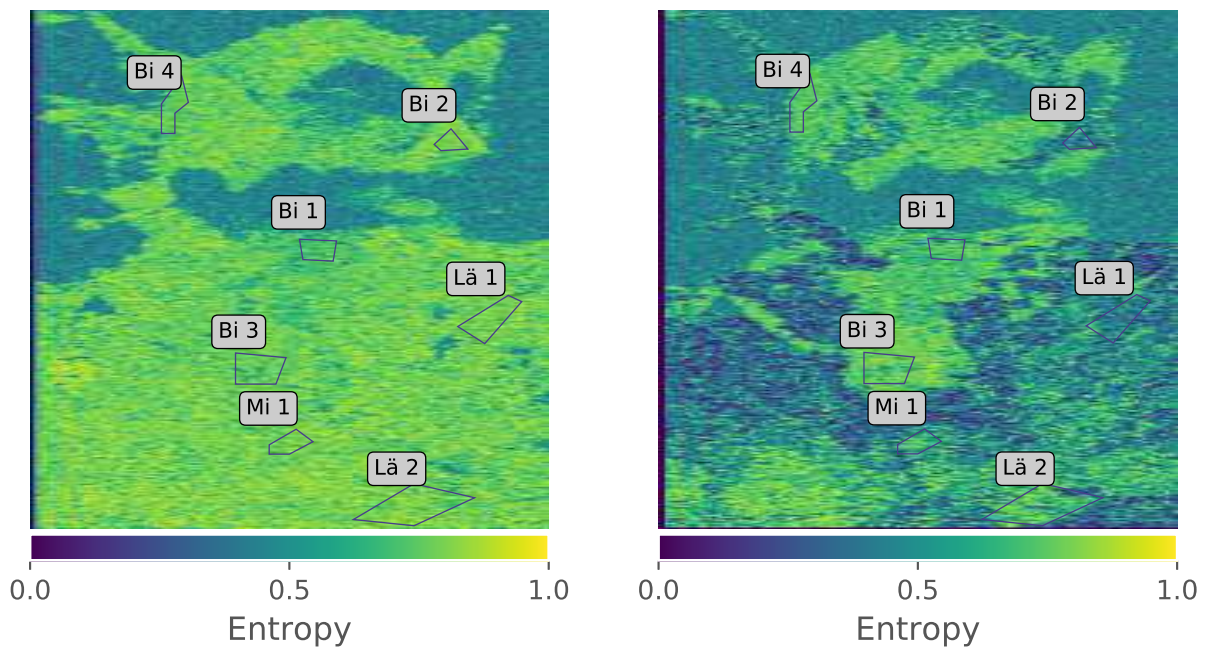
This analysis suggests that, depending on the type of target and the acquisition mode, neither temporal nor spatial averages are completely adequate to estimate entropy. Since $H_{temporal}$ is very sensitive to changes in the scattering properties, its adequacy to characterize depolarizing scattering processes is doubtful when the average is performed using images far apart in time: the samples over which the average is made do not strictly represent the same objects anymore if the surface undergoes large changes, as it can be suspected to happen for the glacier or for vegetated areas.

4.4.4 Mixing Within a Resolution Cell

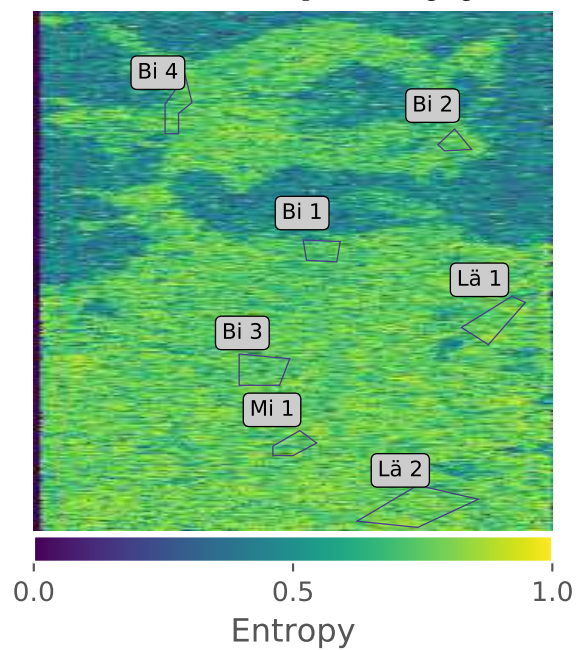
The combination of different scatterers due to a large resolution cell size is another mechanism that may generate high entropy. The level of entropy is affected by the number and types of targets constituting a resolution cell: if a cell contains a low entropy scatterer with a large radar cross section such as a trihedral reflector, the entropy will be low. Otherwise, if the cell contains several scatterers of similar radar reflectivity but differing shape and orientation, the entropy will be higher. Since its estimation requires averaging, if neighboring cells also comprise a mixture of different targets with similar properties, the spatial estimate of entropy will be high.

This effect is controlled by the wavelength: substantial scattering comes from objects larger than several wavelengths. Therefore, as the ratio of wavelength to resolution cell size decreases, the entropy will likely increase as the number of scatterers per resolution cell is expected to increase, which will in turn increase the entropy.

This mechanism could explain the high entropy observed in both datasets: the resolution cells are several orders of magnitude larger than the wavelength and many scattering centers will be observed in a pixel, particularly on non-smooth natural surfaces. Assuming these surfaces to be distributed targets extended over several pixels—so that the effect of mixing of different targets due to multilooking can be excluded—, mixing within the cell would result in high entropy estimates except for those cells where a scatterer has a scattering crosssection significantly larger than other objects in the same pixel and in its neighboring cells in the averaging window, for example a single building, a corner reflector or a large boulder.



(a) H_{boxcar} : Cloude-Pottier entropy estimated by spatial averaging. (b) $H_{temporal}$: Cloude-Pottier entropy estimated by temporal averaging.



(c) H_{IDAN} : Cloude-Pottier entropy estimated with spatial averaging using the IDAN region-growing filter.

Figure 4.10: Comparison between the entropy estimated by spatial averaging (a), the estimate made using temporal averaging (b) and the estimate obtained using the IDAN filter (c).

4.5 CONCLUSIONS

This paper presents an analysis of Ku-Band polarimetric data from two test sites acquired with the KAPRI polarimetric terrestrial radar. The first data sets is a time-series of the Bisgletscher, an alpine glacier in the Swiss Alps, acquired in the summer of 2015. The other dataset was acquired in September 2016 in an agricultural area near Münsingen, Switzerland.

The main characteristic of both datasets is a high Cloude-Pottier entropy parameter H ; higher than 0.5 for natural targets and only observed to be close to 0 for bright, isolated scatterers such as buildings or trihedral corner reflectors. The high entropy is accompanied by an α angle above 50° and a high fraction of crosspolarized backscatter. These values suggest the dominance of depolarizing scattering mechanisms; this interpretation is realistic at the light of the dominance of natural surfaces in both scenes. These mechanisms may be in the form of either volume scattering from vegetation or ice or surface scattering from surfaces that are rough relative to the wavelength, as rock faces or rough soils. However, effects other than depolarizing scattering can cause high entropy to be observed [81, 112].

- Thermal noise in the radar electronics is known to increase the entropy; this explanation is unlikely since the estimated noise equivalent normalized radar crosssection of KAPRI shows that the copolar and the crosspolar channels are affected by different noise levels. Imbalanced, uncorrelated noise should lower the entropy by biasing the eigenvalue of the covariance matrix, but the opposite is observed.
- Spatial multilooking is necessary to estimate depolarization parameters assuming spatial ergodicity. The spatial average may bias the entropy if the scene is very heterogeneous and spatially adjacent pixels do not represent realizations of the same extended target [81].

To test the spatial mixing hypothesis three averaging methods are applied: a boxcar spatial average, the refined IDAN region growing filter, which should reduce the mixing of dissimilar pixels and a temporal average, where pixels are averaged solely along time using several acquisitions taken during the same day. The IDAN and boxcar filter give similar spatial patterns in the entropy, while the temporal average gives much smaller estimates. While this would seem to prove spatial mixing to be the cause of high entropy, there are several reasons that suggest otherwise. Rocks show a high entropy (0.75) in the spatial estimates and a very low entropy in the temporal estimate. High values are observed on ice and vegetation regardless of the chosen method. The difference in entropy between estimation methods and land cover types is suspected to stem from non-ergodicity: rocks are very stable scatterers at the timescales analysed in this work; if the dominant scattering mechanism does not change over the course of time, the samples that will be averaged will be very similar, giving a lower entropy. On the other hand, the scattering properties change radically in time for vegetation and ice, leading to high values of the temporal entropy.

In conclusion, the temporal estimate of entropy is closely related to the temporal stability of scattering processes and should not be assumed to measure depolarization in a strict sense. By the same token, the very similar entropy estimates obtained with the IDAN and boxcar filters suggest that spatial mixing is not likely to be the main cause of high entropy in the datasets analysed.

- Another potential source of increased entropy is the relationship of the resolution cell size to the wavelength. Using a wavelength of 17 mm with pixel sizes between 10 m^2 and 50 m^2 , it is likely that several scatterers of different orientation, size and dielectric properties are observed in a single resolution cell in natural terrain, increasing the scattering randomness and hence the entropy. This point calls for detailed investigation, which are not possible at this time: for example by imaging the same distributed target at different wavelengths with similar resolutions.
- Finally, the effect of incidence angle should also be considered. It is known that for steeper incidence angles the scattering tends to be less diffuse and thus a lower level of depolarization and hence a lower entropy should be observed [113, 114]. In TRI usually very shallow incidence angles are employed, which could contribute to the increase of the observed entropy. This effect could not be tested with the available datasets given the small range of incidence angles employed. This again calls for more specific experiments in order to assess its influence in the estimated entropy.

In summary, the most likely cause of the observed polarimetric parameters seems the presence of depolarizing scattering mechanisms. This is plausible considering the large percentage of natural terrain in the scene. These terrain types are normally modeled as random medias; this randomness is the physical source of the crosspolarized backscatter and of the high entropy. Another factor contributing to the increased entropy is the interplay of the resolution cell size in relation to the employed wavelength, causing mixing of polarimetric responses at the time of the acquisition [81]. The high entropy observed at Ku-Band reduces the separability of scattering types, reducing its suitability for land cover classification compared to data acquired at larger wavelengths. However, more specific experiments are necessary to separate the above mechanisms before coming at a conclusion regarding the applications and the value added by polarimetric observations in Ku-Band TRI.

REFERENCES

- [1] S. Baffelli, O. Frey, and I. Hajnsek, “Polarimetric analysis of natural terrain observed with a Ku-band terrestrial radar”, *IEEE Journal of Selected Topics in Applied Earth Observation and Remote Sensing*, 2018, submission ID JSTARS-2018-00992.
- [2] S. Cloude and E. Pottier, “An entropy based classification scheme for land applications of polarimetric SAR”, *IEEE Transactions on Geoscience and Remote Sensing*, vol. 35, pp. 68–78, 1997. DOI: 10.1109/36.551935.
- [3] J.-S. Lee, M. Grunes, T. Ainsworth, L.-J. Du, D. Schuler, and S. Cloude, “Unsupervised classification using polarimetric decomposition and the complex Wishart classifier”, *IEEE Transactions on Geoscience and Remote Sensing*, vol. 37, pp. 2249–2258, 1999. DOI: 10.1109/36.789621.
- [4] I. Hajnsek, E. Pottier, and S. Cloude, “Inversion of surface parameters from polarimetric SAR”, *IEEE Transactions on Geoscience and Remote Sensing*, vol. 41, pp. 727–744, 2003. DOI: 10.1109/TGRS.2003.810702.
- [5] F. T. Ulaby, D. Held, M. C. Donson, K. C. McDonald, and T. B. A. Senior, “Relating polarization phase difference of SAR signals to scene properties”, *IEEE Transactions on Geoscience and Remote Sensing*, vol. GE-25, pp. 83–92, 1987. DOI: 10.1109/TGRS.1987.289784.
- [6] S. Leinss, G. Parrella, and I. Hajnsek, “Snow height determination by polarimetric phase differences in X-band SAR data”, *IEEE Journal of Selected Topics in Applied Earth Observations and Remote Sensing*, vol. 7, pp. 3794–3810, 2014. DOI: 10.1109/JSTARS.2014.2323199.
- [7] K. Papathanassiou and S. Cloude, “Single-baseline polarimetric SAR interferometry”, *IEEE Transactions on Geoscience and Remote Sensing*, vol. 39, pp. 2352–2363, 2001. DOI: 10.1109/36.964971.
- [8] S. Cloude, J. Fortuny, J. Lopez-Sanchez, and A. Sieber, “Wide-band polarimetric radar inversion studies for vegetation layers”, *IEEE Transactions on Geoscience and Remote Sensing*, vol. 37, pp. 2430–2441, 1999. DOI: 10.1109/36.789640.
- [9] G. Parrella, I. Hajnsek, and K. P. Papathanassiou, “Polarimetric decomposition of L-band PolSAR backscattering over the Austfonna ice cap”, *IEEE Transactions on Geoscience and Remote Sensing*, vol. 54, pp. 1267–1281, 2016. DOI: 10.1109/tgrs.2015.2477168.
- [10] I. Hajnsek, “Inversion of surface parameters using polarimetric SAR”, PhD, Friedrich-Schiller-Universität Jena, 2001.
- [11] S. Brown and J. Bennett, “High-resolution microwave polarimetric imaging of small trees”, *IEEE Transactions on Geoscience and Remote Sensing*, vol. 37, pp. 48–53, 1999. DOI: 10.1109/36.739114.
- [12] K. Morrison, J. Bennett, and S. Solberg, “Ground-based C-band tomographic profiling of a conifer forest stand”, *International Journal of Remote Sensing*, vol. 34, pp. 7838–7853, 2013. DOI: 10.1080/01431161.2013.826836.

-
- [13] R. Horn, A. Nottensteiner, A. Reigber, J. Fischer, and R. Scheiber, "F-SAR—DLR's new multifrequency polarimetric airborne SAR", in *Proceedings of the IEEE International Geoscience and Remote Sensing Symposium*, IEEE, vol. 2, IEEE, 2009, pp. II-902. DOI: 10.1109/IGARSS.2009.5418244.
- [14] S. Angelliaume, P. Dubois-Fernandez, P. Dreuillet, H. Oriot, and C. Coulombeix, "SETHI, the ONERA airborne SAR sensor, and his low frequency capability", in *Proceedings of the IEEE International Geoscience and Remote Sensing Symposium*, IEEE, vol. 4, IEEE, 2009, pp. IV-177. DOI: 10.1109/IGARSS.2009.5417343.
- [15] J. van Zyl, R. Carande, Y. Lou, T. Miller, and K. Wheeler, "The NASA/JPL three-frequency polarimetric AIRSAR system", *Proceedings of the IEEE International Geoscience and Remote Sensing Symposium*, 1992. DOI: 10.1109/igarss.1992.576795.
- [16] P. Rosen, S. Hensley, K. Wheeler, G. Sadowy, T. Miller, S. Shaffer, R. Muellerschoen, C. Jones, S. Madsen, and H. Zebker, "UAVSAR: New NASA airborne SAR system for research", *IEEE Aerospace and Electronic Systems Magazine*, vol. 22, pp. 21-28, 2007. DOI: 10.1109/MAES.2007.4408523.
- [17] A. Rosenqvist, M. Shimada, and M. Watanabe, "ALOS PALSAR: Technical outline and mission concepts", in *Proceeding of the International Symposium on Retrieval of Bio- and Geophysical Parameters from SAR Data for Land Applications*, vol. 1, 2004, pp. 1-7.
- [18] L. C. Morena, K. V. James, and J. Beck, "An introduction to the RADARSAT-2 mission", *Canadian Journal of Remote Sensing*, vol. 30, pp. 221-234, 2004. DOI: 10.5589/m04-004.
- [19] W. Boerner, B. yuen Foo, and H. Eom, "Interpretation of the polarimetric co-polarization phase term in radar images obtained with the JPL airborne L-band SAR system", *IEEE Transactions on Geoscience and Remote Sensing*, vol. GE-25, pp. 77-82, 1987. DOI: 10.1109/tgrs.1987.289783.
- [20] R. Iglesias, A. Aguasca, X. Fabregas, J. J. Mallorqui, D. Monells, C. Lopez-Martinez, and L. Pipia, "Ground-based polarimetric SAR interferometry for the monitoring of terrain displacement phenomena—part I: Theoretical description", *IEEE Journal of Selected Topics in Applied Earth Observations and Remote Sensing*, vol. 8, pp. 1-1, 2014. DOI: 10.1109/JSTARS.2014.2360040.
- [21] L. Pipia, X. Fabregas, A. Aguasca, C. Lopez-Martinez, J. J. Mallorqui, and O. Moraline, "Polarimetric temporal information for urban deformation map retrieval", in *Proceedings of the IEEE International Geoscience and Remote Sensing Symposium*, IEEE, 2007, pp. 192-195. DOI: 10.1109/IGARSS.2007.4422762.
- [22] A. Aguasca, A. Broquetas, J. Mallorqui, and X. Fabregas, "A solid state L to X-band flexible ground-based SAR system for continuous monitoring applications", in *Proceedings of the IEEE International Geoscience and Remote Sensing Symposium*, vol. 2, IEEE, 2004, pp. 757-760. DOI: 10.1109/IGARSS.2004.1368512.
- [23] L. Pipia, X. Fabregas, A. Aguasca, C. Lopez-Martinez, J. J. Mallorqui, and O. Mora, "A subsidence monitoring project using a polarimetric GB-SAR sensor", *European Space Agency, (Special Publication) ESA SP*, 2007.

- [24] L. Pipia, “Polarimetric differential SAR interferometry with ground-based sensors”, PhD thesis, Universitat Politècnica de Catalunya, 2009. DOI: 10.803/6951.
- [25] L. Pipia, X. Fabregas, A. Aguasca, and C. Lopez-Martinez, “Polarimetric temporal analysis of urban environments with a ground-based SAR”, *IEEE Transactions on Geoscience and Remote Sensing*, vol. 51, pp. 2343–2360, 2013. DOI: 10.1109/TGRS.2012.2211369.
- [26] R. Iglesias, A. Aguasca, X. Fabregas, J. J. Mallorqui, D. Monells, C. Lopez-Martinez, and L. Pipia, “Ground-based polarimetric SAR interferometry for the monitoring of terrain displacement phenomena—part II: Applications”, *IEEE Journal of Selected Topics in Applied Earth Observations and Remote Sensing*, vol. 8, pp. 1–14, 2014. DOI: 10.1109/JSTARS.2014.2366711.
- [27] R. Iglesias, D. Monells, X. Fabregas, J. J. Mallorqui, A. Aguasca, and C. Lopez-Martinez, “Phase quality optimization in polarimetric differential SAR interferometry”, *IEEE Transactions on Geoscience and Remote Sensing*, vol. 52, pp. 2875–2888, 2014. DOI: 10.1109/TGRS.2013.2267095.
- [28] H. Lee, S.-J. Cho, N.-H. Sung, and J.-H. Kim, “Development of a ground-based synthetic aperture radar system for highly repeatable measurements”, in *The 9th workshop on subsurface electromagnetic measurement*, 2007, pp. 2–6.
- [29] J. Bennett, K. Morrison, A. Race, G. Cookmartin, and S. Quegan, “The UK NERC fully portable polarimetric ground-based synthetic aperture radar (GB-SAR)”, in *Proceedings of the European Conference on Synthetic Aperture Radar*, IEEE, 2000, pp. 2313–2315. DOI: 10.1109/IGARSS.2000.858393.
- [30] J. Bennett and K. Morrison, “Development of a ground-based, polarimetric synthetic aperture radar”, *Proceedings of the IEEE Aerospace Applications Conference*, vol. 4, 139–146 vol.4, 1996. DOI: 10.1109/AERO.1996.499408.
- [31] M.-K. Kang, K.-E. Kim, H. Lee, S.-J. Cho, and J.-H. Lee, “Preliminary result of polarization property analysis using fully polarimetric GB-SAR images”, in *Proceedings of the IEEE International Geoscience and Remote Sensing Symposium*, IEEE, 2010, pp. 4019–4022. DOI: 10.1109/IGARSS.2010.5650762.
- [32] —, “Preliminary results of polarimetric characteristics for C-band quad-polarization GB-SAR images using $H / A / \alpha$ polarimetric decomposition theorem”, *Korean Journal of Remote Sensing*, vol. 25, pp. 531–546, 2009.
- [33] Z.-S. Zhou, W.-M. Boerner, and M. Sato, “Development of a ground-based polarimetric broadband SAR system for noninvasive ground-truth validation in vegetation monitoring”, *IEEE Transactions on Geoscience and Remote Sensing*, vol. 42, pp. 1803–1810, 2004. DOI: 10.1109/TGRS.2004.832248.
- [34] G. Luzi, M. Pieraccini, D. Mecatti, L. Noferini, G. Guidi, F. Moia, and C. Atzeni, “Ground-based radar interferometry for landslides monitoring: Atmospheric and instrumental decorrelation sources on experimental data”, *IEEE Transactions on Geoscience and Remote Sensing*, vol. 42, pp. 2454–2466, 2004. DOI: 10.1109/TGRS.2004.836792.

-
- [35] O. Monserrat, M. Crosetto, and G. Luzi, “A review of ground-based SAR interferometry for deformation measurement”, *ISPRS Journal of Photogrammetry and Remote Sensing*, vol. 93, pp. 40–48, 2014. DOI: 10.1016/j.isprsjprs.2014.04.001.
- [36] C. D. Ventisette, E. Intrieri, G. Luzi, N. Casagli, R. Fanti, and D. Leva, “Using ground based radar interferometry during emergency: The case of the A3 motorway (Calabria region, Italy) threatened by a landslide”, *Natural Hazards and Earth System Science*, vol. 11, pp. 2483–2495, 2011. DOI: 10.5194/nhess-11-2483-2011.
- [37] S. Rödelisperger, G. Läufer, C. Gerstenecker, and M. Becker, “Monitoring of displacements with ground-based microwave interferometry: IBIS-S and IBIS-L”, *Journal of Applied Geodesy*, vol. 4, pp. 41–54, 2010. DOI: 10.1515/jag.2010.005.
- [38] R. Caduff and T. Strozzi, “Terrestrial radar interferometry monitoring during a landslide emergency 2016, Ghirone, Switzerland”, in *Advancing Culture of Living with Landslides*, Springer International Publishing, 2017, pp. 301–309. DOI: 10.1007/978-3-319-53487-9_34.
- [39] B. Lowry, F. Gomez, W. Zhou, M. Mooney, B. Held, and J. Grasmick, “High resolution displacement monitoring of a slow velocity landslide using ground based radar interferometry”, *Engineering Geology*, vol. 166, pp. 160–169, 2013. DOI: 10.1016/j.enggeo.2013.07.007.
- [40] J. Butt, A. Wieser, and S. Conzett, “Intrinsic random functions for mitigation of atmospheric effects in terrestrial radar interferometry”, *Proceedings of JISDM 2016 Vienna*, vol. 11, pp. 89–98, 2016. DOI: 10.1515/jag-2016-0042.
- [41] T. Strozzi, R. Delaloye, H. Raetzo, and U. Wegmüller, “Radar interferometric observations of destabilized rock glaciers”, in *Proceedings of Fringe, 2010*, p. 5. DOI: 10.1126/science.170.3962.1090.
- [42] D. Voytenko, T. H. Dixon, I. M. Howat, N. Gourmelen, C. Lembke, C. L. Werner, S. D. L. Peña, and B. Oddsson, “Multi-year observations of Breiðamerkurjökull, a marine-terminating glacier in southeastern Iceland, using terrestrial radar interferometry”, *Journal of Glaciology*, vol. 61, pp. 42–54, 2015. DOI: 10.3189/2015JogG14J099.
- [43] D. Voytenko, T. H. Dixon, C. Werner, N. Gourmelen, I. M. Howat, P. C. Tinder, and A. Hooper, “Monitoring a glacier in southeastern Iceland with the portable terrestrial radar interferometer”, in *Proceedings of the IEEE International Geoscience and Remote Sensing Symposium*, IEEE, 2012, pp. 3230–3232. DOI: 10.1109/IGARSS.2012.6350736.
- [44] N. Dematteis, G. Luzi, D. Giordan, F. Zucca, and P. Allasia, “Monitoring alpine glacier surface deformations with GB-SAR”, *Remote Sensing Letters*, vol. 8, pp. 947–956, 2017. DOI: 10.1080/2150704X.2017.1335905.
- [45] T. H. Dixon, D. Voytenko, C. Lembke, S. de la Peña, I. Howat, N. Gourmelen, C. Werner, and B. Oddsson, “Emerging technology monitors ice-sea interface at outlet glaciers”, *Eos*, vol. 93, pp. 497–498, 2012. DOI: 10.1029/2012EO480001.

- [46] G. Luzi, M. Pieraccini, D. Mecatti, L. Noferini, G. Macaluso, A. Tamburini, and C. Atzeni, "Monitoring of an alpine glacier by means of ground-based SAR interferometry", *IEEE Geoscience and Remote Sensing Letters*, vol. 4, pp. 495–499, 2007. DOI: 10.1109/lgrs.2007.898282.
- [47] D. Mecatti, L. Noferini, G. Macaluso, M. Pieraccini, G. Luzi, C. Atzeni, and A. Tamburini, "Remote sensing of glacier by ground-based radar interferometry", in *Proceedings of the IEEE International Geoscience and Remote Sensing Symposium*, IEEE, 2007, pp. 4501–4504. DOI: 10.1109/IGARSS.2007.4423856.
- [48] L. Noferini, D. Mecatti, G. Macaluso, M. Pieraccini, and C. Atzeni, "Monitoring of Belvedere Glacier using a wide angle GB-SAR interferometer", *Journal of Applied Geophysics*, vol. 68, pp. 289–293, 2009. DOI: 10.1016/j.jappgeo.2009.02.004.
- [49] P. Riesen, T. Strozzi, A. Bauder, A. Wiesmann, and M. Funk, "Short-term surface ice motion variations measured with a ground-based portable real aperture radar interferometer", *Journal of Glaciology*, vol. 57, pp. 53–60, 2011. DOI: 10.3189/002214311795306718.
- [50] K. E. Allstadt, D. E. Shean, A. Campbell, M. Fahnestock, and S. D. Malone, "Observations of seasonal and diurnal glacier velocities at Mount Rainier, Washington, using terrestrial radar interferometry", *Cryosphere*, vol. 9, pp. 2219–2235, 2015. DOI: 10.5194/tc-9-2219-2015.
- [51] R. Caduff, A. Wiesmann, Y. Bühler, and C. Pielmeier, "Continuous monitoring of snowpack displacement at high spatial and temporal resolution with terrestrial radar interferometry", *Geophysical Research Letters*, vol. 42, pp. 813–820, 2015. DOI: 10.1002/2014gl062442.
- [52] G. Luzi, L. Noferini, D. Mecatti, G. Macaluso, M. Pieraccini, C. Atzeni, A. Schaffhauser, R. Fromm, and T. Nagler, "Using a ground-based SAR interferometer and a terrestrial laser scanner to monitor a snow-covered slope: Results from an experimental data collection in Tyrol (Austria)", *IEEE Transactions on Geoscience and Remote Sensing*, vol. 47, pp. 382–393, 2009. DOI: 10.1109/tgrs.2008.2009994.
- [53] C. Werner, B. Lowry, U. Wegmüller, N. Pugh, G. Schrock, and W. Zhou, "Deformation time-series derived from terrestrial radar observations using persistent scatterer interferometry in Seattle, Washington", in *Proceedings of the IEEE International Geoscience and Remote Sensing Symposium*, IEEE, 2016. DOI: 10.1109/igarss.2016.7730784.
- [54] L. Pipia, A. Aguasca, X. Fabregas, J. J. Mallorqui, C. Lopez-Martinez, and J. Marturia, "Mining induced subsidence monitoring in urban areas with a ground-based SAR", in *2007 Urban Remote Sensing Joint Event*, IEEE, 2007. DOI: 10.1109/urs.2007.371881.
- [55] R. Caduff, F. Schlunegger, A. Kos, and A. Wiesmann, "A review of terrestrial radar interferometry for measuring surface change in the geosciences", *Earth Surface Processes and Landforms*, vol. 40, pp. 208–228, 2015. DOI: 10.1002/esp.3656.
- [56] S. Brown, S. Quegan, K. Morrison, J. Bennett, and G. Cookmartin, "High-resolution measurements of scattering in wheat canopies-implications for crop parameter retrieval", *IEEE Transactions on Geoscience and Remote Sensing*, vol. 41, pp. 1602–1610, 2003. DOI: 10.1109/tgrs.2003.814132.

-
- [57] S. Zwieback, S. Hensley, and I. Hajnsek, "A polarimetric first-order model of soil moisture effects on the DInSAR coherence", *Remote Sensing*, vol. 7, pp. 7571–7596, 2015. DOI: 10.3390/rs70607571.
- [58] S. Baffelli, O. Frey, C. Werner, and I. Hajnsek, "Polarimetric calibration of the Ku-band advanced polarimetric radar interferometer", *IEEE Transactions on Geoscience and Remote Sensing*, vol. 56, pp. 1–17, 2018. DOI: 10.1109/tgrs.2017.2778049.
- [59] C. Werner, T. Strozzi, A. Wiesmann, and U. Wegmüller, "A real-aperture radar for ground-based differential interferometry", in *Proceedings of the IEEE International Geoscience and Remote Sensing Symposium*, IEEE, 2008, pp. 210–213. DOI: 10.1109/IGARSS.2008.4779320.
- [60] A. Meta, "Signal processing of FMCW synthetic aperture radar data", PhD thesis, TU Delft, 2006.
- [61] A. Stove, "Linear FMCW radar techniques", *IEE Proceedings F Radar and Signal Processing*, vol. 139, p. 343, 1992. DOI: 10.1049/ip-f-2.1992.0048.
- [62] B. Sarkar, R. Roy, and C. Reddy, "Deterioration in resolution of a radar using long slotted waveguide antenna", in *Digest on Antennas and Propagation Society International Symposium*, IEEE, 1989, pp. 1740–1742. DOI: 10.1109/aps.1989.135070.
- [63] O. Frey, E. H. Meier, and D. R. Nüesch, "Processing SAR data of rugged terrain by time-domain back-projection", in *SAR Image Analysis, Modeling, and Techniques VII*, vol. 5980, SPIE, 2005, pp. 598007–598007–9. DOI: 10.1117/12.627647.
- [64] O. Frey, M. Santoro, C. L. Werner, and U. Wegmüller, "DEM-based SAR pixel-area estimation for enhanced geocoding refinement and radiometric normalization", *IEEE Geoscience and Remote Sensing Letters*, vol. 10, pp. 48–52, 2013. DOI: 10.1109/lgrs.2012.2192093.
- [65] M. Raymond, M. Wegmann, and M. Funk, "Inventar gefährlicher Gletscher in der Schweiz", ETH Zurich, Tech. Rep., 2003.
- [66] J. Beutel, B. Buchli, F. Ferrari, M. Keller, M. Zimmerling, and L. Thiele, "X-SENSE: Sensing in extreme environments", in *Design, Automation & Test in Europe*, IEEE, 2011, pp. 1–6. DOI: 10.1109/DATE.2011.5763236.
- [67] S. Cloude and E. Pottier, "A review of target decomposition theorems in radar polarimetry", *IEEE Transactions on Geoscience and Remote Sensing*, vol. 34, pp. 498–518, 1996. DOI: 10.1109/36.485127.
- [68] T. van Emmerik, S. C. Steele-Dunne, J. Judge, and N. van de Giesen, "Impact of diurnal variation in vegetation water content on radar backscatter from maize during water stress", *IEEE Transactions on Geoscience and Remote Sensing*, vol. 53, pp. 3855–3869, 2015. DOI: 10.1109/TGRS.2014.2386142.
- [69] J. Shi, C. Xiong, and L. Jiang, "Review of snow water equivalent microwave remote sensing", *Science China Earth Sciences*, vol. 59, pp. 731–745, 2016. DOI: 10.1007/s11430-015-5225-0.
- [70] J. Shi, "Snow water equivalence retrieval using X and Ku band dual-polarization radar", in *Proceedings of the IEEE International Geoscience and Remote Sensing Symposium*, IEEE, IEEE, 2006, pp. 2183–2185. DOI: 10.1109/IGARSS.2006.564.

- [71] F. T. Ulaby and W. H. Stiles, “The active and passive microwave response to snow parameters: 2. water equivalent of dry snow”, *Journal of Geophysical Research: Oceans*, vol. 85, pp. 1045–1049, 1980. DOI: 10.1029/JC085iC02p01045.
- [72] T. Strozzi and C. Mätzler, “Backscattering measurements of alpine snowcovers at 5.3 and 35 GHz”, *IEEE Transactions on Geoscience and Remote Sensing*, vol. 36, pp. 838–848, 1998. DOI: 10.1109/36.673677.
- [73] F. Ulaby, P. Batlivala, and M. Dobson, “Microwave backscatter dependence on surface roughness, soil moisture, and soil texture: Part I-bare soil”, *IEEE Transactions on Geoscience Electronics*, vol. 16, pp. 286–295, 1978. DOI: 10.1109/TGE.1978.294586.
- [74] K. Sarabandi, Y. Oh, and F. Ulaby, “Polarimetric radar measurements of bare soil surfaces at microwave frequencies”, in *Proceedings of the IEEE International Geoscience and Remote Sensing Symposium*, IEEE, vol. 2, IEEE, 1991, pp. 387–390. DOI: 10.1109/IGARSS.1991.579162.
- [75] W. Wagner, C. Pathe, M. Doubkova, D. Sabel, A. Bartsch, S. Hasenauer, G. Blöschl, K. Scipal, J. Martínez-Fernández, and A. Löw, “Temporal stability of soil moisture and radar backscatter observed by the advanced synthetic aperture radar (ASAR)”, *Sensors*, vol. 8, pp. 1174–1197, 2008. DOI: 10.3390/s80201174.
- [76] S. Cloude, *Polarisation: Applications in Remote Sensing*. Oxford University Press, 2009. DOI: 10.1093/acprof:oso/9780199569731.001.0001.
- [77] T. A. Seliga and V. N. Bringi, “Differential reflectivity and differential phase shift: Applications in radar meteorology”, *Radio Science*, vol. 13, pp. 271–275, 1978. DOI: 10.1029/rs013i002p00271.
- [78] G. Parrella, I. Hajnsek, and K. P. Papathanassiou, “On the interpretation of polarimetric phase differences in SAR data over land ice”, *IEEE Geoscience and Remote Sensing Letters*, vol. 13, pp. 192–196, 2016. DOI: 10.1109/LGRS.2015.2505172.
- [79] P. Di Tommaso, M. Chatzou, E. W. Floden, P. P. Barja, E. Palumbo, and C. Notredame, “Nextflow enables reproducible computational workflows”, *Nature Biotechnology*, vol. 35, pp. 316–319, 2017. DOI: 10.1038/nbt.3820.
- [80] Swiss Federal Statistical Office. (2010). Land use statistics 2004/09 based on the land coverage nomenclature NOLC04, [Online]. Available: <https://www.geocat.ch/geonetwork/srv/eng/catalog.search#/metadata/b53c03bb-a168-491f-b266-c7e9ec0af320>.
- [81] F. Weissgerber, E. Colin-Koeniguer, N. Trouve, and J.-M. Nicolas, “A temporal estimation of entropy and its comparison with spatial estimations on PolSAR images”, *IEEE Journal of Selected Topics in Applied Earth Observations and Remote Sensing*, vol. 9, pp. 3809–3820, 2016. DOI: 10.1109/jstars.2016.2555243.
- [82] A. Freeman and S. Durden, “A three-component scattering model for polarimetric SAR data”, *IEEE Transactions on Geoscience and Remote Sensing*, vol. 36, pp. 963–973, 1998. DOI: 10.1109/36.673687.

-
- [83] S. Ito, T. Oguchi, T. Iguchi, H. Kumagai, and R. Meneghini, "Depolarization of radar signals due to multiple scattering in rain", *IEEE transactions on geoscience and remote sensing*, vol. 33, pp. 1057–1062, 1995. DOI: 10.1109/36.406691.
- [84] R. T. Shin and J. A. Kong, "Radiative transfer theory for active remote sensing of a homogenous layer containing spherical scatterers", *Journal of Applied Physics*, vol. 52, pp. 4221–4230, 1981. DOI: 10.1063/1.329271.
- [85] D. Bricout and C. Brosseau, "Multiply scattered waves through a spatially random medium : Entropy production and depolarization", *Journal de Physique I*, vol. 2, pp. 2047–2063, 1992. DOI: 10.1051/jp1:1992266.
- [86] M. Boregaud and J. Noll, "Analysis of theoretical surface scattering models for polarimetric microwave remote sensing of bare soils", *International Journal of Remote Sensing*, vol. 15, pp. 2931–2942, 1994. DOI: 10.1080/01431169408954293.
- [87] M. F. Chen and A. K. Fung, "A numerical study of the regions of validity of the Kirchhoff and small-perturbation rough surface scattering models", *Radio Science*, vol. 23, pp. 163–170, 1988. DOI: 10.1029/rs023i002p00163.
- [88] S.-B. Kim, H. Huang, T.-H. Liao, and A. Colliander, "Estimating vegetation water content and soil surface roughness using physical models of L-band radar scattering for soil moisture retrieval", *Remote Sensing*, vol. 10, p. 556, 2018. DOI: 10.3390/rs10040556.
- [89] S.-E. Park, W. M. Moon, and D. Kim, "Estimation of surface roughness parameter in intertidal mudflat using airborne polarimetric SAR data", *IEEE Transactions on Geoscience and Remote Sensing*, vol. 47, pp. 1022–1031, 2009. DOI: 10.1109/tgrs.2008.2008908.
- [90] O. Frey, C. L. Werner, R. Caduff, and A. Wiesmann, "A time series of SAR tomographic profiles of a snowpack", *Proceedings of the European Conference on Synthetic Aperture Radar*, pp. 726–730, 2016.
- [91] O. Frey, C. L. Werner, R. Caduff, and A. Wiesmann, "A time series of tomographic profiles of a snow pack measured with SnowScat at X-/Ku-band", in *Proceedings of the IEEE International Geoscience and Remote Sensing Symposium*, IEEE, 2016. DOI: 10.1109/igarss.2016.7728995.
- [92] O. Frey, C. L. Werner, and A. Wiesmann, "Tomographic profiling of the structure of a snow pack at X-/Ku-band using SnowScat in SAR mode", in *Proceedings of the European Radar Conference*, vol. 1, IEEE, 2015, pp. 1–4. DOI: 10.1109/EuRAD.2015.7346227.
- [93] J. M. Lopez-Sanchez, J. D. Ballester-Berman, and S. R. Cloude, "Monitoring and retrieving rice phenology by means of satellite SAR polarimetry at X-band", in *Proceedings of the IEEE International Geoscience and Remote Sensing Symposium*, IEEE, 2011. DOI: 10.1109/igarss.2011.6049781.
- [94] W. H. Stiles and F. T. Ulaby, "The active and passive microwave response to snow parameters: 1. wetness", *Journal of Geophysical Research: Oceans*, vol. 85, p. 1037, 1980. DOI: 10.1029/JC085iC02p01037.

- [95] C. Mätzler, “Applications of the interaction of microwaves with the natural snow cover”, *Remote sensing reviews*, vol. 2, pp. 259–387, 1987. DOI: 10.1080/02757258709532086.
- [96] R. Willatt, K. Giles, S. Laxon, L. Stone-Drake, and A. Worby, “Field investigations of Ku-band radar penetration into snow cover on antarctic sea ice”, *IEEE Transactions on Geoscience and Remote Sensing*, vol. 48, pp. 365–372, 2010. DOI: 10.1109/tgrs.2009.2028237.
- [97] R. Willatt, S. Laxon, K. Giles, R. Cullen, C. Haas, and V. Helm, “Ku-band radar penetration into snow cover on arctic sea ice using airborne data”, *Annals of Glaciology*, vol. 52, pp. 197–205, 2011. DOI: 10.3189/172756411795931589.
- [98] J.-S. Lee and E. Pottier, *Polarimetric Radar Imaging: From Basics To Applications*. CRC press, 2009. DOI: 10.1201/9781420054989.
- [99] B. Brisco, R. Brown, K. J., G. Sofko, and M. Mckibben, “The diurnal pattern of microwave backscattering by wheat”, *Remote Sensing of Environment*, vol. 34, pp. 37–47, 1990. DOI: 10.1016/0034-4257(90)90082-W.
- [100] M. Satake and H. Hanado, “Diurnal change of Amazon rain forest σ^0 observed by Ku-band spaceborne radar”, *IEEE Transactions on Geoscience and Remote Sensing*, vol. 42, pp. 1127–1134, 2004. DOI: 10.1109/tgrs.2004.825589.
- [101] E. P. W. Attema and F. T. Ulaby, “Vegetation modeled as a water cloud”, *Radio science*, vol. 13, pp. 357–364, 1978. DOI: 10.1029/RS013i002p00357.
- [102] M. Pichierri, I. Hajnsek, S. Zwieback, and B. Rabus, “On the potential of polarimetric SAR interferometry to characterize the biomass, moisture and structure of agricultural crops at L-, C- and X-bands”, *Remote Sensing of Environment*, vol. 204, pp. 596–616, 2018. DOI: 10.1016/j.rse.2017.09.039.
- [103] H. McNairn, C. Duguay, B. Brisco, and T. J. Pultz, “The effect of soil and crop residue characteristics on polarimetric radar response”, *Remote Sensing of Environment*, vol. 80, pp. 308–320, 2002. DOI: 10.1016/s0034-4257(01)00312-1.
- [104] D. Evans, T. Farr, J. van Zyl, and H. Zebker, “Radar polarimetry: Analysis tools and applications”, *IEEE Transactions on Geoscience and Remote Sensing*, vol. 26, pp. 774–789, 1988. DOI: 10.1109/36.7709.
- [105] J.-S. Lee, T. L. Ainsworth, J. Kelly, and C. Lopez-Martinez, “Evaluation and bias removal of multi-look effect on entropy/alpha/anisotropy”, in *Proceedings of the IEEE International Geoscience and Remote Sensing Symposium*, IEEE, IEEE, 2007, pp. 172–175. DOI: 10.1109/IGARSS.2007.4422757.
- [106] J.-S. Lee, M. Grunes, and G. de Grandi, “Polarimetric SAR speckle filtering and its implication for classification”, *IEEE Transactions on Geoscience and remote sensing*, vol. 37, pp. 2363–2373, 1999. DOI: 10.1109/36.789635.
- [107] J. Chen, Y. Chen, W. An, Y. Cui, and J. Yang, “Nonlocal filtering for polarimetric SAR data: A pretest approach”, *IEEE Transactions on Geoscience and Remote Sensing*, vol. 49, pp. 1744–1754, 2011. DOI: 10.1109/TGRS.2010.2087763.

-
- [108] C.-A. Deledalle, F. Tupin, and L. Denis, "Polarimetric SAR estimation based on non-local means", in *Proceedings of the IEEE International Geoscience and Remote Sensing Symposium*, IEEE, 2010, pp. 2515–2518. DOI: 10.1109/IGARSS.2010.5653936.
- [109] S. Parrilli, M. Poderico, C. Angelino, G. Scarpa, and L. Verdoliva, "A nonlocal approach for SAR image denoising", in *Proceedings of the IEEE International Geoscience and Remote Sensing Symposium*, IEEE, 2010, pp. 726–729. DOI: 10.1109/igarss.2010.5651432.
- [110] A. Alonso-González, C. López-Martínez, P. Salembier, and X. Deng, "Bilateral distance based filtering for polarimetric SAR data", *Remote Sensing*, vol. 5, pp. 5620–5641, 2013. DOI: 10.3390/rs5115620.
- [111] G. Vasile, E. Trouve, J.-S. Lee, and V. Buzuloiu, "Intensity-driven adaptive-neighborhood technique for polarimetric and interferometric SAR parameters estimation", *IEEE Transactions on Geoscience and Remote Sensing*, vol. 44, pp. 1609–1621, 2006. DOI: 10.1109/tgrs.2005.864142.
- [112] E. Koeniguer Colin, F. Weissgerber, N. Trouvé, and J. Nicolas, "A new light on origins of polarimetric misclassification of the SOMA district, due to the difficulty to predict entropy", in *Proceedings of PolInSAR*, vol. 729, 2015.
- [113] D. Massonnet and J.-C. Souyris, *Imaging with Synthetic Aperture Radar*. EPFL Press, 2008.
- [114] J. Lopez-Sanchez, J. Fortuny-Guasch, S. Cloude, and A. Sieber, "Indoor polarimetric radar measurements on vegetation samples at L, S, C and X band", *Journal of Electromagnetic Waves and Applications*, vol. 14, pp. 205–231, 2000. DOI: 10.1163/156939300x00734.

5

CONCLUSIONS

This chapter presents a brief summary of the investigations made in the course of this dissertation. This is done by presenting the main research questions for each chapter and by summarizing answers and findings.

5.1 MAIN FINDINGS

5.1.1 Chapter 2: *Polarimetric Calibration of the Ku-Band Advanced Polarimetric Radar Interferometer (KAPRI)*

Chapter 2 treats radar data preprocessing and calibration for KAPRI, a Ku-Band real-aperture polarimetric radar interferometer based on the GAMMA Portable Radar Interferometer (GPRI-II). This investigation lays the foundation for all other studies performed with KAPRI, since properly processed and calibrated data, where the measured locations, reflectivities, and phases correspond to the true scatterer responses, is necessary for any application of radar data to environmental monitoring. The main questions addressed in this study are summarized as follows:

1. *How can the raw data processing scheme be adapted in order for the radar's phase and frequency response in all polarimetric channels to be free of systematic effects?*

The first question is closely tied to KAPRI's hardware design: distance resolution is obtained with a dechirp-on-receive architecture employing a frequency-modulated chirp with 200 MHz bandwidth giving an effective range resolution of 1 m. Cross-range resolution necessary for two-dimensional imaging is obtained by scanning a narrow beam emitted by a 2 m long slotted-waveguide antenna with an azimuth beamwidth of 0.48° . This combination permits acquiring two-dimensional radar images avoiding the problem of temporal decorrelation experienced by several rail-based terrestrial SAR systems. This design also allows imaging a larger circular sector. However, the slotted-waveguide antenna suffers from beam squint: as the chirped signal is transmitted, because of the increasing signal frequency the phasing relationship of the waves emitted at the antennas slot change, causing the antenna mainlobe direction to rapidly move in azimuth during the pulse. As a consequence, scatterers are only within the antenna pattern mainlobe during part of the chirp. This rapid beam sweep reduces the effective range bandwidth used to illuminate a given scatterer. At the same time, since the antenna is mechanically scanned at a

rate much slower than rate at which the beam squints; the effective beamwidth experienced by a point scatterer is broadened. Therefore, after performing range compression, the beam squint will deteriorate both range and azimuth resolutions. This effect has been observed experimentally by imaging trihedral corner reflectors (TCR) with oversampled azimuth acquisitions, where the antenna is rotated by angular step smaller than its beamwidth. In these images, the effect of beam-squint was seen in the fast time-azimuth angle plane as a rotation of the scatterer's response, which ideally should consist of a beat signal occupying the azimuth location of the scatterer and whose frequency is proportional to the slant range distance. The amount of rotation observed corresponds to the squint modeled using the antenna design characteristics. Thanks to the oversampled acquisition, the effect of squint can be corrected with a fast time-azimuth interpolation prior to the range compression, simulating the effect of the antenna beam dwelling on the same scatterer for the entire duration of each chirped pulse.

2. *Can the radar's polarimetric distortion parameters be estimated? If so, can they be used, together with the data processing methods mentioned above, to produce properly calibrated polarimetric imagery?*

The second question is a follow-on of the first. After the raw data is correctly processed into single look complex image, the measured polarimetric scattering matrix is distorted by the difference in antenna gains, crosstalk, cable lengths and electronic delays between the two pairs of transmitting and receiving polarimetric channels. Calibration is necessary to obtain full polarimetric imagery where the measured scattering matrices correspond to the true polarimetric signatures of the scatterers. A simplified distortion model that does not assume crosstalk between the transmitting or receiving channels is used to calibrate KAPRI data: this is possible because every element of the polarimetric scattering matrix is acquired separately, moreover a good polarimetric isolation—better than 30 dB—was estimated from the response of a trihedral corner reflector. With this model, the phase and amplitude imbalances between the channels can be determined using a single TCR and a reciprocal scatterer.

The proposed methods were tested using a scene where five TCR were placed. The results show that beam squint correction improves the range resolution by 0.2 m and the azimuth resolution by 0.05° corresponding to a relative resolution improvement of 20 and 10 percent respectively. The azimuth phase ramp in the VV channel is reduced from 40° to less than 10° inside of the beamwidth. Finally, after applying the polarimetric calibration parameters estimated on a TCR, the residual $HH - VV$ phase imbalance is reduced to less than 8° while the amplitude imbalance to less than 1.04.

This investigation shows that KAPRI can be used to reliably and accurately acquire full polarimetric Ku-Band radar data provided that the processing methods described above are used.

5.1.2 Chapter 3: *Geostatistical Analysis and Mitigation of Atmospheric Phase Screens in Ku-Band Terrestrial Radar Interferometric Observations of an Alpine Glacier*

Chapter 3 is an investigation connected to the original application of GPRI, the device from which KAPRI was developed: zero-baseline differential interferometry for displacement mapping. The motivation for

this study was a monitoring project organized in the summer months of 2015, where the device was set up at the Domhütte alpine hut in the Southwestern Swiss Alps to observe the surface displacement velocity of the nearby Bisgletscher glacier. The latter is a small, steep alpine glacier. Optical displacement estimates using a time-lapse camera, performed in the course of previous monitoring projects, showed a displacement velocity of 2 m/day in its steepest parts.

Terrestrial radar interferometry is very suitable to monitor these types of glaciers because it permits acquiring data at day and night with any weather conditions and at high repeat rate. However, temporal variations in phase delay caused by changing atmospheric water vapor content between the acquisitions—the so called atmospheric phase screen (APS)— may severely impair the displacement estimation precision attainable with differential interferometry: the APS phase contribution in the interferogram can be as large as the displacement phase. At first, this may seem to prevent the use of differential interferometry for displacement estimation. Displacement and APS are known to have different spatial and temporal statistical characters, enabling the use of mathematical methods to separate these contributions or to mitigate the effect of APS on the estimation. APS correction can be seen as a form of *phase calibration* necessary for the successful use of radar interferometry.

An extensive literature of APS correction approaches is published: most of these methods are tailored for the analysis of spaceborne InSAR data, where acquisitions of large spatial coverage with repetition times of days or weeks are available. In these cases, the assumption is that the APS shows a degree of spatial correlation but is not correlated in time, owing to the long timespan between subsequent data takes and to the turbulent nature of the atmosphere. Frequently, these assumptions are augmented with deterministic models of atmospheric stratification, that try to predict part of the phase variance with linear regression methods. While these assumptions proved sufficient to apply differential interferometry to spaceborne SAR data, it is not clear how well they translate to terrestrial radar interferometry. To understand to which extent these models apply to the terrestrial radar case, this study assesses the statistical behavior of the APS in Ku-Band terrestrial radar interferometry in the case of frequent acquisition in an Alpine scenario. To do so, statistical analyses were performed on a time-series acquired in 2015 during a campaign to monitor the Bisgletscher glacier. A set of short interferometric stacks was formed, each of these stacks was obtained by collecting all acquisitions within the timespan of an hour at randomly selected dates in the time-series. This random selection is made to sample the space of possible atmospheric conditions, while the short stack length minimizes temporal decorrelation and phase wrapping caused by the fast movement of the glaciers surface. Additionally, a set of persistent scatterers (PS) is detected, restricted to the areas outside of the glacier where displacement at the timescale of the acquisition repeat time is not expected. These points are used to evaluate the statistical behavior of the APS since the interferometric phase at these locations is neither affected by displacements nor by temporal decorrelation. Using these data, the following three questions are addressed:

1. *Can a multiple regression model be used to explain the phase variance caused by the APS?*

Using the differential interferometric phase at the PS, the performance of several multiple regression models of atmospheric stratification found in the literature is tested by fitting each model to the observations and computing the coefficient of determination (R^2) of each model fit. Additionally, cross-validation is performed by subtracting the model prediction from the interfero-

metric phases of another set of stable PS and computing the residual displacement rate from these phases: for these points the estimated velocity is expected to be 0 because they are not moving at the timescales of interest. The result of this analysis answers the first question, showing that the regression models for atmospheric stratification are not capable to explain a sizable fraction of the total phase variance as the lowest average R^2 is 0.5 for the best performing model. These models do not appreciably improve displacement estimation quality as measured by the standard deviation of the residual displacement velocity.

2. *Are the spatio-temporal statistics of the APS in Ku-Band TRI separable? Can the covariance of the APS at any two points in space and time be factored in a purely temporal and a purely spatial covariance?*

The second question generalizes the assumptions regarding the statistics of the APS made in spaceborne InSAR analyses. The APS is commonly assumed to be correlated in space and uncorrelated in time. By this assumption its covariance matrix can be decomposed as a Kronecker product of a spatial and a temporal covariance: the spatial statistics do not change over time. Moreover, as the temporal separation between acquisitions is large, the temporal covariance reduces to the identity matrix. Under these conditions, a single spatial covariance function is used to describe the spatial statistics of the APS. This covariance is used with geostatistical interpolation methods –for example Kriging– to reconstruct an approximation of the APS from a sparse set of points –usually a set of persistent scatterers– whose interferometric phase is not affected by displacement or decorrelation. The extrapolated APS is then subtracted from the interferogram, after which the residual APS can be mitigated by temporal filters exploiting the fact that it is not correlated in time.

How well do these solutions translate to terrestrial radar interferometry? The acquisition repeat times are often much shorter and the spatial extent of the scene is orders of magnitude smaller. In this case, instead of assuming *a priori* the APS to be uncorrelated in time, the assumption is generalized to spatio-temporal separability, where the temporal covariance, instead of being an identity matrix as in the case of temporally uncorrelated APS, is allowed to be any covariance matrix modeling possible temporal correlations of the APS due to the short repeat times.

The spatio-temporal statistics of the APS are estimated using the interferometric phases at the PS locations by computing interferograms with increasingly long temporal baseline and computing the spatial and temporal marginal variograms. The spatial variograms shows little variation as a function of temporal baseline, suggesting the validity of assuming a separable covariance model. Similar behaviors are observed for the temporal variograms, showing that after about 7 minutes the APS can be considered fully decorrelated.

3. *Can the regression model and the spatio-temporal statistics be used to extrapolate the APS from a set of scatterers known not to be affected by displacement? Can the temporal covariance model be used to improve the correction of the APS?*

The last question relates to the application of the above statistical models to the mitigation of APS in differential interferometry. As mentioned above, when a spatial covariance model is available,

it can be used to interpolate the APS at any location from a set of observations at points known not to be undergoing displacement. In this study, the extrapolation is performed using regression-Kriging, which accounts for the spatially correlated aspect of the APS and includes a stratification model in the prediction. In this context, the advantage of assuming a separable spatio-temporal model is that a spatial covariance model has to be determined only once and can then be used to predict the APS in all interferograms. After having removed the APS prediction from the interferogram stack, the temporal covariance model is used to estimate the displacement signal. In this study this is done by assuming a piecewise linear displacement and estimating the displacement parameters using a generalized least square inversion (GLS) employing the temporal covariance model estimated previously.

The performance of this method is assessed in the same manner employed for the stratification models, by inspecting the estimated displacement rate at locations outside of the glaciers outline, where no displacements are expected. This analysis shows that regression-Kriging based APS correction alone reduces the residual standard deviation from 1m/day observed in uncorrected interferograms to 0.25m/day and that the additional GLS inversion further reduces the standard deviation to less than 0.1m/day at the cost of a reduced temporal resolution of the velocity estimates.

In summary, this analysis shows that the combination of regression-Kriging and time-series inversion using a relatively simple separable spatio-temporal APS covariance model is sufficient to achieve a good quality interferometric phase calibration. This enables the estimation of fast ground displacements in the difficult atmospheric conditions encountered in alpine valleys. In terms of residual phase variance, the proposed approach significantly outperforms the standard phase calibration approach based on simple multiple linear regression methods followed by interferogram stacking.

5.1.3 Chapter 4: *Polarimetric Analysis of Natural Terrain Observed With a Ku-Band Terrestrial Radar*

Chapter 4 returns to radar polarimetry after in Chapter 2 it was demonstrated that KAPRI can be used to acquire well calibrated polarimetric datasets.

It is important to assess the applicability of the current radar polarimetric scattering models and techniques to KAPRI data since most studies in radar polarimetry tend to concentrate to the more widely available datasets acquired with air- and spaceborne SAR sensor at longer wavelengths, chiefly L and X bands. To do so, requires to analyze the polarimetric signatures of natural surfaces at Ku-Band. This is performed empirically using two datasets: a polarimetric time-series acquired in the Bisgletscher region, Swiss Alps and a scene acquired in a mixed agricultural and residential area near Bern. The analysis aims at answering two main questions:

1. *How do natural surfaces scatter polarized electromagnetic waves at Ku-Band?*

The first question was addressed by computing standard polarimetric parameters, such as the Cloude-Pottier decomposition parameters like the entropy H and the mean α angle, co- and cross-polar coherence magnitude and phase and backscatter power in all polarimetric channels.

These parameters were evaluated on several regions of interest (ROIS) corresponding to different terrain types. The land cover in the ROIS were verified with the use of orthophotos and land cover classifications maps.

The most salient result of this analysis is that a high -0.75 or more— polarimetric entropy and a significant cross-polarized backscatter are observed for all terrain types, except in correspondence of point-like scatterers such as trihedral reflectors or individual isolated buildings.

2. *How to explain the high polarimetric entropy observed for most natural surfaces at Ku-Band?*

The observation of a high entropy made in addressing the first question suggests the presence of depolarizing scattering processes in most of the scene. Depolarizing scattering is usually attributed to the presence of several elementary scattering centers with different orientations, shapes or dielectric properties in the same resolution cell. At the light of the large resolution cell sizes and of the short wavelength employed by KAPRI, this explanation appears realistic.

However, since averaging is necessary to estimate most polarimetric parameters derived from the second order statistics of the scattering matrix, mixing of heterogeneous pixels in the estimation process—usually performed by spatial multilooking— has been implicated in artificially increasing the observed entropy. This effect has been investigated by comparing different averaging methods: the standard boxcar filter, the IDAN [1] region-growing spatial filter and a temporal entropy estimate obtained averaging data acquired over the timespan of a day.

Little difference in entropy is observed between the two spatial filters, while the entropy estimated using temporal averaging is significantly lower. Large differences in temporal entropy are observed among terrain types: very low for rocks and high for the glaciers surface and vegetated areas, a contrast which is not seen in the spatial estimates. This difference is presumably a consequence of non-ergodicity: the samples of the scattering matrix over which the temporal average is estimated are not independent realizations of the same scattering process because the surface properties are likely to change in the course of time. In the case of the glacier the main factors are assumed to be the fast motion (up to 2 m/day) and changes in ice water content caused by changing weather conditions, which modify the reflectivity of the ice, while in the case of vegetation, motion caused by wind and moisture changes are the presumably drivers of this behavior. The low entropy observed for rocks may also stem from non-ergodic behavior: even if the rock surface is a depolarizing scatterer in the strict sense—a scatterer where many randomly oriented scattering centers are observed in a single resolution cell, as indicated by the significant cross-polar contribution—, the temporal samples would be statistically very similar because no major changes in scattering behavior are expected during the timespan of averaging, decreasing the temporal entropy estimates.

In summary, this analysis shows that modeling polarimetric scattering is a complex problem where sensor characteristics, scatterer properties and parameter estimation methods all contribute to the observed signatures. While proper polarimetric calibration can help reduce this ambiguity in the case of deterministic scatterers, the influence of resolution cell size and of parameter estimation on the signatures of depolarizing scatterers should always be considered when polarimetric data is analyzed.

5.2 OUTLOOK

This dissertation is primarily focused on two aspects of KAPRI, a polarimetric terrestrial radar interferometer developed on the basis of the Gamma Portable Radar Interferometer (GPRI) II [2]. A large part of the thesis is dedicated to the calibration of this device. This part in turn consists of two topics: On the one side, polarimetric calibration and the adaptation of KAPRI's predecessor processing scheme to the newly added polarimetric acquisition mode. On the other side, phase calibration for its original application as a terrestrial radar interferometer, where the statistical modeling and correction of atmospheric phase screens in high repeat rate differential interferometric observations were addressed.

Regarding the issue of phase calibration for differential interferometry, an aspect to be addressed is the use of auxiliary observations such as weather measurements [3, 4], estimates of the wet zenith delay (WZD) obtained from global navigation satellite system (GNSS) [5–7] or of optical observations [8, 9] to model and mitigate the APS. The statistical analysis made in this thesis shows that most of the atmospheric phase error should be attributed to atmospheric turbulence, highlighting the importance of studying the statistics of the APS. In this context, a spatio-temporal covariance model for the turbulent APS was developed, which allows for temporal correlation. To better understand the temporal statistics of the APS, measurement at a faster sampling rate could be used: KAPRI permits stationary measurement where the antenna is not scanned, offering a sampling rate up to 400 Hz. Similarly, a better understanding of the APS statistics would require analyzing datasets acquired at different locations and possibly for longer time periods to assess the temporal stationarity of the APS and its seasonal behavior. This analysis was not possible—because of technical limitations—with the Bisgletscher dataset employed in the study since only data from one season was available. Finally, external displacement estimates from point measurements using GNSS or derived from time-lapse cameras deserve to be considered, as they could help validate the APS correction methods proposed in this thesis.

Moving to the topic of the applications of KAPRI, this thesis includes an assessment of the potential of Ku-band terrestrial radar polarimetry. This was accomplished by analyzing polarimetric signatures of natural terrain. The results indicate that, at this wavelength polarimetric measurements do not show the polarimetric diversity observed in polarimetric SAR studies performed at longer wavelengths. However, carefully controlled experiments would be necessary to understand whether the lack of diversity and the high scattering entropy observed for most terrain types comes about because these scatterers are primarily composed of scattering centers whose size is comparable with the wavelength or rather because several different scattering processes combine in the resolution cell due to the relatively low-resolution observations employed in the study. In the same manner, the preliminary study showed that the averaging methods necessary to estimate the depolarization parameters significantly impact these estimates. Once again controlled experiments may permit to quantify the effect of averaging and to separate it from the scatterer's characteristics and from the sensor own response.

Finally, the combination of GPRI's original purposes—radar interferometry with a spatial baseline and zero-baseline differential interferometry—with KAPRI's polarimetric imaging capabilities is another topic deserving consideration. In the configuration called polarimetric radar interferometry (PolInSAR), polarimetric data acquired along a spatial baseline have been employed to estimate the vertical struc-

ture of vegetation with airborne SAR data [10, 11], usually relying on layered vegetation scattering models [10, 12]. The validity of these models for Ku-Band data could be assessed by carrying out small-scale vegetation monitoring at short repeat times over longer time-spans.

Similarly, polarimetric data can be combined with differential interferometry (PolDInSAR): this can be used to improve the interferometric phase quality by coherence optimization [13, 14] or to improve the selection of persistent scatterers [15–19]. However, as in the PolInSAR case these methods were developed and tested with terrestrial SAR sensors operating at longer wavelengths (mainly X-Band); their applicability to the shorter wavelength employed by KAPRI should be investigated.

REFERENCES

- [1] G. Vasile, E. Trouve, J.-S. Lee, and V. Buzuloiu, “Intensity-driven adaptive-neighborhood technique for polarimetric and interferometric SAR parameters estimation”, *IEEE Transactions on Geoscience and Remote Sensing*, vol. 44, pp. 1609–1621, 2006. DOI: 10.1109/tgrs.2005.864142.
- [2] C. L. Werner, A. Wiesmann, T. Strozzi, A. Kos, R. Caduff, and U. Wegmüller, “The GPRI multi-mode differential interferometric radar for ground-based observations”, in *Proceedings of the European Conference on Synthetic Aperture Radar*, VDE, 2012, pp. 304–307.
- [3] L. Iannini and A. Monti Guarnieri, “Atmospheric phase screen in ground-based radar: Statistics and compensation”, *IEEE Geoscience and Remote Sensing Letters*, vol. 8, pp. 537–541, 2011. DOI: 10.1109/LGRS.2010.2090647.
- [4] X. Fabregas, R. Iglesias, and A. Aguasca, “A new approach for atmospheric phase screen compensation in ground-based SAR over areas with steep topography”, *Proceedings of the European Conference on Synthetic Aperture Radar*, pp. 12–15, 2012.
- [5] T. R. Emardson, M. Simons, and F. H. Webb, “Neutral atmospheric delay in interferometric synthetic aperture radar applications: Statistical description and mitigation”, *Journal of Geophysical Research: Solid Earth*, vol. 108, p. 2231, 2003. DOI: 10.1029/2002jb001781.
- [6] F. Onn and H. A. Zebker, “Correction for interferometric synthetic aperture radar atmospheric phase artifacts using time series of zenith wet delay observations from a GPS network”, *Journal of Geophysical Research: Solid Earth*, vol. 111, pp. 1–16, 2006. DOI: 10.1029/2005JB004012.
- [7] S. Williams, Y. Bock, and P. Fang, “Integrated satellite interferometry: Tropospheric noise, GPS estimates and implications for interferometric synthetic aperture radar products”, *Journal of Geophysical Research: Solid Earth*, vol. 103, pp. 27 051–27 067, 1998. DOI: 10.1029/98JB02794.
- [8] Z. Li, J.-P. Muller, P. Cross, P. Albert, J. Fischer, and R. Bennartz, “Assessment of the potential of MERIS near-infrared water vapour products to correct ASAR interferometric measurements”, *International Journal of Remote Sensing*, vol. 27, pp. 349–365, 2006. DOI: 10.1080/01431160500307342.

- [9] Z. W. Li, W. B. Xu, G. C. Feng, J. Hu, C. C. Wang, X. L. Ding, and J. J. Zhu, “Correcting atmospheric effects on InSAR with MERIS water vapour data and elevation-dependent interpolation model”, *Geophysical Journal International*, vol. 189, pp. 898–910, 2012. DOI: 10.1111/j.1365-246x.2012.05432.x.
- [10] S. Cloude and K. Papathanassiou, “Three-stage inversion process for polarimetric SAR interferometry”, *IEE Proceedings - Radar, Sonar and Navigation*, vol. 150, p. 125, 2003. DOI: 10.1049/ip-rsn:20030449.
- [11] —, “Polarimetric SAR interferometry”, *IEEE Transactions on Geoscience and Remote Sensing*, vol. 36, pp. 1551–1565, 1998. DOI: 10.1109/36.718859.
- [12] M. Pichierri, I. Hajnsek, S. Zwieback, and B. Rabus, “On the potential of polarimetric SAR interferometry to characterize the biomass, moisture and structure of agricultural crops at L-, C- and X-bands”, *Remote Sensing of Environment*, vol. 204, pp. 596–616, 2018. DOI: 10.1016/j.rse.2017.09.039.
- [13] R. Iglesias, D. Monells, X. Fabregas, J. J. Mallorqui, A. Aguasca, and C. Lopez-Martinez, “Phase quality optimization in polarimetric differential SAR interferometry”, *IEEE Transactions on Geoscience and Remote Sensing*, vol. 52, pp. 2875–2888, 2014. DOI: 10.1109/TGRS.2013.2267095.
- [14] L. Pipia, X. Fabregas, A. Aguasca, C. Lopez-Martinez, and J. J. Mallorqui, “Polarimetric coherence optimization for interferometric differential applications”, in *Proceedings of the IEEE International Geoscience and Remote Sensing Symposium*, IEEE, 2009. DOI: 10.1109/igarss.2009.5417712.
- [15] R. Iglesias, A. Aguasca, X. Fabregas, J. J. Mallorqui, D. Monells, C. Lopez-Martinez, and L. Pipia, “Ground-based polarimetric SAR interferometry for the monitoring of terrain displacement phenomena—part II: Applications”, *IEEE Journal of Selected Topics in Applied Earth Observations and Remote Sensing*, vol. 8, pp. 1–14, 2014. DOI: 10.1109/JSTARS.2014.2366711.
- [16] —, “Ground-based polarimetric SAR interferometry for the monitoring of terrain displacement phenomena—part I: Theoretical description”, *IEEE Journal of Selected Topics in Applied Earth Observations and Remote Sensing*, vol. 8, pp. 1–1, 2014. DOI: 10.1109/JSTARS.2014.2360040.
- [17] L. Pipia, X. Fabregas, A. Aguasca, C. Lopez-Martinez, S. Duque, J. J. Mallorqui, and J. Marturia, “Polarimetric differential SAR interferometry: First results with ground-based measurements”, *IEEE Geoscience and Remote Sensing Letters*, vol. 6, pp. 167–171, 2009. DOI: 10.1109/LGRS.2008.2009007.
- [18] V. D. Navarro-Sanchez and J. M. Lopez-Sanchez, “Spatial adaptive speckle filtering driven by temporal polarimetric statistics and its application to PSI”, *IEEE Transactions on Geoscience and Remote Sensing*, vol. 52, pp. 4548–4557, 2014. DOI: 10.1109/TGRS.2013.2282406.
- [19] V. D. Navarro-Sanchez, J. M. Lopez-Sanchez, and L. Ferro-Famil, “Polarimetric approaches for persistent scatterers interferometry”, *IEEE Transactions on Geoscience and Remote Sensing*, vol. 52, pp. 1667–1676, 2014. DOI: 10.1109/TGRS.2013.2253111.

Peer Reviewed Publications

- S. Baffelli, O. Frey, C. Werner, and I. Hajnsek, “Polarimetric calibration of the Ku-band advanced polarimetric radar interferometer”, *IEEE Transactions on Geoscience and Remote Sensing*, vol. 56, pp. 1–17, Apr. 2018. DOI: 10.1109/tgrs.2017.2778049

Publications Submitted For Peer Review

- S. Baffelli, O. Frey, and I. Hajnsek, “Geostatistical analysis and mitigation of atmospheric phase screens in Ku-band terrestrial radar interferometric observations of an alpine glacier”, *IEEE Transactions on Geoscience and Remote Sensing*, 2018, submission ID TGRS-2018-01579
- S. Baffelli, O. Frey, and I. Hajnsek, “Polarimetric analysis of natural terrain observed with a Ku-band terrestrial radar”, *IEEE Journal of Selected Topics in Applied Earth Observation and Remote Sensing*, 2018, submission ID JSTARS-2018-00992

Publications in Conference Proceedings

- S. Baffelli, O. Frey, and I. Hajnsek, “Geostatistical analysis and mitigation of atmosphere induced phase in terrestrial radar interferometric observations of an alpine glacier”, in *Proceedings of the European Conference on Synthetic Aperture Radar*, Jun. 2018
- S. Baffelli, O. Frey, and I. Hajnsek, “Geostatistical analysis and mitigation of atmospheric phase screens in Ku-band terrestrial radar interferometry”, in *Proceedings of the IEEE International Geoscience and Remote Sensing Symposium*, 2018
- S. Baffelli, O. Frey, and I. Hajnsek, “System characterization and polarimetric calibration of the Ku-band advanced polarimetric interferometer”, in *Proceedings of the European Conference on Synthetic Aperture Radar*, 2016, pp. 2–5
- S. Baffelli, A. Marino, and O. Frey, “Ku-band polarimetric-interferometric ground based real aperture radar: Calibration and first observations”, in *Proceedings of PolInSAR*, 2015
- S. Baffelli, O. Frey, and I. Hajnsek, “Improved polarimetric calibration of KAPRI, a Ku-band ground-based polarimetric radar interferometer”, in *Proceedings of PolInSAR*, 2017